Oscillatory and radiative properties of solar magnetic flux concentrations

A thesis submitted for the degree of:

Doctor of Philosophy

by

Damien Francis Przybylski

B. Sci. (Hons), B. Math.

Monash Centre for Astrophysics

School of Mathematical Sciences

Monash University

Australia

February 17, 2017

Table of Contents

Abstract

Forward modelling of wave motions is used to investigate the structure of solar magnetic fields, from small scale intergranular flux tubes to large sunspots. While these structures share some degree of similarity, observationally they differ significantly, due to different physical length scales involved, as well as to instrumental effects and observational resolution. In this thesis we apply computational magnetohydrodynamics and spectral line synthesis to answer two questions about solar magnetic field concentrations; i) how can we use spectropolarimetry to identify observational signatures of wave propagation in a sunspot model, ii) can the Alfvénic "vortices" observed in magnetoconvection simulations heat the solar chromosphere.

The first question involves the study of synthetic centre-to-limb observations of acoustic wave behaviour in sunspots and its implications for helioseismology. Modern observational instruments allow for high resolution Doppler imaging, through instruments such as the Helioseismic and Magnetic Imager (HMI) on the Solar Dynamics Observatory (SDO). To understand the observations made with these instruments we must understand both the magnetohydrodynamic and radiative effects. We produce a model of a sunspot that gives realistic simulated spectropolarimetry and perform magnetohydrodynamic simulations of wave propagation within it. By studying the centre-to-limb variation around the sunspot we identify slow modes in the sunspot umbra as an increase in acoustic power away from the disk centre. This work represents an important step in the comparison of computational helioseismic results with observations.

The second question requires the simulation of waves in a small-scale intergranular magnetic flux tube. We identify the spectropolarimetric signatures of these photospheric vortices, as seen in MURaM magneto-convection simulations. It is shown that current observational equipment is unable to resolve these motions, next-generation solar telescopes will be required. We perform a non-ideal simulation of wave propagation in an intergranular flux tube model and show that ion-neutral interactions can efficiently damp Alfvén waves, heating the chromosphere. This heating is shown to be strongly dependent on non-linear effects, as shocks perturb the flux tube. High frequency waves are shown to be deflected along the outer field lines of the flux tube, leading to lower amplitudes in the flux tube centre and less efficient heating. The dissipation of wave energy through ion-neutral interactions in magnetic structures shows potential to provide an important part of the chromospheric energy balance.

General Declaration

Monash University

Declaration for thesis based or partially based on conjointly published or unpublished work

In accordance with Monash University Doctorate Regulation 17.2 Doctor of Philosophy and Research Masters regulations the following declarations are made:

I hereby declare that this thesis contains no material which has been accepted for the award of any other degree or diploma at any university or equivalent institution and that, to the best of my knowledge and belief, this thesis contains no material previously published or written by another person, except where due reference is made in the text of the thesis.

This thesis includes six (6) original papers published in peer reviewed journals. The core theme of this thesis is mode conversion and its effects around solar active regions. The ideas, development and writing up of all the papers in the thesis were the principal responsibility of myself, the candidate, working within the School of Mathematical Sciences under the supervision of Prof. Paul S. Cally and Dr Sergiy Shelyag.

The inclusion of co-authors reflects the fact that this work came from active collaboration between researchers and acknowledges input into team-based research.

In the case of chapters 3-5, and appendices A-C my contribution to the work involved the following:

Thesis chapter	Publication title	Publication status	Nature and extent of candidate's contribution
3	Centre-to-limb spectro-polarimetric diagnostics of simulated solar magneto-convection: signatures of Alfvén waves	Published, 2014, PASJ 66, SP1, S9	Generation of synthetic observables used in Figure 1 and 2, writing and editing relevant part of paper.
4	Spectropolarimetrically accurate magnetohydrostatic sunspot model for forward modeling in helioseismology	Published, 2015, ApJ 807, 20	Key ideas, development of model and code, production of all results, writing of paper
5	Heating of the partially ionized solar chromosphere by waves in magnetic structures	Published 2016,ApJL 819,L11	Key ideas, assistance with code and model development, assistance with data analysis.
A	MHD Wave Refraction and the Acoustic Halo Effect Around Solar Active Regions: A 3D Study	Published 2015, ApJ 801, 27R	Assistance in Code and model development
B	3D Simulations of Realistic Power Halos in Magnetohydrostatic Sunspot Atmospheres: Linking Theory and	Published 2016, ApJ 817, 45R	Assistance in code and model development
C	Directional time-distance probing of model sunspot atmospheres	Published 2015, MNRAS 449,3,3074	Assistance in code and model development

I have renumbered sections of submitted or published papers in order to generate a consistent presentation within the thesis.

Signature: ....

Name: ....

Date: ....

Acknowledgments

I would like to thank my supervisors, wife, teachers, colleagues, family, friends and all the other random people that kept me sane, interested, happy and sufficiently distracted.

Introduction

Solar physics provides unique insights into stellar structure as the Sun is the only star whose surface and atmosphere we can resolve. The ability to perform high resolution observations of the solar surface phenomena makes the Sun the ideal laboratory to study the formation and evolution of stellar magnetic fields. Despite their importance, many questions still remain about solar magnetic fields; from understanding the solar dynamo and modelling of the solar magnetic cycle, to the formation and evolution of surface magnetic flux concentrations, and the role of magnetic fields in the heating of the chromosphere and corona.

The study of solar oscillations, through helioseismology, provides a method to measure solar structure, subsurface flows and solar convection. Helioseismology involves combining observational data with theoretical and computational modelling of wave propagation to probe the medium which the waves pass through. Observations of the periodic oscillations of the solar surface were first made by Leighton et al. (1962); Evans & Michard (1962). These signals are used by global helioseismology to infer the large scale structure of the Sun. The more modern field of local helioseismology has been developed to study smaller features, such as flows and subsurface structure around solar active regions. The principles of helioseismology can also be applied to the solar atmosphere, using the oscillations of coronal flux tubes to infer the local plasma properties.

Global helioseismology is performed by measuring long time-series of the velocity or intensity at solar surface and comparing the observed frequencies to the eigenmode frequencies of solar models. Three oscillatory mode types are predicted in theoretical studies. Acoustic $p-$modes have pressure as their restoring force and are strongest in the $2-4$ mHz frequency range. There are two types of gravitational modes: $g-$modes, which have a low frequency < 0.5 mHz and propagate below the convection zone, and surface $f-$modes, which are surface gravity waves attached to the photosphere. Internal gravity modes associated with the core have not yet been definitively identified in surface oscillations and therefore cannot be used as seismic probes. The standing modes of the spherical Sun (Stein & Leibacher, 1974) are trapped, as they are reflected from the photosphere and from the increasing sound speed with depth in the solar

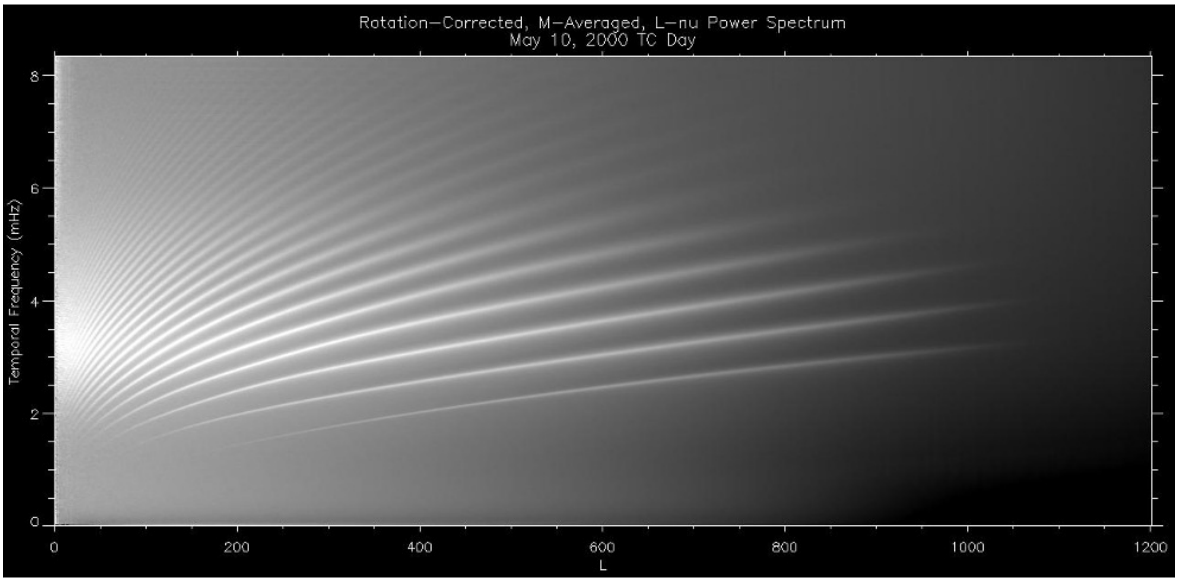

Fig. 1: An l-ν diagram measured using the Global Oscillation Network Group (GONG) instruments. The figure shows the variation in surface velocity power with frequency ν and spherical harmonic degree l, which is proportional to the horizontal wavenumber $k_h = \sqrt{l\,(l+1)}/R_\odot$), where $R_\odot$ is the solar radius. The bright ridges are the $f-$mode and $p-$modes, corresponding to discrete radial order n. Figure from: NSO/GONG.

interior. These modes are characterised by their spherical harmonic degree l, radial order n and azimuthal order m. The eigenmodes can be visualised using an l-ν diagram which show ridges of increased power corresponding to the $f-$ and $p-$modes in the solar interior (Ulrich, 1970). Each ridge corresponds to a discrete value of n (Figure 1).

Local helioseismology was developed to study flows and plasma structures on smaller scales. In order to do this the full wavefield must be interpreted, rather than the global eigenmodes. Modern focuses of local helioseismology include the seismic detection of the plasma properties underneath sunspots, and subsurface flows, with important implications towards understanding of the solar dynamo and the solar cycle. Local helioseismology has so far had no definite success in measuring subsurface magnetic fields. Measurements of subsurface magnetic fields would be an important step in understanding the formation and evolution of active regions, whose magnetic fields contain the energy which can be transported into the solar atmosphere and released in the form of flares and coronal mass ejections.

Time-distance helioseismology is a particular local helioseismic technique that involves measuring the travel times and distances of a wave between two points on the solar surface and thus determining the local sub-surface properties and dynamics (Gizon & Birch, 2005). First, filtering is performed to remove the effect of solar rotation as well as low frequency signals caused by convective motions in the photosphere. The cross-covariance is then calculated between two points, or a ring of points. This gives a measure of the phase and time lag of waves travelling in either direction, between the different positions. By fitting a wavelet to the observed cross-covariance the travel time can be calculated. In Figure 2, a time-distance plot shows a series of wave packets corresponding to the number of bounces, or times the wave has been reflected off the solar surface. Travel time inversion kernels are then used to infer the causes of these travel time differences, whether from magnetic fields, thermodynamic effects or flow perturbations. The first of these is problematic because of the high plasma beta at even moderate depth, and the current lack of practical and accurate magnetic kernels that account for mode conversion.

Theoretical investigations of wave propagation in solar magnetic fields have been performed using geometric ray calculations (infinitely short wavelength approximation). These calculations are performed by following the propagation of a sound-speed perturbation and measuring the shifts in travel time of a ray passing through a inhomogeneous medium. To first order this can be calculated by integrating the unperturbed ray path. This provides an explanation to the coupling of fast and slow magnetoacoustic waves in an idealised vertical magnetic field. A generalised ray theory, which has been formalised to no longer use the perturbation method, can be applied to more complex magnetic field models (Cally, 2007). This new theory has allowed the inclusion of wave transmission and absorption as rays pass through the equipartition level, where the Alfvén velocity is equal to the sound speed and mode conversion between fast and slow magneto-acoustic waves occurs, for a variety magnetic field configurations (Schunker & Cally, 2006). The assumption of infinitely short wavelength made in ray calculations prevents it from providing a complete look at the wave process. Numerical simulations are required.

The interaction of acoustic $p-$modes with solar magnetic fields that occurs when a wave enters a region of strong magnetic field lead to significant changes in the wave travel times used in helioseismic inversions (Moradi & Cally, 2013). Four processes associated with strong magnetic fields dominate wave behaviour in sunspots: fast-to-slow mode conversion at the Alfvén/acoustic equipartition level $v_A/c_s = 1$ allows slow waves to transmit into the upper atmosphere or converts them to magnetic (fast) waves otherwise (Cally, 2006; Schunker & Cally, 2006); the "ramp effect" that reduces

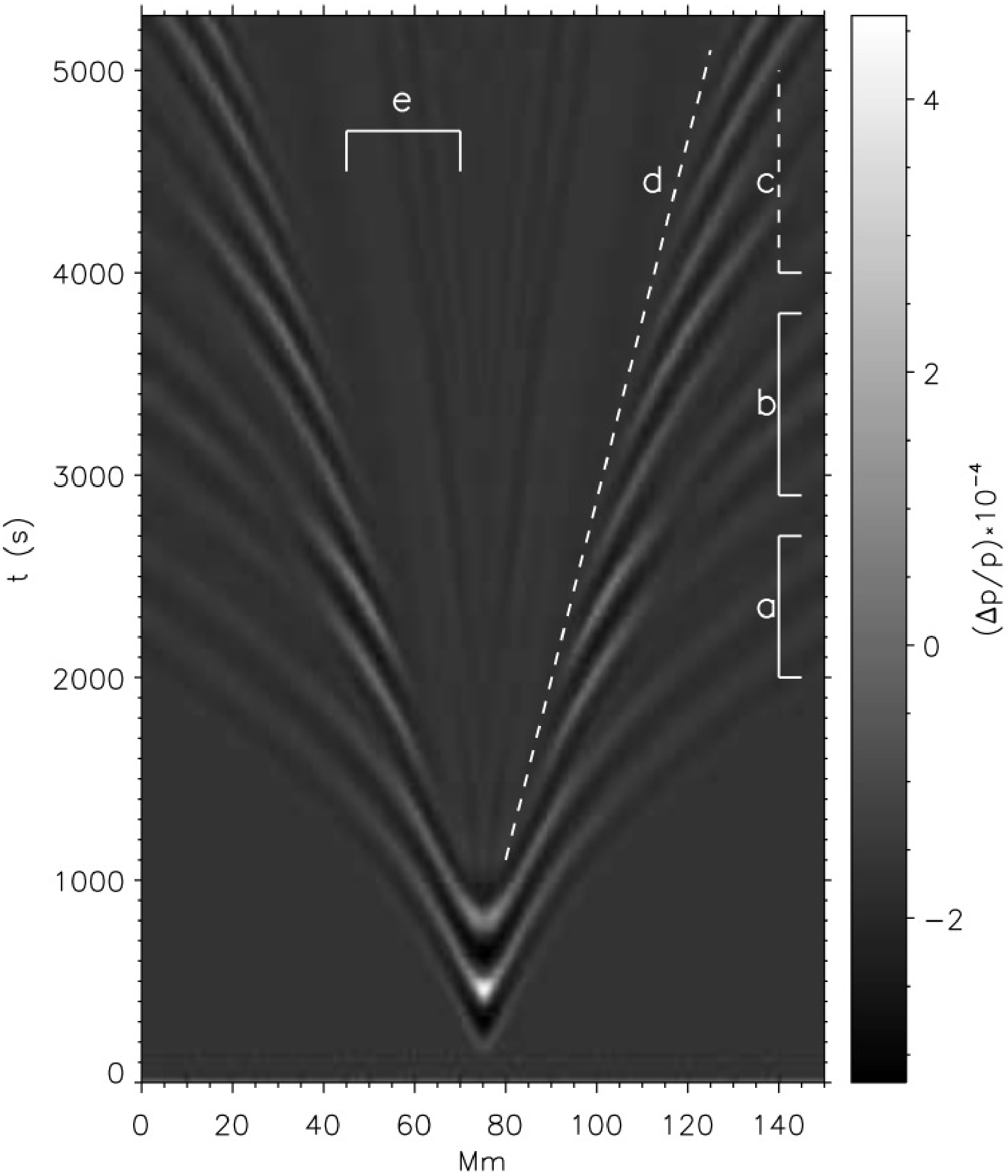

Fig. 2: A time-distance diagram showing the pressure perturbation, scaled by the background pressure, as a function of time and distance for a 2D simulation domain. The diagram shows the different acoustic wave-packets, the first to arrive at the surface is (a) first bounce, followed by (b) second bounce, and (c) higher order bounces. A surface wave is seen as (d), and a wave in the temperature minimum as (e). Figure from Shelyag et al. (2006).

the effective acoustic cutoff frequency depending on the magnetic field direction (Bel & Leroy, 1977); fast wave reflection around the height where the Alfvén speed matches the fast wave horizontal phase speed; and fast to Alfvén mode conversion near the fast wave reflection level, generating upward and downward propagating Alfvén waves (Cally & Hansen, 2011). Fast-to-slow conversion is found to produce large negative travel time shifts, while fast-to-Alfvén conversion generates positive shifts provided the vertical plane of the wave vector is nearly perpendicular to the magnetic field lines (Cally & Moradi, 2013). The complexity and sensitivity to magnetic field of wave motions above the equipartition level makes interpretation of observations difficult. Due to these difficulties the seismic detectability of sub-surface magnetic fields is an active research area. Many techniques are currently in development, such as directional time-distance seismology (Moradi et al., 2015), two-skip helioseismology (Duvall et. al. in prep) and full waveform inversions (Hanasoge et al., 2011; Hanasoge & Tromp, 2014).

Modern solar observational instruments have enabled high resolution, high cadence imaging in a number of wavelengths from infrared to ultraviolet. Using these instruments, the Sun can be imaged from the lowest visible layers of the solar atmosphere through to the high corona. Spectropolarimetric observations, which measure the full polarisation state of light across a range of wavelengths, can be used for Doppler imaging and reconstruction of the vector magnetic field in the solar atmosphere. Measurements of magnetic fields in the optically thin corona is difficult due to the low-level of signal. Current space-based instruments used for local (and global) helioseismology include the Helioseismic and Magnetic Imager (HMI) on the Solar Dynamics Observatory (SDO) (Scherrer et al., 2012), the Michelson Doppler Imager (MDI) on the Solar and Heliospheric Observatory (SOHO), and future missions such as the Solar Orbiter (Müller et al., 2013). Solar spectropolarimetry has allowed the study of the structure of large (Rajaguru et al., 2013) and small scale magnetic field structures (Ishikawa et al., 2008), as well as their temporal evolution (Ishikawa et al., 2010).

Modern ground-based telescopes, such as GREGOR, Vacuum Tower Telescope (VTT), Swedish Solar Telescope (SST) and the New Solar Telescope (NST) provide high-resolution (< 100 km), high-cadence (seconds) observations of the solar surface. Future 4-meter telescopes, such as the planned Daniel K. Inouye Solar Telescope (DKIST) and European Solar Telescope (EST), will have an even higher resolution. Instruments such as HELLRIDE (Staiger, 2012) simultaneously measure multiple spectral lines. As these lines are formed at different heights in the solar atmosphere, this gives a three dimensional view of the solar atmospheric processes. The modern high resolution, high cadence, multi-wavelength view of the Sun reveals a wealth of structure and dynamical complexity that could not have even been guessed a few decades ago. In particular, waves are found everywhere, playing important roles in energy transport and providing seismic information on the parameters of the plasma in which they propagate.

There remains uncertainty about the mechanisms behind the heating of the outer atmosphere of the Sun, causing its temperature to increase from 6420 kelvin at the photosphere to millions of Kelvin in the corona (Grotian, 1939). There are a number of possible mechanisms to provide this energy, such as magnetohydrodynamic waves (Narain & Ulmschneider, 1996; Arregui, 2015) or small scale reconnection-driven events such as nano-flares (Parker, 1988; Cargill et al., 2015). However, there is neither a clear understanding of the energy transport and release mechanism, nor of the amount of energy carried by these processes. This must be determined before we can understand how the observed structures of the chromosphere, transition region and corona are formed and maintained.

The observed features and dynamics of the solar photosphere, chromosphere and corona have their roots in the turbulent magnetoconvection occurring in the solar interior. The convective zone spans the region between the radiative zone at 0.71 solar radii ($R_\odot$) and the photosphere at 1 $R_\odot$. The convective motions are observed at the solar surface as granulation with a spatial scale of around 1.5 Mm. The convective scale increases up to 35 Mm supergranules, first observed using Doppler velocity measurements near the solar limb (Hart, 1954). Granules are regions of hot plasma upflow and are surrounded by a network of cooler downflow regions, known as intergranular lanes. Intergranular lanes concentrate magnetic field leading to the formation of structures up to a few kilogauss strength (Stenflo, 1973; Grossmann-Doerth et al., 1998). Turbulent near-surface magnetoconvection acts as an acoustic source for the stochastic solar $p-$mode spectrum (Goldreich & Keeley, 1977). The observed behaviour exhibited by these waves changes as they travel upwards into the chromosphere and corona, or encounter magnetic fields (Khomenko & Calvo Santamaria, 2013).

Solar physics, and astrophysics in general, is limited as most experimental data is obtained through measurements of electromagnetic radiation. In order to understand the observable surface and atmospheric solar phenomena, we must use forward modelling to investigate the subsurface processes generating them. While simplified analytical models provide an important insight into the physical processes observed, simulations are necessary to extend this to more complicated models and improved realism. Computations with realistic magnetic fields have been limited by the Courant-Friedrichs-Lewy

(CFL) condition (Courant et al., 1928), which gives a maximum timestep Δt for numerical stability when using a finite difference scheme ($\Delta t = C_{max}\frac{\Delta x}{V}$ for velocity V and spatial resolution Δx). Here C_{max} is the CFL coefficient, the maximum value for which the simulation will remain stable. Typically, these coefficients are around 0.5 to 1.5 and will vary with the spatial derivative and temporal integration scheme in use. This gives a demanding restriction in the case of magnetohydrodynamic simulations where we aim to resolve small scale phenomena in regions with a high Alfvén velocity v_A. Rapid improvements in computational power already make it possible to perform forward modeling of magnetohydrodynamic wave propagation and mode conversion in "realistic" solar magnetic field structures using codes such as MANCHA (Felipe et al., 2010), VAC (Shelyag et al., 2008), SLIM (Cameron et al., 2007) and SPARC (Hanasoge, 2011).

Magnetohydrodynamic simulations have been used to investigate the mechanisms behind the formation of acoustic halos around solar active regions (Hanasoge, 2008; Khomenko & Collados, 2009; Rijs et al., 2015, 2016). Magnetohydrodynamic mode-conversion has been simulated in a range of realistic magnetic field structures to determine the efficiency of transmission and conversion of an incoming acoustic wave (Khomenko & Cally, 2012; Felipe et al., 2011). Forward modelling for computational helioseismology has been used to infer subsurface flows (Shelyag et al., 2007; Bhattacharya & Hanasoge, 2016) and study the acoustic response of active regions (Birch et al., 2009).

Modern simulations of the solar photosphere, which include realistic physics, such as non-grey radiation transport and a non-ideal equation of state, show almost ubiquitous torsional waves in magnetic field concentrations that appear to be Alfénic in nature. The generation and propagation of these Alfvénic motions are not well understood, while it is suggested that these motions play a role in the energy transmission through the solar structured-atmosphere. However, Vranjes et al. (2008) argue that the very low ionization fraction around the temperature minimum greatly reduces the energy flux that may be carried by Alfvén waves. Tsap et al. (2011) find that the Alfvén wave amplitudes do not depend on the ionization fraction, similar results were found by Zaqarashvili et al. (2011a,b, 2013). Those who argue for the importance of Alfvén waves generated near the photosphere for the upper atmosphere of the Sun include Cranmer & Van Ballegooijen (2005) and Jess et al. (2009). Better understanding of this process is vital due to its potential to explain the physical mechanisms of solar chromospheric and coronal heating.

Vortex motions have been observed in studies of magnetic bright points (MBP's) in quiet solar regions (Bonet et al., 2008). These motions appear in simulations as small-scale circular or spiral structures located in intergranular field concentrations (Shelyag et al., 2012). The behaviour of these solar vortices is unlike those seen in a purely hydrodynamic "sink" case as both positive and negative vertical components of vorticity are seen, as well as the high horizontal velocities. A strong vertical Poynting flux is observed, indicating the transfer of energy upwards to the solar atmosphere. However, in the lower photosphere these small-scale twisting motions are below the resolution limit of current telescopes (Shelyag & Przybylski, 2014).

Observations and simulations of torsional motions in intergranular magnetic flux tubes provide a means to experimentally measure their interior structure. A range of hydromagnetic waves, i.e. Alfvén, fast and slow magnetosonic waves are produced as well as wave modes, such as kink and sausage modes (Fedun et al., 2011). These could propagate into the upper atmosphere and heat the chromosphere and corona, though a mechanism to efficiently dissipate these waves is currently not well understood.

Magnetic structures, from sunspots to smaller pores, plage and intergranular flux concentrations, are manifestations of solar activity. The importance of magnetic effects in plasma can be quantified by the plasma-β parameter, which is defined as the ratio of gas to magnetic pressure, meaning a high-β plasma is dominated by hydrodynamic forces and a low-β plasma by magnetic ones. Solar surface regions with strong magnetic field (low-β) have a substantially higher magnetic pressure than gas pressure. Maintaining pressure balance with the surrounding plasma that has a lower magnetic field leads to a decreased gas pressure and temperature, and inhibits convective plasma motions. This causes sunspots and pores to appear as dark areas on the solar surface (Rempel & Schlichenmaier, 2011).

Sunspots are one of the most prominent visually observable markers of the solar magnetic field. Since the periodic variation of sunspot number was first noted by Schwabe (1843), observations of sunspot activity have provided an insight into solar magnetic fields and the solar cycle. Sunspots are large, complex regions of kilogauss magnetic field. They range from single isolated spots to complex active regions up to 100 Mm in diameter. Despite their importance in understanding our magnetic Sun, little progress has been made in determining the subsurface structure of sunspots (Couvidat, 2013; Felipe et al., 2014a). The exact nature of the formation of sunspots is still uncertain, with it currently being difficult to discern between the seismic signatures of a deep monolithic flux tube (Cowling, 1946) and shallow "spaghetti" models (Parker, 1975; Efremov et al., 2014).

The observed structure of a sunspot is split into two distinct regions, the central umbra and the outer penumbra (see Figure 3). The umbra is observed as the inner, darkest part of a sunspot and has a high ($2000 - 4000$ Gauss) magnetic field, with the inclination decreasing to about $40°$ from the vertical at the umbra-penumbra boundary (Martínez Pillet, 1997). The sunspot penumbra is formed when the inclination grows above approximately $35°$. Penumbrae show complex, filamentary structure. Jurčák et al. (2015) showed that there is a distinct threshold value of the magnetic field at which magnetoconvection begins to operate and the penumbra begins to form. The inner penumbral boundary then stabilises where the magnetic field reaches threshold value. The field strength continues to decrease until the edge of the visible sunspot ($700 - 800$ Gauss) where the field inclination increases to approximately $70 - 80°$. A twist is often observed in the magnetic field of sunspots, with a twist angle ($\gamma = \tan(B_r/B_\phi)$) of the horizontal magnetic field between $5°$ and $35°$ (Hagyard et al., 1977; Gurman & House, 1981).

In order to test and validate observational and helioseismic techniques there is a need for models of sunspot structure in which accurate numerical simulations of magnetoacoustic wave propagation can be performed. A variety of different sunspot models exist, with different properties based on the methods used to create them and the purpose of the model. These models can be purely numerical or semi-empirical with thermodynamic properties determined using helioseismic inversions of observational data to estimate temperature, pressure, density and magnetic field strength (Moradi et al., 2010). There are a number of elements of sunspot structure that must be incorporated in a realistic sunspot model. The model must provide a smooth transition from the sunspot axis to a quiet Sun background model in addition to a realistic magnetic field strength and inclination throughout the umbral and penumbral regions. To study and disambiguate the effects that magnetic field geometry and thermodynamic structure have on oscillations in sunspots, it is important to study a range of models in which these parameters are varied independently. A sunspot model suitable for computational seismology will therefore include the ability to adjust a number of parameters to generate sunspots with a variety of different sizes and field strengths.

Helioseismic Doppler measurements are made using the shifts in a spectral line, such as Fe I 6173 Å for the HMI instrument on the Solar Dynamics Observatory and Ni I 6768 Å line for the MDI instrument on the Solar and Heliospheric Observatory. Due to the different thermal structure inside a sunspot there will be a change in the

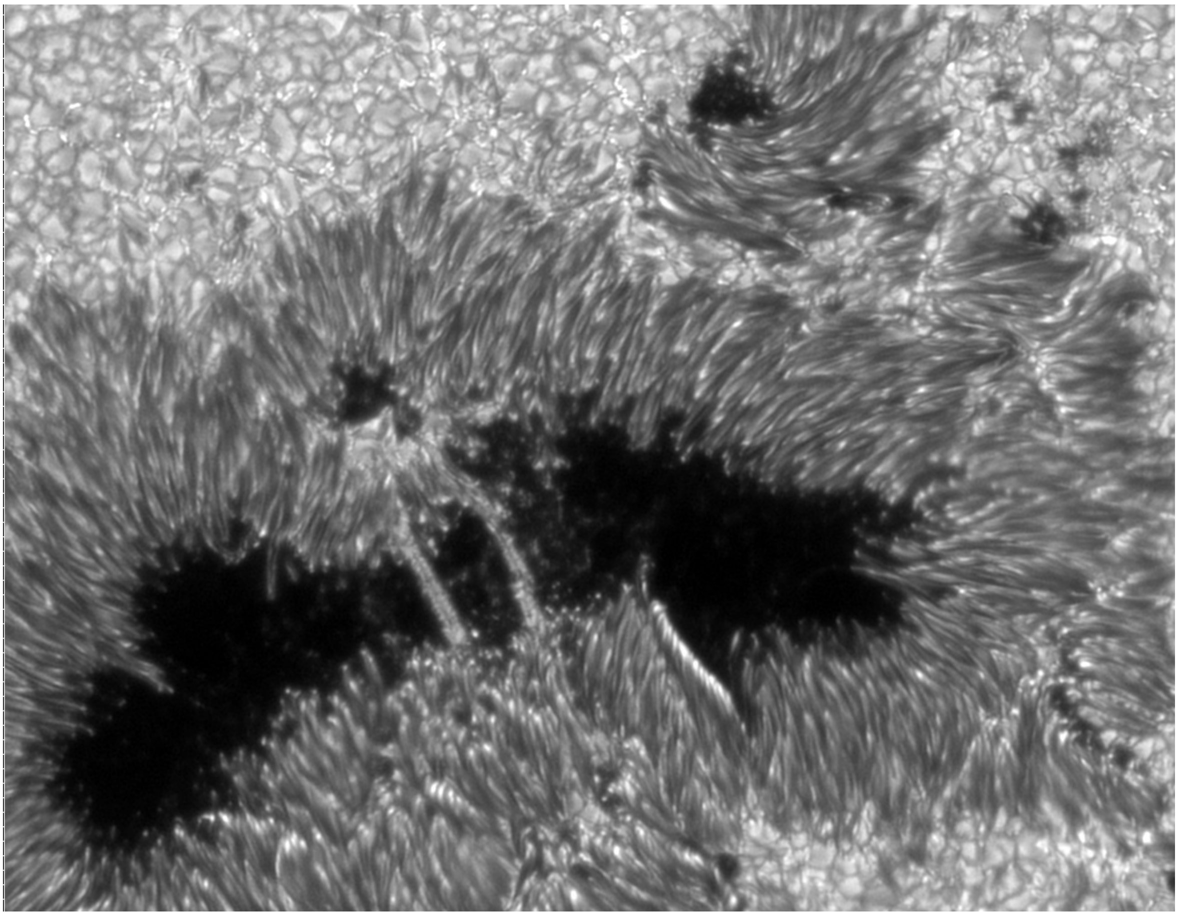

Fig. 3: An image of an active region, showing the dark umbral regions and a complex penumbral structure. Two 'light bridges' can be seen bisecting the sunspot. A number of smaller pores surround the large sunspot. Image credit G. Scharmer, L. Rouppe van der Voort et al., using the Swedish vacuum solar telescope.

height at which radiation at a particular wavelength is emitted. The solar photosphere is typically defined as the lowest height at which photons of 5000 Å radiation are able to escape, or $\log(\tau_{5000}) = 0$. Observational constraints for the reduction in photospheric height vary greatly, ranging from 500 − 1500 km in the sunspot umbra, decreasing at the umbral boundary and remaining constant at around 100 km in the penumbra (Solanki et al., 1993). This reduction is known as the Wilson depression and is caused by cooler plasma inside the sunspot. Sunspot models require a realistic Wilson depression in order to accurately mimic radiative properties for comparison of simulations with observations.

To understand the behaviour of waves in a magnetohydrodynamic simulation we require a static background, which will not evolve in the timescale of the oscillations being studied. This is provided through using a magnetohydrostatic model, in which the magnetic and hydrostatic forces are in equilibrium. One of the first widely used three-dimensional magnetohydrostatic models of solar magnetic field concentrations was the self-similar model of Schlüter & Temesváry (1958). Variations and modifications of this model are still widely in use today (Low, 1975, 1980; Moradi et al., 2008; Hanasoge, 2008; Shelyag et al., 2009; Murawski et al., 2015). Typically, the global solar model S (Christensen-Dalsgaard et al., 1996) is used for the solar interior, and semi-empirical quiet Sun models of chromospheric and coronal plasma (Vernazza et al., 1981; Avrett & Loeser, 2008; Avrett et al., 2015) are used for the solar atmosphere. Self-similar models provide a strict magnetohydrostatic equilibrium.

While self-similar models can be used to construct toy sunspot models and investigate MHD effects in sunspots, they are unable to make realistic sunspots. Due to the simplified magnetic field prescriptions and physics used in these models, high magnetic field strengths can lead to unphysical pressures and densities in the umbra. They do not provide a realistic distribution of pressure, density and temperature in the umbra, as it is calculated from the non-magnetic thermodynamic model, either numerically or based on an analytic prescription. Instead, pressure-distributed models, as introduced by Pizzo (1986), can be used to distribute the magnetic and thermodynamic structure between multiple semi-empirical models. These models are used to create sunspots with realistic magnetic and thermodynamic properties (Khomenko & Collados, 2008; Cameron et al., 2011).

Finally, highly realistic dynamical sunspots can be created through introducing a strong field into a radiative magnetohydrodynamic simulation (Rempel et al., 2009). Accounting for radiative transfer and an appropriate choice of boundary conditions (including somewhat questionable boundary conditions at the top of the computational box) will generate a sunspot with realistic penumbral fine structure and allow for the study of the time evolution of a sunspot, including its formation and decay. These models, however, are computationally expensive due to the radiative transport, non-linear magnetohydrodynamics and low CFL number. This makes them less suitable for wave simulations for helioseismology, as investigating different sunspot models, driving functions and frequencies requires multiple simulations of large time series. These models are also far too shallow for helioseismic applications.

Observational measurements are restricted by variations of the velocity, magnetic field and opacity in the region at which the radiation is formed. There are also limitations from the spatial, temporal and spectral resolution of the instrument used. With modern spectral synthesis codes it is now possible to directly compare numerical simulations with observations. The radiation output of the simulated solar photosphere and chromosphere can be calculated. This synthesised spectrum can then be degraded to imitate the effects of observational equipment, allowing direct comparisons to be drawn between simulated and observed data. Applications of this include using a 3D radiation-hydrodynamic code with a spectral-line synthesis code, and applying filters to imitate the effects of HMI-like measurement on the line profiles of Fe I 6173 Å line, and MDI-like measurement on the NiI 6768 Å line (Fleck et al., 2011). Instruments such as MDI and HMI sample the spectral line at a series of discrete wavelengths using instrument transfer functions, known as filtergrams. Filtergrams have been directly applied to synthesised spectra to obtain multi-height observations of simulated magnetoconvection (Nagashima et al., 2014).

To compare simulations with the observations made with these instruments we must understand both the complex magnetohydrodynamic effects as well as the effects of non-locality and non-uniformity of radiation formation in solar magnetic structures. Stokes analysis of simulated and observational data produced by the MURaM code (Vögler et al., 2005) was used (Khomenko et al., 2005) and compared to observational data for the quiet Sun (Khomenko et al., 2003). Specifically, it was used to investigate Stokes profiles of Fe I 6301.5 Å, 6302.5 Å, and 15648 Å, and 15652 Å spectral lines. Quantitative agreement was found between a lot of the measurements, with features of the solar surface such as magnetic bright points observed (Shelyag et al., 2004). The effect of the lower resolution observations was simulated and found to decrease the contrast of the simulated images (Shelyag & Przybylski, 2014).

The availability of modern supercomputing facilities has made it possible to introduce realistic physics into the study of waves in solar structures. The high Alfvén velocities present in magnetic field concentrations lead to computationally intensive simulations due to a restrictive CFL condition and consequently small simulation time-steps. Large computational resources are required to simulate these structures with high spatial and temporal resolution. With the introduction of non-ideal terms in the magnetohydrodynamic equation system, it is also possible to include the effects of partial ionisation, such as ambipolar diffusion and the Hall effect. The ionisation fraction is as low as 10^{-4} throughout much of the solar photosphere and chromosphere, allowing the non-ideal terms to have a significant effect on wave propagation in strong magnetic field regions. The incorporation of radiative losses, whether through a simplified Newton cooling model or more detailed radiative transport, is required to simulate the formation of the chromosphere. The introduction of these physical processes into simulations brings us closer to a better understanding of energy transfer, conversion and diffusion in magnetic field structures.

This research will provide a general study of wave interaction with solar magnetic field concentrations on a variety of scales. In Chapter 1 the equations of linear magnetohydrodynamics, MHD waves and the SPARC linear MHD code, which has been developed for helioseismology of magnetic regions, are described. Chapter 2 describes a problem with the driving of acoustic sources for helioseismic simulations, and the solution to generate realistic acoustic spectra. Chapter 3 is dedicated to radiative transport, spectral synthesis and synthetic observations of solar magnetic structures. Chapter 4 describes a sunspot model developed to give accurate spectropolarimetry and allow computational helioseismology to be performed on synthetic observations. Finally, in Chapter 5 we describe non-linear, non-ideal simulations of small scale flux tubes to investigate the role of ambipolar diffusion in damping Alfvén waves.

Chapter 1

Magnetohydrodynamics and the SPARC code

In this chapter we provide an introduction to ideal magnetohydrodynamics. We then derive the linear magnetoacoustic wave equation and dispersion relations. The behaviour of fast, slow and Alfvén waves in magnetic fields is described, including MHD mode conversion and the effect of a stratified atmosphere on the waves. We then describe the Seismic Propagation through Active Regions and Convection (SPARC) code used throughout this thesis, including the improvements made in the parallelisation algorithm and boundary conditions.

1.1 Magnetohydrodynamics

The magnetohydrodynamic equations can be derived using a number of methods. For a strict derivation of these equations from the Boltzmann equations see Goedbloed & Poedts (2004). We will present a simple derivation for a charged, stratified fluid. The description of ideal magetohydrodynamics begins with Maxwell's equations (here, written in cgs units):

$$\nabla \times \mathbf{B} = \frac{4\pi}{c}\mathbf{J} + \frac{1}{c}\frac{\partial \mathbf{E}}{\partial t}, \tag{1.1}$$

$$\nabla \times \mathbf{E} = -\frac{1}{c}\frac{\partial \mathbf{B}}{\partial t}, \tag{1.2}$$

$$\nabla \cdot \mathbf{B} = 0, \tag{1.3}$$

$$\nabla \cdot \mathbf{E} = 4\pi\sigma. \tag{1.4}$$

Here $\mathbf{B}$, $\mathbf{E}$, and $\mathbf{J}$ are the magnetic field, electric field and electric current density vectors, respectively, while c is the speed of light in a vacuum, t the time and σ the electric charge density.

These Equations can be simplified by considering non-relativistic fluid velocities $v \ll c$. Then, for the Maxwell-Ampere Equation 1.1, using Equation 1.2, we have

$$\frac{1}{c}\left|\frac{\partial \mathbf{E}}{\partial t}\right| \approx \frac{v^2}{c^2}\frac{B}{l_0} \ll \frac{B}{l_0} \approx \left|\nabla \times \mathbf{B}\right|. \tag{1.5}$$

This assumption simplifies Equation 1.1 to give

$$\mathbf{J} = \frac{c}{4\pi}\nabla \times \mathbf{B}. \tag{1.6}$$

The equations of electrodynamics 1.1 - 1.4 are combined with the equations of fluid mechanics to give the magnetohydrodynamic equations. The conservation of mass is described by the continuity equation

$$\frac{\partial \rho}{\partial t} + \nabla \cdot (\rho \mathbf{v}) = 0, \tag{1.7}$$

for the plasma density ρ and velocity $\mathbf{v}$. To describe the conservation of momentum in a charged, gravitationally stratified fluid, two additional terms will supplement the standard momentum equation of hydrodynamics. Firstly, the force of gravity will be included, $\mathbf{F_g} = \rho\mathbf{g}$. For an ionised, quasi-neutral fluid, the Lorentz force per unit volume is given by

$$\mathbf{F} = \frac{1}{c}\mathbf{J} \times \mathbf{B} + \sigma \mathbf{E}. \tag{1.8}$$

The inclusion of these two terms gives the momentum equation for magnetohydrodynamics

$$\rho \frac{\partial \mathbf{v}}{\partial t} = -\rho \left(\mathbf{v} \cdot \nabla\right) \mathbf{v} - \nabla p + \rho \mathbf{g} + \frac{1}{c}\mathbf{J} \times \mathbf{B} + \sigma \mathbf{E}, \tag{1.9}$$

for a gas pressure p. In the momentum Equation 1.9, by using Equations 1.2 & 1.4 again considering only non-relativistic velocities $v \ll c$, we find

$$\sigma \mathbf{E} \approx \frac{v^2}{c^2}\frac{B^2}{l_0} \ll \frac{B^2}{l_0} \approx |\mathbf{J} \times \mathbf{B}|, \tag{1.10}$$

allowing one to remove the $\mathbf{E}$ term from the momentum Equation 1.9. This removes the electric field from the system of equations 1.7-1.10.

In a plasma, the relationship between the current density and electric field is given by Ohm's law. In ideal MHD the plasma is considered to be a perfectly conducting fluid, the electric field strength in the co-moving frame of reference $\mathbf{E}'$ is zero. Considering the transformation back to the non-inertial frame gives the ideal Ohm's law

$$\mathbf{E}' = \mathbf{E} + \frac{1}{c}\mathbf{v} \times \mathbf{B} = 0. \tag{1.11}$$

Substituting this into Faradays Equation 1.2, and simplifying gives the induction equation

$$\frac{\partial \mathbf{B}}{\partial t} - \nabla \times \left(\mathbf{v} \times \mathbf{B}\right) = 0. \tag{1.12}$$

Substituting Equation 1.6 into the momentum Equation 1.9 gives

$$\rho \frac{\partial \mathbf{v}}{\partial t} = -\left(\mathbf{v} \cdot \nabla\right) \mathbf{v} - \nabla p + \rho \mathbf{g} + \frac{1}{4\pi}\left(\nabla \times \mathbf{B}\right) \times \mathbf{B}. \tag{1.13}$$

The reduced system of equations given by the momentum Equation 1.13, continuity Equation 1.7, and induction Equation 1.12 describe the behaviour of plasma in ideal magnetohydrodynamics.

The constraint of Equation 1.3, or no magnetic monopoles, must be maintained. This can cause problems in computational MHD, where certain discretisations will not conserve $\nabla \cdot \mathbf{B}$, potentially leading to numerical instabilities.

Finally, the system of equations is closed by solving an energy equation, such as the internal energy (e_{int})

$$\frac{\partial e_{int}}{\partial t} + \mathbf{v} \cdot \nabla e_{int} + (\gamma - 1) e_{int} \nabla \cdot \mathbf{v} = 0, \tag{1.14}$$

or the total energy (e_{tot}) of the system

$$\frac{\partial e_{tot}}{\partial t} = -\nabla \cdot \left(\mathbf{v} \left(e_{tot} + p + \frac{|\mathbf{B}|^2}{8\pi} \right) - \frac{1}{4\pi} \mathbf{B} \left(\mathbf{v} \cdot \mathbf{B} \right) \right) + \left(\rho \mathbf{g} \cdot \mathbf{v} \right). \tag{1.15}$$

The ideal MHD approximation has been applied successfully to describe many solar phenomena. The assumption of perfect ionisation made in ideal MHD is broken in large regions of the photosphere and chromosphere. For many of the temporal and spatial scales studied, the non-ideal effects are small allowing the ideal approximation to be used (Khomenko, 2015). In magnetic regions of the chromosphere and corona the ideal approximation breaks down and non-ideal effects, such as ion-neutral drift (ambipolar diffusion) and the Hall effect must be considered. Non-ideal magnetohydrodynamics is covered in greater detail in Chapter 5. However, Cally & Khomenko (2015) show that the Hall term is negligible in the lower solar atmosphere for the low frequency wave (several mHz) that concern us here.

1.2 Magnetohydrodynamic waves

To study the linear waves propagating in a solar plasma we write the system of equations of ideal magnetohydrodynamics (Priest, 2012; Cally & Andries, 2016, in prep) in terms of a time-independent background and a time-varying perturbation. Expanding the density, pressure, magnetic field and velocity in terms of perturbations ($\rho_1, p_1, \mathbf{B_1}, \mathbf{v_1}$) around a background state ($\rho_0, p_0, \mathbf{B_0}, \mathbf{v_0}$) gives

$$\begin{aligned}
\rho &= \rho_0 + \rho_1, \\
p &= p_0 + p_1, \\
\mathbf{B} &= \mathbf{B_0} + \mathbf{B_1}, \\
\mathbf{v} &= \mathbf{v_0} + \mathbf{v_1}.
\end{aligned} \tag{1.16}$$

With a background model in magnetohydrostatic equilibrium, satisfying

$$-\nabla p_0 + \rho_0 \mathbf{g} + \frac{1}{4\pi} \left(\nabla \times \mathbf{B_0} \right) \times \mathbf{B_0} = 0, \tag{1.17}$$

we can use Equation 1.16 and 1.17 to rewrite equations 1.7, 1.12 and 1.13. This is performed by expanding and removing non-linear terms as well as cancelling the background terms in magnetohydrostatic equilibrium from the momentum equation. In order to study the case of no background flows we set $\mathbf{v_0} = 0$ and a small time dependent perturbation $\mathbf{v_1}$. Then, the momentum Equation 1.13 can be written as

$$\rho_0 \frac{\partial \mathbf{v_1}}{\partial t} = -\nabla p_1 + \rho_1 \mathbf{g} + \frac{1}{4\pi} (\nabla \times \mathbf{B_0}) \times \mathbf{B_1} + \frac{1}{4\pi} (\nabla \times \mathbf{B_1}) \times \mathbf{B_0}. \tag{1.18}$$

Similarly, we linearise the continuity equation

$$\frac{\partial \rho_1}{\partial t} + \nabla \cdot (\rho_0 \mathbf{v_1}) = 0, \tag{1.19}$$

and the induction equation

$$\frac{\partial \mathbf{B_1}}{\partial t} - \nabla \times (\mathbf{v_1} \times \mathbf{B_0}) = 0. \tag{1.20}$$

This system is closed with the linearised energy equation (written for gas pressure):

$$\frac{\partial p_1}{\partial t} = c_s^2 \frac{\partial \rho_1}{\partial t}, \tag{1.21}$$

where $c_s = \sqrt{\frac{\gamma p_0}{\rho_0}}$ is the local sound speed and γ the adiabatic index. Taking the time derivative of the linear momentum Equation 1.18 with a constant background field, we can simplify $\nabla \times \mathbf{B_0} = 0$. Equations 1.19, 1.20 and 1.21 can then be used to remove ρ_1, p_1 and $\mathbf{B}_1$ from Equation 1.18, giving

$$\frac{\partial^2 \mathbf{v_1}}{\partial t^2} = -c_s^2 \nabla (\nabla \cdot \mathbf{v_1}) + g \nabla \cdot (\mathbf{v_0} + \mathbf{v_1}) + \frac{1}{4\pi \rho_0} (\nabla \times (\nabla \times (\mathbf{v_1} \times \mathbf{B_0}))) \times \mathbf{B_0}. \tag{1.22}$$

Taking a solution of the form $\mathbf{v_1} = \mathbf{V} \exp(i(\mathbf{k} \cdot \mathbf{r} - \omega t))$ with a position vector $\mathbf{r} = (x, y, z)$, a wavenumber $\mathbf{k}$ and frequency ω gives

$$\omega^2 \mathbf{V} = c_s^2 \mathbf{k} (\mathbf{k} \cdot \mathbf{V}) - \frac{1}{4\pi \rho_0} (\mathbf{k} \times (\mathbf{k} \times (\mathbf{V} \times \mathbf{B_0}))) \times \mathbf{B_0}. \tag{1.23}$$

For the hydrodynamic case, with no magnetic field $\mathbf{B_0} = 0$ we get

$$\omega^2 \mathbf{V} = c_s^2 \mathbf{k} (\mathbf{k} \cdot \mathbf{V}). \tag{1.24}$$

This gives us a longitudinal sound wave $\mathbf{V} \parallel \mathbf{k}$ with a phase velocity $\frac{\omega}{|\mathbf{k}|}\mathbf{k} = \pm c_s \mathbf{k}$ and the group velocity $\frac{\partial \omega}{\partial \mathbf{k}} = c_s \mathbf{k}$. The wave-vector parallel to the magnetic field is given by $k_\parallel^2 = |\mathbf{k}|^2 \cos^2(\theta_B)$, where θ_B is the angle between the wave-vector $\mathbf{k}$ and the magnetic field $\mathbf{B_0}$.

For solutions in the case of a non-zero magnetic field, we take the scalar product of Equation 1.23 with $\mathbf{k}$, $\mathbf{B_0}$ and $\mathbf{k} \times \mathbf{B_0}$:

$$\begin{pmatrix} \omega^2 - \left(v_A^2 + c_s^2\right)|\mathbf{k}|^2 & a^2|\mathbf{k}|^2 k_\parallel & 0 \\ c_s^2 k_\parallel & -\omega^2 & 0 \\ 0 & 0 & \omega^2 - v_A^2 k_\parallel^2 \end{pmatrix} \begin{pmatrix} \mathbf{k} \cdot \mathbf{V} \\ \mathbf{B_0} \cdot \mathbf{V} \\ \mathbf{k} \times \mathbf{B_0} \cdot \mathbf{V} \end{pmatrix} = \begin{pmatrix} 0 \\ 0 \\ 0 \end{pmatrix} \tag{1.25}$$

Here $v_A = \sqrt{B_0^2/4\pi\rho_0}$ represents the Alfvén speed in the plasma. Solutions to Equation 1.25 only exist when the determinant of the coefficient matrix is zero,

$$\left(\omega - v_A^2 k_\parallel^2\right)\left(\omega^4 - \left(v_A^2 + c_s^2\right)k^2\omega^2 + v_A^2 c_s^2 |\mathbf{k}|^2 k_\parallel^2\right) = 0. \tag{1.26}$$

This gives two dispersion relations. The first term describes the Alfvén wave,

$$\omega - v_A^2 k_\parallel = 0, \tag{1.27}$$

and the second the magnetoacoustic wave modes

$$\omega^4 - \left(v_A^2 + c_s^2\right)k^2\omega^2 + v_A^2 c_s^2 |\mathbf{k}|^2 k_\parallel^2 = 0. \tag{1.28}$$

The Alfvén wave mode, given by Equation 1.27, can also be recovered from Equation 1.23 by setting $\mathbf{k} \cdot \mathbf{V} = 0$. This gives a transverse wave with the velocity perpendicular to the background magnetic field, phase velocity $v_A \cos(\theta_B)\mathbf{k}$ and the group velocity $v_A \mathbf{B_0}$.

Taking Equation 1.28 and solving it for ω^2 gives two other wave modes:

$$\omega^2 = \frac{|\mathbf{k}|^2}{2}\left(v_A^2 + c_s^2 \pm \sqrt{\left(v_A^2 + c_s^2\right)^2 - 2v_A^2 c_s^2 \cos(2\theta_B)}\right), \tag{1.29}$$

Here the fast mode corresponds to the $+$ sign, and the slow mode to the $-$ sign. The fast (v_f) and slow (v_s) wave-velocities depend on the direction of propagation through the magnetic field. A fast wave will have the maximum velocity of $v_f = \sqrt{c_s^2 + v_A^2}$ when travelling perpendicular to the magnetic field, and a minimum velocity $v_f = \max[v_A, c_s]$, when parallel.

The nature of fast and slow waves varies depending on the relative magnitudes of v_A and c_s. From Equation 1.29, when $v_A \ll c_s$, the fast wave will be acoustic in nature, with the velocity of an acoustic sound wave. As the plasma-β decreases, the fast wave becomes magnetic in nature, and isotropic when $v_A \gg c_s$.

A slow wave achieves its maximum speed $v_s = \min[v_A, c_s]$ when traveling parallel to the magnetic field and is unable to propagate perpendicularly, though it has a finite maximum velocity $v_s \rightarrow \frac{v_A c_s}{\sqrt{v_A^2 + c_s^2}}$ as $\theta_B \rightarrow \frac{\pi}{2}$. The slow wave mode is magnetic when $v_A \ll c_s$, traveling transverse to the magnetic field, while when $v_A \gg c_s$ the slow mode becomes acoustic and the polarisation is aligned with the magnetic field.

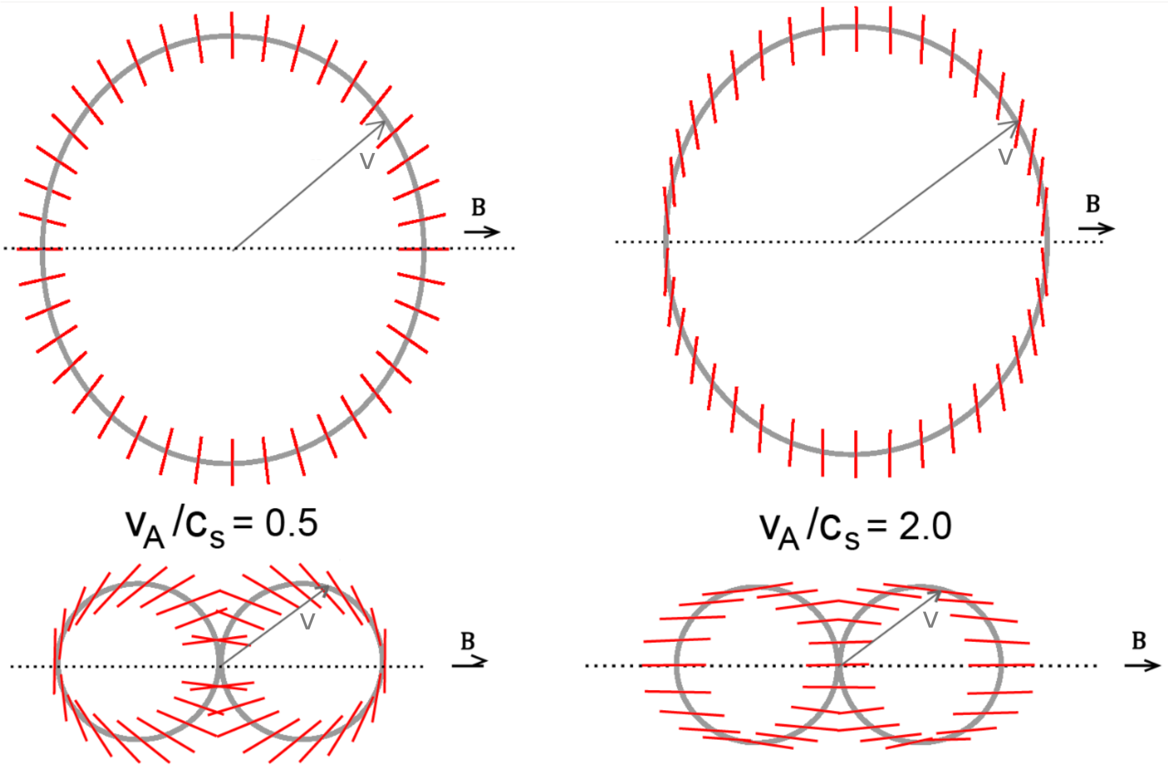

Fig. 1.1: The fluid displacement (red) as the direction of the velocity **v** changes relative to a background magnetic field $\mathbf{B_0}$ pointing in the positive x direction. The upper panel shows the fast wave, while the lower panel shows the slow wave. Two cases are shown, the left figure shows the case where $c_s/v_A = 0.5$, and the right figure shows the face where $c_s/v_A = 2.0$. Figure from Spruit (2013)

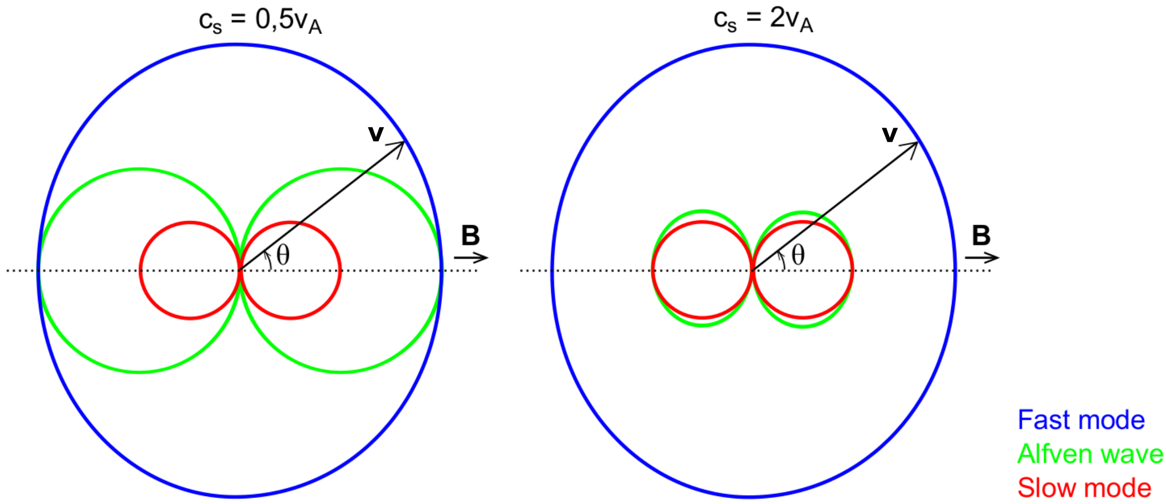

Fig. 1.2: The phase speed of the fast, slow and Alfvén wave modes as the direction of the velocity $\mathbf{v}$ changes relative to a background magnetic field $\mathbf{B_0}$ pointing in the positive x direction. Two cases are shown, the left figure shows the case where $c_s/v_A = 0.5$, and the write figure shows the face where $c_s/v_A = 2.0$. Figure from Spruit (2013)

1.2.1 Waves in a stratified atmosphere

The $p-$modes travelling through the solar interior are trapped acoustic waves. In the non-magnetised quiet Sun regions of the stratified solar atmosphere, when the region is small and the spherical geometry can be ignored, the wave equation can be determined using the plane parallel approximation (Deubner & Gough, 1984; Balraforth & Gougb, 1988). For a vertically stratified background, considering the wavenumber as $|\mathbf{k}|^2 = k_z^2 + k_h^2$, where k_h is the horizontal wavenumber, k_z the vertical wavenumber, and applying the Wentzel-Kramers-Brillouin (WKB) approximation (Gough, 2007) gives a dispersion relationship

$$\omega^2 - c_s^2|\mathbf{k}|^2 - \omega_c^2 + \frac{c_s^2 N^2 k_h^2}{\omega^2} = 0, \tag{1.30}$$

where N is the Brunt-Väisälä frequency, representing the oscillation frequency of a pure gravity wave. When the Brunt-Väisälä frequency is real ($N^2 > 0$), the parcel of gas will oscillate vertically, and the stratified background model will be convectively stable as seen in most of the solar atmosphere. For an imaginary Brunt-Väisälä frequency ($N^2 < 0$), the plasma is unstable, and as small perturbations are unable to be damped, they will grow and convection occurs.

The acoustic cutoff frequency ω_c is calculated as

$$\omega_c^2 = c_s^2 \frac{1 - 2H'}{4H^2} \tag{1.31}$$

for a density scale height H. The acoustic cutoff frequency is a dubious concept and theoretical calculations vary. A number of different equations can be calculated, depending on the formulation of the wave equations used (Schmitz & Fleck, 2003). Although these forms give the same result in an isothermal atmosphere, for a realistic solar atmosphere they will differ. The form used in Equation 1.31 can lead to large spikes in the acoustic cutoff frequency, violating the WKB approach used in theoretical calculations. The inclusion of magnetic fields will further complicate things, changing the acoustic cutoff frequency and allowing lower frequency waves to escape higher into the atmosphere (McIntosh & Jefferies, 2006).

The dispersion relation (Equation 1.30) gives a number of insights into the behaviour of the modes trapped in the solar interior. We can see the waves are able to propagate vertically when $(\omega^2 - \omega_c^2) + k_h^2 c_s^2 (N^2/\omega^2 - 1) > 0$. The lower turning point is given by the Lamb depth, where $\omega^2 = c_s^2 k_h^2$ as $c_s k_h >> \omega_c$ deep in the solar interior. At the upper turning point waves will be reflected as they reach the acoustic cutoff frequency $\omega < \sqrt{c_s^2 k_h^2 (N^2/\omega^2 - 1) + \omega_c^2} < \omega_c$ (Cally & Moradi, 2013).

When fast acoustic waves travel in a magnetised region, the acoustic cutoff frequency and its effects are changed in a number of ways (Bogdan & Judge, 2006; Cally, 2007). In addition to the mode conversion processes discussed below, which allow acoustic and magnetic waves to interact, a magnetic field will change the acoustic cutoff frequency. For a field aligned slow wave in a region where $v_A \gg c_s$, propagation will be allowed when $\omega^2 > \omega_c^2 \cos^2(\theta_B)$. This modification by the attack angle θ_B, the angle between the magnetic field $\mathbf{B}$ and the wave vector $\mathbf{k}$, allows for slow waves to propagate higher into the solar atmosphere where they are observed as 'magnetic portals' (Jefferies et al., 2006).

1.2.2 Mode Conversion

Around the equipartition region, where the Alfvén velocity and sound speed are equal $(v_A/c_s = 1)$, interaction between the fast and slow waves will occur. In this region, mode conversion and transmission will enable energy to be transmitted and converted between the fast and slow magnetoacoustic wave modes. Below the equipartition layer the fast wave is predominantly acoustic in nature and the slow mode magnetic in nature. Above the equipartition layer the slow mode is acoustic in nature, and the fast wave is magnetic. Transmission refers to the wave changing from the fast branch to the slow branch (or slow-to-fast) remaining acoustic in nature. Conversion will occur if the wave remains in the fast branch, changing nature from acoustic to magnetic.

This transmission (acoustic-to-acoustic) will be stronger in a number of situations: 1) a small angle between the wave vector $\mathbf{k}$ and the magnetic field $\mathbf{B}$, 2) lower frequencies and 3) a thin region where $v_A \approx c_s$ (the interaction region), occurring when Alfvén speed gradient is steep (Cally, 2007).

As an upward-travelling fast-acoustic wave enters a region of low plasma-β, part of its energy is transmitted into an upward-travelling field-aligned slow-acoustic mode as it crosses the equipartition layer. The remaining energy is converted into a fast-magnetic wave. Then, after reflecting from the upper turning point, the magnetic-fast mode will again transmit energy into a downward travelling slow-magnetic mode with the remaining energy converting to a fast-acoustic wave (Cally, 2006). As seen in Figure 1.3, the inclination of the field plays a role in determining the strength of the conversion process. Since most incoming acoustic $p-$modes will approach the solar surface at a steep angle, conversion of these waves to acoustic slow modes will occur preferentially in near-vertical fields, such as sunspot umbra (Cally et al., 2016).

In regions above the $v_A/c_s = 1$ layer, near the fast wave reflection height, energy may be lost from the fast-magnetic wave to the Alfvén wave through mode conversion. While fast to slow conversion can occur in a simplified 2D geometry, fast to Alfvén mode conversion is a three-dimensional process, occuring only when the wavevector is at an angle to the plane of the magnetic field (Cally & Hansen, 2011). Wave propagation studies in a simple magnetic field geometry have found that the energy lost from the reflected fast wave can exceed that lost through transmission to slow waves (Cally & Goossens, 2008). The efficiency of energy loss was found to be greatest in field inclinations of $30° - 40°$ and when the wave is propagating at a large angle from the magnetic field plane ($60° - 80°$).

Numerical studies of fast to Alfvén conversion were performed in a 2.5D sunspot model (Khomenko & Cally, 2012). By comparing the acoustic and magnetic energy fluxes above the $v_A/c_s = 1$ layer, the efficiency of conversion to Alfvén waves was found to behave as described above for simplified inclined field models. A few points of difference were noticed. Firstly, the inclination at which maximum energy is transmitted to the atmosphere is lower than in the simple inclined model. Secondly, it was found that when the angle between the wave vector and magnetic field is $90° - 180°$, the conversion to upwards traveling Alfvén waves is inefficient. As expected from theory, after reflection of the fast wave has occurred, conversion to downwards traveling Alfvén waves is more efficient.

Three-dimensional studies of fast-to-Alfvén conversion found that the maximum energy is achieved at high inclinations and with an angle between the wave vector and magnetic field of $50° - 120°$ (Felipe, 2012), although the magnetic field strength was low (900 G). Investigations of the interaction of Alfvén waves with a realistic chromosphere, transition region and corona have shown that the Alfvén flux reaching the corona is produced through fast mode conversion (Hansen & Cally, 2012). In three-dimensional studies of sunspot acoustic halos, the 'moat' separating the concentric halos was seen to correspond to a region of penumbral field where returned fast waves are efficiently converted to downwards traveling Alfvén waves (Rijs et al., 2016). Realistic simulations in a sunspot atmosphere have yet to be performed due to computational limitations from the extreme Aflvén velocities found in kilogauss magnetic fields in combination with chromospheric and coronal densities. Current simulations either use a low upper boundary, decreasing the region in which conversion can occur, or introduce an Alfvén speed limiter. Although these limiters have a minimal effect on the solar $p-$mode spectrum (Moradi & Cally, 2014), they will greatly reduce the Alfvénic flux.

1.3 SPARC

Forward modelling for computational helioseismology is necessary to develop and test helioseismic techniques. Validation of helioseismic measurements is performed by directly comparing inferred plasma properties to those in a simulated model. In order to correctly use phase and travel-time shifts to diagnose sub-surface properties in magnetic regions we must first understand how the magnetic fields will effect these measurements. This involves modelling the physical processes impacting $p-$modes travelling through the solar interior and the variations they cause in the observed surface velocity observations.

A number of codes are currently in use, including linear (SPARC (Hanasoge, 2011), and SLIM (Cameron et al., 2007)) and non-linear (MANCHA (Felipe et al., 2010), VAC (Shelyag et al., 2008), and FLASH (Murawski et al., 2013)). The SPARC code has been widely used and validated for local helioseismology (Hanasoge et al., 2007; Hanasoge,

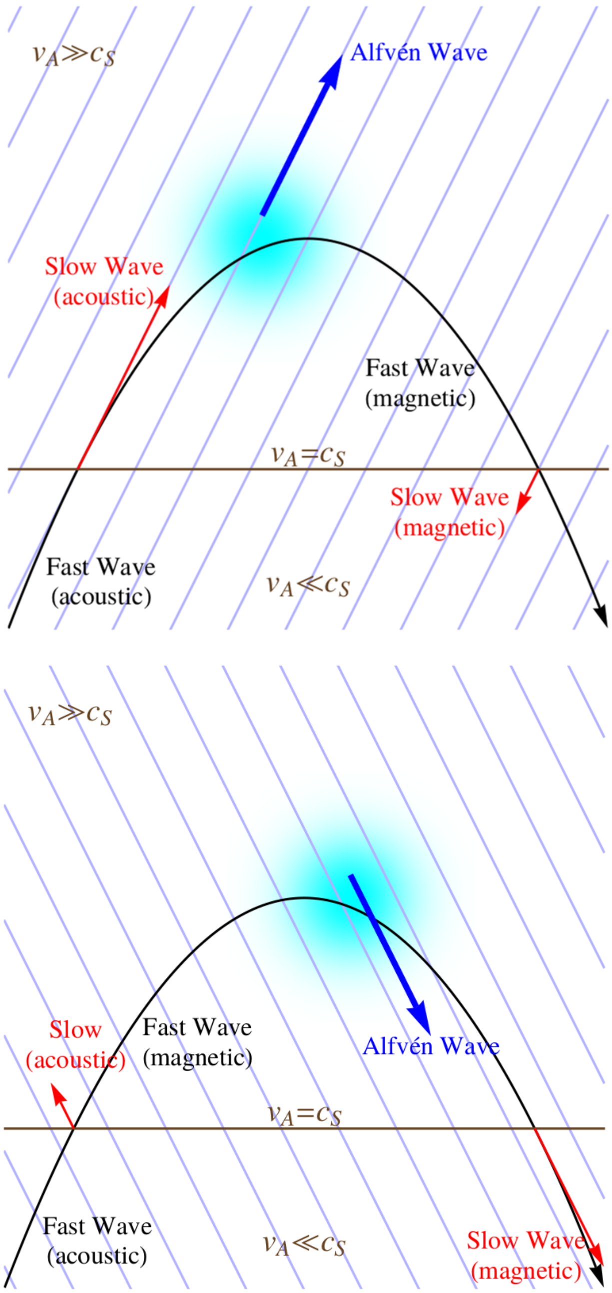

Fig. 1.3: This figure shows the two different mode conversion processes of an incoming fast wave in a simple inclined field model; fast-to-slow conversion occurs at the $v_A = c_s$ level, and fast-to-Alfvén conversion occurs near the fast wave turning point. In the case of a low attack angle (top panel) we see a large amount of transmission to upward travelling slow modes, the magnetic fast wave can now convert to upward travelling Alfvén waves before returning to the solar interior. Conversion to slow modes is again seen as the equipartition layer. For the case of a large attack angle (bottom panel) the transmission to upwards travelling slow modes is greatly reduced, with more energy transmitted to downward travelling Alfvén and downward travelling slow waves. Figure taken from Khomenko & Cally (2012).

2011). Modern radiative MHD codes such as MURaM, CO5BOLD and MANCHA are now available, however their large computational requirements make it expensive to perform simulations of a sufficient length for helioseismology. The low frequencies, large spatial scales, long simulation times and inherently linear nature of helioseismic methods make linear MHD simulations an ideal tool for computational helioseismology.

We have improved the SPARC code significantly over the original. The introduction of an explicit derivative and filtering scheme allows the domain to be decomposed in three dimensions. A new decomposition and parallelisation algorithm is introduced, greatly increasing the scaling with number of cores. Finally, the high-fidelity Perfectly Matched Layer (PML) boundaries previously only applied on the vertical boundaries have been added to the horizontal boundaries and tuned for maximum efficiency.

The structure of this section is as follows. In Subsection 1.3.1 we describe the equations of linear magnetohydrodynamics solved by the SPARC code. Then we describe the layout of the code, including numerical scheme in Subsection 1.3.2, the parallelisation algorithm in Subsection 1.3.3 and finally the PML boundary conditions in Subsection 1.3.4.

1.3.1 Equations

The SPARC code uses the set of equations derived by Hanasoge et al. (2010) in the previous versions of the code. The code calculates the perturbations around a magnetohydrostatically stable background model, satisfying Equation 1.17.

The linear MHD equations are written in terms of pressure (p), density (ρ), sound speed (c_s), gravity (g) and magnetic field ($\mathbf{B}$) and velocity ($\mathbf{v}$). Variables subscripted with 0 are the values of the background model, or, in the case of velocity, describe a weak flow field $|\mathbf{v_0}| << \omega L_0$ for a frequency ω and length-scale L_0. The equations are written in non-conservative form as:

$$\frac{\partial \rho}{\partial t} = -\nabla \cdot (\rho_0 \mathbf{v}) - \nabla \cdot (\rho \mathbf{v}_0), \tag{1.32}$$

$$\begin{aligned} \rho_0 \left(\frac{\partial}{\partial t} + \Gamma \right) \mathbf{v} = & - \rho_0 \mathbf{v}_0 \cdot \nabla \mathbf{v} - \rho_0 \mathbf{v} \cdot \nabla \mathbf{v_0} - \nabla p - \rho g_0 \mathbf{e_z} \\ & + \frac{1}{4\pi} [(\nabla \times \mathbf{B}_0) \times \mathbf{B} + (\nabla \times \mathbf{B}] \times \mathbf{B}_0) + \mathbf{S} - \rho_0 \sigma_{damp} \mathbf{v}, \end{aligned} \tag{1.33}$$

$$\frac{\partial p}{\partial t} = -c_s^2 \rho_0 \nabla \cdot \mathbf{v} - \mathbf{v} \cdot \nabla p_0 - \mathbf{v}_0 \cdot \nabla p, \tag{1.34}$$

$$\frac{\partial \mathbf{B}}{\partial t} = \nabla \times (\mathbf{v}_0 \times \mathbf{B}) + \nabla \times (\mathbf{v} \times \mathbf{B}_0) \, . \tag{1.35}$$

Two additional terms are introduced to the right hand side of the momentum equation: the driving source term $\mathbf{S}$, and a frictional damping sponge σ_{damp} boundary condition (Colonius, 2004). A wave-damping Γ term is present on the left hand side of the momentum equation. This allows better approximation of the solar $p-$mode spectrum (Schunker et al., 2011).

The SPARC code can be run in full 3D or in a reduced 2D geometry to allow for quick testing of new models and simulation parameters. For simulations with magnetic field a 2.5D mode is available, solving for the full $\mathbf{v} = (v_x, v_y, v_z)$, and $\mathbf{B} = (B_x, B_y, B_z)$ in a 2D geometry ($\frac{\partial}{\partial y} = 0$). The code can be run in three modes: hydrodynamic with a uniform background in x and y (quiet Sun), 3D hydrodynamic, or 3D magnetohydrodynamic.

1.3.2 Numerical Scheme

For efficient calculation with minimal communication in a three-dimensional decomposed domain the implicit derivative schemes and FFT-based Orszag two-third rule horizontal filtering used in the original SPARC code have been replaced. To calculate spatial derivatives a five-point central difference scheme (Vögler et al., 2005) and an eleven-point optimised finite difference scheme (Bogey & Bailly, 2004) are available for use in both the horizontal and vertical derivatives. The high order scheme offers lower dispersion and dissipation errors in wavenumber at the cost of computational time. Also included are uncentred derivatives for the boundary cells when absorbing or reflecting boundary conditions are used (Berland et al., 2007).

Finally, to perform the temporal integration, an optimised five-step Runge-Kutta scheme is used (Berland et al., 2006). Explicit filters are included to prevent aliasing and numerical instabilities in the solution, stabilising the system. Two filters are available, the 7-point filter described by Parchevsky & Kosovichev (2007) and the 11-point de-aliasing filter of Vichnevetsky & Bowles (1982). The frequency of application of these filters is specified. For most simulations, vertical filtering every $10-20$ timesteps, and horizontal filtering every $50-100$ timesteps are sufficient to ensure stability. For atmospheres with large horizontal density and pressure gradients, for example a sunspot with a deep Wilson depression, the frequency of horizontal filtering may need to be increased. To deal with the large variation in physical parameters over the domain from the convective zone to chromosphere, the code uses a vertical grid spacing based on the sound speed. The z-directional grid spacing is distributed such that the acoustic travel times between each cell are the same for the quiet Sun, $\Delta z \propto 1/c_s$.

The code includes a Lorentz force limiter, which is required due to the high Alfvén speed in the upper chromosphere. Although unphysical, it is necessary to prevent reduction of the time-step and excessive computational times. Moradi & Cally (2014) show that the Alfvén limiter has negligible effect on the seismology provided the Alfvén speed plateau is comfortably above the horizontal phase speed of the $p-$modes under consideration. This is applied by setting the maximum Alfvén velocity $v_{a,max}$ and calculating the reduction $R_{mag}(x, y, z)$ needed, according to

$$R_{mag} = \frac{v_{a,max}^2}{v_{a,max}^2 + \frac{v_A^2(x,y,z)}{c_q^2(z)}}, \tag{1.36}$$

where $v_A(x, y, z)$ is the local Alfvén velocity and $c_q(z)$ is the quiet Sun sound speed (Rempel et al., 2009). The functional form of the Equation 1.36 limits the maximum fast wave velocity, sufficiently relaxing the time-step restriction, while having a minimal effect below the equipartition layer $c_s/v_A = 1$ (Cameron et al., 2011). The reduction is then applied to the Lorentz force terms in the right hand side of the magnetohydrodynamic equations.

In previous versions of the code the Lorentz force limiter was applied directly to the background magnetic field. Reducing the magnetic field using a limiter of the form given by Equation 1.36 in a magnetic atmosphere where v_A/c_q changes quickly causes a steep decline of the background magnetic field B_0 with z, which is both unphysical and numerically problematic. This requires a further reduction of the vertical derivatives $R_{mag}\frac{\partial B_0 x}{\partial z}$, and $R_{mag}\frac{\partial B_0 y}{\partial z}$ in the $\nabla \times \mathbf{B}_0$ terms of the momentum equation to maintain stability. As the limiter is now applied directly to the momentum equation, this reduction is no longer included. The new method also prevents the formation of a 'magnetic bottle', leading to an eventual numerical instability in certain magnetic field topologies, such as a sunspots with a realistic umbral magnetic field strength and density.

Convective instabilities are fatal to linear simulations leading to exponential growth of amplitude of oscillatory modes and, consequently, to a numerical blow-up. The condition for convective stability is the Brunt-Väisälä frequency (see Chapter 2),

$$N^2 = g(\frac{1}{\gamma}\frac{\partial \log(\rho)}{\partial z} - \frac{\partial \log(p)}{\partial z}), \tag{1.37}$$

must be positive. This is usually achieved through the use of either a solar-like polytropic (Hanasoge et al., 2008) or artificially stablised (Schunker et al., 2011; Parchevsky & Kosovichev, 2007) background model.

1.3.3 Parallelisation Algorithm

In order to run efficiently on a distributed memory system the simulation domain must be decomposed. Efficient computation is achieved when the simulation time T_{sim} decreases inversely proportionally to the number of cores $T_{sim} \propto 1/n_{cores}$. The previous version of SPARC decomposed the 3D domain into 2D x-z directional slices. This scheme was only able to scale efficiently up to $n_{cores} = n_y/2$, for n_y the number of grid points in the y-horizontal direction. Therefore the maximum number of cores that could be used was n_y providing a substantial bottleneck in high resolution simulations. In order to increase the scalability of the code to thousands of cores a new decomposition scheme is used, dividing the simulation domain into 3D cubes.

For a parallel simulation run on multiple cores, the simulation domain must have its x, y, z directions split into (g_x, g_y, g_z) pieces, where number of cores must be equal to $g_x g_y g_z$. This will give sub-domains of size (b_x, b_y, b_z), dividing the full (n_x, n_y, n_z) domain. The grid size does not need to be divisible by block-sizes, although it will give optimal load balancing. Communication is performed through non-blocking send-receives in the derivative and filtering routines. The number of cells sent and received in the (x, y, z) dimensions is $(2(b_x + m_x)b_y b_z g_x, 2b_x(b_y + m_y)b_z g_y, 2b_x b_y(b_z + m_z)g_z)$, where $m_{x,y,z}$ is the number of ghost cells required for the derivative or filtering stencil. The 2.5D version of the code is parallelised with $b_y = n_y = 1$, and domain decomposition of the x and z dimensions.

In an effort to mask communication with computation of the derivatives and filtering routines, we calculate the interior points while waiting for the boundary cells as follows:

1. Allocate arrays, for the x-dimension $(-m_x + 1 : b_x + m_x, b_y, b_z)$

2. Call non-blocking MPI send and recieve routines.

3. Calculate derivatives for the interior of the sub-domain, for the x-dimension looping over $i = m_x + 1 : b_x - m_x$, $j = 1 : b_y$, $k = 1 : b_z$.

4. Call MPI_WAIT to pause until the communication with adjacent cores from step (1) is complete.

5. Calculate boundary cells depending on the simulation set-up (Periodic, Dirichlet, Neuman), for the x-dimension looping over the lower $i = 1 : m_x$, $j = 1 : b_y$, $k = 1 : b_z$ and upper $i = b_x - m_x + 1 : b_x$,$j = 1 : b_y$,$k = 1 : b_z$ boundaries.

A similar method is used for the y and z derivatives.

The FITS datatype does not have a parallel library for input/output. This causes a significant bottleneck to the code operation for large simulations. To prevent excessive communication requirements for input/output with a large number of cores the FITS file type has been replaced with HDF5. There are two output files provided during the operation of the SPARC code: a background file and a perturbation output file. Additionally, a 3D sub-domain can be selected for the perturbation output.

The code outputs initial conditions to the 0th save, simulation output to saves $1 : n$ for n output snapshots. If the simulation crashes, all arrays are dumped to a full output save. Table 1.1 outlines these two files and the datatypes and attribute information within. A routine is included with the code to convert the old background files of SPARC. The code also includes the option to restrict the perturbation output to a subset of the simulation domain allowing for a reduced storage requirement. The code can be re-initialised from a full simulation domain output.

To test the scaling of the new version of the SPARC code we have run two typical simulations; one hydrodynamic and one magnetic, each run for 0.25 hour of simulated time. A domain of $x, y = 300$ Mm^2, with z varying from -50 Mm to 2 Mm has been used in both simulations. The higher-order 11 point derivative scheme is used with the 11 point filter applied every 20 iterations in the z-direction and every 80 iterations in the x, y-direction. Data output is made of a slice at the height of measurement of the HMI-instrument (200 km) every 45 seconds, with a full data-cube saved every 300 seconds. The hydrodynamic simulation requires a timestep of 1.5 seconds, while the introduction of a magnetic field reduces this to 0.2 seconds. The resultant scaling with the number of cores can be seen in Figure 1.4. Although sub-linear, it represents a significant improvement over the previous implementation.

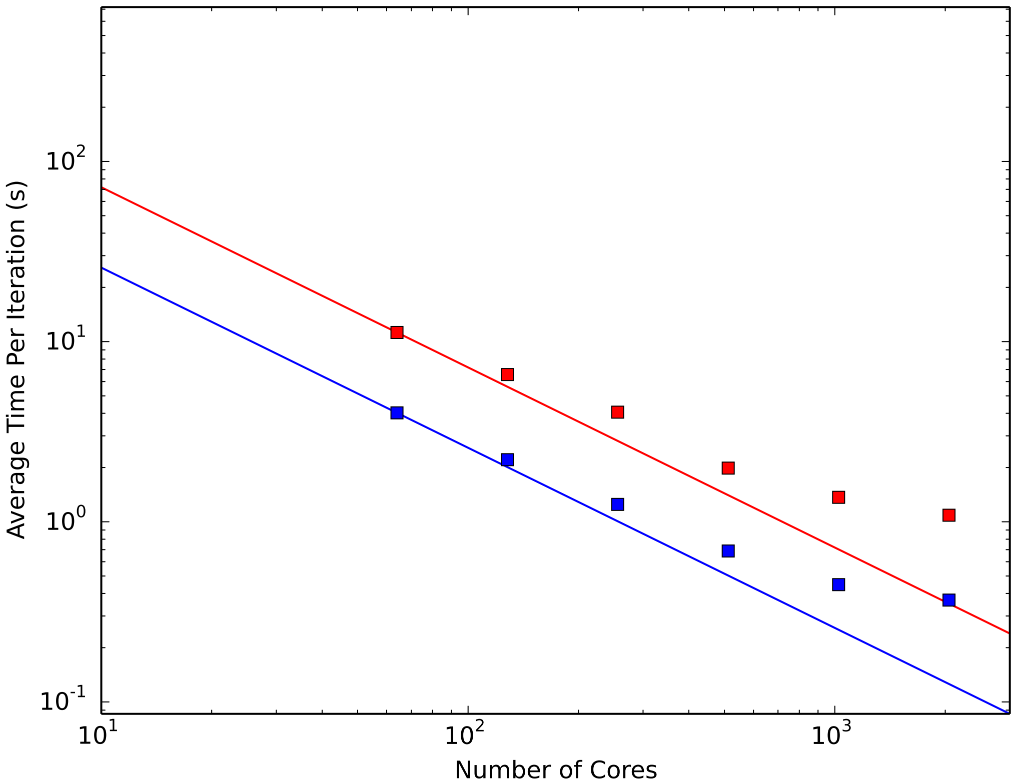

Fig. 1.4: Average simulation time per iteration showing the scaling of the SPARC code from 64, up to 2048 cores for a typical magnetic (red) and hydrodynamic (blue) simulation. The solid lines show ideal, linear scaling.

Table 1.1: Output Files

File	Background	Perturbation Output
Attributes	Background Name Dimensions (n_x, n_y, n_z) Max Δt (seconds, CFL 1.5) Xlength (cm) Ylength (cm)	Simulation Name Dimensions: (n_x, n_y, n_z) Time of Output (t seconds) Norm of Energy $(\lvert E_{mag}\rvert, \lvert E_{kin}\rvert, \lvert E_{therm}\rvert)$ Xlength (cm) Ylength (cm) $(n_{xpmlb}, n_{xpmlt}, n_{ypmlb}, n_{ypmlt}, n_{zpmlt}, n_{zpmlb})$
Contains	$z\,(n_z)$ p_0 ρ_0 c_{s0} Alfvén Limiter (R) Damping Sponge (S_p)	$z\,(n_z)$ p ρ v_x, v_y, v_z
If Magnetic	B_{x0}, B_{y0}, B_{z0}	B_x, B_y, B_z
If Flows	v_{x0}, v_{y0}, v_{z0}	
If PML and Magnetic		Ψ_x, Ψ_y, Ψ_z η_x, η_y, η_z $\mathbf{\Phi_x}, \mathbf{\Phi}_y, \mathbf{\Phi}_z$

1.3.4 Boundary Conditions

To perform local helioseismic simulations high-fidelity absorbing boundary conditions are desired to prevent spurious reflection of waves interfering with measurements. Of particular importance is the absorption of waves with a frequency above the acoustic cut-off ω_c, which should escape through the upper boundary, and the removal of $p-$modes with low spherical harmonic degree ℓ which will travel deeper than the bottom of the simulated domain. Absorbing boundaries in complex magnetic field structures are non-trivial, due to differences in behaviour of the various magnetohydrodynamic wave modes. High frequency acoustic waves will escape out the top boundary and low-ℓ waves will not be reflected before the bottom of the simulation domain. Two options are included for absorbing boundary conditions.

A simple absorbing sponge, or constant frictional term can be added to the right hand side of the momentum and continuity equations (Colonius, 2004). While very stable, sponge boundary conditions require a small damping coefficient and many cells to perform effectively. This makes them computationally infeasible for the simulations of size and length we wish to perform in local helioseismology. To better absorb the variety of wave modes present in MHD, a convoluted perfectly matched layer (cPML) boundary conditions are applied to the top, bottom and side boundaries. A full derivation of the cPML for MHD in a stratified media is described by Hanasoge et al. (2010), using an auxiliary differential equation (ADE) formulation (Gedney & Zhao, 2010). This method has been applied to work in all boundary layers of a three-dimensional simulation. To summarise, the ADE-cPML layer transforms the wave-number k_x,k_y and k_z of a wave travelling in the PML layer, for the x, y and z boundary layers by applying the following relation

$$k_{\parallel}^{*} \rightarrow k_{\parallel}\left[\kappa_{\parallel} + \frac{d_{\parallel}}{\alpha_{\parallel} - i\omega}\right], \tag{1.38}$$

where $\parallel$ is the direction parallel to the boundary. The function $d_{\parallel}$ is a damping function, while $\alpha_{\parallel}$ is the frequency dependant term, which acts as a filter, and $\kappa_{\parallel}$ is an additional parameter that damps evanescent waves. For example, in the z-dimension we have

$$d(x,y,z) = R_c \frac{N+1}{2L}\sqrt{c_s(x,y,z_0)^2 + v_A(x,y,z_0)^2}\left(\frac{z}{L}\right)^{N}, \tag{1.39}$$

where c_s is the sound speed at the beginning of the PML layer (z_0) and v_A is the Alfvén velocity. In the z direction κ will be described as

$$\kappa(z) = 1 + (\kappa_{max} - 1)\left(\frac{z}{L}\right)^{N}, \tag{1.40}$$

and α as

$$\alpha(z) = \pi f_0 \frac{z}{L}. \tag{1.41}$$

This leaves us with four free parameters: the maximum of the evanescent damping term (κ_{max}), the characteristic frequency (f_0), the order of the polynomial at which κ and d increases (N) and a reflection coefficient (R_c) which increases the strength of damping in the PML.

This wave-number transformation can be described as a grid stretching, as the derivatives inside the PML layer are performed in terms of the stretched coordinates. In the z-direction the z-derivative will be stretched, and the behaviour will be similar in x and y boundary layers. The transformed derivative, for the direction parallel to the boundary layer, is calculated as

$$\partial_{\parallel}\Psi_{\parallel}^{*} = \left[\frac{1}{\kappa_{\parallel}} - \frac{d_{\parallel}/\kappa_{\parallel}^{2}}{(d_{\parallel}/\kappa_{\parallel} + \alpha_{\parallel}) - i\omega}\right]\partial_{\parallel}\Psi_{\parallel}. \tag{1.42}$$

For the z-PML, this requires the computation of the terms $\Psi_{\|}$ in the continuity equation 1.32, $\mathbf{\Phi}_{\|} = (\Phi_x, \Phi_y, \Phi_z)$ in the momentum equation 1.33 and $\eta_{\|} = (\eta_{\perp 1}, \eta_{\perp 2})$ in the induction equation 1.35. The new version of SPARC has cPML's implemented on all the boundaries. The method of implementation remains the same with the introduction of 6 arrays required in each of the PML layers. These must also be updated in time, giving six extra equations to solve for the appropriate boundary layer. These are solved in the PML for the derivative parallel to the boundary:

$$\frac{\partial \Psi_{\|}^*}{\partial t} = \frac{d_{\|}}{\kappa_{\|}^2} \partial_{\|} \mathbf{v}_{\|} - \left(\frac{d_{\|}}{\kappa_{\|}} + \alpha_{\|} \right) \Psi_{\|}, \tag{1.43}$$

$$\frac{\partial \mathbf{\Phi}^*{}_{\|}}{\partial t} = \frac{d_{\|}}{\kappa_{\|}^2} \partial_{\|} \left[\frac{B_{0\|}\mathbf{B}}{4\pi} + \frac{\mathbf{B}_{\|}\mathbf{B_0}}{4\pi} - \left(p + \frac{\mathbf{B} \cdot \mathbf{B_0}}{4\pi} \right) \mathbf{e}_{\|} \right] - \left(\frac{d_{\|}}{\kappa_{\|}} + \alpha_{\|} \right) \mathbf{\Phi}_{\|}, \tag{1.44}$$

$$\frac{\partial \eta^*{}_{\|}}{\partial t} = \frac{d_{\|}}{\kappa_{\|}^2} \partial_{\|} \left[B_{0\|}\mathbf{v} - v_{\|}\mathbf{B} \right] - \left(\frac{d_{\|}}{\kappa_{\|}} + \alpha_{\|} \right) \eta_{\|}. \tag{1.45}$$

For the vertical PMLs the stratification must be adjusted in the boundary layer to ensure hydrostatic equilibrium. The derivatives of the background pressure and density are reduced as

$$\partial_z p_0^* = \frac{\alpha/\kappa}{d/\kappa + \alpha} \partial_z p_0, \tag{1.46}$$

$$\partial_z \rho_0^* = \frac{\alpha/\kappa}{d/\kappa + \alpha} \partial_z \rho_0, \tag{1.47}$$

while to preserve hydrostatic equilibrium the gravity is also reduced according to

$$g_0^* = \frac{\alpha/\kappa}{d/\kappa + \alpha} g_0. \tag{1.48}$$

As there is no stratification in the horizontal boundaries, this is not applied to the horizontal derivatives of the background pressure and density. In the corners of the simulation domain the PML layers are simply stacked on top of each other. A weak absorbing sponge has also been included inside the PML to prevent numerical errors, with a value given by

$$\sigma_{damp} = \sigma_0 \sqrt{c_s(x, y, z_0)^2} \left(\frac{z}{L} \right)^{N+1}, \tag{1.49}$$

where σ_0 is a constant.

Due to the large differences in the plasma-β and density over the simulation domain the wave type and direction of incidence will also vary. This has led to a selection of $R_z = 30.0$, $N_z = 2.0$ and $\kappa_z = 8.0$ for the upper vertical boundary, $R_z = 5$, $N_z = 2.0$ and $\kappa_z = 8.0$ for the lower vertical boundary and $R_{xy} = 15.0$, $N_{xy} = 3.0$ and $\kappa_{xy} = 8.0$ for the horizontal boundaries. The values of R, N and κ can be adjusted in the code for different driver amplitudes or different simulation domains.

Chapter 2

Excitation of the acoustic wavefield in the solar interior

In this chapter we investigate gaps in the acoustic power spectrum seen in a number of numerical simulations. An eigensolver is used to calculate solutions to the solar $p-$modes in combination with hydrodynamic simulations of wave excitation in the stratified solar atmosphere. It is found that the gaps are caused by driving at nodes of solar eigenfunctions. A distributed pulse driver is developed to overcome this problem and provide more accurate generation of waves.

The field of helioseismology uses the eigenfrequencies of resonant $p-$modes in the solar interior to determine subsurface structure. The most prominent observational manifestation of these resonant modes is a ν-k, or ν-ℓ diagram, where ℓ is the spherical harmonic degree. This diagram represents the power in the oscillations measured at the solar surface in terms of their frequency ν and horizontal wavenumber k. These diagrams show a series of ridges, each of which is an eigenmode of different radial order n, corresponding to the number of nodes in the radial eigenfunction (Gizon & Birch, 2005).

In time-distance helioseismology, phase-speed filters are used to isolate particular parts of the ν-k diagram, corresponding to $p-$mode wavepackets travelling between two surface locations. Alternatively, ring diagram analysis fits ν-k power spectra for a local region of the solar surface (Hill, 1988; Schou & Bogart, 1998) and uses it to measure local velocity flows and plasma parameters. Accurate measurements of the solar acoustic wavefield are necessary in order to perform realistic computational helioseismology.

The solar $p-$mode spectrum is stochastically driven by turbulent convection near the solar surface. In the solar interior the source of these perturbations is turbulent Reynolds stress (Schwarzschild, 1948; Goldreich et al., 1994). Nearer to the surface, acoustic waves are excited by non-adiabatic pressure fluctuations, produced by the interaction between convection and radiative cooling (Stein & Nordlund, 1989). 3D numerical simulations have been used to investigate the interaction between $p-$mode oscillations and near-surface magneto-convection (Stein & Nordlund, 2001). Comparing the different perturbation mechanisms, Nordlund & Stein (2001) concluded that the pdV work of stochastic gas pressure (p) fluctuations in the non-adiabatic layers is the primary driving mechanism of the solar $p-$mode spectrum.

For computational studies of acoustic wave propagation we need a driving function that can approximate the characteristic frequencies of solar interior magnetoconvection. The driving of acoustic sources is typically performed using a number of distributed pulse sources (Parchevsky et al., 2008; Felipe et al., 2016) or a plane of randomised sources with suitable wavenumber and frequency distribution (Hanasoge & Duvall, 2007; Rijs et al., 2016). The central frequency of the source is typically set to the peak in the observed solar power spectrum at 4.5 mHz using pulses like a Richter wavelet (Parchevsky & Kosovichev, 2007) or a truncated sinusoid (Shelyag et al., 2009). The pulses are distributed at a set depth, typically around $100 - 150$ km, which Kumar & Basu (2000) found to be the optimal height for exciting $p-$modes in the required

2 − 5 mHz frequency range. The source function is typically added to the right hand side of the vertical component of the momentum equation.

Gaps in the acoustic power spectrum have been seen in a number of simulations (Parchevsky & Kosovichev, 2007; Rijs et al., 2015; Przybylski et al., 2015); see Figure 2.1 for an example. We wish to understand the cause of these anomalies, and remove them from our simulations. Absorption of power at certain frequencies typically represents a problem with boundary conditions. By varying the box size and using periodic, sponge and perfectly matched layer (PML) boundary conditions, this potential source of error was ruled out. The power gaps remain the same in all cases.

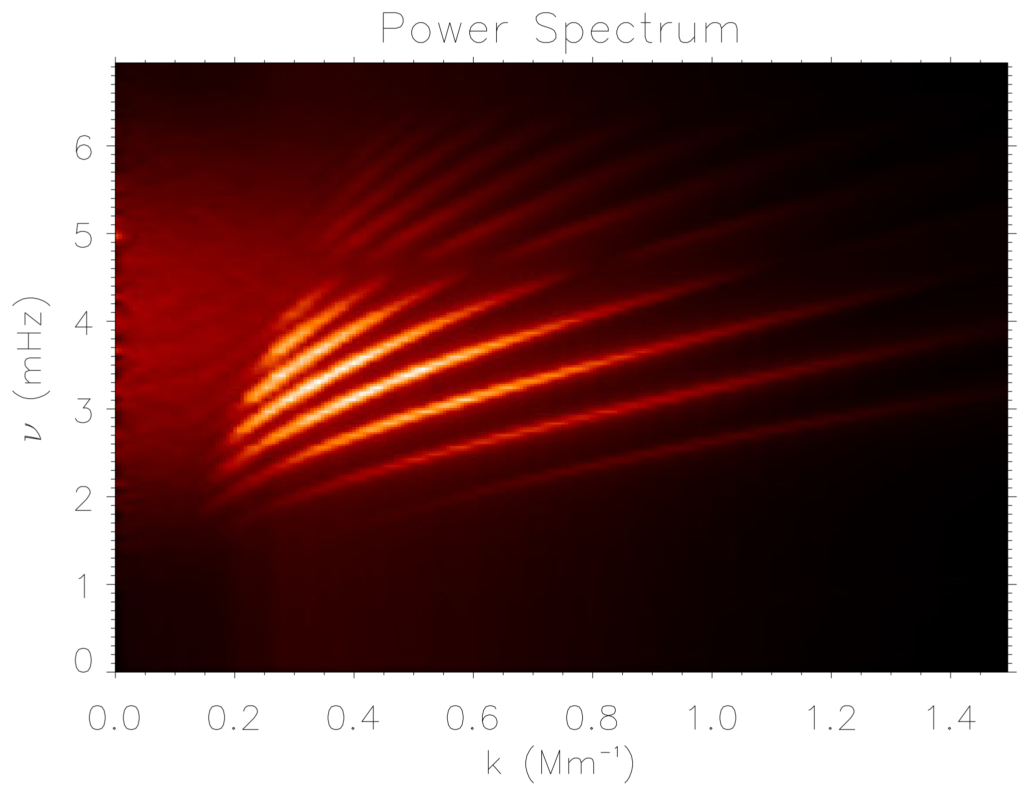

Fig. 2.1: The ν-k power ridges of the stratified solar atmosphere from a 4 hour simulation with a pulse driver.

In this chapter we will investigate the cause of the gaps in the acoustic power spectrum observed in our numerical simulations, and develop a new method of driving to resolve this problem. In Section 2.1 we generate a convectively stable solar model, used in MHD simulations for computational helioseismology throughout this thesis. In Section 2.2 we use a boundary value method to solve for the eigenmodes of the solar interior. We apply this solver and find that driving at nodes of the eigenfunction could be the cause of these gaps. In Section 2.3 we perform numerical simulations of acoustic wave propagation in the solar interior, comparing the results to those obtained from the eigensolver to verify the nodes as the cause. Finally, in Section 2.4 we describe the new driving function to resolve the issues presented.

2.1 Convectively Stabilised Solar Model

In order to perform helioseismic inversions an accurate background model is required to compute the $p-$mode spectrum of the solar interior. In this thesis we simulate the output radiation spectrum of solar magnetic field structures in addition to performing computational helioseismology. We require a background that we can use to achieve both goals: convective stability for linear simulations, and a realistic semi-empirical pressure, density and temperature distribution over the photospheric spectral line formation region.

Linear modelling is frequently applied to helioseismic problems due to its speed and the long simulation times required. A linear simulation requires a background model which is both convectively and hydrostatically stable to prevent fatal instabilities. To provide a convectively stable quiet Sun background model, the method described by Parchevsky & Kosovichev (2007) is used. We generate a convectively stable quasi-solar model with minimal changes to the photospheric line formation regions and the correct sound speed profile below the surface, at the expense of a slightly reduced density and pressure in the deeper regions.

A measure of convective stability is the Brunt-Väisälä frequency:

$$N^2 = \frac{g}{\gamma p}\frac{\partial p}{\partial z} - \frac{g}{\rho}\frac{\partial \rho}{\partial z}, \tag{2.1}$$

calculated in terms of the pressure p, density ρ, adiabatic index γ and gravitational acceleration g of the solar model used. This represents the oscillatory frequency of a parcel of gas in a gravitationally stratified fluid. Convective stability is achieved when $N^2 > 0$, or the Brunt-Väisälä frequency is real and the parcels of gas oscillate stably.

In addition to convective stability we require hydrostatic equilibrium to prevent exponential growth of perturbations. Strict hydrostatic equilibrium is also required to generate the magnetohydrostatic sunspot model presented in Chapter 4. The hydrostatic equilibrium is calculated as:

$$\frac{\partial p}{\partial z} = -\rho g. \tag{2.2}$$

Following the method of Parchevsky & Kosovichev (2007) we rearrange Equations 2.1 and 2.2 in terms of $\partial\rho/\partial z$, introducing a free parameter α;

$$\frac{\partial \rho}{\partial z} = -\frac{g\rho^2}{\gamma p} - \alpha\frac{\rho N^2}{g}, \tag{2.3}$$

where the gravity acceleration g, Brunt-Väisälä frequency N, and the adiabatic index γ are functions of depth. The free parameter α must be greater than zero to enforce convective stability. Using a shooting method, α is increased between 0 and 2 in order to match the pressure in the model at a chosen depth in the solar interior. Equations 2.2 and 2.3 are solved using a fourth-order Runge-Kutta method on a one-dimensional grid.

To enforce convective stability, the Brunt-Väisälä frequency is modified. This involves setting the negative values in the convectively unstable solar interior to small positive ones, scaled inversely with gravity. Some smoothing of the Brunt-Väisälä frequency function is required around the super-adiabatic layer, in order to achieve a realistic sub-surface distribution. The plasma distribution above the photosphere is left untouched, apart from enforcing strict hydrostatic equilibrium through integration of Equation 2.2. This causes minor changes to the pressure and temperature of the model.

The method described above can be applied to any solar model. In general, for average quiet Sun distributions a model is created by smoothly joining a photospheric model, such as VALIIIC (Vernazza et al., 1981) or the updated models of Avrett & Loeser (2008); Avrett et al. (2015) to the Standard Solar Model S (Christensen-Dalsgaard et al., 1996) at around $z = -0.5$ Mm. An equispaced grid covering the height range from -150 to 20 Mm is used, with a vertical resolution of $\Delta z = 0.0068$ Mm. Using the modified Brunt-Väisälä frequency, Equations 2.2 and 2.3 are integrated downwards from the upper boundary, set to $z = 10$ Mm. The free parameter giving the closest match at the lower boundary ($z = -50$ Mm) is $\alpha = 0.95$.

The density, pressure, temperature and sound speed of the convectively stabilised solar model is plotted in Figure 2.2. Comparison of the stabilised thermodynamic variables to the original semi-empirical distribution (blue-dotted line) shows a close match over the photosphere and chromosphere. The density and pressure are increased in the interior with only a slight change to the resulting sound-speed. The new model is also compared to two models previously used in solar MHD simulations. Firstly, the modified Model S of Hanasoge et al. (2008) is shown (red line). This model is designed for computational helioseismology and accurately replicates the solar $p-$mode power spectrum. The modified Model S is convectively stabilised, with a realistic photosphere and chromosphere replaced by an isothermal layer. Secondly, the model used by Khomenko & Collados (2008) is plotted (green line). This model provides a close match to the VAL-IIIC photosphere and chromosphere at the expense of an increased pressure, density and sound speed in the interior.

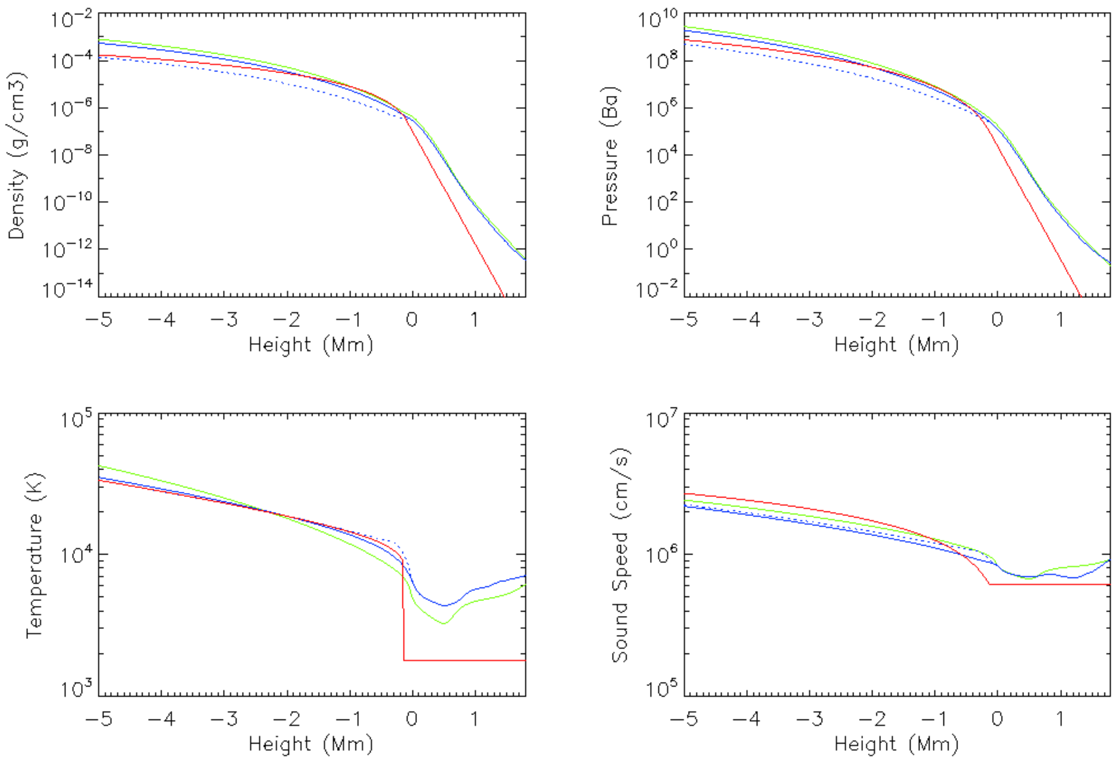

Fig. 2.2: Plots of the density, pressure, temperature and sound speed of the original solar model (blue dotted line) and the convectively stabilised model (blue solid line). Also compared are the modified Model S of Hanasoge (solid red line), and the convectively stabilised model used by Khomenko (solid green line)

2.2 Eigenmodes of the Solar Interior

We wish to understand the nature of the gaps observed in the solar $p-$mode power spectra of our linear magnetohydrodynamic simulations. With the assumption that the wavelength is substantially shorter than the solar radius, the equations of motion for solar acoustic waves can be written in Cartesian form and the effects of spherical geometry can be ignored (Lamb, 1932). Modelling linear perturbations of normal mode oscillations in the non-magnetic Sun can be elegantly written in terms of Ψ, defined as

$$\Psi = \rho^{1/2} c_s^2 \nabla \cdot \boldsymbol{\xi}, \tag{2.4}$$

where ρ is the density, c_s the sound speed and $\boldsymbol{\xi}$ the fluid displacement (Deubner & Gough, 1984).

The equation of motion for adiabatic perturbations in a stratified atmosphere is written as

$$\left(\nabla^2 - \frac{\omega_c^2}{c_s^2} - \frac{1}{c_s^2}\frac{\partial^2}{\partial t^2}\right)\frac{\partial^2 \Psi}{\partial t^2} + N^2 \nabla_h^2 \Psi = 0, \tag{2.5}$$

in terms of the Brunt-Väisälä frequency N and the acoustic cut off frequency ω_c (Cally, 2006). An alternate form of the Brunt-Väisälä frequency to Equation 2.1 is defined in terms of density scale height $H(z)$ and gravitational acceleration g, as

$$N^2 = \frac{g}{H} - \frac{g^2}{c_s^2}, \tag{2.6}$$

and the acoustic cutoff frequency ω_c is calculated as

$$\omega_c^2 = \frac{c_s}{4H^2}\left(1 - 2\frac{\partial H}{\partial z}\right). \tag{2.7}$$

For solutions to propagate, the angular frequency ω must exceed the cutoff frequency. The sharp changes in density and pressure near the solar surface introduce a spike in the pressure scale height, giving a cutoff frequency of around 5.3 mHz.

To directly compare the results to our simulations we use the model described in Section 2.1, with the Solar Model S to describe the interior, and the model of Avrett et al. (2015) for the atmosphere. Figure 2.3 shows the density scale height, sound speed, Brunt-Väisälä and acoustic cutoff frequencies of the model used.

Assuming a solution of the form $\Psi = \Psi_z \exp\left(i\left(k_x x + k_y y - \omega t\right)\right)$ allows Equation 2.5 to be simplified to a second order ordinary differential equation:

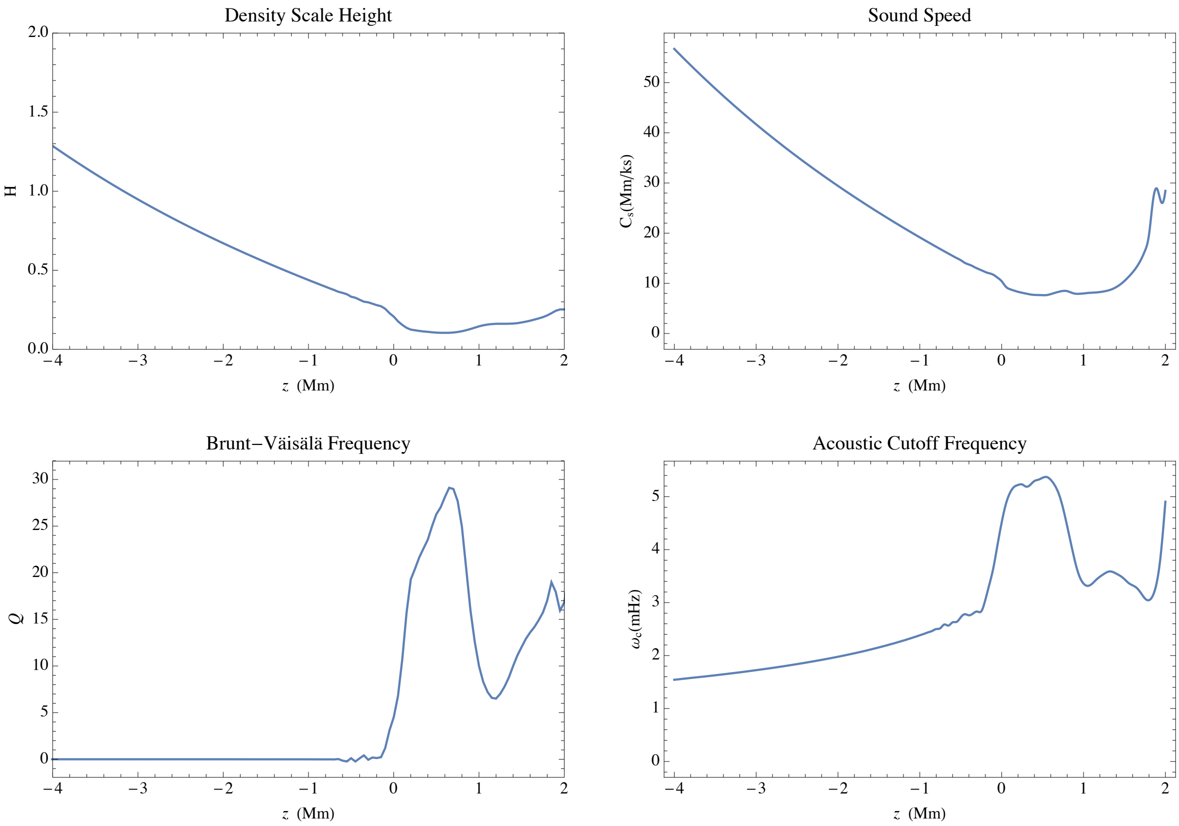

Fig. 2.3: The density scale height (top left), sound speed (top right), Brunt-Väisälä frequency (bottom left) and acoustic cutoff frequency (bottom right) of the convectively stablised quiet Sun model.

$$\frac{\partial^2 \Psi}{\partial z^2} = K(z)\Psi, \tag{2.8}$$

where K is the vertical wavenumber,

$$K^2 = \frac{\omega^2 - \omega_c^2}{c_s^2} + k_h^2 R_\odot^2 \left(\frac{N^2}{\omega^2} - 1\right). \tag{2.9}$$

The horizontal wavenumber can be written as $k_h^2 = k_x^2 + k_y^2 = \frac{\ell(\ell+1)}{R_\odot^2}$ for spherical harmonic number ℓ and the solar radius $R_\odot$. In Figure 2.4 the dependence of the vertical wavenumber on frequency and wavenumber is plotted for the model described above. For lower frequencies and higher wavenumbers the turning point is seen to lie deeper in solar interior. For higher frequencies, the region in which waves cannot propagate is narrow, eventually disappearing as it reaches frequencies above the acoustic cutoff. Waves can easily tunnel across this gap.

To explore the form of the solar eigenfunctions in a realistic atmosphere we use a shooting method to solve the second order ODE described above in Equation 2.8. This will solve for the eigenfunction of each of the $p-$mode ridges at a chosen frequency. The choice of starting wavenumber k for a particular frequency and $p-$mode can be made from either the simulated or observed solar acoustic power spectrum. Using the "NDSolve" package of Mathematica with evanescent boundary conditions, we solve for the eigenfunction Ψ as defined in Equation 2.4, and the wavenumber k of each $p-$mode ridge at the chosen frequency.

The vertical displacement ξ and the horizontal displacements $i\zeta$ are recovered from the eigenfunction Ψ (Equation **??**) as

$$ik_h\zeta = \frac{1}{\rho^{1/2}c_s^2}\Psi \tag{2.10}$$

$$\frac{\partial \xi}{\partial z} = \frac{1}{\rho^{1/2}c_s^2}\Psi \tag{2.11}$$

Figure 2.5 shows the solutions of vertical displacement with depth for the $n = 1$ to $n = 6$ $p-$mode ridges. The method used is unable to solve for the higher order $p-$modes at low frequencies.

From the calculated eigenfunctions we can immediately notice a bunching in frequency of the nodes for the different higher-order $p-$modes, as has been seen in the simulated ν-k diagrams. The heights of the nodes are ≈ -1.4 and -3.6 Mm at 3.5 mHz

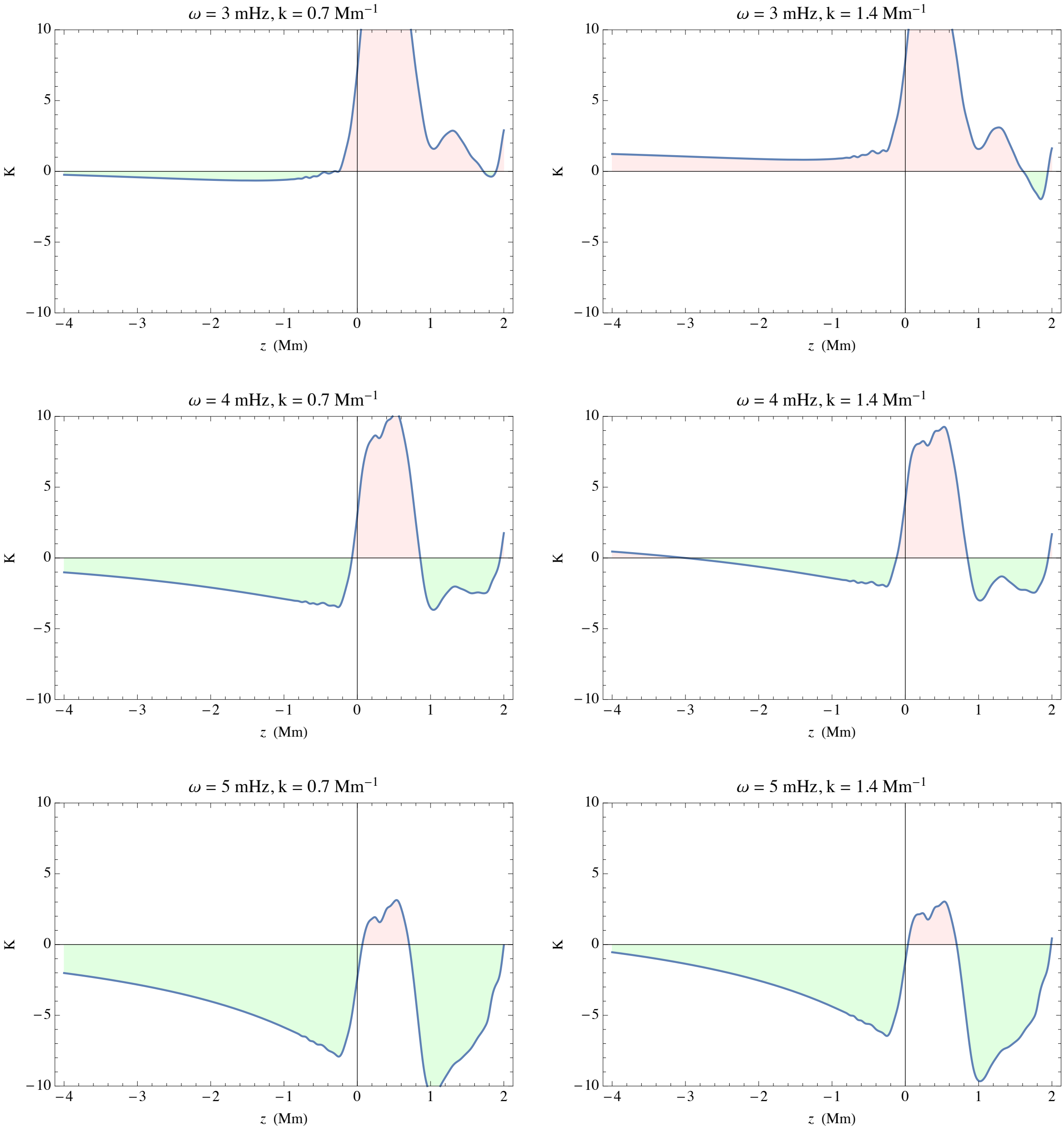

Fig. 2.4: The vertical wavenumber K, for a number of frequencies and wavenumbers. The wave is trapped in the region where $K < 0$ and will be reflected and become evanescent at the acoustic cutoff, around $z = -0.5$ Mm, where $K > 0$.

increasing to ≈ -0.4 and -1.6 Mm at 5 mHz. We can therefore reasonably assume that for a given node depth, the frequencies of the solar $p-$modes will also be bunched. In order to test this assumption we will perform 3D hydrodynamic simulations of acoustic waves, with the depth of the driving functions varied.

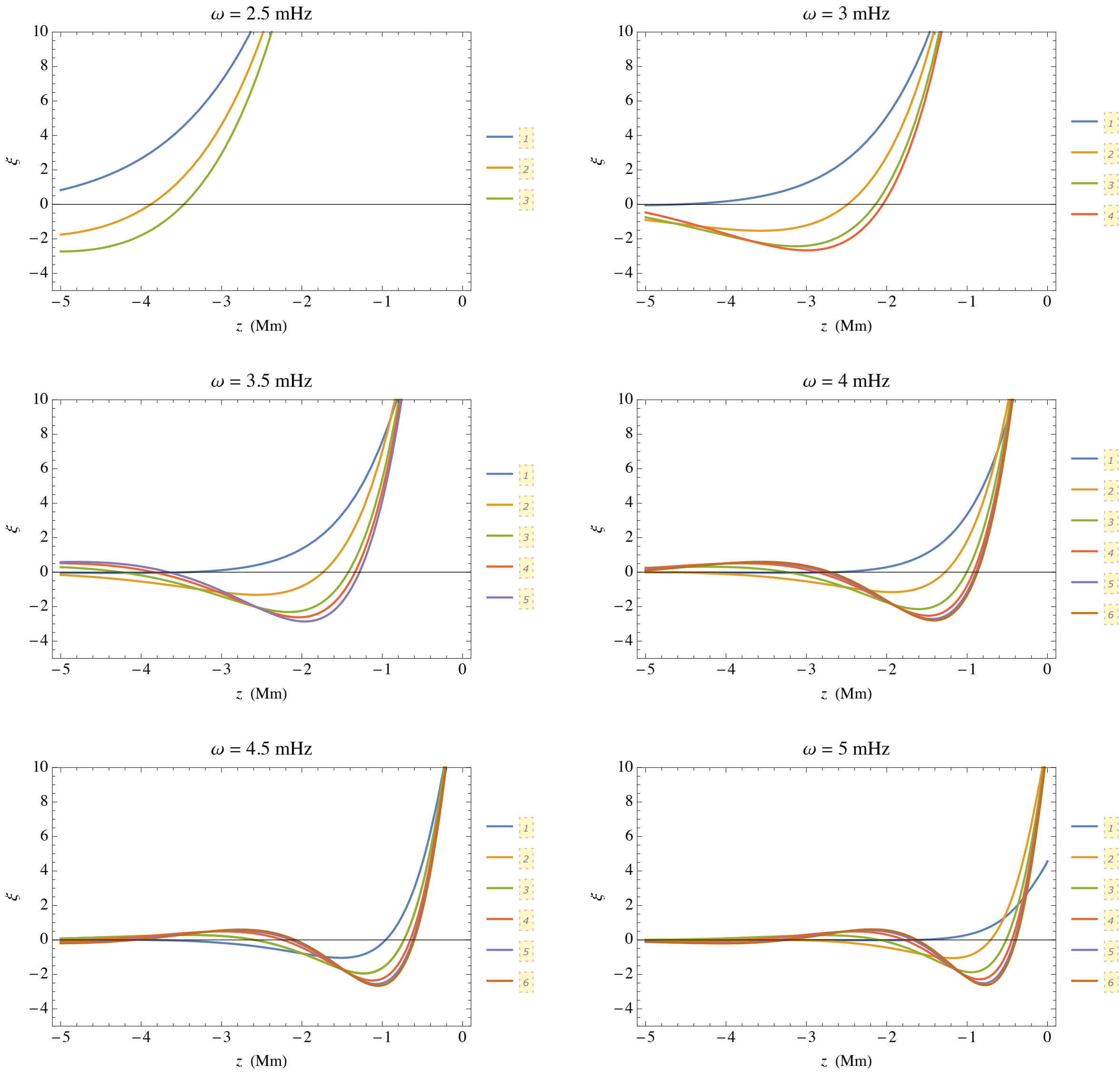

Fig. 2.5: The vertical displacement ξ, for the eigen-solutions of the wave equation. A selection of frequencies are shown and the $n = 1$ to $n = 6$ $p-$modes plotted. For low frequencies, the solution method used is unable to find the higher $p-$modes.

2.3 Numerical Simulations

We perform a number of simulations of acoustic wave propagation in the model described in Section 2.1. The simulations are performed with the SPARC code, as described in Chapter 1.3. The code solves the linearised ideal MHD equations for wave propagation in a stratified solar environment. We use the 11 point central difference scheme for the spatial derivatives in combination with the 11 point explicit filter to prevent numerical instabilities in the solution.

For boundary conditions, we use a Perfectly Matched Layer (PML) (Hanasoge et al., 2010) at the top and bottom boundaries, allowing for efficient absorption of the outgoing waves. The side boundaries are periodic.

The simulation domain has horizontal extent of $n_x = n_y = 256$ grid points, with a physical size of 300 Mm, giving a resolution of $\Delta x = \Delta y = 1.176$ Mm in the horizontal directions. To deal with the large variation in physical parameters over the domain from the convective zone to chromosphere, the code uses a vertical grid spacing based on the sound speed. The grid has $n_z = 400$ points between -25 and 1.5 Mm and is distributed such that the acoustic travel times between each cell are the same for the quiet Sun, $\Delta z \propto 1/c_s$. This gives a resolution of around 50 km near the photosphere, and around 500 km in the lower solar interior.

In order to test the cause of the observed gaps a plane of 1000 pulse sources is used. Each of these sources is represented by a 3-dimensional Gaussian ball in space, and a sinusoid truncated by a Gaussian in time, as described in Shelyag et al. (2009). The sources are applied to the RHS of the momentum equation (1.33) as a vertical acceleration perturbation,

$$\begin{aligned} S\left(x,y,z,t\right) &= A_0 \sin\left(\frac{2\pi t}{t_o}\right) \exp\frac{-\left(t-t_1\right)^2}{\sigma_t^2} \\ &\times \exp\frac{-\left(\left(x-x_0\right)^2+\left(y-y_0\right)^2\right)}{\sigma_h^2} \exp\frac{-(z-z_0)^2}{\sigma_z^2}, \end{aligned} \tag{2.12}$$

where $t_0 = 300$ s, $t_1 = 300$ s, $\sigma_t = 75$ s, $\sigma_h = 1.5$ Mm, $\sigma_z = 0.15$ Mm. The horizontal position of the pulse is $(x_0,\ y_0)$ is randomly assigned and the depth below the photosphere, z_0, varied to investigate the changes in the acoustic power spectrum. Six simulations are run, with z_0 set to a depth of $100, 200, 300, 500, 1000,$ and 2000 km below the photosphere. The simulations are run for 6 hours to allow the domain to be excited to a steady state, output is then recorded at the HMI observation height of

Table 2.1: Nodes of vertical fluid displacement ξ

$p-$mode	Frequency (mHz)	Wavenumber (Mm^{-1})	Node height (Mm)
3	3.075	0.380	-2.003
4	4.740	0.852	-2.005
5	3.840	0.381	-0.999
6	4.720	0.510	-0.506
6	5.200	0.662	-0.304
6	5.35	0.720	-0.202

$z = 200$ km for a further 12 hours, with an output cadence of 30 seconds.

In Figure 2.6 we can observe how the wave energy at the solar surface depends on the depth of the driving function. For sources near the solar surface, < 300 km depth, the gaps are moved above the acoustic cutoff frequency, where they are difficult to observe. Deeper drivers will have gaps at a lower frequency, until eventually a second set of nodes becomes visible. To check our results we use the solver described in Section 2.2. For each $p-$mode we use the frequency and wavenumber of the gaps in the simulated power spectrum to calculate the eigenmode. We then search for the node(s) to check if their depth matches that of the driving function.

Calculating solutions of the $n = 6$ $p-$mode at a frequency of 4.72 mHz and a wavenumber of 0.51 Mm^{-1} give a node in the ξ at -0.506 Mm. This result matches the gap in power ridge of the $n = 6$ $p-$mode for the case of driving at -0.5 Mm, marked with a $+$ in the middle-right panel of Figure 2.6. Again, for an $n = 6$ $p-$mode, a frequency of 5.2 mHz, and a wavenumber of 0.662 Mm^{-1} the node of ξ is at -0.304 Mm. Table 2.1 gives a list of the solutions marked on Figure 2.6. All are located towards the top of a gap in the acoustic power.

In many simulations a driving depth of $100 - 200$ km is used. This moves the gaps higher in frequency, where the solar acoustic cutoff will greatly reduce the power above 5.3 mHz, masking the gaps. The high frequency gaps are very sensitive to small changes in driving height. A shallow source < 100 km using a Gaussian ball of FWHM $\sigma_z = 50$ km or greater will show no observable power gaps.

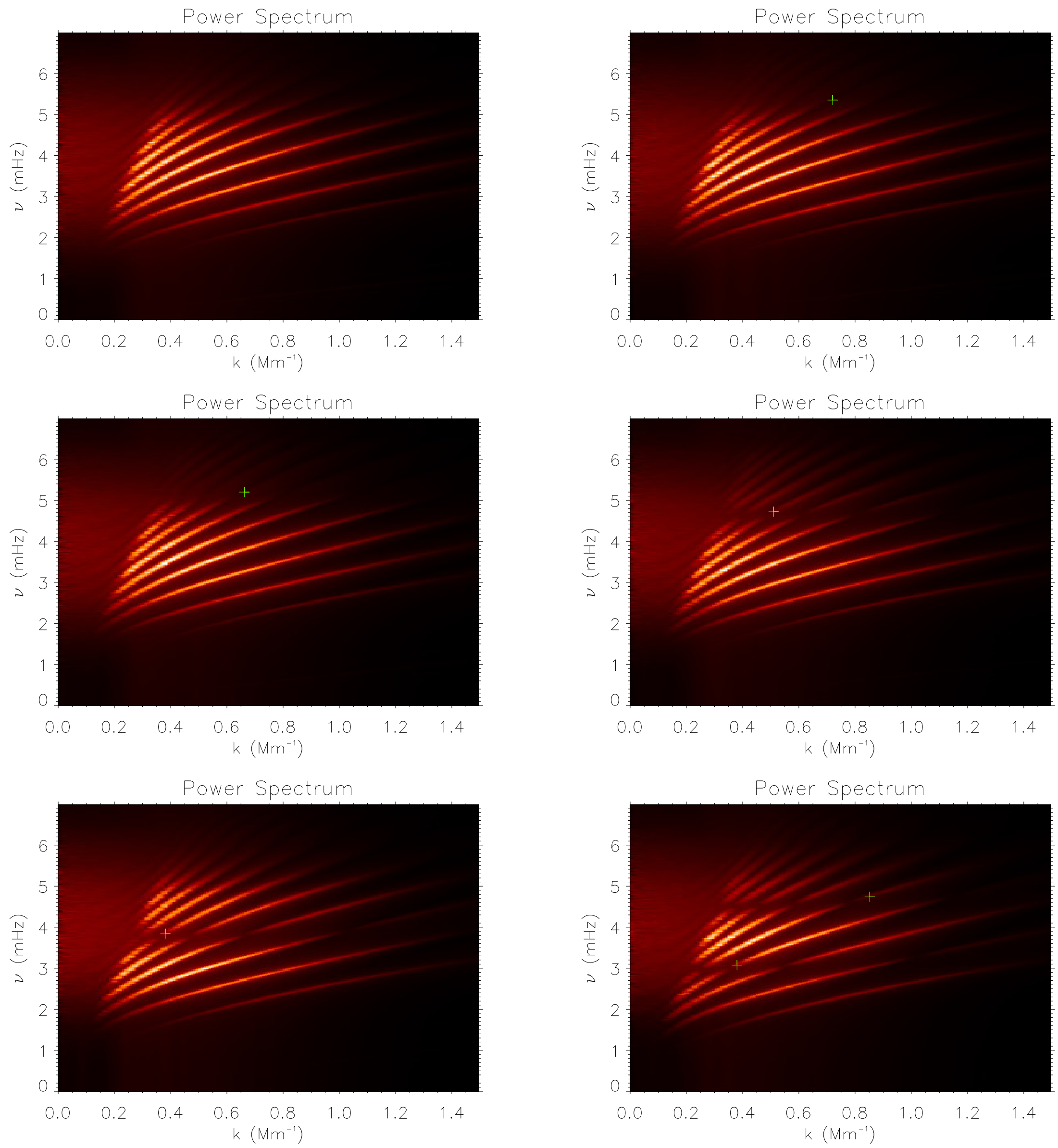

Fig. 2.6: The ν-k power ridges of the stratified solar atmosphere. Each represents a simulation with a different depth at which the driving function is placed. Of interest are the gaps in the ridges at a nearly constant frequency. Top left) Driver at -0.1 Mm, top right) Driver at -0.2 Mm, middle left) Driver at -0.3 Mm, gaps at $\approx$ 5.2 mHz, middle right) Driver at -0.5 Mm, Gaps at $\approx$ 4.7 mHz, bottom left) Driver at -1 Mm, gaps at $\approx$ 3.75 mHz, bottom right) Driver at -2 Mm, gaps at $\approx$ 3.0 mHz and 4.5 mHz. Green + symbols represent solutions of the eigensolver with a node at the appropriate driving height.

2.4 A pseudo-random forcing function for helioseismic simulations

A "realistic" solar driving function will be distributed in all three dimensions in a narrow layer below the solar surface, representing the convective buffeting. In order to remove the power gaps discussed above, in addition to providing a more realistic excitation of acoustic waves in the solar interior, a pseudo-random three-dimensional set of pulses is created.

A number of pulses n_{pulses} are chosen. For each of these pulses, described in Equation 2.12, the variables required $(x_0, y_0, z_0, \sigma_h, \sigma_z, t_0, t_1, \sigma_t, A_0)$ are picked. An additional variable, t_{end} is defined, and after $t > t_{end}$ a new set of variables is selected. The variables are chosen using the following prescription:

1. The horizontal position variables, x_0 and y_0, are uniformly distributed over the horizontal extent of the simulation domain.
2. The vertical position, z_0, is uniformly distributed between -100 km and -2000 km
3. The pulse amplitude A_0 is picked from a Gaussian distribution around a mean value $\mu_{amp} = 1\ \mathrm{m\,s^{-1}}$ with a standard deviation $\sigma_{amp} = 0.25\mu_{amp}$.
4. To ensure a resolved pulse, σ_h is chosen from a normal distribution with a mean of $2\Delta_x$ and a standard deviation of $0.25\Delta_x$. Where Δ_x is the grid resolution.
5. The vertical extent of the pulse, σ_z is chosen from a normal distribution, the mean varies with height, from 50 km at -100 km to 100 km at -2000 km. A standard deviation of $0.25\Delta_x$ is used.
6. The value of the period of oscillation t_1 is picked from a Gaussian distribution with a mean corresponding to the peak frequency of the solar power spectrum, 1/4.5 mHz, and a standard deviation of 1/2.0 mHz.
7. The temporal distribution of the Gaussian σ_t, is set to $0.5t_1$
8. The mean time of the pulse t_0 is chosen uniformly from between $t + 4\sigma_t$ and $t + 6\sigma_t$.
9. The end time of the pulse t_{end} is set to be $t_0 + 4\sigma_t$

The forcing function is created by summing all pulses, scaled with the inverse of the background density $1/\rho_0$ and added to the right hand side of the momentum equation.

This application of a large number of pulses is computationally expensive in a serial simulation, or over a small number of CPU cores. However in the large parallel simulations typically undertaken with the SPARC code the uniform distribution of sources allows us to speed this process up. Each core will only calculate the sources if part of the ball $(x_0 \pm \sigma_h, y_0 \pm \sigma_h, z_0 \pm \sigma_z)$ lies within its domain.

We use the simulation domain and computational setup described in Section 2.3. The plane of pulses is replaced with the randomly distributed pulses following the prescription described, and n_{pulses} is set to 2000. One downside of this approach is the simulation must be allowed to stir until the domain is sufficiently random. This is achieved by waiting until the norm of the kinetic-energy in the box $\rho v^2/2$ plateaus.

Figure 2.7 shows the ν-k diagram from this new simulation. Overplotted are solutions to the $p-$mode ridges calculated from the eigensolver described in Section 2.2. These show a close match between the simulated and calculated values and no gaps in the power ridges.

2.5 Summary and Conclusions

In this chapter we have investigated the cause of gaps in the acoustic power spectrum of helioseismic solar simulations. Through the use of a boundary-value solver for the solar interior and linear hydrodynamic simulations we have determined it can be seen that the cause of these gaps is driving at nodes of the solar $p-$mode eigenfunction. To summarise the results:

1. Anomalous gaps have been found in linear helioseismic MHD simulations.
2. Using a boundary value solver and SPARC MHD simulations we have shown that the cause of gaps is driving at nodes in the solar $p-$mode eigenfunction.
3. Two solutions are identified; placing sources at a low depth, or distributing sources in z.
4. We have developed a pseudo-random distribution of sources that yields more realistic spectra.

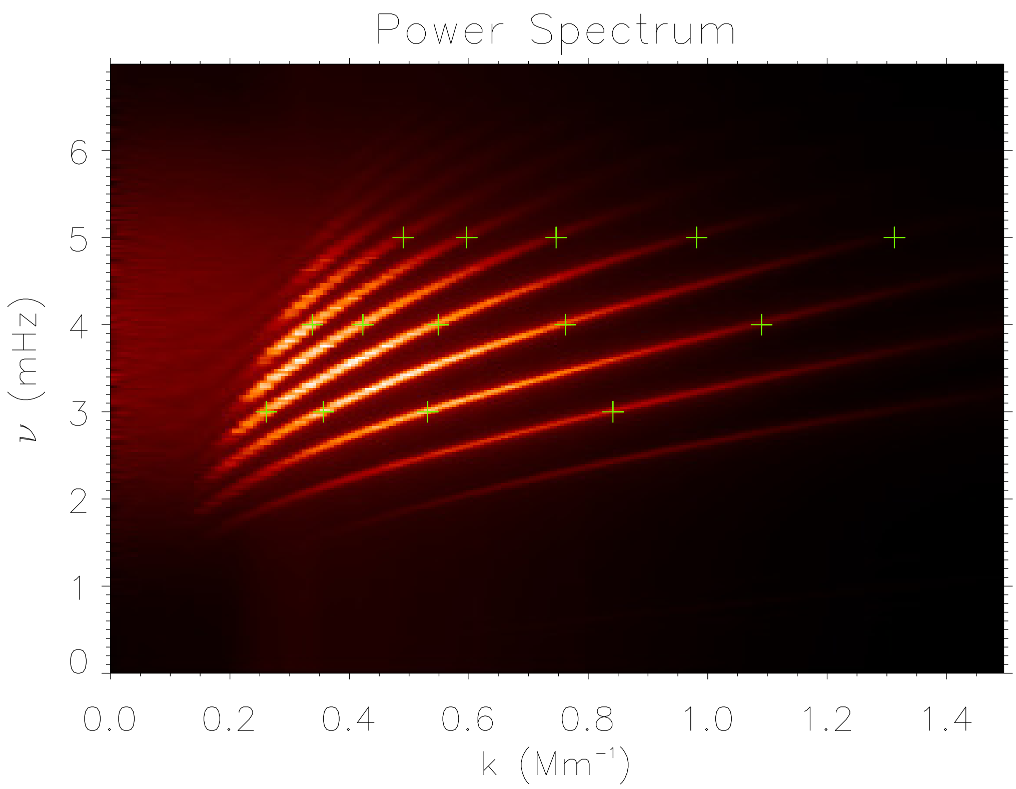

Fig. 2.7: The ν-k power ridges of the stratified solar model simulated with the distributed sources routine. Results from the eigensolver are overplotted with green $+$.

A number of possible avenues exist to further improve the excitation mechanism in future work. Firstly, we aim to match the observed power spectrum with that of the distributed sources. This could be performed by using a machine learning approach to adjust the random variables to better fit the solar $p-$mode ridges.

The excitation of waves under and around a sunspot is a problem which needs to be investigated. Strong magnetic fields, like sunspots, inhibit convection. This affects the height at which preferential driving occurs. Currently, for simulations using the sources described in Section 2.4 and a strong magnetic field, an additional scaling of the driver is performed by multiplication of the source function with the plasma-β squared ($D_{mag} = \max(1, \beta^2)$). Future work will adjust the forcing function in and around a sunspot, to determine a best match to the acoustic power measured in observed active regions.

Chapter 3

Synthetic Observations with MHD Simulations

In this chapter we calculate synthetic observables for magnetohydrodynamic simulations. An introduction to radiative transfer and spectral synthesis is provided. Finally we study the observational signatures of photospheric "vortices" previously identified in the MURaM magneto-convection simulations. In order to observe these torsional motions synthetic centre-to-limb observations are made using the Fe I 6302 Å spectral line. The effect of degrading the spatial and spectral resolution on simulated observables is studied. It is found that the line-of-sight Doppler shifts and Stokes$-V$ signatures of the vortices are unresolvable at the resolution of the Solar Optical Telescope on board the Hinode satellite. In order to observe these motions the 20 km resolution of next-generation 4 m telescopes, such as DKIST and EST, will be required.

Monash University

Declaration for Thesis Chapter 3

Declaration by candidate

In the case of Chapter 3, the nature and extent of my contribution to the work was the following:

Nature of contribution	Extent of contribution (%)
Generation of synthetic observables used in Figure 1 and part of Figure 2. Writing and editing relevant part of paper.	25

The following co-authors contributed to the work. If co-authors are students at Monash University, the extent of their contribution in percentage terms must be stated:

Name	Nature of contribution	Extent of contribution (%) for student co-authors only
Sergiy Shelyag	Key Ideas, modelling and production of results, writing of paper.	

The undersigned hereby certify that the above declaration correctly reflects the nature and extent of the candidate's and co-authors' contributions to this work*.

Candidate's Signature	[redacted]	**Date** 17/2/17
Main Supervisor's Signature	[redacted]	**Date** 17/2/17

*Note: Where the responsible author is not the candidate's main supervisor, the main supervisor should consult with the responsible author to agree on the respective contributions of the authors.

Observations of the Sun can be made using a number of techniques, including imaging, where the intensity of radiation is sampled at a particular wavelength, and spectroscopy, which measures the intensity over a grid of wavelengths, allowing the study of spectral lines. In addition the polarisation state of the radiation can be measured using polarimetry. Spectropolarimetry uses the full Stokes vectors for light, over a chosen wavelength range, to gain an understanding of the plasma properties in the region where the radiation is formed.

Imaging can be performed at a number of wavelengths. This allows for simultaneous observation at a number of heights in the atmosphere. Using these observations we can develop a three-dimensional picture of wave propagation from the photosphere to the corona. Study of the power spectrum and phase differences between different observation heights and angles can be used to identify MHD wave modes.

Magnetic fields and strong velocity gradients present at the solar surface impart polarisation signatures on the radiation formed. An understanding and interpretation of the formation, transmission, measurement of polarized light allows us to extract more information from the observed radiation spectrum. However, measuring the different polarisation states requires a higher photon count. In particular, spectropolarimetry has been successfully applied to the measurement and study of solar magnetic fields using Zeeman splitting and the Hanle effect (Trujillo Bueno, 2003).

In Section 3.1 we give a description of electromagnetic radiation using Stokes vectors, in Section 3.1.2 we provide the fundamentals of computational radiative transfer, including the Zeeman effect, and in Section 3.2 we show synthetic spectropolarimetry of a MURaM simulation.

3.1 Spectral Synthesis

3.1.1 Stokes Vector

The electric field vector $\mathbf{E}$ of a monochromatic electromagnetic wave travelling in the z-direction is given by:

$$E_x = A_x \cos(2\pi\nu t - \phi_x), \tag{3.1}$$

$$E_y = A_y \cos(2\pi\nu t - \phi_y), \tag{3.2}$$

where ν is the frequency, A_x, A_y are the amplitudes and ϕ_x, ϕ_y are the phases. The Stokes vector $\mathbf{I} = (I, Q, U, V)$ provides a complete description of the polarisation state of light (Stokes, 1852). The Stokes-I value gives the intensity of the light, Stokes$-Q$ and $-U$ profiles are the intensity differences between linear polarisation states, the former between 90° and 0° and the latter between 45° and −45°, and the Stokes$-V$ profile represents the intensity difference between right and left circularly polarised light (Stenflo, 2013):

$$\begin{aligned} I &\equiv A_x^2 + A_y^2, \\ Q &\equiv A_x^2 - A_y^2, \\ U &\equiv 2A_xA_y\cos(\phi_x - \phi_y), \\ V &\equiv 2A_xA_y\sin(\phi_x - \phi_y), \\ I^2 &\geq Q^2 + U^2 + V^2. \end{aligned} \tag{3.3}$$

The intensity of the polarised component is I_p:

$$I_p^2 = Q^2 + U^2 + V^2, \tag{3.4}$$

and the unpolarised component is I_u, which satisfies $I = I_u + I_p$. The degree of polarisation P is then calculated as

$$P = \frac{I_p}{I_u + I_p} = \frac{I_p}{I}.$$

As a light ray passes through plasma, the effect of the medium on the Stokes vector is described by a 4×4 Mueller matrix M. The emergent radiation vector $\mathbf{I}'$ will be:

$$\mathbf{I}' = M\mathbf{I}, \tag{3.5}$$

or, for a ray of light passing through multiple plasma regions, the final state of the emergent radiation will be a product of the matrices, corresponding to the different regions, and the incoming intensity:

$$\mathbf{I}' = M_nM_{n-1}...M_3M_2M_1\mathbf{I}. \tag{3.6}$$

In order to study the propagation of light through the solar atmosphere we define the Stokes vectors in terms of the coordinate system given in Figure 3.1, where z is the line-of-sight (*los*). The local plasma properties, such as vector magnetic field and vector velocity, will be projected onto this new reference frame.

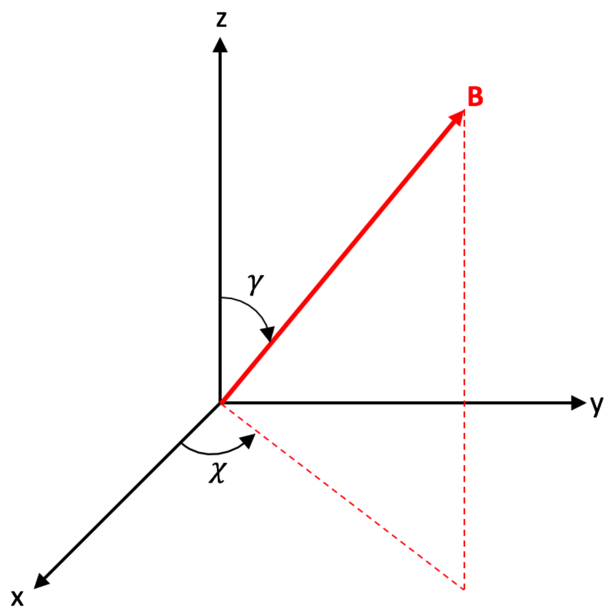

Fig. 3.1: The x,y,z frame of reference used in radiative transfer equations; where z is the line-of-sight. In order to account for magneto-optical effects, the magnetic field vector B must be projected onto the new reference frame. The inclination angle γ, and azimuthal angle χ are used to determine the absorption and dispersion of polarised radiation passing through the plasma.

3.1.2 Radiative transfer

In this section we briefly summarise the method of solving the radiative transfer equation, as used by common spectral synthesis codes, following the description of Rees et al. (1989). We consider local thermodynamic equilibrium, which for the photospheric lines studied in this thesis is a reasonable, although not perfectly valid, assumption (Shchukina et al., 2005). The radiative transfer equation (or Unno-Rachkovsky equation, Unno, 1956) is given by

$$\frac{\partial \mathbf{I}}{\partial z} = -\mathbf{K}\mathbf{I} + \mathbf{j}, \tag{3.7}$$

for an absorption matrix $\mathbf{K}$,

$$\mathbf{K} = \kappa_c \mathbf{1} + \kappa_0 \mathbf{\Phi}, \tag{3.8}$$

and an emission vector $\mathbf{j}$,

$$\mathbf{j} = \kappa_c S_c \mathbf{e_0} + \kappa_0 S_l \mathbf{\Phi} \mathbf{e_0}. \tag{3.9}$$

Here, $\mathbf{e_0}$ is the vector $(1,0,0,0)^T$, $\mathbf{1}$ is the 4×4 unit matrix, κ_c is the unpolarised continuum opacity, κ_0 is the line-centre opacity, S_c is the continuum source function, and S_l is the line source function. In local thermodynamic equilibrium (LTE) $S_l = S_c$. The source function is calculated from the Planck function at the local temperature $S_c = B_\nu(T)$. The line-absorption matrix $\mathbf{\Phi}$ is calculated as

$$\mathbf{\Phi} = \begin{pmatrix} \phi_I & \phi_Q & \phi_U & \phi_V \\ \phi_Q & \phi_I & \phi'_V & -\phi'_U \\ \phi_U & -\phi'_V & \phi_I & \phi'_Q \\ \phi_V & \phi'_U & -\phi'_Q & \phi_I \end{pmatrix}.$$

The components of the matrix are given by:

$$\begin{aligned}
\phi_I &= \frac{1}{2}\phi_p \sin^2(\gamma) + \frac{1}{4}\left(\phi_r + \phi_b\right)\left(1 + \cos^2(\gamma)\right), \\
\phi_Q &= \left(\frac{1}{2}\phi_p - \frac{1}{4}\left(\phi_r + \phi_b\right)\right)\sin^2(\gamma)\cos(2\chi), \\
\phi_U &= \left(\frac{1}{2}\phi_p - \frac{1}{4}\left(\phi_r + \phi_b\right)\right)\sin^2(\gamma)\sin(2\chi), \\
\phi_V &= \frac{1}{2}\left(\phi_r - \phi_b\right)\cos(\gamma), \\
\phi'_Q &= \left(\frac{1}{2}\phi'_p - \frac{1}{4}\left(\phi'_r + \phi'_b\right)\right)\sin^2(\gamma)\cos(2\chi), \\
\phi'_U &= \left(\frac{1}{2}\phi'_p - \frac{1}{4}\left(\phi'_r + \phi'_b\right)\right)\sin^2(\gamma)\sin(2\chi), \\
\phi'_V &= \frac{1}{2}\left(\phi'_r - \phi'_b\right)\cos(\gamma).
\end{aligned} \tag{3.10}$$

These are described in terms of the inclination and azimuthal angles γ and χ of the magnetic field vector, generalized absorption profiles $\phi_{p,b,r}$ and anomalous dispersion profiles $\phi'_{p,b,r}$ for p, b, and r the π (unshifted), blue-, and red-shifted σ components of a Zeeman triplet.

The Zeeman effect occurs when a magnetic field is present. It produces strong polarisation signatures which can be used to study solar magnetic fields. To observationally determine the structure of magnetic flux concentrations over the full range of field strengths seen on the Sun, the polarization signatures of the Zeeman effect must be understood. The longitudinal Zeeman effect allows measurement of the magnetic field component along the *los*, while the transverse Zeeman effect can be used to measure magnetic fields perpendicular to the *los*.

The Zeeman effect leads to a splitting of the energy levels into three components, based on the magnetic quantum numbers of the upper (M_u), and lower (M_l) states of the line transition. Each allowed transition $k(= u, l)$ has a set of quantum numbers: L_k is the orbital angular momentum, S_k the spin, J_k the total angular momentum, and M_k the magnetic quantum number. A magnetic field will split each level into $2J_k + 1$ states, where the allowed quantum numbers are $M_k = -J_k, .., +J_k$, and $J_k = |L_k - S_k|, ..., |L_k + S_k|$. The introduction of a magnetic field removes the degeneracy of M_j, displacing the energy level and leading to a wavelength shift of the i_j Zeeman component, where $i_j = 1, ...N_j$ for $j = p, b, r$. This wavelength shift will be

$$\nabla\lambda_{i,j} = \frac{e\lambda_0^2|\mathbf{B}|}{4\pi mc^2}\left(g_l M_l - g_u M_u\right)_{i,j}, \tag{3.11}$$

for electron charge e , atomic weight m, speed of light c and Landé g-factor

$$g_k = \frac{3}{2} + \frac{S_k\left(S_k+1\right) - L_k\left(L_k+1\right)}{2J_k\left(J_k+1\right)}. \tag{3.12}$$

Each component has a corresponding strength S_{i_j}, which is normalised according to:

$$\sum_{i_j=1}^{N_j} S_{i_j} = 1, \tag{3.13}$$

for $j = p, b, r$. The generalised profiles are then written as

$$\phi_j = \sum_{i_j=1}^{N_j} S_{i_j} H\left(a, v - v_{i_j} + v_{los}\right), \tag{3.14}$$

and

$$\phi'_j = 2\sum_{i_j=1}^{N_j} S_{i_j} F\left(a, v - v_{i_j} + v_{los}\right). \tag{3.15}$$

Here $H(a, v)$ is a Voigt profile

$$H\left(a, v\right) = \frac{a}{\pi}\int_{-\infty}^{\infty} \frac{e^{-y^2}}{\left(v-y\right)^2 + a^2}dy, \tag{3.16}$$

and $F(a, v)$ a Faraday-Voigt profile

$$F(a, v) = \frac{1}{2\pi} \int_{-\infty}^{\infty} \frac{(v - y)\, e^{-y^2}}{(v - y)^2 + a^2} dy, \tag{3.17}$$

with a collisional (Lorentzian) line-broadening parameter:

$$a = \Gamma \lambda_0^2 / 4\pi c \nabla \lambda_D, \tag{3.18}$$

and a shift from line centre v, describing Doppler (Gaussian) broadening:

$$v = (\lambda - \lambda_0) / \nabla \lambda_D. \tag{3.19}$$

Here Γ is the line damping parameter, λ, the line wavelength, and $\nabla \lambda_D$, the Doppler width, expressed as $\nabla \lambda_D = \lambda_0 v_T / c$. For a Maxwellian velocity distribution (thermal broadening), $v_T = (2kT/m)^{1/2}$, where T is temperature, and k the Boltzman constant, so $v_{i_j} = \nabla \lambda_{i_j} / \nabla \lambda_D$.

For a Zeeman triplet with a transition from $J_u = 1$ to $J_l = 0$ the wavelengths of the three components can be determined based on the Landé g-factor and magnetic field strength. The wavelengths of the three components are:

$$\begin{aligned} \lambda_\pi &= \lambda_0 \\ \lambda_b &= \lambda_0 - g_u \Delta \lambda_B \\ \lambda_r &= \lambda_0 + g_u \Delta \lambda_B \end{aligned} \tag{3.20}$$

where λ_B is the wavelength shift, for $\mathbf{B}$ measured in Gauss:

$$\Delta \lambda_B = 4.6686 \times 10^{-10} \lambda_0^2 |\mathbf{B}| \mathrm{mA}. \tag{3.21}$$

The longitudinal Zeeman effect imparts a Stokes$-V$ (circular polarisation) signature, occurring when the magnetic field component is parallel to the *los*. The transverse Zeeman effect responds to magnetic field values perpendicular to the *los* and is detected in Stokes$-Q$ and $-U$ (linear polarisation) signatures. Figure 3.2 summarises the polarisation signatures of the Zeeman effect depending on the direction between the magnetic field and *los*. As a ray of radiation passes through the solar atmosphere, the local plasma properties along the line-of-sight will act as sources and sinks of polarisation signals.

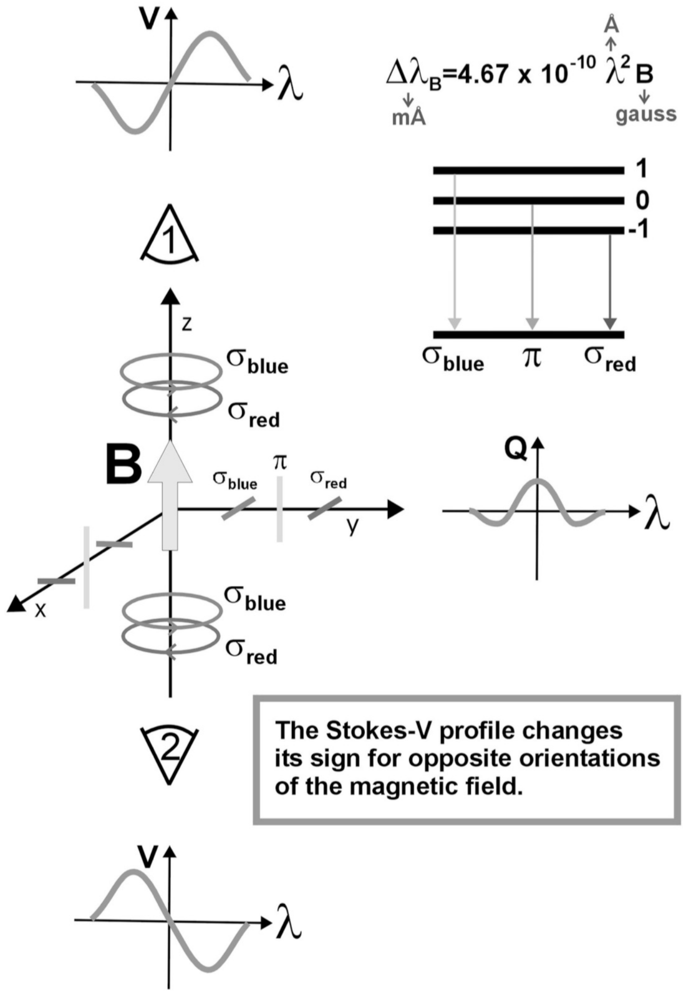

Fig. 3.2: The polarisation signatures of the Zeeman effect depending on the direction of the magnetic field relative to the *los*. The Stokes$-V$ signature shows two lobes, which change sign if the magnetic field direction reverses. The linear polarisation signature observed in Stokes-Q has three lobes and does not change when the magnetic field direction is reversed. Figure from Trujillo Bueno (2003).

3.1.3 Computation of Synthetic Spectral Lines

The spectropolarimetry codes MODCON/STOPRO (Solanki, 1987; Shelyag et al., 2007) and NICOLE (Socas-Navarro et al., 2015) have been used in this thesis to calculate the radiation emitted from the output of MHD simulations performed with the MANCHA, MURaM or SPARC codes. The process followed to synthesise a radiation spectrum remains similar for any pairing of MHD and spectral synthesis code.

For 1-dimensional radiative transfer calculations the output plasma parameters must be taken from the MHD code and input column-by-column into the spectral synthesis code. Depending on the direction of observation, calculation of the plasma parameters along the new *los* is performed by shifting the simulation domain around the horizontal photospheric layer $z = 0$. The observed domain then decreases in the direction of inclination as $\Delta x' = \Delta x \cos(\gamma)$, where γ is the inclination from the vertical. The velocity and magnetic field components are projected from the standard reference frame of the MHD simulations, with z the radial direction, into the line-of-sight reference frame. To simulate centre-to-limb observations, images for a number of inclination angles must be computed, from the disk centre (viewing cosine $\mu = \cos(\gamma) = 1.0$) to the solar limb ($\mu = \cos(\gamma) = 0.0$).

Synthetic spectropolarimetric diagnostics of MHD simulations will require calculation of the radiation output for a large number of pixels; a synthesised spectrum will be required for each pixel at each of the simulation snapshots. For example, in a helioseismic simulation performed over 4 hours at 15 second cadence, there will be 960 snapshots, each requiring a synthesised Fe I 6173 Å spectrum calculated at 5 different observation angles for all 256^2 horizontal pixels. This can quickly give $10^7 - 10^8$ total pixels, requiring parallel computation.

In the case of the MODCON/STOPRO synthesis codes, as used in Chapter 4, a Fortran 90 OpenMPI master code was written to distribute the load to individual cores running the MODCON/STOPRO codes. The NICOLE code is used in Section 3.2. It is a modern synthesis code that has been designed for massively parallel computation, using a master Python code to perform the preproduction and inclination of the physical domain and execute a FORTRAN/OpenMPI synthesis code.

The inputs required for operation of the two synthesis codes are similar, with the plasma properties required summarised in Table 3.1, and the spectral line profile parameters in Table 3.2. The spectral line parameters required are taken from the ATLAS9 database (Kurucz, 1993), with the exception of the line broadening parameters, which are taken from the calculations of Barklem et al. (1998). An overview of the process followed is:

1. A background model of the magnetic field structure is calculated,
2. This model is perturbed in a MHD simulation,
3. The plasma parameters are extracted from the simulation, and the domain is inclined by shifting the photosphere in the direction of *los*
4. The vector magnetic field and velocity are projected onto the new coordinate system
5. The optical depth along the ray path is calculated
6. The Unno-Rachkovsky Equation 3.7, is solved for each surface pixel, and finally,
7. The output spectral line is used to calculate synthetic spectropolarimetric observables.

Both radiative transfer codes require a 'master' code to perform the manipulation of the input plasma parameters. These codes calculate the correct input parameters and spectral line data, before feeding them into a dedicated line synthesis routine. The NICOLE code uses more modern numerical methods than the STOPRO code, however it lacks the ability to calculate molecular lines. The move from STOPRO to the NICOLE code has been primarily driven by the increased computational speed and ease of use when calculating large numbers of spectral lines on HPC clusters. An additional benefit is the NICOLE code is open-sourced and community supported, receiving regular updates and bug fixes.

3.2 Synthetic spectropolarimetry of simulated magneto-convection

The MURaM radiative magnetohydrodynamic code (Vögler et al., 2005) was used to generate a model of solar photospheric magneto-convection. A simulation domain of

Table 3.1: Plasma properties required for spectral synthesis

	Quantity	Units
T	Temperature	Kelvin
p	Pressure	g cm^{-1} s^{-2}
ρ	Density	g cm^{-3}
$\|\mathbf{B}\|$	Magnetic field magnitude	Gauss
γ	Inclination angle of magnetic field from *los*	Degrees
χ	Azimuthal angle of magnetic field from *los*	Degrees
v_{los}	Line of sight velocity	cm s^{-1}
v_{mt}	Micro-turbulence velocity	cm s^{-1}

Table 3.2: Atomic transition parameters required for spectral synthesis

	Description	Units	Fe I 6173	Fe I 6302
Z	Atomic number	(-)	26	26
ION	Ionisation state, 1-N, 2-+, 3-++	(-)	1	1
λ_0	Central wavelength	(Å)	6173.3343	6302.4940
LW	Line width	(Å)	2	2
P_{exc}	Excitation potential	(eV)	2.2227	3.6860
Log(gf)	Oscillator strength	(-)	-2.88	-1.13
${}^{2S_u+1}L_{uJ_u}$	Term description, upper level	(-)	5P1.0	5P1.0
${}^{2S_l+1}L_{lJ_l}$	Term description, lower level	(-)	5D0.0	5D0.0
σ	Collisional cross section	(au)	281.0	850.2
α	Collisional velocity parameter	(-)	0.266	0.239

$12 \times 12 \times 2.56$ Mm was used, with a grid of $n_x = 480$, $n_y = 480$ and $n_z = 256$ points giving a resolution $\Delta_x = 25$ km, $\Delta_y = 25$ km and $\Delta_z = 10$ km. The upper boundary is closed, the lower boundary open and the horizontal boundaries periodic. A tabulated equation of state is used (Irwin, 2012).

The process for generating the models is the same as that described in Shelyag et al. (2012). A non-magnetic convection simulation is run until a statistically steady state model is achieved. A 200 G unipolar magnetic field is then introduced and the simulation is allowed to evolve until a steady state is again reached. This simulation setup is used to imitate a solar Plage region. The convective motions distribute magnetic field into the intergranular lanes, allowing the formation of the magnetic field structures in which photospheric "vortices" are found. The chosen initial conditions lead to the formation of intergranular magnetic flux concentrations with a maximum strength of $1-2$ kG. A detailed study of a simulation using similar initial conditions was performed by Vögler et al. (2005) and the morphology and lifetime of the magnetic field concentrations was shown to be consistent with observations.

Once a steady state simulation had been reached the NICOLE code (Socas-Navarro et al., 2015) was used to simulate the Fe I 6302.5 Å spectral line in LTE. The full Stokes vector $\mathbf{I}(\lambda) = (I(\lambda), Q(\lambda), U(\lambda), V(\lambda))$ is calculated with 400 wavelength points at a spectral resolution of 0.0015 Å around the central wavelength. The parameters for the Fe I 6302.5 Å spectral line can be seen in Table 3.1.

In order to investigate the Hinode satellite's capability to detect spectropolarimetric signatures of torsional Alfvén waves, a number of synthetic observables are calculated. The observation of torsional oscillations in a vertical flux tube requires the measurement of horizontal velocity components. Measurements made using spectropolarimetry determine the velocity along the *los*

$$v_{los} = v_z \cos\gamma + v_h \sin\gamma, \tag{3.22}$$

where v_z is the vertical component of velocity, and v_h the horizontal component relative to the solar surface. The angle γ is between the line-of-sight at which the observation is made, and the direction vertical to the solar surface. Observational measurements of a horizontal velocity will therefore require a high inclination (γ). For observations of the solar limb, projection effects will lead to a reduction of resolution with γ, proportional to $\cos(\gamma)$. This means when determining the radiation spectrum of a simulation snapshot of resolution Δ_x, the effective observational resolution is $\Delta_x \cos(\gamma)$.

Three different angles of observation are simulated, at inclinations of $\gamma = 0°$, $30°$ and $60°$ degrees from the vertical. These values correspond to a viewing cosine of $\mu = 1.0$, 0.866 and 0.5 respectively. Figure 3.3 shows the continuum intensity at 6302.8Å of the simulated photosphere. The images with the original simulation resolution of $\Delta_x = 25$ km, $\Delta_y = 25$ km and $\Delta_\lambda = 0.0015$ Å are shown in the left panels. For comparison with current observational instruments, the right hand panels show observation at the resolution of the Solar Optical Telescope (SOT), on board the Hinode satellite (Tsuneta et al., 2008). The degradation of the simulated observations has been performed though convolution of the Stokes vector with Gaussian kernel of $\sigma_x = 145$ km, $\sigma_y = 145$ km and $\sigma_\lambda = 0.2515$ Å. Much of the fine structure seen in the intergranular lanes is lost with the decreased resolution, although intergranular bright structures can still be seen.

The width of a spectral line is calculated as:

$$W_l = \sqrt{\frac{\int (I_c - I)\,(\lambda - \lambda_{cog})^2\, d\lambda}{\int (I_c - I)\, d\lambda}}, \tag{3.23}$$

where I_c is the continuum intensity, $I(\lambda)$ the intensity (Stokes$-I$) in terms of wavelength λ. The centre of gravity wavelength λ_{cog} of the shifted spectral line is calculated as

$$\lambda_{cog} = \frac{\int (I_c - I)\lambda d\lambda}{\int (I_c - I) d\lambda}. \tag{3.24}$$

The linewidth provides a measure of the thermal and magnetic effects on the spectral line. Figure 3.4 shows the variation of the measured line width with resolution and angle of observation. For the magnetically sensitive Fe I 6302.5 Å spectral line the regions of extreme high and low width are seen in the intergranular lanes with strong magnetic field concentrations. The decreased resolution has a large impact on the observed line width. The intergranular regions can still be observed, however the extreme high and low values are no longer resolved.

The line-of-sight velocity (v_{los}) is calculated from the shift in wavelength. This is measured using the centre of gravity wavelength of the simulated line profile:

$$v_{los} = c\frac{\lambda_0 - \lambda_{cog}}{\lambda_0}, \tag{3.25}$$

where c is the speed of light and λ_0 is the central wavelength of the spectral line.

The *los* velocities in the simulation are shown in Figure 3.5. At disk centre (top

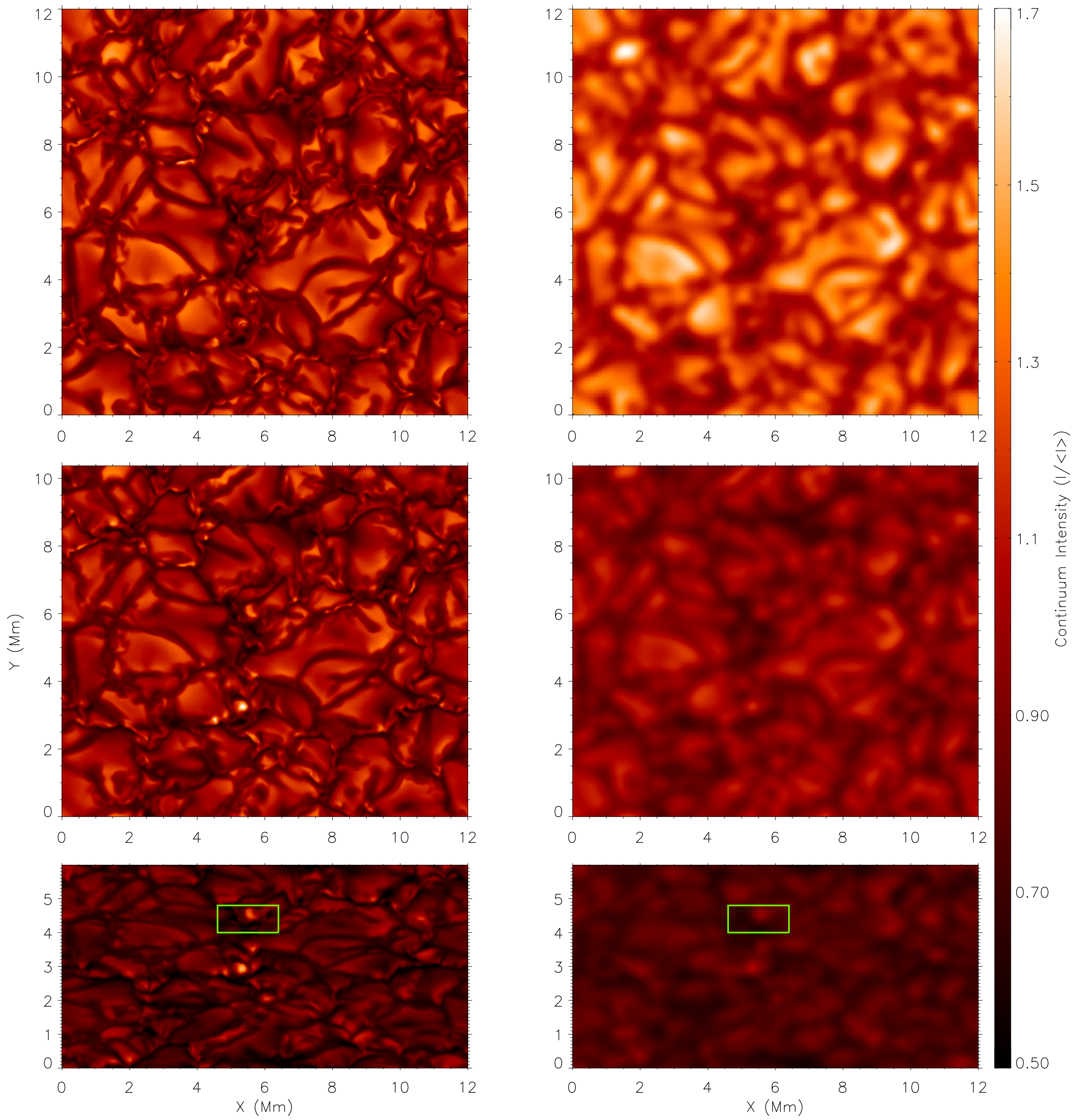

Fig. 3.3: The normalized continuum intensity at 6302.8 Å calculated for the MURaM simulated photospheric model. The panels show, from top to bottom, observations at 0°, 30° and 60° to the vertical. The left panels show the original simulation results, with a resolution of 25 km, while the right hand panels show those degraded to 145 km, the resolution of the SOT on board Hinode. The region highlighted shows one of the structures studied in more detail.

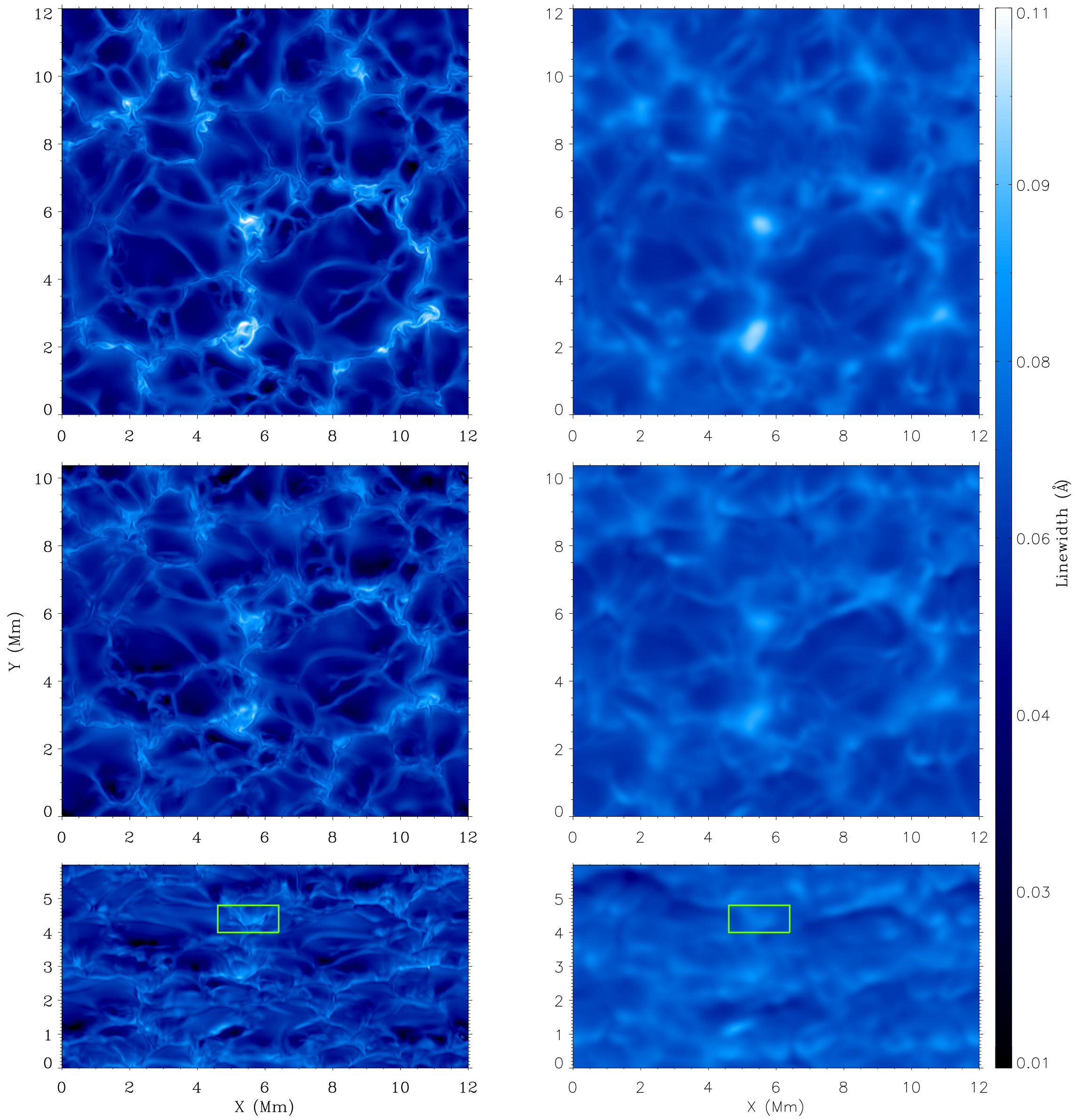

Fig. 3.4: The linewidth of the Fe I 6302.5 Å spectral line, calculated for the MURaM simulated photospheric model. The panel layout is the same as in Figure 3.3.

panels) the observation is dominated by the upflow in convective cells and intergranular downflows. At high inclinations, a number of small-scale structures, seen as alternating bands of positive and negative velocity become visible. One example of these structures has been highlighted in the bottom panel of Figures 3.3-3.6. However, when degraded to the resolution of the Hinode satellite the signatures of these motions are smoothed out.

The Stokes$-V$ area asymmetry is calculated by integrating the Stokes$-V$ profile and normalising it by the total area

$$\delta A_V = \frac{\int V d\lambda}{\int |V| d\lambda}. \tag{3.26}$$

The presence of these asymmetries has been seen to occur towards the edge of granules, and in the intergranular lanes. Highly asymmetric line profiles are seen when there are strong gradients of the velocity and magnetic field in the direction of the *los* (Grossmann-Doerth et al., 2000). At high inclination there are more regions with highly asymmetric Stokes$-V$ profiles as there is more gradient in physical parameters along the *los*. When the resolution of observation is reduced, regions of high asymmetry are still observed in the intergranular lanes. However, the fine-scale Stokes$-V$ signatures of the vortex structure are no longer observed, this can be seen in the highlighted region of the bottom panel of Figure 3.6.

Comparison of the degraded observations with the original 25 km simulation shows the decreased resolution will simply smear out the small scale structures seen in the intergranular magnetic field concentrations. These patterns are the observational signatures of the photospheric "vortices" observed in simulations as Alfvénic oscillations. In particular, the observed patterns of red- and blue-shifted horizontal Doppler velocity (Figure 3.5) and the fine variations in Stokes$-V$ area asymmetry (Figure 3.6) become unresolvable.

By convolving the 60° radiation spectrum to a number of resolutions we can identify the spatial resolution required to see these structures in observations. Figure 3.7 shows the results of observation at resolutions of 25 km, 50 km, and 100 km, with a reduced spectral resolution of 0.2515 Å. The structure is clearly visible at a resolution of 25 km, and the velocity pattern of the vortex region can still be made out at 50 km. Once the resolution has been reduced to 100 km, the alternating red- and blue-shifted velocity pattern can no longer be seen.

Due to the 145 km resolution of the Hinode SOT, it will be unable to observe

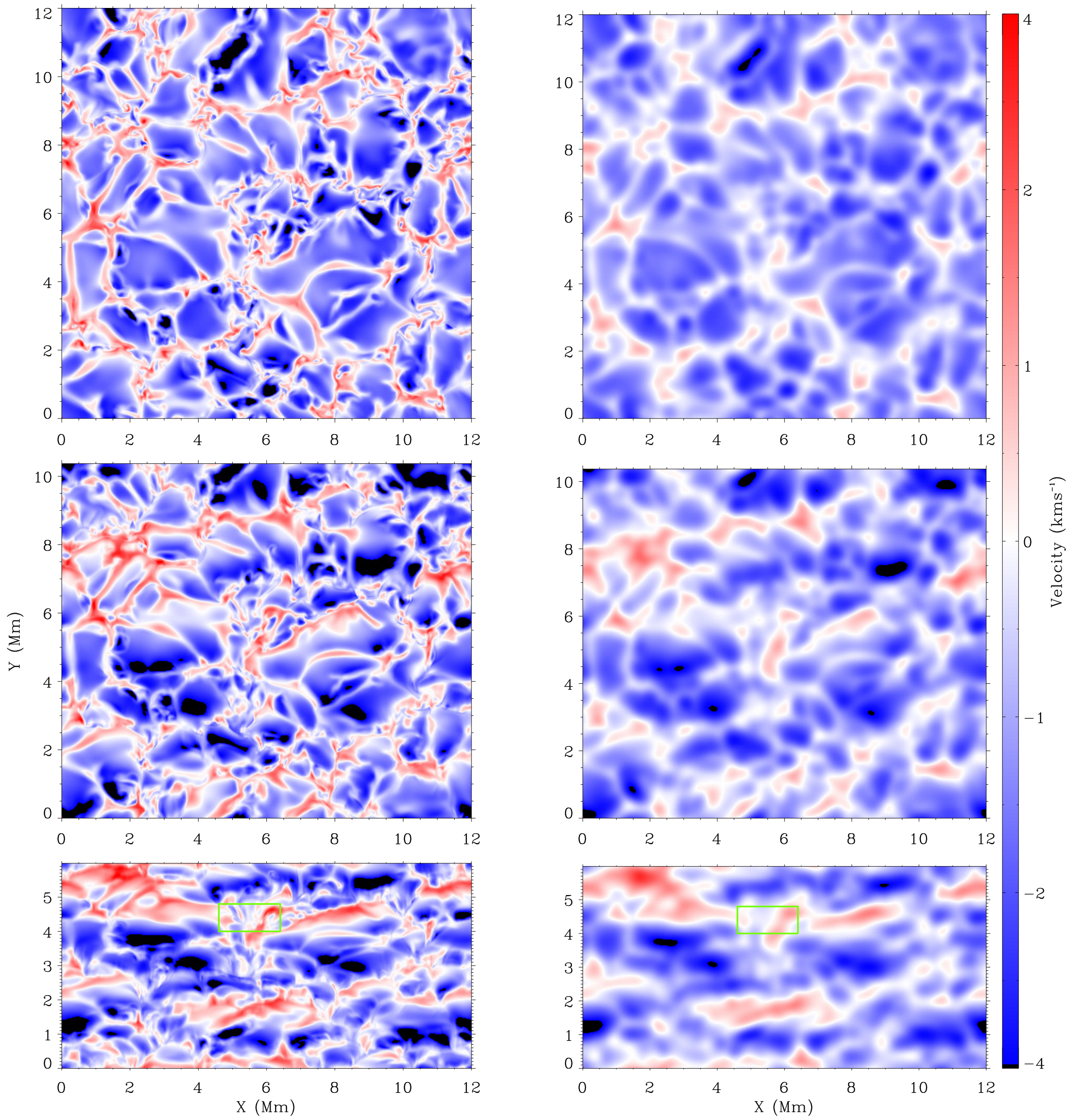

Fig. 3.5: *los* Doppler shifts of the Fe I 6302.5 Å spectral line synthesised from a MURaM photospheric magnetoconvection model. The panel layout is the same as in Figure 3.3.

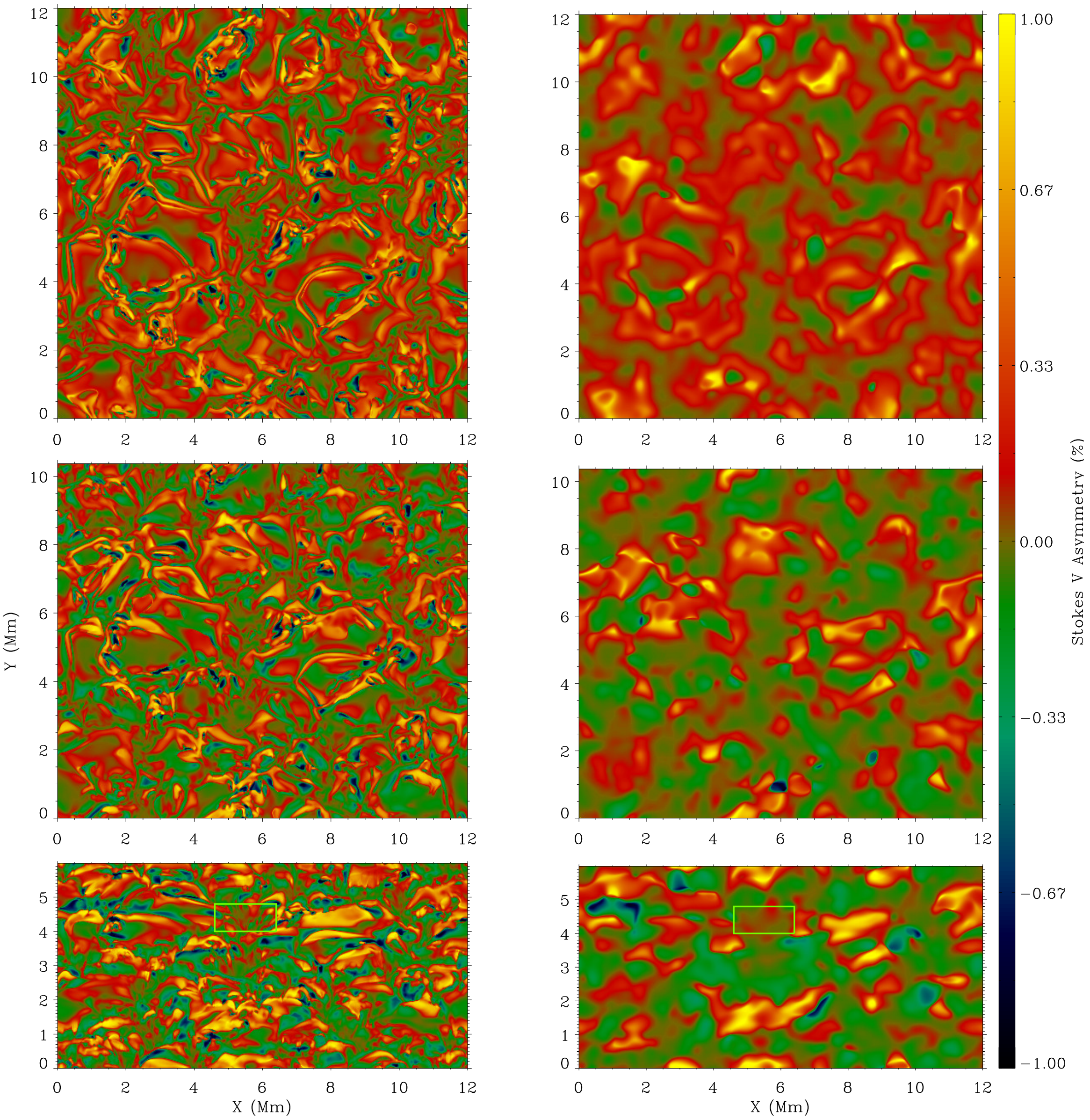

Fig. 3.6: The Stokes−V area asymmetry of the simulated photosphere, calculated with the Fe I 6302.5 Å spectral line. The panel layout is the same as in Figure 3.3.

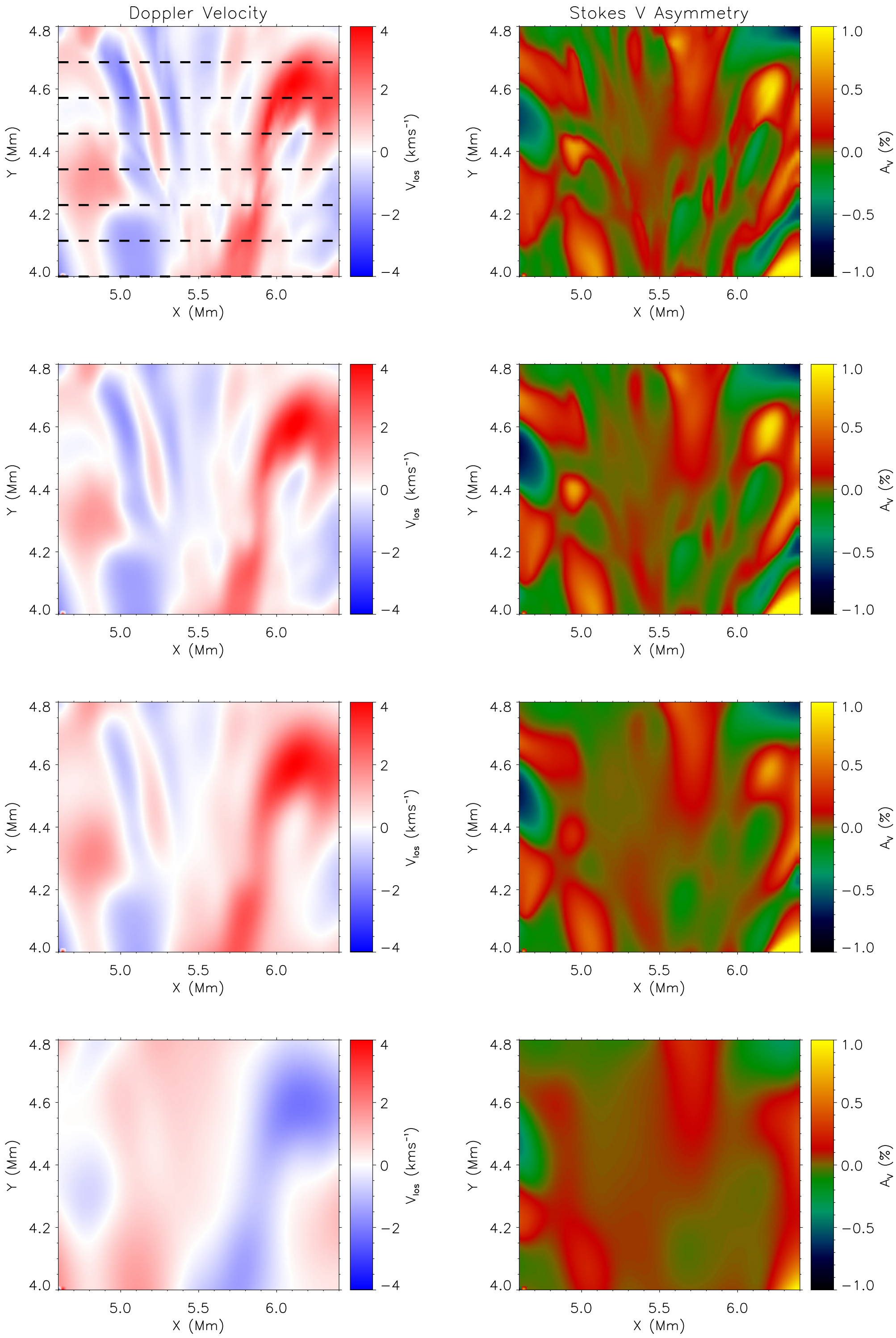

Fig. 3.7: The line-of-sight Doppler velocity (left) and Stokes$-V$ asymmetry (right) for observation at 60° from the vertical ($\mu = 0.5$). The panels show the effect of lowering the spatial resolution on observation of the region highlighted in Figures 3.3-3.6. From top to bottom: Observation at the original simulation resolution of 12.5 km in x and y, at 25 km, at 50 km, and at 100 km. The horizontal lines in the top left panel show the location of the bisectors taken in Figure 3.9.

the Alfvénic vortex motions. The largest solar telescopes currently available, such as GREGOR and NST have a mirror size of around 1.5 m. This corresponds to a spatial resolution of approximately 70 km at disk centre. At this resolution, telescopes will struggle to pick out the torsional motions identified. Next generation telescopes which use a 4 m mirror are already under construction (DKIST and EST) and will have an estimated spatial resolution of down to ≈ 20 km at disk centre. These next generation instruments will be able to resolve the torsional motions, as observed in our simulations.

With a high spectral resolution we can also perform multi-height observations by calculating spectral line bisectors. The relative intensity I_{rel} is determined by normalising the intensity by the continuum value, $I_{rel} = I/I_c$. This gives a value between 0 and 1. A bisector is then calculated by finding the two wavelengths at which the line has a specified relative intensity and calculating the midpoint wavelength (λ_{bsr}).

A set of bisectors is determined for one hundred intensity values, spaced between $I_{rel} = 0.1$ and 1.0. This allows measurement of velocities throughout the line formation region. Bisectors taken at higher relative intensities, near the continuum value, will correspond to lower heights. The continuum formation height is the lowest value at which light will escape, corresponding to $\log(\tau_{6302}) = 0$. Measurements made at lower relative intensities, near the line core, will correspond to higher in the atmosphere.

The *los* velocity is calculated using the Doppler shift of the perturbed bisectors from the central wavelength λ_0 of the spectral line:

$$v_{bsr} = c\frac{\lambda_0 - \lambda_{bsr}}{\lambda_0}. \tag{3.27}$$

Two examples of bisectors of Fe I 6302.5 Å spectral line are shown in Figure 3.8 on top of the Stokes$-I$ profile. Two examples are shown, one non-magnetic, unsplit profile and the second from a strongly magnetic pixel, showing Zeeman splitting of the spectral line. For highly asymmetrical profiles, the calculation of bisectors near the line-core can be problematic, as one of the components may be deeper than the other.

A number of bisectors are taken along slits through the region studied in Figure 3.7, marked in the top-left panel. The bisector velocity shifts are shown in 3.9 and give a two-dimensional view along the slit and over the line formation region. Comparison of the centre-of-gravity velocity across the slits sampled with the bisector velocity shifts show strong similarity to the velocity measured at the continuum intensity. The slits that sample the observed vortex structure are between $y = 4.34$ Mm and 4.69 Mm and $x = 5.1$ Mm and 5.8 Mm. These measurements show only minimal change in the

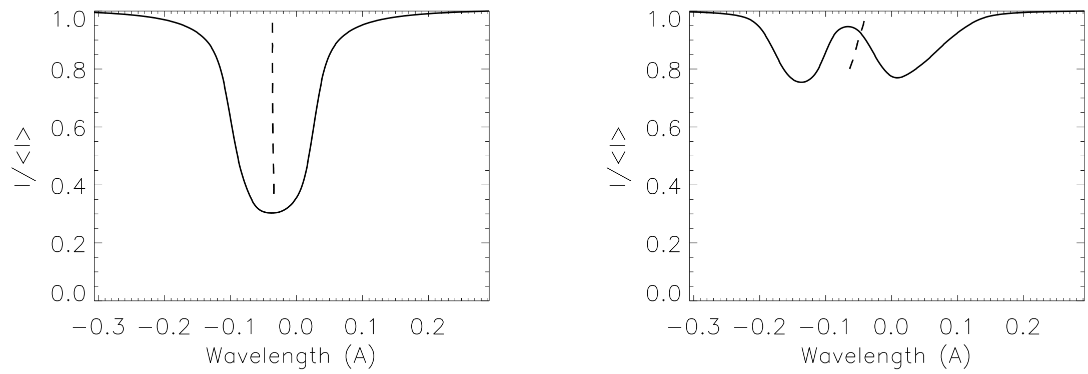

Fig. 3.8: Two simulated Fe I 6302 Å spectral lines: left, for a non-magnetic pixel chosen from the centre of a photospheric granule; right, for a Zeeman split profile from a pixel in a kilogauss intergranular flux concentration. The dashed line shows the spectral line bisector calculated for each profile.

alternating velocity bands over height.

3.3 Conclusion

It is important for us to bridge the gap between numerical simulations and observations of the solar surface and atmosphere. Although spectral synthesis is computationally expensive it is necessary to understand the various features seen in observations of the Sun. We can then explain these based on the subsurface and unresolved behaviour that can be studied in realistic numerical simulations, but not with current observational limitations. In addition, these simulations allow us to predict possible targets of interest to direct next generation observations.

In this chapter we summarised the numerical process that is required to perform synthetic observations of a solar numerical simulation. In addition we studied the observational manifestation of photospheric vortices through observations of MURaM simulations. To summarise the results: 1) centre-to-limb spectropolarimetric observables were calculated for the Fe I 6302.5 Å, as used in the Hinode satellite, 2) observation at high resolution and large viewing cosine $\mu > 0.5$ allow the observation and investigation of torsional motions in solar magnetic field structures, seen as alternating bands of red and blue shifted velocities, 3) modern telescopes are unable to resolve these small-scale structures, however next generation observations will have a high enough resolution.

Future work will involve repeating this experiment with different spectral lines, to

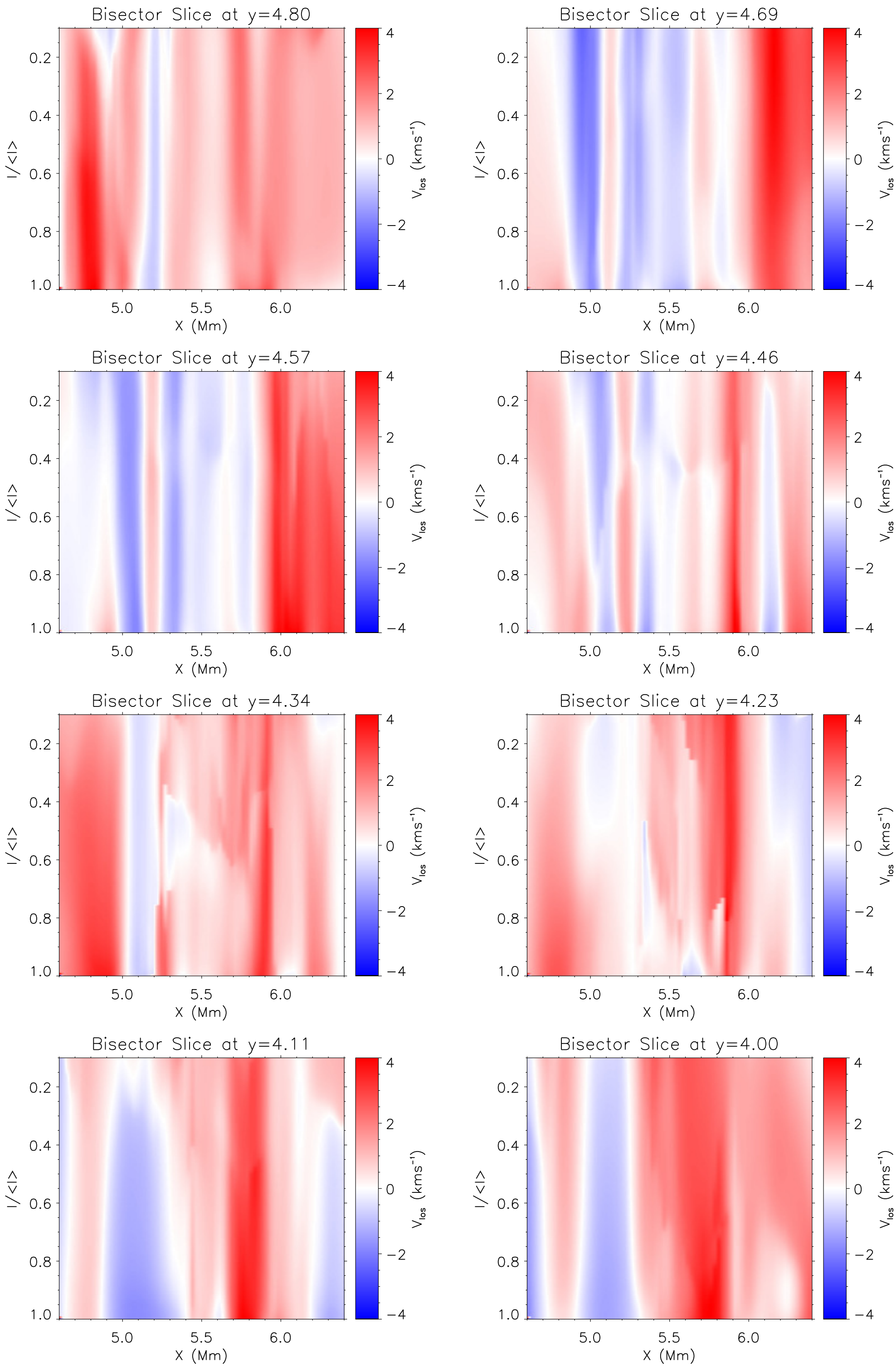

Fig. 3.9: A number of bisector slices, taken from $I_{rel} = 0.1, 1.0$ and along a slit from $x = 4.6$ to 6.4 Mm. Each panel shows various y-values, which have been highlighted in Figure 3.7. This roughly corresponds to a 2D slice of the solar atmosphere, with $I_{rel} = 1$ the lowest, and $I_{rel} = 0.1$ the highest. Note that this slice does not correspond to a constant height in the simulation domain, as the height of radiation formation varies with local plasma properties.

identify which will be the most suitable to observe and identify these motions. This will also allow an investigation of the observational structure vortices exhibit at different heights in the solar atmosphere. A study of a higher cadence time-series will also be required to better understand the evolution of these structures.

A study of the ability of these Alfvénic waves to heat the chromosphere is presented in Chapter 5. This is performed using non-ideal MHD simulations of a flux tube mimicking the one at the centre of the vortex studied in this chapter.

Chapter 4

Spectropolarimetrically Accurate Magnetohydrostatic Sunspot Model for Forward Modelling in Helioseismology

In this chapter we present a technique to construct a spectropolarimetrically accurate magnetohydrostatic model of a large-scale solar magnetic field concentration, mimicking a sunspot. Using the constructed model we perform a simulation of acoustic wave propagation, conversion and absorption in the solar interior and photosphere with the sunspot embedded into it. With the Fe I 6173 Å magnetically sensitive photospheric absorption line of neutral iron, we calculate observable quantities such as continuum intensities, Doppler velocities, as well as full Stokes vector for the simulation at various positions at the solar disk, and analyse the influence of non-locality of radiative transport in the solar photosphere on helioseismic measurements. Bisector shapes were used to perform multi-height observations. The differences in acoustic power at different heights within the line formation region at different positions at the solar disk were simulated and characterised. An increase in acoustic power in the simulated observations of the sunspot umbra away from the solar disk centre was confirmed as the slow magneto-acoustic wave.

Monash University

Declaration for Thesis Chapter 4

Declaration by candidate

In the case of Chapter 4, the nature and extent of my contribution to the work was the following:

Nature of contribution	Extent of contribution (%)
Key Ideas, development of model and code, production of all results, writing of paper.	70

The following co-authors contributed to the work. If co-authors are students at Monash University, the extent of their contribution in percentage terms must be stated:

Name	Nature of contribution	Extent of contribution (%) for student co-authors only
Sergiy Shelyag	Supervision and guidance	
Paul Cally	Supervision and guidance	

The undersigned hereby certify that the above declaration correctly reflects the nature and extent of the candidate's and co-authors' contributions to this work*.

Candidate's Signature	[redacted]	**Date** 17/2/17
Main Supervisor's Signature	[redacted]	**Date** 17/2/17

*Note: Where the responsible author is not the candidate's main supervisor, the main supervisor should consult with the responsible author to agree on the respective contributions of the authors.

4.1 Introduction

Techniques of local helioseismology are currently unable to unambiguously determine sub-surface structure of the flows and sound speed perturbations in and around large-scale solar magnetic field concentrations, such as sunspots and pores (Shelyag et al., 2007; Gizon et al., 2009; Moradi et al., 2010). Due to the complexity of magnetohydrodynamic processes involved, our understanding of the behaviour of magnetoacoustic waves as they are absorbed, reflected and refracted by sunspots is far from complete.

There are also possible significant discrepancies in travel time measurements originating from the effects of non-locality of radiative transport in the solar atmosphere. Changes in spectral line formation heights due to magnetic field presence (see e.g. Shelyag et al., 2007), systematic centre-to-limb variations in absorption line formation (Shelyag & Przybylski, 2014), as well as instrumental effects, such as stray light, and other processes involved in formation and measurement of radiation intensities and Doppler shifts result in our inability to unambiguously measure the travel time perturbations and, therefore, infer solar sub-surface structure (Rajaguru, 2011).

Rapid improvements in computational power already make it possible to perform forward modelling of magnetohydrodynamic wave propagation and mode conversion in "realistic" solar magnetic field structures (Shelyag et al., 2009; Moradi et al., 2008; Felipe et al., 2010; Cameron et al., 2011; Khomenko & Cally, 2012; Felipe, 2012; Zharkov et al., 2013; Felipe et al., 2014b). Spectral line synthesis codes and radiative diagnostics tools also allow computations of mock observables from the simulated plasma parameters, allowing for direct comparison between simulations and observations in computational helioseismology.

Creating a sunspot that is both spectropolarimetrically accurate and magnetohydrostatically stable is inherently difficult, as the sound speed and temperature can change significantly with small changes in the density and pressure stratification. The sunspot model of Khomenko & Collados (2008) was created to allow empirical quiet and umbral solar models to be used in the near-surface layers in combination with a Schlüter-Temesváry flux tube model (Schlüter & Temesváry, 1958) in the interior. However, the model created this way is still not convectively stable. Convective instability is fatal to linear MHD simulations, but these codes are less expensive than full non-linear simulations, and ideal for the long time series required in helioseismology; for the study of fast and slow magneto-acoustic waves; and for simulating fast-slow and fast-Alfvén mode conversion in the photosphere and lower chromosphere. The effects of convective stabilisation on the eigenmodes of solar models for helioseismic simulations were studied by Schunker et al. (2011). A technique for stabilising the atmosphere is discussed in Section 2.1.

In this paper, we present a model of a magnetohydrostatic and spectropolarimetrically accurate sunspot. Our model is based on the sunspot-like model of Khomenko & Collados (2008). The model was adjusted to provide a more accurate replication of photospheric sunspot properties taken from semi-empirical models, while still maintaining a smooth transition of physical properties between the magnetic and non-magnetic regions required for stable numerical simulation. This technique makes it possible to obtain accurate photospheric absorption line formation heights as well as allowing the study of observational signatures of acoustic wave propagation in the simulated model at different positions on the solar disk. We perform a magnetohydrodynamic simulation of the propagation of a wave through this sunspot-like model and investigate the behaviour of acoustic waves in the simulated model using the synthesised radiation, as if it were observed. We also investigate effects of the centre-to-limb variation effects on Doppler velocity measurements and study the line bisector shapes to allow for a multi-height view in the line formation region, which can be used to observationally disentangle wave mode conversion process in the solar atmosphere.

The structure of the chapter is as follows. In Section 4.2 we describe the background model. In Section 4.3 we explain the magnetohydrodynamic simulation and the spectral synthesis methods used to provide artificial observables. Section 4.4 provides results and description of the radiative effects on acoustic wave measurements in observations. In Section 4.5, we discuss our findings.

4.2 Model

Following the method described by Khomenko & Collados (2008), an axisymmetric sunspot model is created in cylindrical geometry using three parameters a, η and B_0 which change the sunspot radius, magnetic field inclination and strength, respectively. A full description of the effects of these parameters on the magnetic field configuration is given by Khomenko & Collados (2008). The model is defined on a two-dimensional r-z plane discretised into a domain from -10 to 2 Mm in height, with a radius of 100 Mm and resolution of $\Delta z = 0.1$ Mm and $\Delta r = 0.2$ Mm.

Below -1 Mm depth a Low-type magnetic flux tube (Low, 1980) is constructed using an extension of the exact Schlüter-Temesváry formulation (Schlüter & Temesváry, 1958).

For the near-surface layers $z_d > -1$ Mm and in the atmosphere a Pizzo-type magnetic flux tube is used (Pizzo, 1986). The Pizzo method creates a pressure-distributed magnetic field structure through an extension of the Low formulation used above. The magnetohydrostatic equation for a non-twisted, cylindrical structure can be simplified by introducing a magnetic vector potential (Low, 1975). This allows the problem to be reduced to a single equation for a scalar $u(r,z)$ (Pizzo, 1986)

$$\frac{\partial^2 u}{\partial r^2} - \frac{1}{r}\frac{\partial u}{\partial r} + \frac{\partial^2 u}{\partial z^2} = -4\pi r^2 \frac{\partial p(u,z)}{\partial u}, \tag{4.1}$$

where the partial derivative with respect to u represents the change in gas pressure ($p(u,z)$) along the field lines. The self similar model is created with a, η, B_0 and a depth z_0, which gives the height of the lower boundary where the field is vertical. Then, for a chosen height where the two models will be joined, z_d, the bottom boundary condition for the field line constant u will be

$$u = r_e^2 B_P \frac{1 - e^{-\frac{r^2}{r_e^2}}}{2}, \tag{4.2}$$

where r_e and B_P are

$$r_e = \frac{(z_d - z_0)^2 + a^2}{\eta}, \tag{4.3}$$

$$B_P = B_0 \frac{2h_p^2}{(z_d - z_0)^2 + a^2}. \tag{4.4}$$

Additionally, the Pizzo method boundary conditions require both a quiet Sun (denoted with index q) and umbral (denoted with index um) pressure, density, temperature, and pressure scale height ($h = \frac{p}{\rho g}$) and temperature distributions as functions of depth. The quiet Sun model (p_q,ρ_q,h_q) generated above was used for the outer boundary condition. For the inner boundary the Avrett semi-empirical model (Avrett, 1981) is used, which is then joined to the pressure and density profiles at the axis of the self-similar flux tube using log-linear interpolation. This is then convectively stabilised using Equations 2.2 and 2.3 as described in detail in Chapter 2.

The Wilson depression is a measure of the reduction in the height of the photosphere due to the reduced gas pressure inside of a sunspot. The height at which observations of a Sunspot are made is impacted by the depth of its Wilson depression. An accurate

Wilson depression is important to directly compare our model with observations. The Wilson depression in the sunspot model can be prescribed by shifting the $\log(\tau_{5000}) = 0$ of the umbral model (p_{um}, ρ_{um}, h_{um}).

The pressure and scale height are then distributed throughout the domain using the following:

$$p(u, z) = p_q(z) - (p_q(z) - p_{um}(z)) \left(1 - \frac{u(r, z)}{u_{max}}\right)^2, \tag{4.5}$$

$$h(u, z) = h_q(z) - (h_q(z) - h_{um}(z)) \left(1 - \frac{u(r, z)}{u_{max}}\right)^2. \tag{4.6}$$

Where u_{max} is the maximum value of the potential $u(r, z)$, and is reached at the quiet sun boundary. The potential solution given by Equation 4.1 is used as an initial guess. The pressure distribution given by Equations 4.5 and 4.6 is iterated together with Equation 4.1 using a Gauss-Seidel method. Thus, the complete force balance is calculated with a specified precision, giving a final distribution of the potential and pressure.

The Pizzo and Low type flux tubes are then joined at $z_d = -1$ Mm and recalculated using Equations 4.5-4.6. The density is then calculated from the ideal gas law

$$\rho(r, z) = \frac{p(r, z)}{g(z)h(r, z)}, \tag{4.7}$$

Finally, the radial and vertical components of the magnetic field vector B_r, B_z are calculated from the variation of the field line constant u

$$B_r(r, z) = -\frac{1}{r}\frac{\partial u}{\partial z}, \tag{4.8}$$

$$B_z(r, z) = \frac{1}{r}\frac{\partial u}{\partial r}. \tag{4.9}$$

To extend this model below $z = -10$ Mm a vertical flux tube with a constant B_z and zero B_r is used, and the pressure and density profiles are continued smoothly downwards.

Finally, the FreeEOS equation of state (Irwin, 2012) is applied to find the adiabatic index, temperature and sound speed at each grid cell in the model. The model is then converted to Cartesian geometry, giving the full set of physical parameters required for the MHD simulations and radiative transfer calculations.

Using the procedure explained above the magnetic field structure pictured in Figure 4.1 was constructed. The background coloured contour map in the figure shows the modulus of magnetic field B. The field lines are nearly vertical in the "umbral" region ($r < 10$ Mm), and show inclination of about 60° in the "penumbral" region, $r > 10$ Mm, of the sunspot model.

In the figure, the dashed line shows the $\log(\tau_{5000}) = 0$ layer, while the dotted contours represent $c_s/v_A = 0.1$, 1, and 10 levels. As is evident from the figure, in the umbral region at the axis of the sunspot, the $\log(\tau_{5000}) = 0$ layer is positioned higher than $c_s/v_A = 1$ layer, suggesting formation of the continuum radiation in the magnetically-dominated sunspot atmosphere.

The 6173 Å photospheric absorption line of neutral iron is used for observations of the full solar disk with the Helioseismic Magnetic Imager (HMI) onboard the Solar Dynamic Observatory (SDO). Therefore, this line was chosen to carry out radiative diagnostics of the sunspot model using the SPINOR code (Solanki, 1987; Shelyag et al., 2007). For each one-dimensional column of the model, continuum intensity and spectral line profile calculations are performed by solving the Unno-Rachovsky (Unno & Simoda, 1963) radiative transfer equation for the Stokes vector $[I, V, Q, U]$. Off disk centre observations are simulated by inclining the numerical domain and interpolating the density, temperature, magnetic field and velocities onto the new line of sight (los). The slanting is performed around the $z = 0$ km height and in the direction of negative y (Figure 4.2). The velocity and magnetic field vectors are then projected into the new reference frame. The calculation uses 500 wavelength points with a $\delta\lambda = 0.002$ Å to ensure the spectral line is highly resolved. The los velocity is given by $v_{los} = v_z \cos\gamma + v_x \sin\gamma$. The magnetic field is recalculated using a similar relation.

Figure 4.2 shows the continuum images of the sunspot model calculated for $\gamma = 0°$, 30° and 60° angles between the surface and the los, which correspond to viewing cosine $\mu = \cos\gamma = 1.$, 0.866 and 0.5, respectively. We find that the model produces a realistic limb darkening dependence with a continuum value of 79% of the disk centre intensity at $\mu = 0.5$. This is only slightly higher than the 75% of the limb darkening curve determined by Foukal et al. (2004).

The velocity response functions of the 6173 Å spectral line are shown in Figure 4.3 for the quiet Sun, two penumbral regions at ±10 Mm, and in the centre of the sunspot umbra for the chosen positions at the solar disk. These locations have been marked with crosses in Figure 4.2. Since, for observations away from solar disk centre, two points at the same distance from the sunspot axis are not equivalent, the penumbral

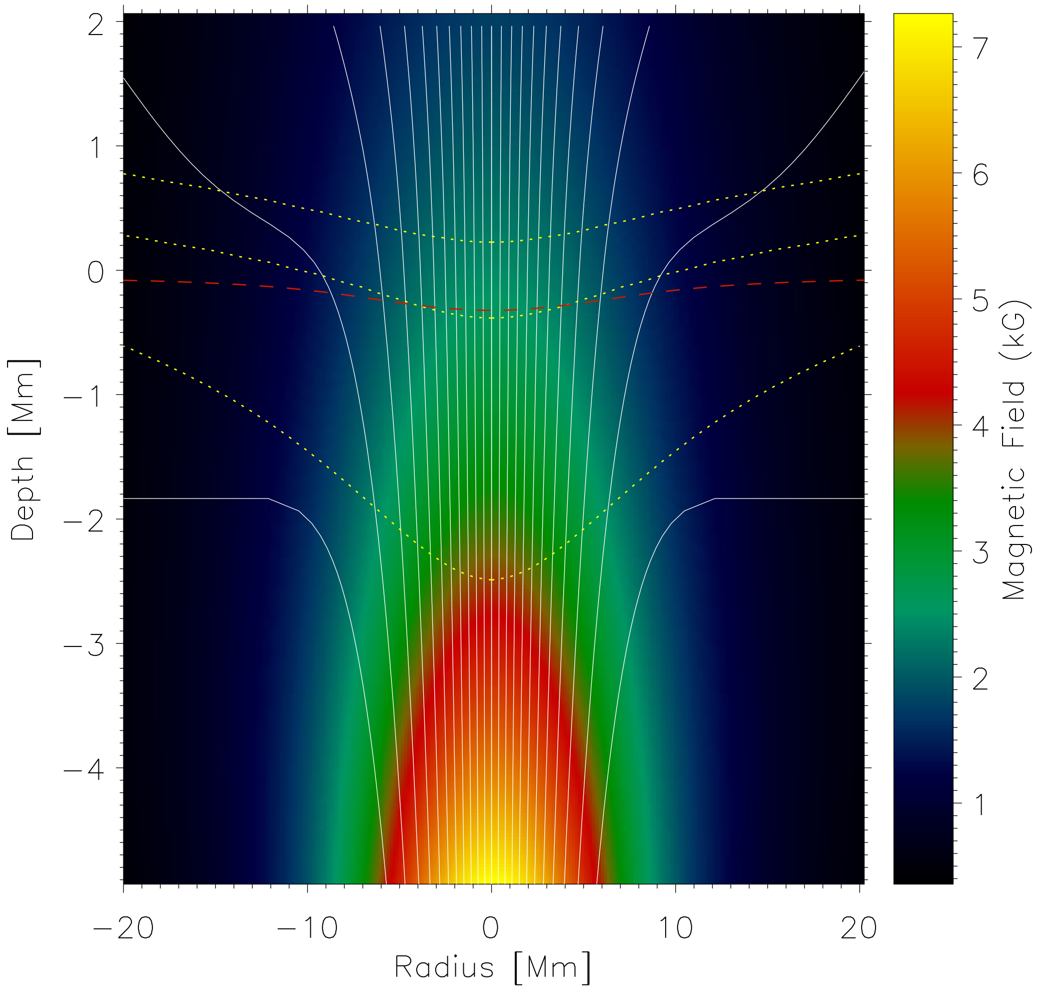

Fig. 4.1: Magnetic field structure of the sunspot model. The magnetic field strength is shown with the magnetic field lines overplotted (solid). Also shown are the $c_s/v_A = 1$ (middle dotted), 0.1 (upper dotted) and 10 (lower dotted) contours. The dashed line is the $\log(\tau_{5000}) = 0$ contour, representing the visible photosphere. Note that the aspect ratio is severely stretched.

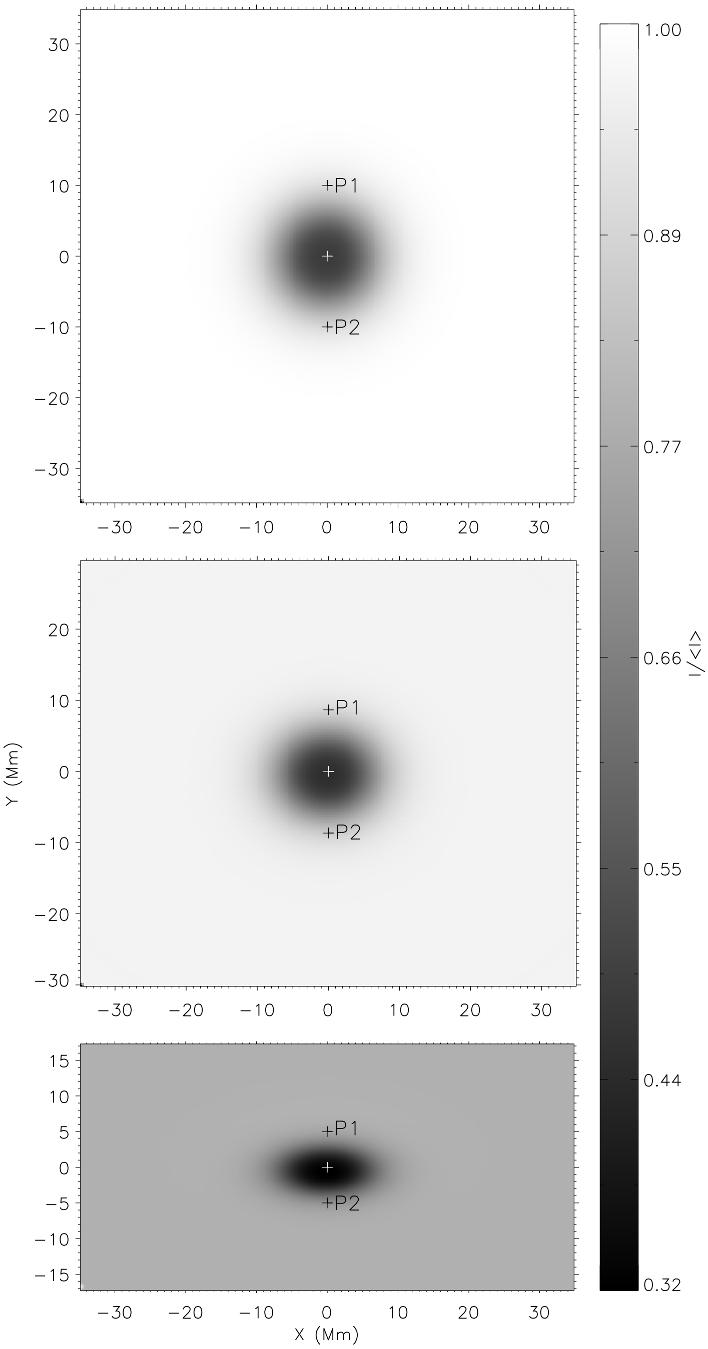

Fig. 4.2: 6173 Å continuum intensity of the sunspot model at the observational angles (top to bottom) 0°, 30° and 60° to the vertical. The figures have been normalised to the quiet Sun value at 0° inclination. Inclination is performed towards an observer displaced in the negative y direction. The crosses show the two penumbral, and one umbral point used in Figure 4.3.

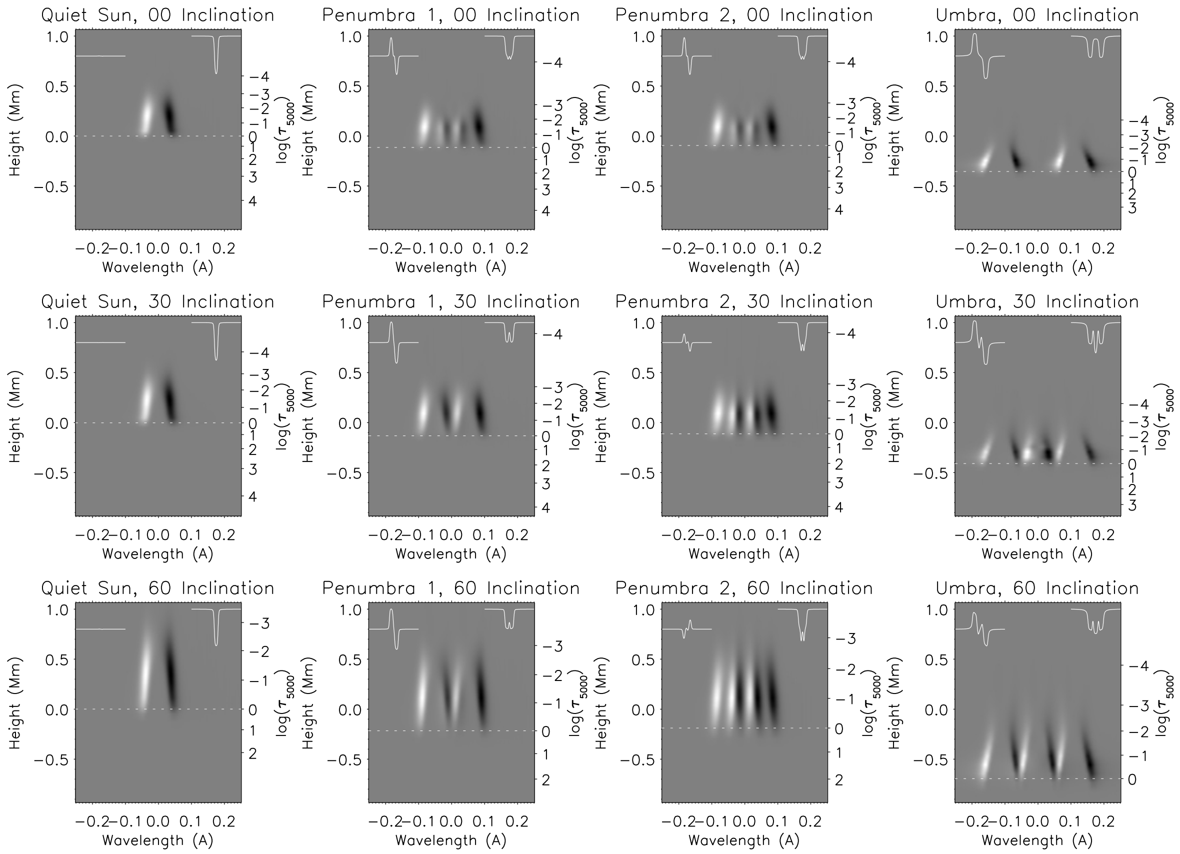

Fig. 4.3: *los* velocity response functions of Stokes$-I$ profile of 6173 Å Fe I line computed for the models of quiet Sun (first column), far-side and near-side penumbrae (second and third columns, respectively), and umbra (fourth column) for $\mu =$ 1.0, 0.866 and 0.5 positions at the solar disk. The y-axis represents the height along the *los* at which the perturbation is placed, where 0 Mm represents the $\log \tau_{5000} = 0$ layer for the quiet Sun photosphere. The 5000 Å optical depth axis is also shown, with a dashed line showing the observed depression of the photosphere. The corresponding Stokes$-I$ (top right) and Stokes-V (top-left) profile shapes were over-plotted in white in each panel over the wavelength range shown in the figure.

models have been chosen so that *los* of P1 crosses the umbral region, while the *los* of P2 inclines further into the penumbra. The response functions were calculated by computing a perturbed profile with a small positive (directed towards the observer) *los* velocity perturbation and subtracting from it an unperturbed profile for the same location.

The top row of Figure 4.3 shows the response functions of the four points in the model for the disk centre calculation. The perturbation is directed towards the observer, causing the line to be blue-shifted. The lobes of the response function tilt inwards towards the line core, marked as 0.0 Å in the plots, clearly demonstrating dependence of the sensitivity of the profile on height; the regions closer to the line core (on the x-axis) are formed higher in the atmosphere.

The top-right figure shows a fully Zeeman-split profile in a strong umbral magnetic field. Notably, while the line formation height range is narrower compared to the quiet Sun, the response function lobes are wider in wavelength, suggesting higher sensitivity of the line to velocity perturbations.

The two penumbral points are identical in the solar disk centre simulation due to the symmetry of the sunspot. As the penumbral magnetic field is weaker, the line is not completely split. In the line core, the response function shows two smaller regions of sensitivity to the velocity perturbation.

Figure 4.3 demonstrates that the line formation height range increases with the inclination angle. In the case of the quiet Sun (left column of the figure), it increases from $\sim$ 400 km at the disk centre to $\sim$ 800 km at $\mu = 0.5$. As the line width does not change significantly, the wavelength range of the response function does not change with the inclination.

For the cases of magnetised penumbral and umbral atmospheres, the observed visible sunspot surface increases with the inclination angle. Between $\mu = 1$ and 0.5, the $\log \tau_{5000} = 0$ level for the penumbral points P1 and P2 is shifted downwards by $\sim$ 100 km, and by $\sim$ 400 km for the umbra. The line sensitivity height range also increases further away from the disk centre, similarly to the quiet Sun.

Notably, the line profiles and the response function shapes for P1 and P2 are very different. The far-side umbra (second column of Figure 4.3, P1 in Figure 4.2) has a formation range that extends into the highly magnetic umbra. This can be observed as an increasingly split profile as inclination increases in the 2nd and 3rd rows. The near-side penumbral pixel (third column, P2) similarly forms in a region of lower magnetic field. Due to the inclination of the magnetic field, P1 measures a higher magnetic field strength along the *los* while P2 inclines against the direction of field line inclination.

The angle of the two ridges is seen to be larger in the umbral distributions than the quiet Sun. For a small wavelength range in the quiet Sun up to 500 km of the atmosphere will be measured. Comparitively, in the umbral distribution a similar filter would only sample around 100 km.

The large range of responses seen in the different penumbral and umbral positions will lead to larger uncertainty in the observation height of velocity measurements. The impact of Zeeman-split profiles on velocity measurements is only amplified at larger inclinations.

4.3 Numerical Simulations

We perform a simulation of acoustic wave propagation in the simulated model with the SPARC code, discussed in detail in Section 1.3. The code was designed to solve the linearised ideal MHD equations for wave propagation in a stratified solar environment (Hanasoge, 2011). The version of the code we employ for the simulations uses Message Passing Interface (MPI) to parallelise the computation and reduce computation time. It uses an implicit compact 6th order finite difference scheme applied to the horizontal and vertical derivatives. An explicit filter is used to prevent numerical instabilities in the solution.

The boundary conditions used in the simulation include a Perfectly Matched Layer (PML) (Hanasoge et al., 2010) at the top and bottom boundaries, allowing for efficient absorption of the outgoing waves. A 12.5 Mm 'sponge' type absorbing layer is used on the side boundaries, which adds a linear friction term to the governing equations (Colonius, 2004). The code includes a Lorentz force limiter (Rempel et al., 2009), which is required due to the high Alfvén speed in the solar atmosphere. The limiter, although unphysical, prevents reduction of the time step and excessive computational times (see 1.3.2). The Alfvén speed limiter is set at $v_A = 125\ \mathrm{km\,s^{-1}}$, which is sufficiently high to allow fast MHD waves of interest, which have horizontal phase speed less than this, to propagate and refract correctly while still allowing us to use a manageable time step. Our cap is large enough for this not to be an onerous constraint. The implications of the limiter on helioseismic travel time shifts have been studied in detail by Moradi & Cally (2014).

The numerical grid has horizontal extent of $n_x = n_y = 256$ grid points, with a physical size of 140 Mm, giving a resolution of $\Delta x = \Delta y = 0.55$ Mm in the horizontal directions. To deal with the large variation in physical parameters over the domain from the convective zone to chromosphere, the code uses a vertical grid spacing based on the sound speed. The grid has $n_z = 300$ points between 1.5 and -25 Mm and is distributed such that the acoustic travel times between each cell are the same for the quiet Sun, $\Delta z \propto 1/c_s$. This gives a resolution of around 50 km near the photosphere, and around 1 Mm in the lower solar interior. This means we do not resolve slow waves in the large-β regime, but these are effectively decoupled from the system anyway, so their neglect is not important. The following acoustic source, similar to that described by Shelyag et al. (2009), was used:

$$v_z = A_0 \sin(\frac{2\pi t}{T_o}) \exp \frac{-(t-T_1)^2}{\sigma_t^2} \exp \frac{-(r-r_0)^2}{\sigma_r^2} \times \exp \frac{-(z-z_0)^2}{\sigma_z^2}, \tag{4.10}$$

where $T_0 = 300$ s, $T_1 = 600$ s, and $\sigma_t = 100$ s. The horizontal position of the pulse is given by $r_0(x, y)$, with $x = 45$ Mm and $y = 70$ Mm, and the vertical position is $z_0 = -0.65$ Mm. The standard deviation of the Gaussian ball is set to $\sigma_r = 1$ Mm for the horizontal dimension and $\sigma_z = 0.25$ Mm for the vertical dimension.

The SPARC code solves the MHD equations for the perturbations around the MHS background model. A master-slave Open-MPI code has been written to take these perturbations, combine them with the background model and incline them as required. The SPINOR routines are then applied to each pixel to generate the full Stokes vector for each pixel. Using the generated Stokes$-I$ profiles, the *los* centre-of-gravity Doppler velocity (v_{cog}) is calculated by computing the position of the centre of gravity of the line profile and determining its shift from the unperturbed counterpart, computed for the background model as

$$v_{cog} = c\frac{\lambda_0 - \lambda_{cog}}{\lambda_0}, \tag{4.11}$$

where λ_{cog} is the centre of gravity of the spectral line

$$\lambda_{cog} = \frac{\int (I_c - I)\lambda d\lambda}{\int (I_c - I) d\lambda}. \tag{4.12}$$

To calculate bisector Doppler velocities from the spectral line the relative intensity I_{rel} was determined by normalising the measured Stokes$-I$ between 0 and 1. Bisectors of the spectral line were calculated at 100 evenly spaced values between $0.05 - 0.95$ of I_{rel}. The bisectors were calculated for the background model and for each output snapshot, as described in detail in Section 3.2. A Doppler velocity (v_{bsr}) was then determined for each snapshot using the shift of the bisector wavelength (λ_{bsr}) from the unperturbed background value, according to:

$$v_{bsr} = c\frac{\lambda_0 - \lambda_{bsr}}{\lambda_0}. \tag{4.13}$$

4.4 Results

Using the model described in Section 2 and methodology given in Section 3, a 2.5 hour simulated observation of wave propagation through the sunspot model was performed. The top panel in Figure 4.4 shows a time-distance plot of the centre-of-gravity *los* Doppler velocity measured using Equation 4.12. The first three wave bounces can be easily seen. A shift in the wave arrival time can be observed as a flattening of the wavefront as it passes through the sunspot umbra at $y = 0$ Mm. The middle panel of Figure 4.4 shows a time-distance plot of the vertical component of velocity at the $z = 0$ Mm level of the simulation domain. A comparison between the top two panels shows that the vertical velocity in the domain and the *los* Doppler velocity are visually identical. Some reflection can be seen from the top and bottom PMLs, and from the side boundaries.

The bottom panel of Figure 4.4 shows the horizontal component of velocity, scaled by $\sqrt{\rho}$ to provide a view of the slow magnetoacoustic wave in the strong magnetic field. A slice is taken through the centre of the simulated sunspot ($x = 0, y = 0$). The fast wave can be seen to propagate through the sunspot in the lower interior where plasma-β is high. At around $z = -0.400$ Mm in the umbra, the incoming fast wave hits $c_s/v_A = 1$ layer (see Figure 4.1) and undergoes partial transmission as a slow mode (effectively acoustic in $c_s < v_A$). The slow magnetoacoustic wave (now magnetic in $c_s > v_A$) can be seen to propagate back down into the sunspot as a flattening banding in the time distance plot. The wave amplitude in the atmosphere is low due to scaling by the very low densities, however, it still can be seen to continue to travel upwards above the photosphere and escapes through the absorbing upper boundary.

Figure 4.5 shows a power spectrum plotted with azimuthally averaged wavenumber and frequency. The spectrum has been calculated from the 2.5 hour time-series of centre-of-gravity velocities calculated from the synthesised line profile. The power

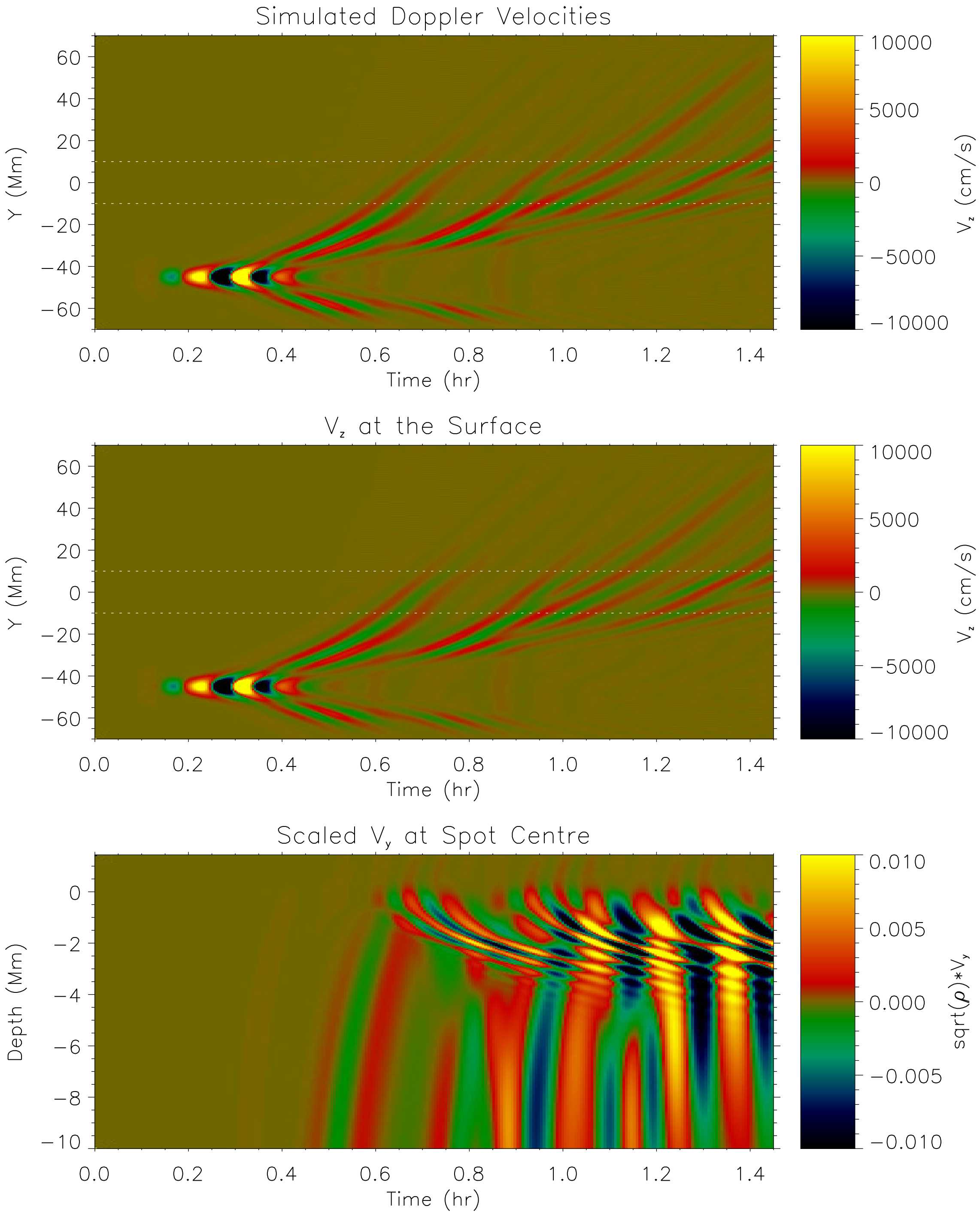

Fig. 4.4: Response of the model to the acoustic source. Top panel - simulated Doppler velocities at 0° inclination, measured at $x = 0$ Mm. Middle panel - simulated vertical component of velocity at a geometric height $z = 0$ Mm, measured at $x = 0$ Mm. The differences between these two are found to be small. Bottom panel - $\sqrt{\rho}v_y$ through spot centre (0,0) Mm showing the propagation of slow modes down through the box. Two dashed horizontal lines in the top plots mark the position of the sunspot umbra.

ridges are well resolved, although there are gaps in power at 4.5 mHz and shifts seen for high l. Similar gaps are found in the simulations of Parchevsky & Kosovichev (2007) with high top boundary (1.75 Mm; their Figure 6c), and attributed to trapping of acoustic modes. The source of these gaps were investigated in detail in Chapter 2. It was found that gaps appear when driving with a spatially localised pulse source, as the height of this source is at a node of the solar $p-$mode eigenfunction.

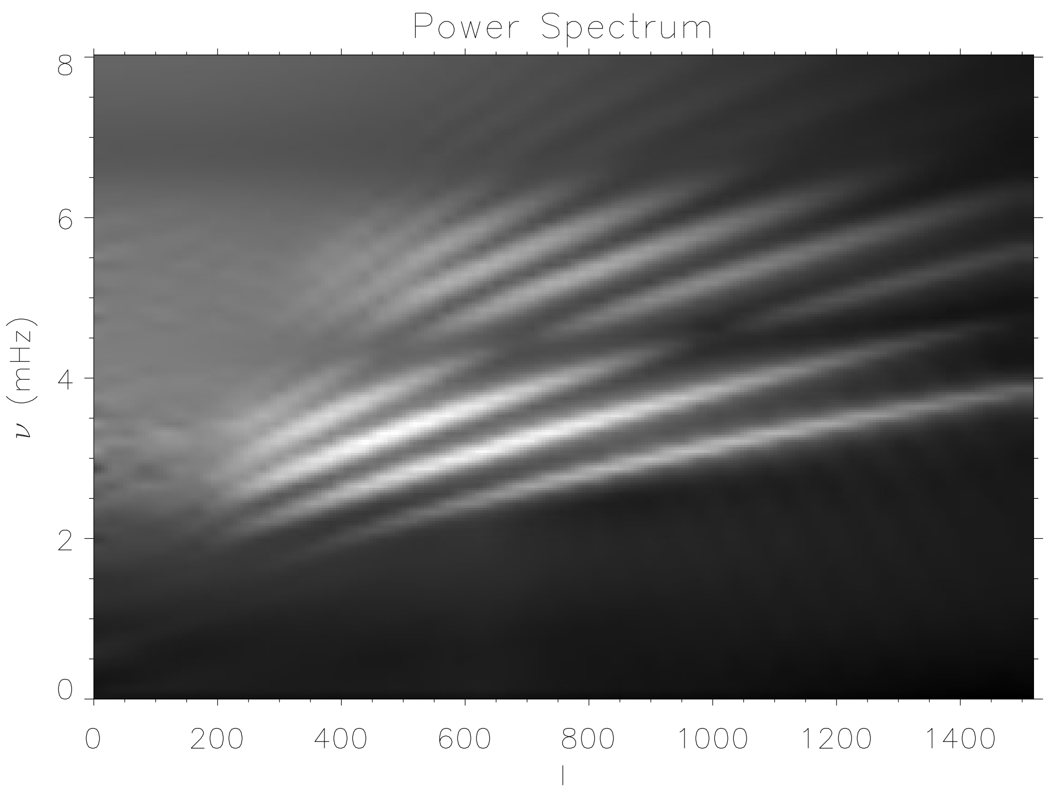

Fig. 4.5: A $\nu - l$ power spectrum for the sunspot box calculated from synthetic Doppler velocities.

Using the Fe I 6173 Å spectral line data, velocity shifts were calculated for each bisector as the differences between the perturbed and background values (Equation 4.13). From the 2.5 hour time series of these velocities acoustic power maps of wave propagation in the sunspot were created. The power maps are calculated for 100 bisector depth positions by taking the fast Fourier transform of the velocity time series for each of the (x, y) pixels in the model. The acoustic power is binned into different frequency bins by applying a Gaussian filter with a FWHM of 0.5 mHz around the chosen central frequency. For each frequency band and inclination the acoustic power is normalised by its average in the simulation domain.

By taking the Doppler velocity measurements at multiple bisector depths, it was possible to disentangle the dependence of the wave behaviour on the height within the line formation region. As Figure 4.3 shows, bisectors taken higher in the line profile are formed deeper and closer to the continuum formation height, at a physical height of around 150 km, while bisectors taken deeper are closer to the absorption line core and formed higher at a physical height of around 500 km. As was already noted, these formation heights vary significantly in the penumbra and umbra of the sunspot, with an offset of 350 km due to the prescribed Wilson depression.

First we aim to investigate the horizontal distribution of acoustic power throughout the simulation domain. The region of the acoustic source at $x = 45$ Mm, $y = 70$ Mm has been masked in the power maps. Figures 4.6 and 4.7 show the acoustic power calculated from the Doppler shifts measured at the bisector positions of 0.3 I_{rel} and 0.9 I_{rel}, respectively. The acoustic power was binned into 1 mHz frequency bands centred at 3, 4, 5, 6 and 7 mHz (left to right in the figures), and the disk positions of $-60°$, $0°$ and $60°$ were used (top to bottom). *los* velocity measurements off the disk centre are affected by a larger line formation region and the presence of horizontal velocity components in the *los* velocities. Immediately obvious in the figure is a series of concentric rings of power travelling out from the source. These rings can be thought of as the spatial analogue of the ridges seen in Figure 4.5 and occur at discrete values because a single point-like source was used in the simulation.

The differences between the acoustic power maps in Figure 4.6 and 4.7 represent changes in the wave behaviour over the formation height of the spectral line. This formation height can span almost a megametre close to the solar limb (see Figure 4.3), and the differences are substantially more pronounced in the magnetic regions.

In the acoustic power maps (Figures 4.6 and 4.7) a solid line representing the sunspot umbra is overplotted. Outside the sunspot umbra the sunspot shadow is observed at all frequencies. In the sunspot shadow, the power from the pulse has been absorbed or reflected by the magnetic field structure. This is most obvious at lower frequencies (left two columns). As frequency increases, the ridges of increased acoustic power can still be seen behind the sunspot. Interestingly, the magnetic field perturbs the concentric rings seen at 7 mHz, as the fast wave propagation speed and turning height change. Behind the sunspot in the 7 mHz band (right column), a small region of increased power can be seen between the two outermost rings of the power ridges (around $y = 30$ Mm). As this is seen in high frequencies and as a ring around the sunspot, rather than around the source, it appears to be a far-side acoustic halo. Acoustic halos are seen around active regions as an excess of acoustic power compared to the quiet sun. [1]

Comparison of the weakly-magnetic regions of each column in Figure 4.6 shows little variation with inclination, regardless of frequency. In these regions the propagating fast wave dominates the simulated observations as there is little magnetic field to alter the fast-wave turning point or to allow for mode-conversion process to take place. Inside the umbral region, the acoustic power maps for the disk centre case show very little power in 3 and 4 mHz, and the power in the vertically-aligned oscillations is seen to be almost completely absorbed. As the inclination increases, the 3 and 4 mHz power in the umbra remains low, while the 5, 6 and 7 mHz power bands show a significant power enhancement.

From the response function (first column in Figure 4.3) we expect there to be larger differences in power between the line core (Figure 4.6) and line wings (Figure 4.7) as we observe further away from the solar disk centre. There is little difference found in the disk centre cases (middle row) between the two figures. However, at 60° inclination significant differences can be seen between the power maps at the line core and line wings. Particularly, (1) the umbral power increase is only seen at the line core (Figure 4.6); (2) the ring-like structure (marked by the dashed circle in the left panel of Figure 4.6) found at around $y = -20$ Mm in the bottom left two panels is somewhat wider at the line core than in the line wings (Figure 4.7). This structure is most apparent in the $3 - 4$ mHz frequency bands (first two columns), and the power in it decreases with increasing frequency. While the inclination of the magnetic field at the surface at the radius of 20 Mm is 60° degrees from vertical the magnetic field strength is low, and the equipartition layer $c_s = v_A$ is located above the line formation region. Therefore, the ring is of acoustic nature and cannot be related to the slow magneto-acoustic mode, as it is found at the source side in both $-60°$ and $60°$ inclinations corresponding to the *los* direction which is either parallel or highly inclined to the magnetic field.

As demonstrated, the umbral and penumbral acoustic power structures are mostly seen near the line core (Figure 4.6). In the *los* velocities measured from bisectors in the line wings (Figure 4.7) only a faint structure can be seen at high inclinations, again more obvious in the 7 mHz power band (bottom right).

To better understand the three-dimensional structure of the umbral power increase,

[1] A more comprehensive look at the physics of acoustic halos, based on three-dimensional simulations of this sunspot model can be found in Rijs et al. (2015, 2016), see Appendices A & B, which expands on the previous works of Hanasoge (2008); Khomenko & Collados (2009). They are attributed to fast MHD waves reflected in active region atmospheres by the steep Alfvén speed gradients there.

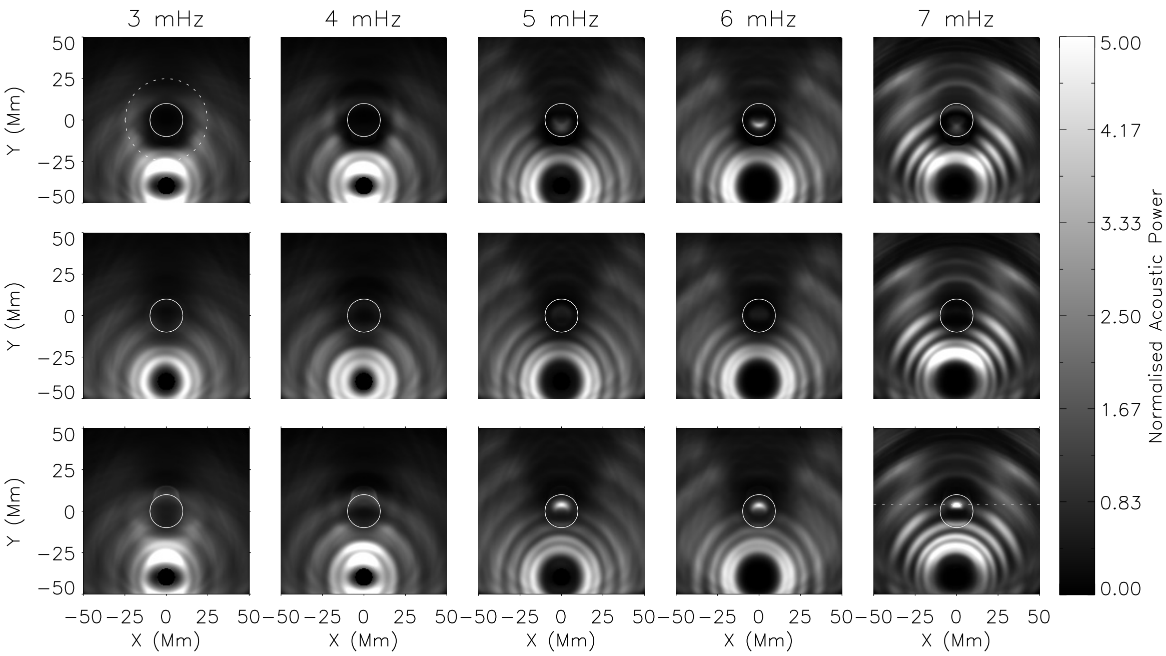

Fig. 4.6: Acoustic power map calculated from the shifts in the bisector of the Fe I 6173 Å line at a bisector height of 0.3 I_{rel}. The columns, from left to right, show power in the 3, 4, 5, 6 and 7 mHz bands. The rows, from top to bottom, show measurements made at $-60°$, $0°$ and $60°$ inclination from the vertical, where the field of view has been inclined in the y-direction. The power at each inclination angle has been normalised by its average in each frequency band. This represents a velocity measurement made near the line-core, showing the behaviour higher in the atmosphere. The sunspot umbra has been marked with a solid circle, while the dashed line in the bottom right panel represents the slice taken in Figure 4.8. The low frequency ring has been marked in the top left panel.

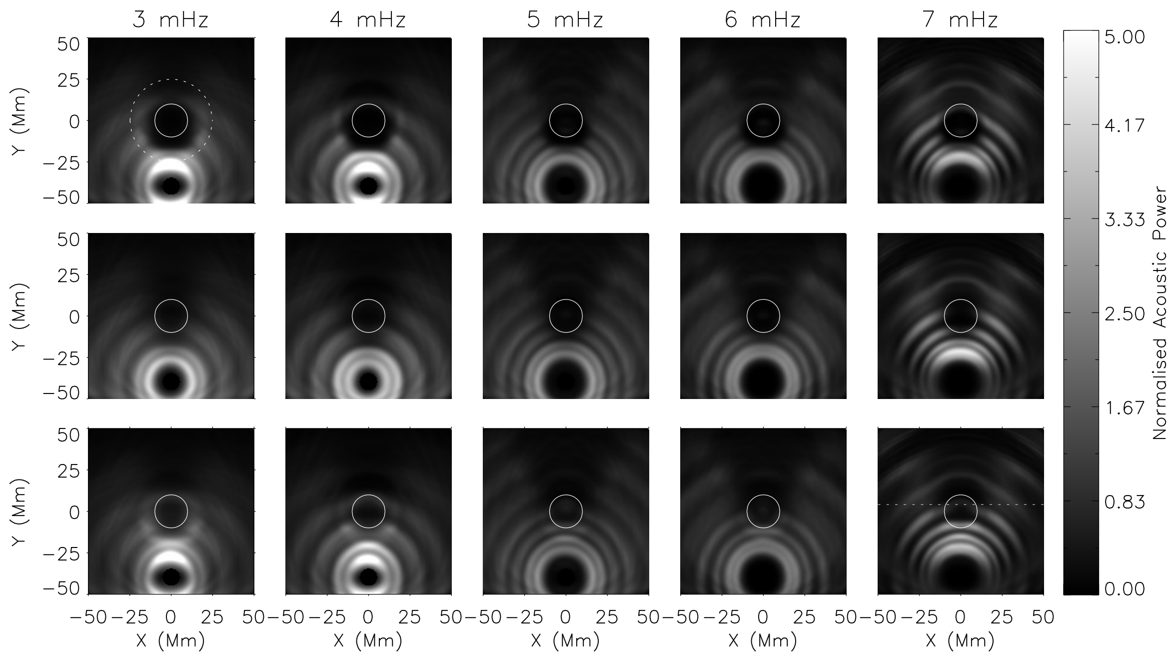

Fig. 4.7: Acoustic power map calculated from the shifts in the bisector of the Fe I 6173 Å line at a bisector height of 0.9 I_{rel}. The layout of the columns and rows is as seen in Figure 4.6. This figure represents measurements made near the line wings.

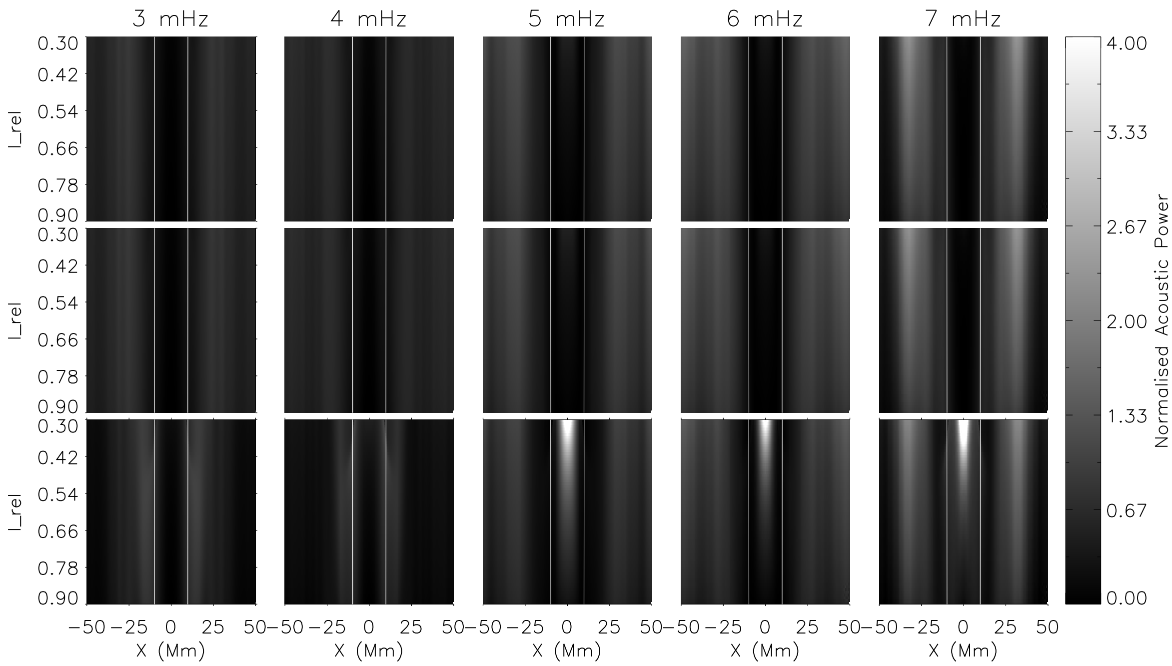

Fig. 4.8: Bisector power map at x = 0 Mm. The layout of the columns is as in Figure 4.6. The rows, from top to bottom, show measurements made at 0°, 30° and 60° inclination from the vertical. The vertical axis in this figure represents the line depth where the bisector wavelength and Doppler velocity are measured and covers a large part of the line formation region of 400 − 800 km in length. The formation region depends on the magnetic field strength and inclination (Figure 4.3).

in accordance with the response functions shown in Figure 4.3, a multi-height observation is made by computing the Doppler velocities from bisector shifts measured at different line depths within the line formation region. In Figure 4.8, a Doppler velocity map for a slice marked by a dashed line in Figure 4.7 is plotted for each bisector depth in the range $0.3 - 0.9\ I_{rel}$.

For the 0° and 30° inclinations (top and middle rows of Figure 4.8), the changes in the structure and magnitude of acoustic power over the line formation range are limited to an increase in power in the high frequency bands for observations made closer to the line core. This matches the observations of acoustic halos by Rajaguru et al. (2013), where the acoustic power was weaker using filtergrams close to the line wings. At 60° inclination (bottom row, left two columns) the faint $x = \pm 20$ Mm radius low frequency ring can be made out, increasing in radius at larger heights.

The vertical extent of the umbral power structure, seen at high inclinations at 6–7 mHz (bottom right two panels in Figure 4.6–4.8) shows a significant increase in power higher in the formation region. The formation of this acoustic power structure seems to start mid-way up the line formation region, suggesting a highly localised phenomenon. The inclination of the field lines at the centre of this power increase ($y = 4.11$ Mm) is approximately 20° from the vertical. Taking into account the observation angle of ±60°, the field line is almost perpendicular to the line-of-sight. Comparison with Figure 4.1 shows the continuum formation height of the spectral line and the $c_s/v_A = 1$ layer cross at $z = 0$ Mm and 4 Mm radius from the sunspot centre, allowing for direct observation of conversion of fast (parallel to the magnetic field line, perpendicular to the *los*) waves to slow (perpendicular to the magnetic field line, and parallel to the *los*) waves. The increased power in this region corresponds to the slow magneto-acoustic wave in the region where the magnetic field is close to perpendicular to the *los*. This result confirms previous findings by Zharkov et al. (2013) that the observed acoustic power increase in the sunspots is a signature of slow magneto-acoustic waves.

4.5 Discussion and Conclusion

In this chapter we have: (1) described a modification of the Khomenko sunspot model we developed to provide a more accurate line formation region, allowing for accurate spectral synthesis to be performed; (2) analysed response functions in our model to understand our synthesised centre-to-limb observations of the Fe I 6173 Å spectral line in a model sunspot; (3) have investigated wave propagation through the model using a three-dimensional simulation of magnetoacoustic wave propagation; (4) computed the spectral line profiles and provided a time series of the simulated observations of the sunspot model using the simulation data; (5) used spectral line bisector measurements to perform multi-height simulated observations over the line formation region; (6) studied maps of the acoustic power in the sunspot to better understand the absorption line response to the oscillations in sunspots and the effects of non-locality of radiative transport on helioseismic measurements.

The sunspot is found to absorb or scatter the incoming acoustic wave energy in all but the 6 and 7 mHz frequency band. There are signatures of a slight power enhancement seen around the sunspot, similar to those seen in observations of acoustic halos.

Small ridges of acoustic power can be seen in the 7 mHz band in the shadow of the sunspot. Zharkov et al. (2013) showed in a simple 2D simulation that there was a significant power enhancement as a far-side acoustic halo. We can see slight power enhancements in the range of 25-40 Mm from the sunspot. Comparing the different rows in Figures 4.6 and 4.7 shows that outside the sunspot umbra, the horizontal and vertical velocities behave similarly, with only minor differences in the power maps.

The appearance of a high-frequency anomalous acoustic power excess in the sunspot centre – the umbral "belly button" – can be seen predominantly in the case of 60° inclination with faint traces at lower inclinations. This geometry suggests that it is driven by slow magneto-acoustic waves, as it is seen when the horizontal velocity component dominates the *los* velocity (bottom rows of Figure 4.6 and 4.7). It can be seen as a crescent-like structure, which is most dominant towards the line core (higher in the atmosphere, Figure 4.6 and very faint in the spectral line wings (lower in the atmosphere, Figure 4.7. Umbral power enhancements are seen in the space-based (Zharkov et al., 2013, HMI) and ground based (Balthasar et al., 1998) observations of sunspots. Notably, no power excess was observed in the G band (Nagashima et al., 2014). The appearance of this power increase in a simulated sunspot suggests a magneto-acoustic phenomenon, rather than photon noise. There are many differences in both sunspot properties and the radiative effects on HMI measurements that could explain the lack of the umbral power increase in *all* acoustic observations of sunspots. These include changes in the Wilson depression, the wide range of the velocity response function in a magnetic structure (Figure 4.3), low resolution and high-noise measurements off the disk centre or issues with using discrete filters on highly split profiles.

Current measurements of acoustic travel times in computational helioseismology are largely performed using measurements at the geometric heights in the simulation domain (Moradi & Cally, 2013), or on a surface roughly representing the continuum formation height determined by the $\log(\tau_{5000}) = 0$ layer in the simulation domain (Khomenko & Cally, 2012; Moradi et al., 2015). Despite the fact that the physical velocity in the simulation matches reasonably well to the *los* velocities calculated from the simulated spectral lines, this method misses a lot of information that can otherwise be gained from the range of formation of the spectral lines. As we show, this range also changes substantially if the simulation is performed for positions at the solar disk away from the centre. Using the model we described, artificial observables mimicking the HMI and MDI pipelines can be made (Scherrer et al., 2012; Fleck et al., 2011), as well as comparisons to ground-based observations.

The multi-height Doppler measurements made by Nagashima et al. (2014), using the HMI filtergrams provide a similar approach to multi-height measurements as the bisectors used in this study. Rather than velocity measurements made using shifts in Stokes-I, HMI uses measurements of both Stokes-$(I + V)$ and Stokes-$(I - V)$. As the next step, it will be important to fully simulate the HMI data pipeline response to a variable magnetic atmosphere before a direct comparison to the HMI measurements can be made.

Chapter 5

Dissipation of Alfvén Waves by Ambipolar Diffusion

In this chapter we investigate the ability of ion-neutral interactions to dissipate Alfvén waves in the solar chromosphere. An acoustic driver is used to generate perturbations in a self-similar magnetohydrostatic flux tube model. As these waves travel into the centre of the magnetic field concentration, where plasma-$\beta < 1$, mode conversion occurs and a significant Alfvén wave component is seen. In order to quantify the absorption of wave energy through ion-neutral interactions we compare the energy and Poynting flux in simulations with, and without ambipolar diffusion. It is found that the inclusion of the ambipolar term can dissipate a significant amount of energy, a factor of 20 higher than the dissipation of static currents. This heating is caused by the damping of magnetic waves, as seen by a decrease in Poynting flux by up to 90% when ambipolar diffusion is included. The dependence of this energy dissipation with resolution, driver amplitude and frequency is studied.

Monash University

Declaration for Thesis Chapter 5

Declaration by candidate

In the case of Chapter 5, the nature and extent of my contribution to the work was the following:

Nature of contribution	**Extent of contribution (%)**
Key Ideas, assistance with code and model development. Assistance with data analysis.	20

The following co-authors contributed to the work. If co-authors are students at Monash University, the extent of their contribution in percentage terms must be stated:

Name	**Nature of contribution**	**Extent of contribution (%) for student co-authors only**
Sergiy Shelyag	Key Ideas,development of model and code, writing of paper.	
Elena Khomenko	Key Ideas, development of model and code.	
Angel De Vincente	Code development.	

The undersigned hereby certify that the above declaration correctly reflects the nature and extent of the candidate's and co-authors' contributions to this work*.

Candidate's Signature	[redacted]	Date 17/2/17
Main Supervisor's Signature		Date 17/2/17

*Note: Where the responsible author is not the candidate's main supervisor, the main supervisor should consult with the responsible author to agree on the respective contributions of the authors.

5.1 Introduction

In Chapter 3 we investigated the observational signatures of photospheric "vortices". These vortex motions have been identified as Alfvénic motions (Shelyag et al., 2013) and shown to carry a substantial Poynting flux into the chromosphere (Shelyag et al., 2012). However the dissipation of these Alfvénic motions, required if they are to heat the chromospheric plasma, is difficult in ideal magnetohydrodynamics. Non-ideal effects, in particular ambipolar diffusion, show potential for the dissipation of these waves.

The recent increases in supercomputing power and availability have allowed the inclusion of partial ionisation into numerical magnetohydrodynamic codes, both through inclusion of non-ideal MHD terms describing ion-neutral interaction and non-ideal equations of state. In this chapter we investigate the ability of ambipolar diffusion to damp Alfvénic waves, and thereby heat the solar chromosphere. To do this we use the newly implemented non-ideal module of the MANCHA MHD code.

First, we discuss the implications of non-ideal magnetohydrodynamics for wave heating of the chromosphere in Section 5.1.1. Next, in Section 5.1.2 we give a summary of the non-linear MHD processes important to this chapter. In Section 5.2 we describe the flux tube model used, designed to mimic a region similar to that studied in Chapter 3. Then the MANCHA code, and simulation setup used are described in Section 5.3. A study of wave heating with variations in simulation resolution, driver amplitude and driver frequency is presented in Section 5.4. Finally, in Section 5.5 we discuss the results.

5.1.1 Non-Ideal Magnetohydrodynamics

Due to the low degree of ionisation in the photosphere and chromosphere, deviations from the ideal magnetohydrodynamic assumption are found to be important for numerous processes in the solar atmosphere, see the review of Khomenko (2016) for a detailed explanation. The effects of partial ionisation have been investigated for a number of solar applications, including flux emergence (Arber et al., 2007, 2009), the development and growth of instabilities (Fontenla, 2005; Vranjes et al., 2006; Pandey & Wardle, 2012; Soler et al., 2012; Díaz et al., 2014) as well as magnetic reconnection (Zweibel, 1989; Brandenburg & Zweibel, 1994; Leake et al., 2012; Murphy & Lukin, 2015; Hillier et al., 2016). Of particular interest, the addition of neutral atoms in the chromospheric plasma provides a possible mechanism to heat the chromosphere through the dissipation of static currents. The dominant non-ideal effects which must be considered in the magnetised solar chromosphere are that of Ohmic resistivity, ambipolar diffusion and the Hall effect.

Ohmic resistivity leads to an additional diffusive term, due to the drift between electrons and ions/neutrals. In the solar atmosphere it is only significant in the lower regions ($0 - 500$ km), with low magnetic field strength (Khomenko & Collados, 2012). The time-scale of this diffusion was found to be large (10^7 s) and so the contribution to chromospheric heating is small.

The Hall effect in a weakly ionised plasma is caused by the drift between ions and electrons, with the former remaining pinned to the magnetic field. For solar magnetic field regions the Hall effect will be higher than Ohmic diffusion in magnetic fields greater than ≈ 100 G (Pandey & Wardle, 2008). In addition, the Hall effect has the ability to couple Alfvén and magnetoacoustic fast waves (Kato & Tsutomu, 1956; Waters et al., 2013) and facilitate fast reconnection (Shay et al., 2001; Rogers et al., 2001; Birn et al., 2001). For photospheric and chromospheric regions, the conversion of low frequency (mHz) seismic waves into Alfvénic oscillations through the Hall effect was found to be inefficient except in regions of low magnetic field, of the order of a few gauss (Cally & Khomenko, 2015). Suitable regions are prevalent in the quiet Sun, so the Hall effect shows potential to be significant in the generation of the transverse waves observed in the corona. At higher frequencies the Hall effect becomes stronger, however a power law is expected for the velocity power spectrum leading to low power at these high frequencies. It is important to not though that the Hall effect is not diffusive; it just redistributes energy between the Alfvén and fast waves.

Ambipolar diffusion represents drift between the charges and neutrals, with the charges remaining pinned to the magnetic field. It is proposed that the dissipation of currents in the chromosphere is an important heating mechanism (De Pontieu & Haerendel, 1998; Judge, 2008; Krasnoselskikh et al., 2010; Martínez-Sykora et al., 2012). Ambipolar diffusion provides another mechanism to dissipate perpendicular currents, allowing for heating orders of magnitude higher than seen in the fully ionised case (Khomenko & Collados, 2012). Ion-neutral drift provides a possible source of heating through the damping of magnetohydrodynamic waves.

Partial ionisation effects have been shown to have a large impact on the generation and propagation of waves in solar magnetic flux concentrations. In the solar photosphere and chromosphere changes in viscosity, friction and conductivity occur due to interaction with neutrals, which damp waves (Khodachenko et al., 2004; Forteza et al., 2007). This damping depends on the collisional frequencies and ionisation fraction (Kumar & Roberts, 2003; Pandey et al., 2008). The ion-neutral friction can become significant relative to the magnetic tension term, allowing for the dissipation of Alfvén and fast magnetoacoustic waves (Piddington, 1956; Osterbrock, 1961; Haerendel, 1992; De Pontieu et al., 2001; Leake et al., 2005; Soler et al., 2013, 2014, 2015). Using a single-fluid approximation cut-off frequencies have been proposed for Alfvén and kink waves (Soler et al., 2009; Barceló et al., 2011), these were shown to be unphysical and caused by neglected terms which are solved using two fluid magnetohydrodynamics (Zaqarashvili et al., 2011b). However, in two fluid MHD additional cutoffs are present, suppressing the propagation and excitation of Alfvén waves. The Alfvénic flux may be significantly lower when interactions with the neutrals are included (Soler et al., 2013; Vranjes et al., 2008).

Magnetoacoustic waves and Alfvénic motions carry a significant Poynting flux into the solar chromosphere (Osterbrock, 1961; Goodman, 2005; Steiner et al., 2008; Krasnoselskikh et al., 2010; Goodman & Kazeminezhad, 2010; Goodman, 2011; Shelyag et al., 2012, 2013; Shelyag & Przybylski, 2014). These Alfvénic motions will generate currents. Ambipolar diffusion provides a potential mechanism for the dissipation of these currents, though it is argued by Arber et al. (2016) that the shock heating will be more important than the dissipation of Alfvén waves through ion-neutral interaction.

In order to incorporate the presence of neutral species into ideal MHD simulations we must supplement the ideal MHD equations. Two methods are typically used to do this: a multi-fluid approach, or a single-fluid quasi-MHD. In a multi-fluid formulation the MHD equations are solved for the different plasma components; ions, electrons and neutrals. The equations for different species are coupled through collisional terms. For a single-fluid approach the ideal MHD equations are supplemented with a number of additional terms, calculated through the summation of the effects from the various plasma components.

A three-fluid approach involves solving MHD-like equations for ions, electrons and neutrals, averaging over the different ion and neutral species. A two-fluid approach assumes that the neutral species and ion species are sufficiently coupled, thus leading to two coupled sets of equations, one for an average charge and a second for an average neutral. This approach requires a stronger coupling between two charged particles than between one neutral and one charged and can fail if the neutral-neutral collisional coupling is weak compared to ion-neutral coupling (Zaqarashvili et al., 2011a,b).

The collisional coupling of plasma is strong in the solar chromosphere, this allows a quasi-MHD single-fluid approach to be used. A full description of this approach is available in Khomenko et al. (2014), including discussion of the assumptions made and comparison to a two fluid approach. The single-fluid equations for a multi-component plasma are calculated by summing up the various neutral and ionised components to obtain an equation for an average atom. This approach considers only singly ionised ions and assumes charge neutrality.

Here we provide a derivation of only the necessary equations, the generalised Ohm's law, with additional non-ideal terms, and the non-ideal induction equation. This derivation is given in SI units. Throughout this section the subscripts $e, i,$ and n represent electrons, ions and neutrals while the subscript c is used to describe the total effect of all charges. When summing over the different species we use α for the ions and β for the neutrals.

For a charged fluid with density ρ, charge q, number density n, magnetic field $\mathbf{B}$, electric field $\mathbf{E}$, centre of mass velocity $\mathbf{u}$ and gravity $\mathbf{g}$ we have the ion momentum equation:

$$\rho_\alpha \frac{D\mathbf{u}_\alpha}{Dt} = n_\alpha q_\alpha \left(\mathbf{E} + \mathbf{u}_\alpha \times \mathbf{B}\right) + \rho_\alpha \mathbf{g} - \nabla \hat{\mathbf{p}}_\alpha + \mathbf{R}_\alpha - \mathbf{u}_\alpha S_\alpha, \tag{5.1}$$

where $\mathbf{R}$ represent elastic collision terms, S are the inelastic collision terms and $\hat{\mathbf{p}}_\alpha$ the ion pressure tensor. Similarly, the electron momentum equation is:

$$\rho_e \frac{D\mathbf{u}_e}{Dt} = -en_e \left(\mathbf{E} + \mathbf{u}_e \times \mathbf{B}\right) + \rho_e \mathbf{g} - \nabla \hat{\mathbf{p}}_e + \mathbf{R}_e - \mathbf{u}_e S_e, \tag{5.2}$$

where $\hat{\mathbf{p}}_e$ is the electron pressure tensor. The continuity equation for charges is

$$\frac{\partial \rho_c}{\partial t} + \nabla \cdot (\rho_c \mathbf{u}_c) = S_c, \tag{5.3}$$

where $\rho_c = \sum_{\alpha=1}^{N+1} \rho_\alpha + \rho_e$ and $S_c = S_e + S_i$.

To calculate Ohm's law we multiply the equations of each species 5.1 & 5.2 by q_α / m_α, where $\alpha = 1, .., N$ represents the ions, and $\alpha = N + 1$ represents electrons. Summing these equations for each component, and expanding the material derivative

$$\frac{D\mathbf{u}}{Dt} \equiv \frac{\partial \mathbf{u}}{\partial t} + \mathbf{u} \cdot \nabla \mathbf{u} \tag{5.4}$$

gives

$$\sum_{\alpha=1}^{N+1}\left(n_\alpha q_\alpha \frac{\partial \mathbf{u}_\alpha}{\partial t} + n_\alpha q_\alpha \mathbf{u}_\alpha \cdot (\nabla \mathbf{u}_\alpha) + \frac{q_\alpha}{m_\alpha}\mathbf{u}_\alpha S_\alpha\right) =$$
$$\sum_{\alpha=1}^{N+1}\left(\frac{n_\alpha q_\alpha^2}{m_\alpha}(\mathbf{E} + \mathbf{u}_\alpha \times \mathbf{B}) + n_\alpha q_\alpha \mathbf{g} - \nabla \frac{q_\alpha}{m_\alpha}\mathbf{p}_\alpha + \frac{q_\alpha}{m_\alpha}\mathbf{R}_\alpha\right). \tag{5.5}$$

Applying the continuity equation 5.3 to the left hand side, and cancelling the gravity terms due to charge neutrality gives

$$\frac{\partial \mathbf{J}}{\partial t} + \nabla\cdot(\mathbf{J}\mathbf{u} + \mathbf{u}\mathbf{J}) + \nabla\cdot\sum_{\alpha=1}^{N+1}(n_\alpha q_\alpha \mathbf{w}_\alpha \mathbf{w}_\alpha) = \sum_{\alpha=1}^{N+1}\left(\frac{n_\alpha q_\alpha^2}{m_\alpha}(\mathbf{E} + \mathbf{u} \times \mathbf{B}) - \nabla \frac{q_\alpha}{m_\alpha}\hat{\mathbf{p}}_\alpha + \frac{q_\alpha}{m_\alpha}\mathbf{R}_\alpha\right), \tag{5.6}$$

where dyadic notation is used and $\mathbf{w}$ is the drift velocity. The current density $\mathbf{J}$ is defined

$$\mathbf{J} = e\sum_\alpha n_\alpha \mathbf{u}_\alpha - e n_e \mathbf{u}_e. \tag{5.7}$$

For the Lorentz force term, we neglect terms proportional to m_e/m_α,

$$\sum_{\alpha=1}^{N+1}\frac{n_\alpha q_\alpha^2}{m_\alpha}(\mathbf{E} + \mathbf{u} \times \mathbf{B}) \approx \frac{e^2 n_e}{m_e}(\mathbf{E} + \mathbf{u} \times \mathbf{B}) + \frac{e^2}{m_e}\sum_{\alpha=1}^{N} n_\alpha \mathbf{w}_\alpha \times \mathbf{B} - \frac{e}{m_e}\mathbf{J} \times \mathbf{B}, \tag{5.8}$$

and assume $\mathbf{w}_\alpha \approx \mathbf{u}_i - \mathbf{u}$, that is, the drift velocity of individual items is approximately their average drift velocity. Here $\mathbf{u}_i$ is the centre of mass velocity and $\mathbf{u}$ the average velocity is calculated according to

$$\mathbf{u} = \xi_c \mathbf{u}_c + \xi_n \mathbf{u}_n, \tag{5.9}$$

where ξ_n is the neutral fraction, and ξ_c the fraction of charges. Including the Lorentz force from Equation 5.8 and assuming that currents are stationary, Equation 5.6 becomes

$$\mathbf{E}' = (\mathbf{E} + \mathbf{u} \times \mathbf{B}) = -\xi_n \mathbf{w} \times \mathbf{B} + \frac{\mathbf{J} \times \mathbf{B}}{e n_e} - \frac{\nabla \mathbf{p}}{e n_e}$$
$$+ \frac{\rho_e}{(e n_e)^2}\left(\sum_{\alpha=1}^{N}\nu_{ei_\alpha} + \sum_{\beta=1}^{N}\nu_{en_\beta}\right)\mathbf{J} - \frac{\rho_e}{e n_e}\left(\sum_{\beta=1}^{N}\nu_{en_\beta} - \sum_{\alpha=1}^{N}\sum_{\beta=1}^{N}\nu_{i_\alpha n_\beta}\right)\mathbf{w}. \tag{5.10}$$

Here ν represents the collisional frequencies between electrons and ions $\nu_{e;i_\alpha}$, electrons and neutrals $\nu_{e;n_\beta}$, and ions and neutrals $\nu_{i_\alpha;n_\beta}$ for each species of ions α, and neutrals

β. The expression for $\mathbf{w}$ is calculated following Braginskii (1965) as

$$\mathbf{w} = \frac{\xi_n}{\alpha_n}\mathbf{J}\times\mathbf{B} - \frac{\mathbf{G}}{\alpha_n} + \sum_{\beta=1}^{N} \rho_e \nu_{en_\beta} \frac{J}{n_e e \alpha_n}, \tag{5.11}$$

and the vector $\mathbf{G}$ is

$$\mathbf{G} = \eta_n \nabla \hat{\mathbf{p}}_{ie} - \eta_i \nabla \hat{\mathbf{p}}_n. \tag{5.12}$$

Here $\hat{\mathbf{p}}_n$ is the neutral pressure tensor. The final single-fluid generalised Ohm's law is then:

$$\mathbf{E}' = \eta_O \mu \mathbf{J} + \frac{\eta_H \mu}{|\mathbf{B}|}(\mathbf{J}\times\mathbf{B}) - \frac{\eta_A \mu}{|\mathbf{B}|^2}(\mathbf{J}\times\mathbf{B}\times\mathbf{B}) - \frac{\eta_p \mu}{|\mathbf{B}|}\nabla \hat{\mathbf{p}}_e + c_{pt}\mathbf{G} + c_{ptb}(\mathbf{G}\times\mathbf{B}), \tag{5.13}$$

for electron pressure tensor $\hat{\mathbf{p}}_e$, where the subscripts $e, i,$ and n represents electrons, ions and neutrals. The Ohmic, Hall, ambipolar and pressure diffusivities $(\eta_O, \eta_H, \eta_A, \eta_p)$ and the coefficients (c_{pt}, c_{ptb}) can be calculated as:

$$\begin{aligned}
\eta_O &= \frac{1}{\mu_0}\frac{1}{(en_e)^2}\left(\sum_{\alpha=1}^{N}\rho_e\nu_{ei_\alpha} + o\sum_{\beta=1}^{N}\rho_e\nu_{en_\beta}\right) \approx \frac{\alpha_e}{(en_e)^2}, \\
\eta_H &= \frac{|\mathbf{B}|}{\mu_0}\frac{1}{en_e}\left(1 - 2\xi_n\epsilon_1 + \xi_n\epsilon_2\right), \\
\eta_A &= \frac{|\mathbf{B}|^2}{\mu_0}\frac{\eta_n^2}{\alpha_n}, \qquad\qquad (5.14)\\
\eta_p &= \frac{|\mathbf{B}|}{\mu_0}\frac{1}{en_e}, \\
c_{pt} &= \frac{1}{en_e}\left(\epsilon_1 - \epsilon_2\right), \\
c_{ptb} &= \frac{\eta_n}{\alpha_n}.
\end{aligned} \tag{5.15}$$

In these equations n_e is the electron number and e is the electron charge. The parameters $\alpha_n, \epsilon_1, \epsilon_2,$ and o are defined according to:

$$
\begin{aligned}
\alpha_n &= \sum_{\beta=1}^{N} \rho_e \nu_{e;n_\beta} + \sum_{\alpha=1}^{N}\sum_{\beta=1}^{N} \rho_i \nu_{i_\alpha;n_\beta}, \\
\alpha_e &= \sum_{\alpha=1}^{N} \rho_e \nu_{e;i_\alpha} + \sum_{\beta=1}^{N} \rho_e \nu_{e;n_\beta}, \\
\epsilon_1 &= \sum_{\beta=1}^{N} \frac{\rho_e \nu_{e;n_\beta}}{\alpha_n} \ll 1, \\
\epsilon_2 &= \sum_{\alpha=1}^{N}\sum_{\beta=1}^{N} \frac{\rho_e \nu_{i_\alpha;n_\beta}}{\alpha_n} \ll 1, \\
o &= \sum_{\alpha=1}^{N}\sum_{\beta=1}^{N} \frac{\rho_\alpha \nu_{i_\alpha;n_\beta}}{\alpha_n} \approx 1.
\end{aligned}
\tag{5.16}
$$

Using the newly derived Ohm's law, Equation 5.13, with Faraday's and Ampere's laws, Equations 1.2 & 1.6, we can derive a generalised induction equation

$$
\begin{aligned}
\frac{\partial \mathbf{B}}{\partial t} = \nabla \times \Bigg[& (\mathbf{u} \times \mathbf{B}) - \eta_O \mu_0 \mathbf{J} + \frac{\eta_H \mu_0}{|\mathbf{B}|} (\mathbf{J} \times \mathbf{B}) + \frac{\eta_A \mu_0}{|\mathbf{B}|^2} ((\mathbf{J} \times \mathbf{B}) \times \mathbf{B}) \\
& - \frac{\eta_p \mu_0}{|\mathbf{B}|} \nabla \mathbf{p_e} - c_{pt} \mathbf{G} - c_{ptb} (\mathbf{G} \times \mathbf{B}) \Bigg].
\end{aligned}
\tag{5.17}
$$

We have a number of terms in addition to the convective term of the non-ideal induction equation, from left to right: 1) Ohmic resistivity, 2) The Hall effect, 3) ambipolar diffusion, 4) Bierman battery, and 5) & 6) pressure gradients. In the solar chromosphere the later terms 4)-6) are many orders of magnitude lower than the Ohmic, Hall effect and ambipolar term at the spatial resolutions used in MHD simulations.

5.1.2 Non-linear Magnetohydrodynamics

In Chapter 1 we studied MHD wave processes in the linear regime. For cases with high perturbation amplitudes the non-linear terms in the MHD equations will become important. Once the wave amplitudes become high enough the waves will distort due to non-linear steepening, caused by differences in the local phase velocity.

Considering the hydrodynamic case, wave solutions to the fluid equations can lead to the development of infinite gradients, see Kulsrud (2005). The non-linear steepening and eventual breakdown of the hydrodynamic equations lead to the formation of a shock. Shocks are dissipative processes that will conserve energy, but not entropy, allowing them to heat the plasma. The shock itself will propagate with a speed $v_s > c_s$, where c_s is the local sound speed.

The formed shock must satisfy a series of jump relations before and after the shock front, known as Rankine-Hugoniot relations, which are derived from conservation laws (Kennel et al., 1989). For a magnetohydrodynamic shock in the $\mathbf{x}$ direction, the subscript T representing a projection onto the shock plane and $[A] = A_2 - A_1$ signifies the difference between the upstream (A_1) and downstream (A_2) values. Rankine-Hugoniot relations can be written as: the conservation of mass

$$[\rho \mathbf{u}_x] = 0, \tag{5.18}$$

the conservation of momentum:

$$\left[\rho \mathbf{u}_x^2 + p + \frac{1}{\mu_0}\mathbf{B}_T^2\right] = 0, \tag{5.19}$$

$$\left[\rho \mathbf{u}_x \mathbf{u}_T + p + \frac{1}{\mu_0}\mathbf{B}_x\mathbf{B}_T\right] = 0, \tag{5.20}$$

the conservation of energy,

$$\left[\frac{\rho \mathbf{u}_x}{2}\left(\mathbf{u}_x^2 + \mathbf{u}_T^2\right) + \frac{\gamma \mathbf{u}_x p}{\gamma - 1} + \left(\frac{1}{2\mu_0}\mathbf{u}\mathbf{B}^2 - \frac{1}{\mu_0}\mathbf{B}\left(\mathbf{B}\cdot\mathbf{u}\right)\right)_x\right] = 0, \tag{5.21}$$

and finally Faraday's law

$$\left[-\left(\mathbf{u}\times\mathbf{B}\right)_T\right] = 0. \tag{5.22}$$

The magnetohydrodynamic Rankine-Hugoniot relations possess six solutions, fast shocks, slow shocks and four types of intermediate shocks (De Hoffmann & Teller, 1950; Lehmann & Wardle, 2016). These solutions come from transitions between the four regions separated by the fast, Alfvén and slow wave speeds. For a fast MHD shock, the Alfvén Mach number $M_A = v_s/v_A > 1$, while for intermediate shock $M_A < 1$, and the sonic Mach number $M = v_s/c_s > 1$. The study of magnetohydrodynamic shocks is more complex than the hydrodynamic ones due to the dependence of the fast and slow wave speeds on the angle between the magnetic field and direction of wave propagation.

5.2 Flux Tube Model

In order to simulate the propagation and dissipation of Alfvénic waves in a vortex-like solar magnetic flux concentration a suitable flux tube model is required. For simulations with the MANCHA code we require a background model in magnetohydrostatic equilibrium. We generate a 3D self-similar Schlüter-Temesváry-like flux tube following the method described in Shelyag et al. (2010); Fedun et al. (2011); Gent et al. (2013). To begin, the background magnetic field $\mathbf{B} = [B_x, B_y, B_z]$ is calculated as

$$B_x = -xB_0(z)G(f)\frac{dB_0(z)}{dz}, \tag{5.23}$$

$$B_y = -yB_0(z)G(f)\frac{dB_0(z)}{dz}, \tag{5.24}$$

$$B_z = B_0^2(z)G(f). \tag{5.25}$$

The two functions, $G(f)$ and $B_0(z)$ describe the opening of the magnetic flux tube with radius, and the distribution of B_z along the flux tube axis respectively. A quadratic polynomial is used for $B_0(z)$, decreasing from 1446 kG at the photosphere to 30 G at 1.8 Mm. The function $G(f)$ is a piecewise continuous quadratic function, with f calculated as

$$f(x, y, z) = \left(x^2 + y^2\right) B_0(z). \tag{5.26}$$

The function $G(f)$ is carefully chosen to give a high field strength and low plasma-β region without giving negative pressures. Field lines of the resulting magnetic flux concentration are shown in Figure 5.1.

The flux tube is embedded in a VALIIIC quiet Sun model (Vernazza et al., 1981). The pressure deficit inside the flux tube is calculated by integrating the horizontal component of the magnetohydrostatic Equation 1.17 from the quiet Sun to the tube centre as

$$\Delta p_x = \int_\infty^0 (\mathbf{J} \times \mathbf{B})_x \, dx, \tag{5.27}$$

$$\Delta p_y = \int_\infty^0 (\mathbf{J} \times \mathbf{B})_y \, dy. \tag{5.28}$$

The density is then calculated from the vertical component of the MHS Equation 1.17,

$$\rho = -\frac{1}{g}\left(\frac{dp}{dz} - (\mathbf{J} \times \mathbf{B})_z\right). \tag{5.29}$$

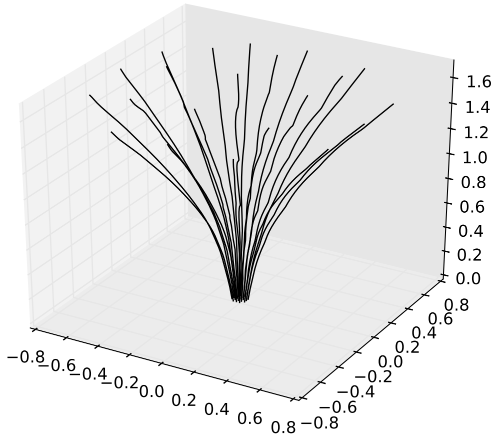

Fig. 5.1: Field lines of the perturbed magnetic flux tube model. The snapshot is taken 250 seconds into a simulation with a 25 mHz acoustic driver placed at the photosphere.

The magnetic field, pressure and density of the resulting flux tube are shown in Figure 5.2. Magnetic field lines are shown in white, and a significant reduction in the pressure and temperature are seen inside the flux tube. The plasma-$\beta = 1$ contour is over-plotted as a dashed black line and shows a region with $\beta < 1$ extending down to about 0.6 Mm.

5.3 Numerical Simulations

We perform simulations of non-linear wave propagation in the flux tube model described above using the MANCHA magnetohydrodynamics code (Felipe et al., 2010). This code solves the non-linear non-ideal MHD equations for perturbations around a background model. The equations of continuity, momentum and energy, as solved by the MANCHA code, are:

$$\frac{\partial \rho_1}{\partial t} + \nabla \cdot \left(\left(\rho_0 + \rho_1 \right) \mathbf{u}_1 \right) = \left(\frac{\partial \rho_1}{\partial t} \right)_{diff}, \tag{5.30}$$

$$\begin{aligned} \frac{\partial \left(\rho_0 + \rho_1 \right) \mathbf{u}_1}{\partial t} + \nabla \cdot \Bigg(\left(\rho_0 + \rho_1 \right) \mathbf{u}_1 \mathbf{u}_1 + \left(p_1 + \frac{\mathbf{B}_1^2}{2\mu_0} + \frac{\mathbf{B}_1 \mathbf{B}_0}{\mu_0} \right) \mathbf{I} \\ - \frac{1}{\mu_0} \left(\mathbf{B}_0 \mathbf{B}_1 - \mathbf{B}_1 \mathbf{B}_0 - \mathbf{B}_1 \mathbf{B}_1 \right) \Bigg) = \rho_1 \mathbf{g} + \left(\frac{\partial \left(\rho_0 + \rho_1 \right) \mathbf{u}_1}{\partial t} \right)_{diff}, \end{aligned} \tag{5.31}$$

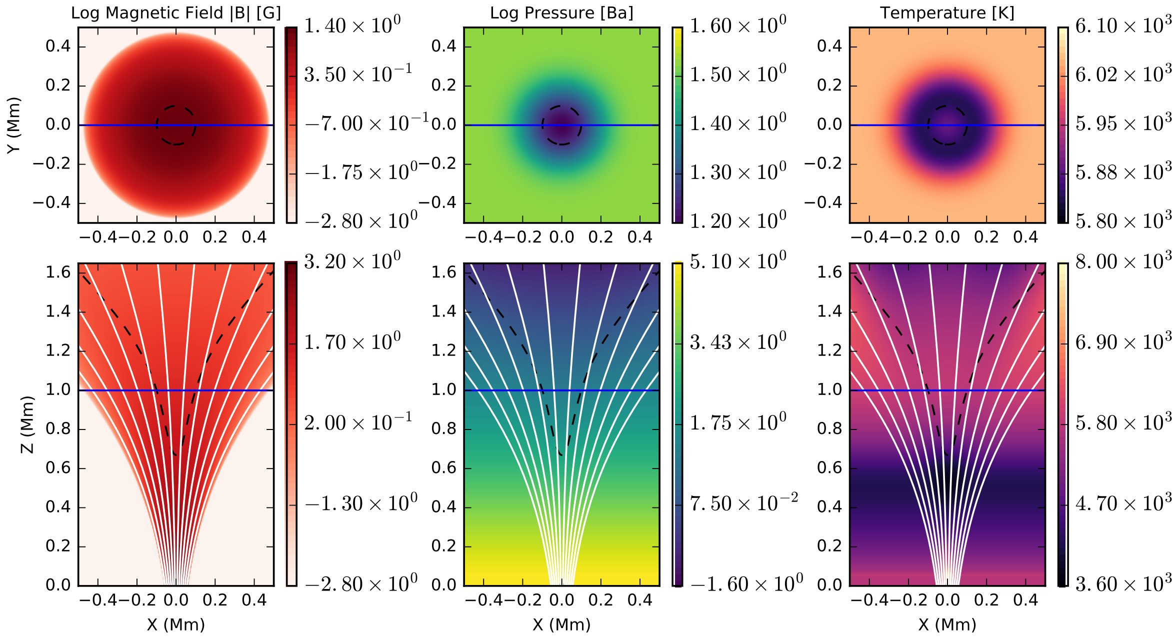

Fig. 5.2: The magnetic field, pressure and temperature of the magnetohydrostatic background model. The blue horizontal line shows the location of the horizontal (bottom) and vertical (top) cuts taken through the domain. The black dashed line shows the $\beta = 1$ contour and magnetic field lines are overlaid in white.

$$\frac{\partial e_1}{\partial t} + \nabla \cdot \left(\mathbf{u}_1 \left(e_0 + e_1 + p_0 + p_1 + \frac{|\mathbf{B}_0 + \mathbf{B}_1|^2}{2\mu_0} \right) - \frac{1}{\mu_0} \left(\mathbf{B}_0 + \mathbf{B}_1 \right) \left(\mathbf{u}_1 \cdot \left(\mathbf{B}_0 + \mathbf{B}_1 \right) \right) \right)$$
$$= \left(\rho_0 + \rho_1 \right) \left(\mathbf{g} \cdot \mathbf{u}_1 \right) + \left(\frac{\partial e_1}{\partial t} \right)_{diff}, \tag{5.32}$$

where we use an ideal equation of state. The terms subscripted with $diff$ are numerical diffusion terms required for numerical stability.

In addition we require a modified induction equation, containing the non-ideal terms derived in section 5.1.1. The solar plasma in the upper photosphere and chromosphere is only weakly ionised, causing a breakdown of the infinite conductivity assumption in ideal magnetohydrodynamics. As the collisional coupling in the solar chromosphere is still strong it is possible to use a quasi-MHD approach rather than solving the multi-fluid equations.

Although the Hall term is significant in the density and magnetic field range considered, it is not a dissipative term, instead introducing a new whistler wave mode and allowing oscillations between the Fast and Alfvén wave modes to occur. In addition, in non-ideal simulations we must place an additional constraint on the time-step;

$$\Delta t_{nonideal} < C_{NI} \frac{\min\left(\Delta x^2, \Delta y^2, \Delta z^2\right)}{|\max\left(\eta_{OR}, \eta_{HE}, \eta_{AD}, \eta_{hyp}\right)|}. \tag{5.33}$$

Here c_{NI} is a nonideal analogue to the CFL condition. The final simulation timestep is then

$$\Delta t = \min\left(\Delta t_{adv}, \Delta t_{diff}, \Delta t_{nonideal}\right). \tag{5.34}$$

The Hall term gives an incredibly restrictive time-step, and does not directly contribute to chromospheric heating through dissipation of Alfvén waves. Therefore, we do not include it in these simulations. However, the Hall term does allow for an additional mechanism with which Alfvén waves can be generated though conversion from fast waves. It will be necessary to incorporate this term in future simulations to provide a complete understanding of the interactions of acoustic waves in the magnetic flux tube.

In the weakly ionised solar plasma the vector **G**, defined by Equation 5.12, is small. The terms which contain **G** are not included. The Bierman battery term is also small in the density and magnetic field regime studied. With these exclusions the generalised Ohm's law and generalised induction equation are simplified to include only the Ohmic and ambipolar terms:

$$\frac{\partial \mathbf{B}}{\partial t} = \nabla \times \left(\mathbf{u}_1 \times (\mathbf{B}_0 + \mathbf{B_1}) - \eta_O \mathbf{J} + \eta_A \frac{(\mathbf{J} \times (\mathbf{B}_0 + \mathbf{B_1})) \times (\mathbf{B}_0 + \mathbf{B_1})}{|B|^2} \right) + \left(\frac{\partial B_1}{\partial t} \right)_{diff}, \tag{5.35}$$

and

$$[\mathbf{E} + \mathbf{u} \times (\mathbf{B}_0 + \mathbf{B_1})] = \eta_O \mathbf{J} - \eta_A \frac{(\mathbf{J} \times (\mathbf{B}_0 + \mathbf{B_1})) \times (\mathbf{B}_0 + \mathbf{B_1})}{|B|^2}. \tag{5.36}$$

In the realistic solar atmosphere small-scale dissipative effects are present. Finite difference schemes, such as that used in the MANCHA code, are unable to resolve these diffusive terms. In order to prevent the growth of instabilities hyperdiffusion terms are used (Caunt & Korpi, 2001; Vögler et al., 2005). These diffusion terms represent viscosity forces in the equations of motion, Joule dissipation in the energy equation and magnetic diffusivity in the induction equation. An additional diffusion term is added to the continuity equation, which has no physical equivalent. These diffusivity coefficients ν are applied to the perturbed variables u for each spatial coordinate x_j,

$$\nu_{x_j}(u) = \nu_{x_j}^{shk}(u) + \nu_{x_j}^{hyp}(u) + \nu_{x_j}^{0}(u) \tag{5.37}$$

The third term is calculated as

$$\nu^0_{x_j} = (c_s + v_A)\,\Delta x_j F(x, y, z), \tag{5.38}$$

where $F(x, y, z)$ is the spatial extent, typically a Gaussian function. The variable diffusion term is calculated as

$$\nu^{hyp}_{x_j}(u) = c_{hyp}(v + c_s + v_A)\Delta x_j \frac{\max_3\left(\Delta^3_{x_j} u\right)}{\max_3\left(\Delta^1_{x_j} u\right)}, \tag{5.39}$$

where $\max_3$ is the maximum value over the cube $(x \pm \Delta x, y \pm \Delta y, z \pm \Delta z)$, $\Delta^3_{x_j}$ is the magnitude of the third derivative, and $\Delta^1_{x_j} u$ the magnitude of the first derivative. Finally, the shock diffusion term is calculated as

$$\begin{aligned} v^{shk}_{x_j} &= c_{shock}\,(\Delta x_j)^2\,|\nabla \cdot \mathbf{v}| && \text{where } \nabla \cdot \mathbf{v} < 0, \\ v^{shk}_{x_j} &= 0 && \text{where } \nabla \cdot \mathbf{v} > 0. \end{aligned} \tag{5.40}$$

These diffusivity coefficients are then introduced into the right hand side of the magnetohydrodynamic equations

$$\left(\frac{\partial \rho_1}{\partial t}\right)_{diff} = \sum_{x_j} \frac{\partial}{\partial x_j}\left(\nu_{x_j}\left(\rho_1 \frac{\partial \rho_1}{\partial x_j}\right)\right), \tag{5.41}$$

$$\left(\frac{\partial (\rho_0 + \rho_1)\mathbf{v_1}}{\partial t}\right)_{diff} = \nabla \cdot \tau, \tag{5.42}$$

$$\left(\frac{\partial \mathbf{B}_1}{\partial t}\right)_{diff} = -\nabla \times \epsilon, \tag{5.43}$$

$$\left(\frac{\partial e_1}{\partial t}\right)_{diff} = \nabla \cdot (\mathbf{v}_1 \tau) + \nabla \cdot (\mathbf{B}_1 \times \epsilon)\,. \tag{5.44}$$

Here τ is a numerical equivalent to the viscosity tensor,

$$\tau = \frac{1}{2}\,(\rho_0 + \rho_1)\left(\nu_{x_i}\left(v_{1x_j}\right)\frac{\partial v_{1x_j}}{\partial x_i} + \nu_{x_j}\left(v_{1x_i}\right)\frac{\partial v_{1x_i}}{\partial x_j}\right). \tag{5.45}$$

Finally, ϵ represents the diffusion of magnetic field,

$$\epsilon = \begin{pmatrix} \nu_y (B_{1z}) \frac{\partial B_{1z}}{\partial y} - \nu_z (B_{1y}) \frac{\partial B_{1y}}{\partial z} \\ \nu_z (B_{1x}) \frac{\partial B_{1x}}{\partial z} - \nu_x (B_{1z}) \frac{\partial B_{1z}}{\partial x} \\ \nu_x (B_{1y}) \frac{\partial B_{1y}}{\partial x} - \nu_y (B_{1x}) \frac{\partial B_{1x}}{\partial y} \end{pmatrix}. \tag{5.46}$$

5.4 Results

The Equations 5.30 - 5.32 & 5.35 are solved with the MANCHA numerical code, as described in Section 5.3. The non-ideal effects are modelled using a single fluid quasi-MHD approach as described in Section 5.1.1. The Message Passing Interface (MPI) is used for parallelisation to increase computational speed. Spatial derivatives are calculated using the fourth order scheme of Vögler et al. (2005) and temporal integration is performed using a fourth-order Runge-Kutta method.

For our simulations in the flux tube model of Section 5.2 we use a resolution of $\Delta x = \Delta y = \Delta z = 10$ km with $n_x = n_y = 300$ and $n_z = 186$. This gives a domain of 1.5 Mm radius around the flux tube centre and extending from the photosphere up to 1.86 Mm into the solar atmosphere. To stabilise the simulation we use the constant artificial diffusion formulation with $c_0 = 0.024$ and a Gaussian distribution with a FWHM of $10\Delta x$. The hyperdiffusive shock term is included, with the coefficient $c_{shock} = 1.0$. In addition to the hyperdiffusion terms, filtering is performed every 0.9 s, using the filter described in Parchevsky & Kosovichev (2007).

Berenger perfectly matched layers (PML) (Berenger, 1994) are employed to efficiently absorb incoming waves. The PMLs are formulated as described in Parchevsky & Kosovichev (2007), which is equivalent to the (cPML) described in Section 1.3.4 with $\kappa = 1$, $N = 2$ and the convolution term $\alpha = 0$. We use a 10-point PML on the horizontal boundaries with a strength of 1.0. On the upper boundary we employ a 15-cell PML with a strength of 3.0 and the ambipolar diffusion is masked in the top 17 cells. In addition a Gaussian of enhanced numerical diffusion ($\mu = 1.81$ Mm$, \sigma = 40$ km) is added at the beginning of the PML. These upper boundary conditions are chosen to efficiently damp outgoing waves while leaving the region up to 1.65 Mm untouched.

The bottom boundary employs self-consistent perturbations of velocity, pressure and density as prescribed by Mihalas & Weibel-Mihalas (1999). These are used to excite fast waves given the following prescription

$$\Delta v_z = V_0 \exp\left(\frac{z}{2H_p} + k_{zi}z\right) \sin\left(\omega t - k_{zr}z\right), \tag{5.47}$$

$$\frac{\Delta p}{p_0} = V_0|P| \exp\left(\frac{z}{2H_p} + k_{zi}z\right) \sin\left(\omega t - k_{zr}z + \phi_P\right), \tag{5.48}$$

$$\frac{\Delta \rho}{\rho_0} = V_0|R| \exp\left(\frac{z}{2H_p} + k_{zi}z\right) \sin\left(\omega t - k_{zr}z + \phi_R\right), \tag{5.49}$$

where V_0 is the pulse amplitude, and H_p is the pressure scale height. No perturbation is applied to the magnetic field or horizontal velocity components. The vertical wave number is given by

$$k_z = k_{zr} + ik_{zi} = \frac{\sqrt{\omega^2 - \omega_c^2}}{c_s}, \tag{5.50}$$

with real and complex parts k_{zr} and k_{zi}. The wave frequency is given by ω, and $\omega_c = \gamma\nu/2c_s$. The relative amplitude and phase of the pressure $(|P|, \phi_P)$ and density $(|R|, \phi_R)$ perturbations are:

$$|P| = \frac{\gamma}{\omega}\sqrt{k_{zr}^2 + \left(k_{zi} + \frac{1}{2H_p}\frac{\gamma - 2}{\gamma}\right)^2}, \tag{5.51}$$

$$|R| = \frac{1}{\omega}\sqrt{k_{zr}^2 - \left(k_{zi} + \frac{1}{2H_p}\right)^2}, \tag{5.52}$$

$$\phi_P = \arctan\left(\frac{k_{zi}}{k_{zr}} + \frac{1}{2H_p k_{zr}}\frac{\gamma - 2}{\gamma}\right), \tag{5.53}$$

$$\phi_R = \arctan\left(\frac{k_{zi}}{k_{zr}} - \frac{1}{2Hk_{zr}}\right). \tag{5.54}$$

First we perform a proof-of-concept test of the dissipation of Alfvén waves through ion-neutral diffusion, using an acoustic driver placed near the flux tube axis. We choose a driver period of 40 seconds ($\eta = 25$ mHz), and an amplitude of 500 $\mathrm{m\,s^{-1}}$ representing a typical photospheric motion. The pulse is located 100 km away from the flux tube axis with the horizontal extent represented by a Gaussian with $\sigma_{x,y} = 100$ km. The simulation is run for ≈ 350 s, after which wave heating causes instabilities in the upper PML.

For an ideal MHD simulation of the flux tube model with no external perturbation, the only changes are from the numerical resistivity. This will be small in the magnetohydrostatic equilibrium of the background model. However, if non-ideal effects are included, the dissipation of static currents will lead to changes in the thermodynamic variables driving flows and waves inside the flux tube. We run three simulations to disambiguate the changes in the flux tube caused by waves, dissipation of static currents through ion-neutral interactions and dissipation of the wave motions through ion-neutral interactions. In the first simulation (A), the only perturbation is through the inclusion of the ambipolar diffusion term. The second simulation (W) includes perturbation by the acoustic wave driver described above, but does not include non-ideal terms. The final simulation (AW) includes both ambipolar diffusion and the acoustic wave driver.

The acoustic source used in this simulation lies well below the $c_s/v_A = 1$ equipartition layer and generates fast acoustic waves. These waves travel upwards until they hit the equipartition layer, where they undergo mode conversion. This leads to splitting of the wave energy, with some being converted from fast acoustic waves into fast magnetic waves and the rest is transmitted from fast acoustic waves into slow acoustic waves. As the fast magnetic wave travels in the interior of the flux tube, where $c_s/v_A < 1$, conversion to Alfvén waves occurs.

In order to view different wave modes present in the flux tube we decompose the velocity and magnetic field perturbations into fast, longitudinal and Alfvén components. The wave components are calculated by projecting the perturbations from the computational domain into three characteristic directions with respect to the background magnetic field direction (Khomenko & Cally, 2012; Santamaria et al., 2015). The vectors for the fast, longitudinal and Alfvén wave components are defined as

$$\mathbf{e}_{\text{long}} = [\cos\phi\sin\theta,\ \sin\phi\sin\theta,\ \cos\theta], \tag{5.55}$$

$$\mathbf{e}_{\parallel} = [\sin\phi,\ -\cos\phi, 0], \tag{5.56}$$

$$\mathbf{e}_{\perp} = [\cos\phi\cos\theta,\ \sin\phi\cos\theta,\ -\sin\theta], \tag{5.57}$$

where θ and ϕ represent the inclination and azimuthal angles of the magnetic field vector. These three projections will only correctly disambiguate the wave modes in regions where $v_A > c_s$. In Figure 5.3 the three projections are shown for an example magnetic field. In a low-β plasma the slow wave velocity perturbation is directed along the background magnetic field (See Figure 1.1). It is extracted using a vector pointing in the direction of the background magnetic field ($\mathbf{e}_{\text{long}}$). The Alfvén wave is extracted using the second vector $\mathbf{e}_{\parallel}$, which is directed perpendicular to the background magnetic field. The final vector $\mathbf{e}_\perp$ is perpendicular to the first two vectors and will extract the fast wave component.

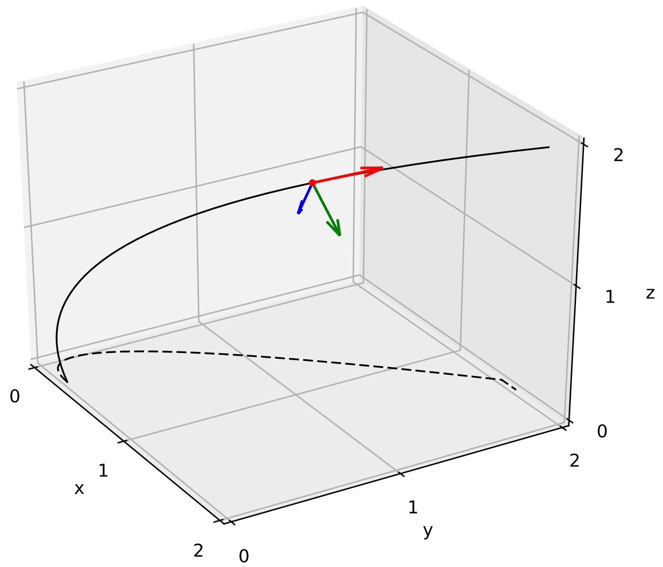

Fig. 5.3: The three projections used to decompose velocity and magnetic field perturbations into the different wave components. The solid black line shows a magnetic field line. The three projections are then calculated at a point on the field line, the red arrow shows the direction which extracts the slow component ($\mathbf{e}_{\rm long}$), the blue arrow the direction for the Alfvén component ($\mathbf{e}_\parallel$) and the green arrow the direction for the fast component ($\mathbf{e}_\perp$).

The three different wave components are plotted in Figure 5.4, after 150 seconds and 250 seconds of simulation. The slow wave ($\mathbf{e}_{\rm long}$, left column), the Alfvén wave ($\mathbf{e}_\parallel$, middle column), and the fast wave ($\mathbf{e}_\perp$, right column) are shown, calculated using Equations 5.55-5.57. After 150 seconds the first wavefronts are beginning to reach the upper chromosphere of the flux tube. The waves can be seen to reach amplitudes as high as $6-8$ km s^{-1} leading to the formation of shocks. These shocks significantly deform the $\beta = 1$ contour of the flux tube. After 250 seconds a number of shock fronts have passed through the upper chromosphere further perturbing the flux tube from its equilibrium state.

Without the inclusion of ambipolar diffusion, heating by waves in the magnetic flux tube occurs due to dissipative processes. In ideal MHD the only dissipative terms are those introduced by the numerical diffusion. The shocks that form as the waves steepen in the low density, upper chromospheric regions of the flux tube will lead to strong heating of the plasma as the plasma is compressed by the shock wave. In

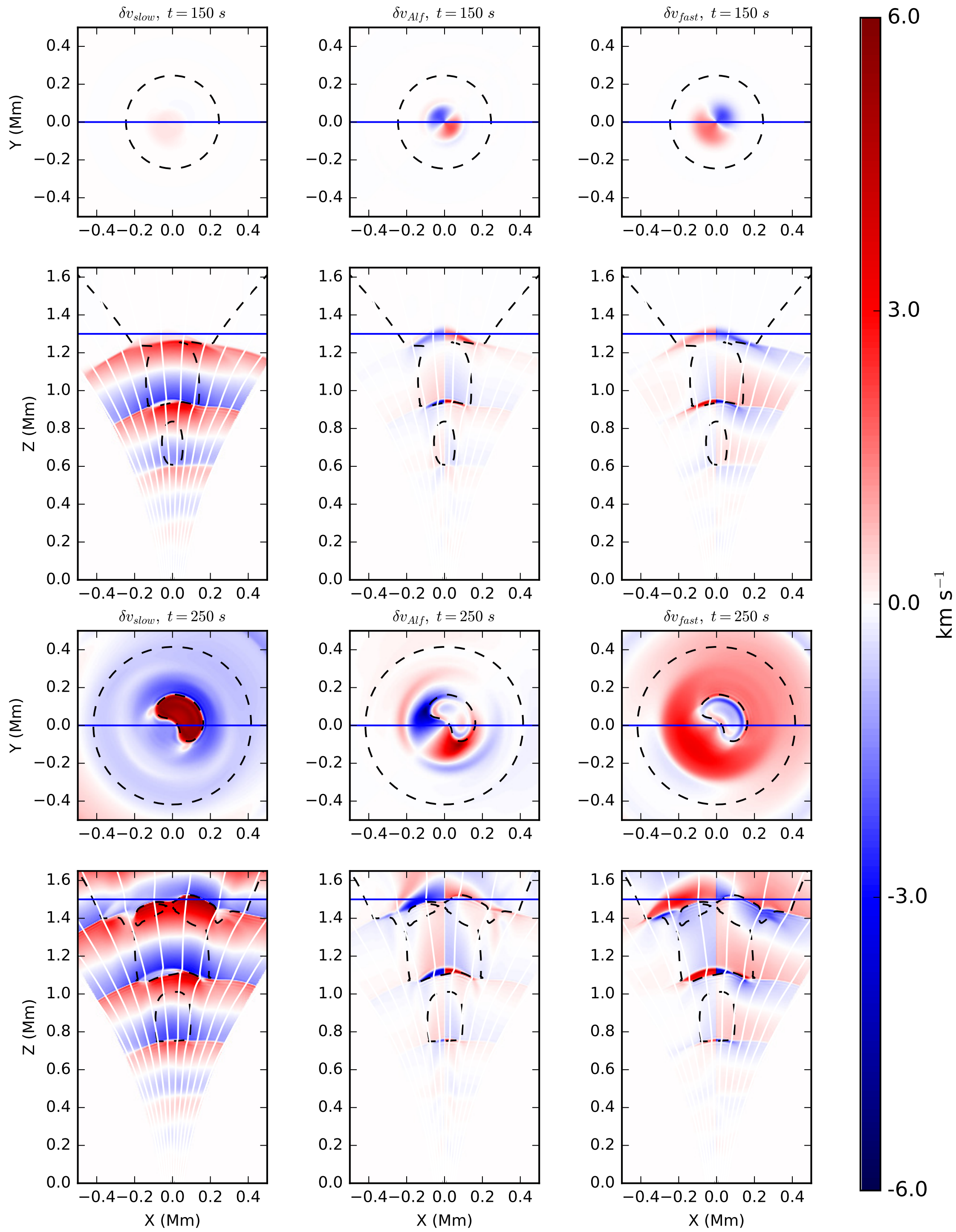

Fig. 5.4: Snapshot of the waves excited in the magnetic flux tube by an acoustic driver of frequency 25 mHz placed at the photosphere. The panels show (from left to right): the slow, Alfvén and fast wave modes. The top panel is taken after 150 seconds of simulation time and the bottom panel after 250 seconds. Horizontal cuts are taken at 1.5 Mm above the photosphere, and vertical cuts are taken through the centre of the sunspot (0 Mm). The wave components are calculated by projecting the velocity perturbations onto the background magnetic field using Equations 5.55-5.57.

addition, ion-neutral interactions gives another source of heating. We wish to quantify the changes in the thermal, kinetic and magnetic energy when ambipolar diffusion is included in the simulations. In order to study this, the magnetic, thermal and kinetic energy densities are calculated according to

$$E_{mag} = \frac{|B|^2}{2\mu_0}, \tag{5.58}$$

$$E_{kin} = \frac{\rho v^2}{2}, \tag{5.59}$$

$$E_{therm} = \frac{p}{\gamma - 1}, \tag{5.60}$$

where the total energy is

$$E_{tot} = E_{mag} + E_{kin} + E_{therm}. \tag{5.61}$$

The energies are calculated for each snapshot, and averaged over a volume around the flux tube centre. For each component the background energy is then subtracted to give the perturbation from the background state. We calculate each of these energies and average them over a region of the flux tube interior, with radius $r = 50$ km and a height range from $1 - 1.65$ Mm. These values are shown in Figure 5.5, for each of the A, W, and AW simulations.

The top panel of Figure 5.5 shows the energy for simulation A, with no wave perturbation included. The magnetic energy decreases and the thermal energy increases, this represents dissipation of static currents in the flux tube.

The simulations that include a wave driver (middle two panels of Figure 5.5) show a large oscillating perturbation in the thermal energy. The thermal fluctuations are about an order of magnitude higher than those of the kinetic energy, and the thermal energy steadily increases over the simulation. The increase in thermal energy is offset by a steady decrease in the magnetic energy in the wave equations. To quantify the heating due to dissipation of magnetoacoustic waves through ion-neutral interactions the difference in energy perturbations $\Delta E^{AW} = E^{AW} - E^{W} - E^{A}$ is calculated and plotted in the bottom panel of Figure 5.5. Ion-neutral damping of the waves increases the thermal energy and decreases the magnetic energy. The increase in the thermal energy is a factor of 20 higher than from the dissipation of static currents E^{A} (top panel).

In the bottom panel of Figure 5.5 there is a difference between the thermal energy gain and the sum of the magnetic and kinetic energy loss. This apparent generation of energy is due to the fact that the energy curves produced and plotted do not reflect the whole picture. There are several processes entering the domain in which the averaging is performed, and it is difficult to separate. In controlled wave experiments, with no Poynting flux entering or leaving the domain, good convergence is found.

Inside the flux tube magnetohydrodynamic waves carry energy upwards into the chromosphere. Any additional heating through dissipation of these wave motions by ambipolar diffusion should be evident as a reduction in the energy carried by fast and Alfvén waves. In order to compare the magnetic energy flux inside the magnetic field concentration we calculate the Poynting flux

$$\mathbf{F_{mag}} = -\frac{1}{4\pi}\mathbf{B} \times (\mathbf{v} \times \mathbf{B})\,. \tag{5.62}$$

Comparison of the upwards energy flux is performed by taking the z-component of the Poynting flux with height and averaging it. Spatial averaging is performed over a region of radius 250 km around the flux tube centre and temporal averaging is performed over two wave periods from $250 - 330$ seconds of the simulation. In Figure 5.6 the vertical Poynting flux is shown as F^W, for the wave simulation, and as F^{AW}, corresponding to the simulation with both ambipolar diffusion and the wave driver.

The photospheric driver is located slightly off-axis of the flux tube model. The maximum Poynting flux reached is 4×10^5 erg cm^{-2} s^{-1} at 200 km above the photosphere. For the first 800 km the Poynting flux for the wave simulation (red curve) and the ambipolar and wave simulation (black curve) are identical. Above this height the energy flux in the two simulations differs. The difference between the two curves grows slowly until 1500 km, at which point the vertical flux in the ambipolar simulations greatly decreases. The Poynting flux absorption is calculated as $1 - F_{AD}/F^W$ and shows a gradual increase to 0.4 at 1400 km before sharply increasing to 0.95 at 1650 Mm. This represents an almost total absorption of the Poynting flux.

5.4.1 Resolution Dependence

Ambipolar diffusion has a small length scale. In order to test that it is properly resolved in our simulations we wish to increase the resolution and study the impact this has on the simulated wave behaviour. The numerical diffusivities present in the simulation also scale with resolution, so an increased resolution will allow us to check

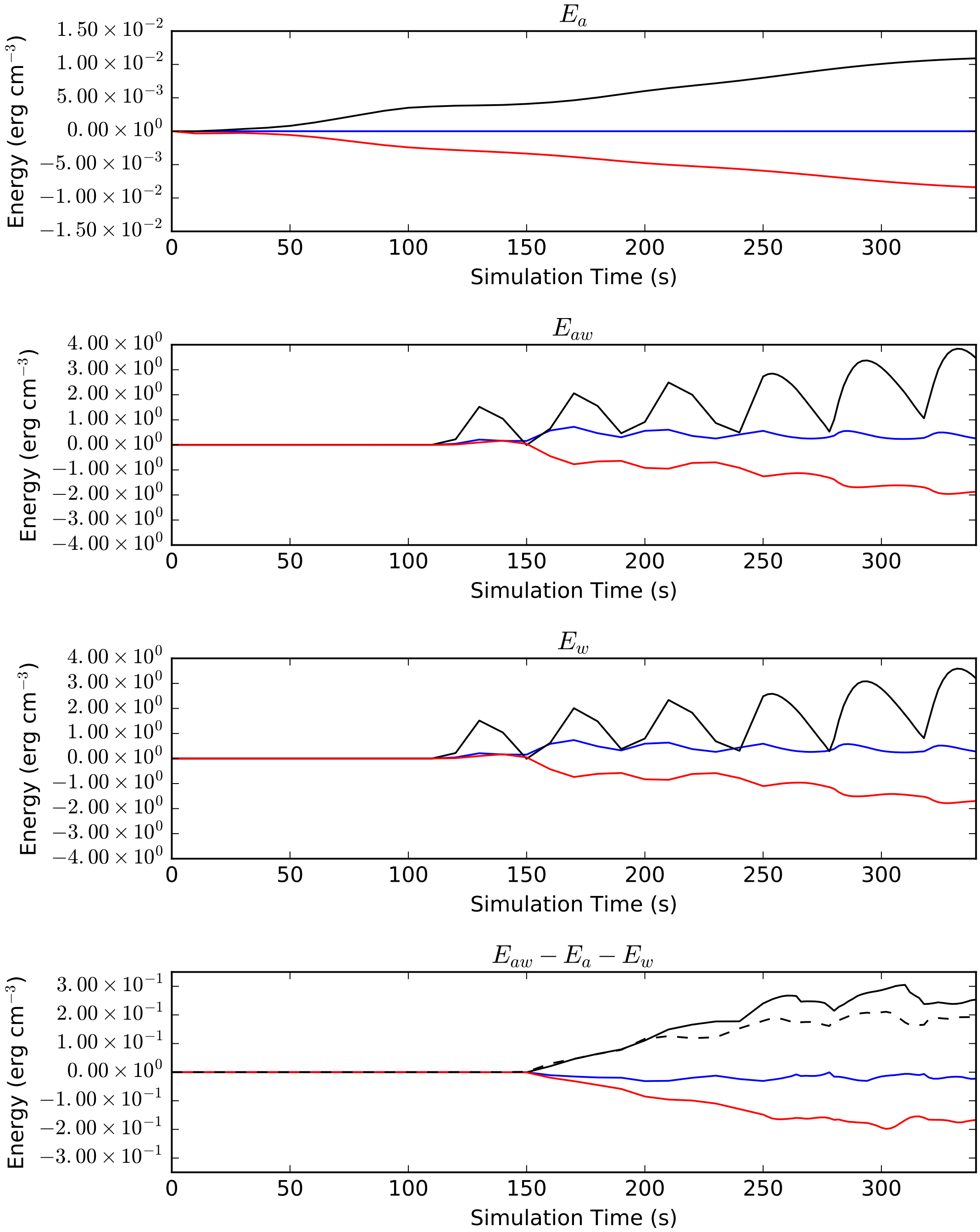

Fig. 5.5: Averaged energy perturbation from the background value. Averaging is performed over a radius of 50 km and a height range of $1-1.65$ Mm in the flux tube. The magnetic (red), kinetic (blue) and thermal (black) energies are shown. The four panels show, from top to bottom, energy perturbations of: the simulation including only the ambipolar term (A), the simulation which includes an acoustic wave driver (W) described above, and the simulation with both the wave driver and the ambipolar term (AW). The energy perturbation caused by ambipolar diffusion damping the waves ($\Delta E^{AW} = E^{AW} - E^{W} - E^{A}$) is shown in the bottom panel. The black dashed line shows the absolute value of the sum of the kinetic and magnetic energies.

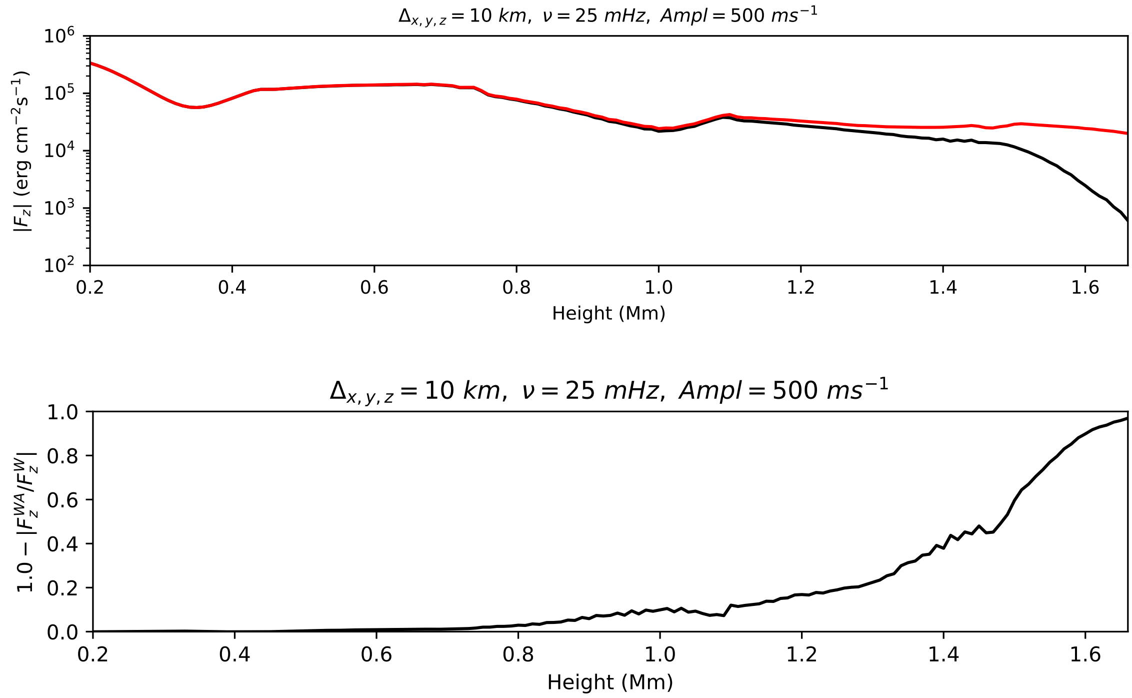

Fig. 5.6: The change with height of the vertical component of the Poynting flux $\mathbf{F_{mag,z}}$, calculated with Equation 5.62. Left panel: the vertical component of the Poynting flux for the wave perturbation simulation (F^W, red) and the simulation with both the wave source and ambipolar diffusion term (F^{AW}, black). For each vertical point, the Poynting flux is averaged over a disk of radius 250 km around the centre of the flux tube and from 250 to 330 seconds of simulation time. Right: the Poynting flux absorption through the inclusion of ambipolar diffusion, calculated as $1 - F^{AW}/F^{W}$.

the observed heating is not caused by the numerical diffusion terms. Finally, simulation with a higher frequency source will require higher resolution to adequately resolve the magnetohydrodynamic waves.

In order to determine whether the dissipation of Poynting flux and heating rate are resolution dependant, we double the simulation resolution. The flux tube model described in Section 5.2 above is recalculated with a resolution of $\Delta x = \Delta y = \Delta z =$ 5 km, $n_x = n_y = 600$ and $n_z = 360$. The resulting model differs slightly, as integrating Equations 5.27 - 5.29 with a higher resolution gives a more accurate pressure and density.

The numerical setup is identical to that described above, with the exception of the boundary conditions. We increase the PML at the top of the domain to 17 cells with a strength of 3.0, and the horizontal PML's to 40 cells with a strength of 1.0. The enhanced diffusion profile is identical to that in the lower resolution simulation above ($\mu = 1.81$ Mm, $\sigma = 40$ km) and ambipolar mask is set to 23 cells, so that the region up to 1.65 Mm is not influenced by the boundary conditions.

To test the dependence on resolution we recalculate the kinetic, magnetic and thermal energy for each of the three simulations (A, W, and WA). The energy perturbations are shown in Figure 5.7, using the same method and layout as Figure 5.5. A few differences can be seen in the energy curves. For simulations with only ambipolar diffusion (A) perturbing the MHS equilibrium, a small decrease is found in the magnetic energy loss, and kinetic energy gain. This is likely caused by an improvement in the magnetohydrostatic equilibrium when generating the flux tube at a higher resolution.

The simulation of wave heating, (AW) shows a slight increase in conversion to thermal energy. This increase is smaller in the (W) simulations. The impact of resolution on the dissipation of wave energy through ambipolar diffusion ($AW - A - W$), is seen in the bottom panels of Figures 5.5 and 5.7. The doubling in resolution leads to an increase in the dissipation of wave energy, by a factor of 1.2. As this increase is reasonably small, the ambipolar diffusion processes are adequately resolved in the 5 km simulation.

The recalculated mean Poynting flux $\mathbf{F_{mag}}$, and the absorption coefficient $1 - F_z^{AW}/F_z^{W}$ are shown in Figure 5.8. Comparison of this to the 10 km simulation (Figure 5.6) show around a 20% increase in the mean Poynting flux F_z at 200 km and a 50% increase in the flux reaching the upper boundary in the wave simulation F_z^W. A similar increase is seen in F_z^{WA} giving a minor decrease (2%) in the Poynting flux absorbed at

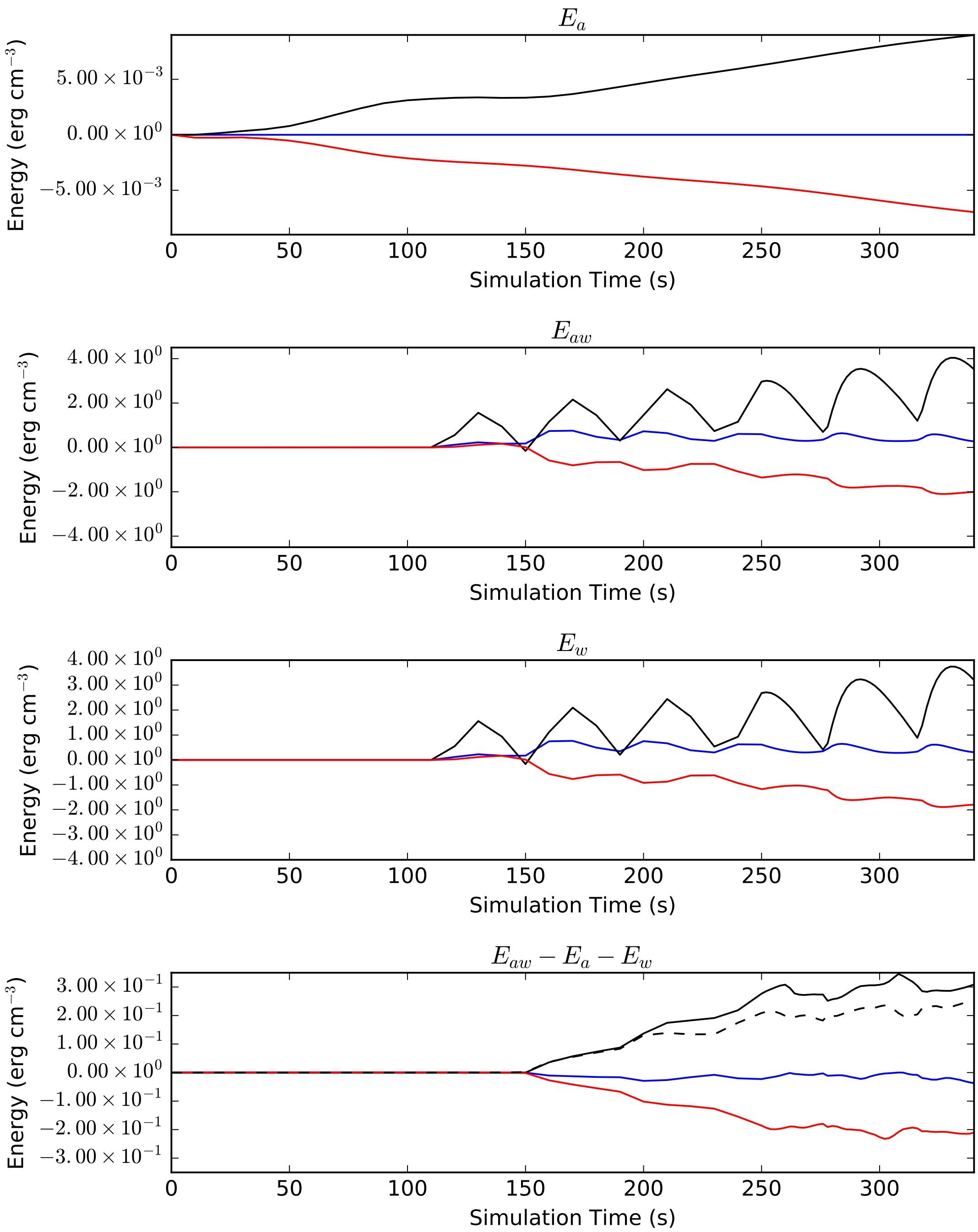

Fig. 5.7: Averaged energy perturbation from the background value, averaging is performed over the same volume as in Figure 5.5. The magnetic (red), kinetic (blue) and thermal (black) energies are shown. The layout of the four panels are the same as in Figure 5.5.

1.65 Mm when the resolution is doubled. When the resolution is increased to 5 km, the difference in two simulations is not significant until around 1.1 Mm, compared to about 0.8 Mm in the original 10 km simulation. The region in which the wave energy is dissipated due to the inclusion of ambipolar diffusion is limited to a smaller section of the upper chromosphere.

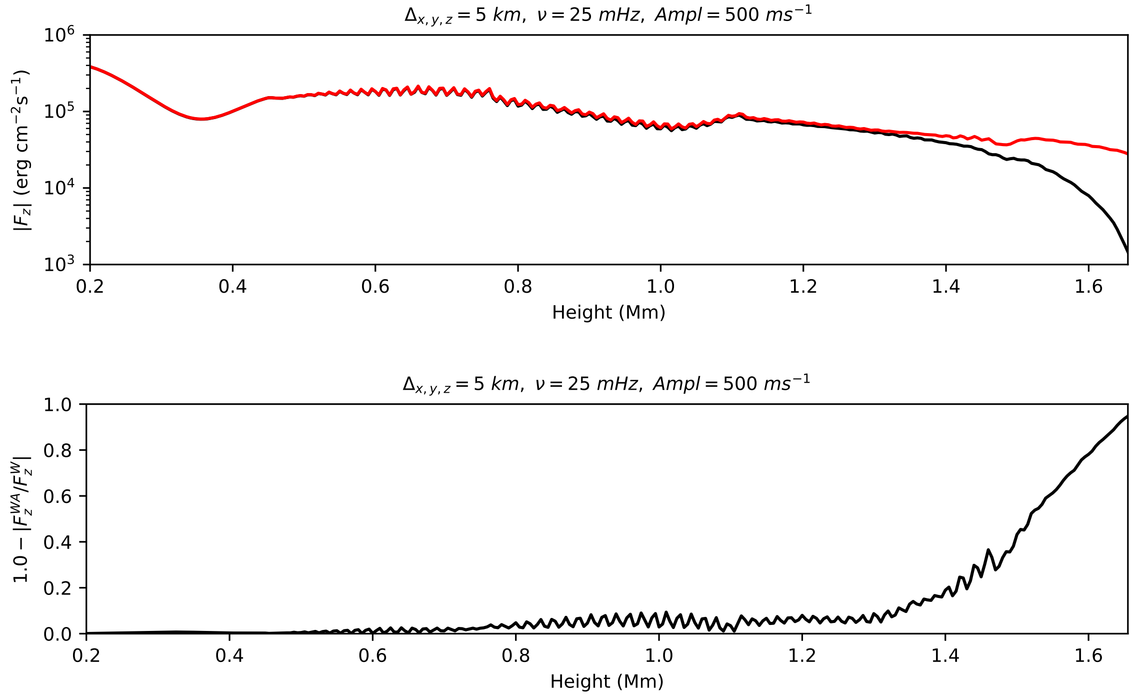

Fig. 5.8: Poynting flux absorption in the flux tube for the 5 km resolution simulation. Left panel: the vertical component of the Poynting flux for the wave perturbation simulation (F^W, red) and the simulation with both the wave source and ambipolar terms (F^{AW}, black). The Poynting flux is averaged as in Figure 5.6. Right Panel: The Poynting flux absorption with height, calculated as $1 - F^{AW}/F^W$.

5.4.2 Driver Amplitude

In order to study the importance of non-linear terms, a number of simulations are performed with varying driver amplitude. Simulations are run at 25 mHz with driver amplitudes of $5\ \mathrm{m\,s^{-1}}$, $50\ \mathrm{m\,s^{-1}}$, and $250\ \mathrm{m\,s^{-1}}$ in addition to the unperturbed and $500\ \mathrm{m\,s^{-1}}$ simulations already performed. The model and simulation setup are identical to the simulation performed in Subsection 5.4.1 above.

The dependence of the flux tube heating term $\eta_A J_\perp$ on the driver amplitude is shown in Figure 5.9. The top-left panel shows the term in the unperturbed background model. The remaining panels show simulation snapshots after 250 s. Comparison of the unperturbed value to the ambipolar simulation (top-left panel) shows no discernible evolution of the heating term. The top-right panel of the figure shows the heating from the 5 $\mathrm{m\,s^{-1}}$ amplitude source. Moderate heating can be seen in the upper layers of the chromosphere, above 1 Mm, mostly in the walls of the flux tube.

Strong heating, with values of $\eta_\perp J$ above 10^{10}, is not seen until the driver amplitude is increased to 50 $\mathrm{m\,s^{-1}}$ (bottom-left panel). This occurs as shocks begin to form above 1.4 Mm. As the driver amplitude is further increased to 250 $\mathrm{m\,s^{-1}}$ (bottom-centre), and 500 $\mathrm{m\,s^{-1}}$ (bottom-right), the shocks lead to a significant perturbation of the flux tube. Large values of $\eta_\perp J$ are seen down as low 0.5 Mm where the shocks begin to form. The heating also becomes spread over much larger regions of the flux tube. The regions of strong heating can be seen to coincide with the regions of $\beta < 1$ in between the shock fronts.

The change in height at which high values of the ambipolar heating term are seen should correspond to Poynting flux decrease through current dissipation. We plot the averaged Poynting flux for each of the different amplitude sources in Figure 5.10 (the process used is the same as that used for Figure 5.8). At 5 $\mathrm{m\,s^{-1}}$ (top-panel) the ambipolar term significantly changes the Poynting flux over the majority of the domain, though no significant region of reduction is evident. These differences could be caused larger by variation due to the diffusive terms, both ambipolar and numerical, at the low wave amplitudes. By performing simulations using the linearised version of the MANCHA code we are investigating the differences seen at low simulation amplitudes.

When the driver amplitude is increased to 50 $\mathrm{m\,s^{-1}}$ (second panel), a decrease in the Poynting flux is found between the two simulations above about 1.3 Mm. This corresponds to the regions of the upper chromosphere at which a high $\eta_A J_\perp^2/\rho$ is seen in Figure 5.9. The values of F_z^{WA} and F_z^{W} never deviate significantly. The largest value of the Poynting flux absorption in the 50 $\mathrm{m\,s^{-1}}$ simulation is $1 - F^{AW}/F^{W} = 0.2$.

For high driver amplitudes, 250 $\mathrm{m\,s^{-1}}$ (third panel) and 500 $\mathrm{m\,s^{-1}}$ (bottom panel), the inclusion of ambipolar diffusion leads to a sustained reduction in the Poynting flux throughout the upper chromosphere, above 1.0 Mm. The reduction grows significantly above 1.4 Mm, and at the top of the domain (1.65 Mm) the absorption is $1 - F^{AW}/F^{W} = 0.86$ for a driver amplitude of 250 $\mathrm{m\,s^{-1}}$ and $1 - F^{AW}/F^{W} = 0.94$ for 500 $\mathrm{m\,s^{-1}}$. These results suggest that non-linear processes are important for efficient absorption of Poynting flux. Once the wave amplitude becomes high enough, the perturbation of the flux tube leads to only a small fraction of the Poynting flux reaching

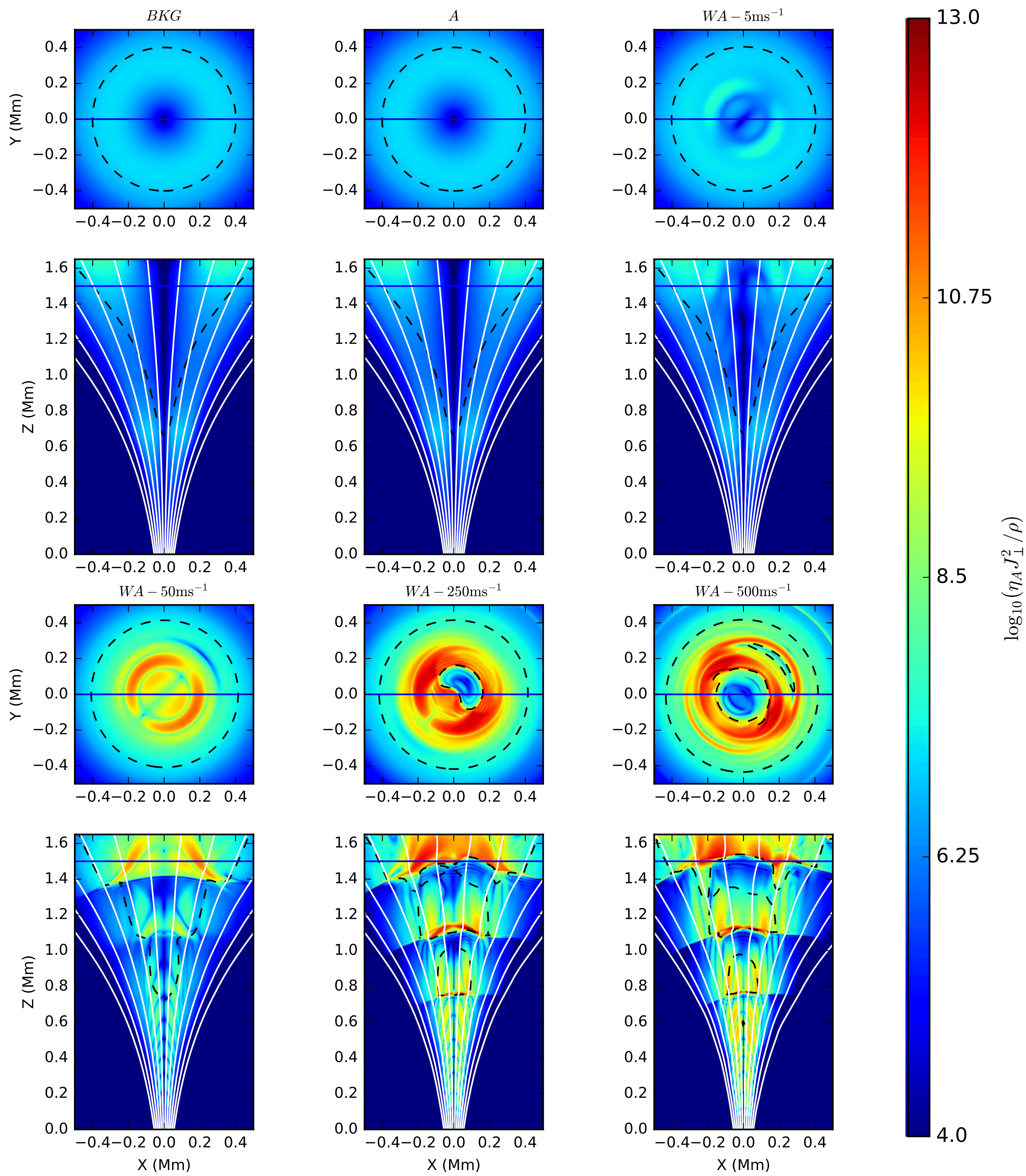

Fig. 5.9: The ambipolar heating term $\eta_A J_\perp^2/\rho$. The horizontal slice is taken at 1.5 Mm above the photosphere, and the vertical slice is taken through the centre of the flux tube. The top-left panel shows the background model, the middle-left to bottom-right panels show simulations after 250 seconds perturbed by: only the ambipolar term, and a wave driver at 5 $\mathrm{m\,s^{-1}}$, 50 $\mathrm{m\,s^{-1}}$, 250 $\mathrm{m\,s^{-1}}$, and 500 $\mathrm{m\,s^{-1}}$. The field lines are over-plotted in white, and the $\beta = 1$ contours in dashed black.

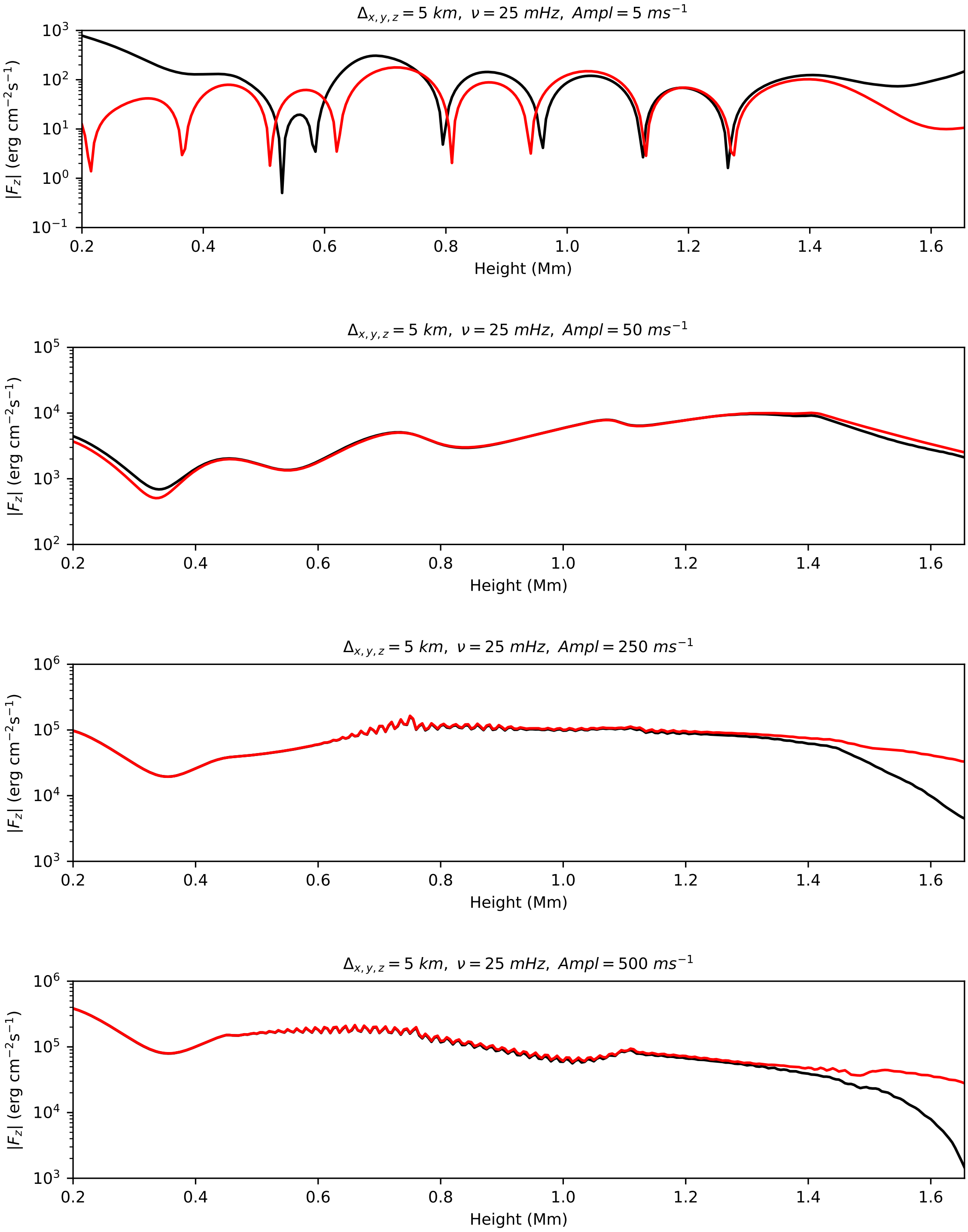

Fig. 5.10: Vertical Poynting flux, for simulations of varying amplitude. From top to bottom, 5 $\mathrm{m\,s^{-1}}$, 50 $\mathrm{m\,s^{-1}}$, 250 $\mathrm{m\,s^{-1}}$, 500 $\mathrm{m\,s^{-1}}$. The layout is the same as the left panel of Figure 5.6,with F^W the red line, and F^{AW} the black line.

the upper boundary. In these simulations this point lies somewhere between 50 $\mathrm{m\,s^{-1}}$ and 250 $\mathrm{m\,s^{-1}}$.

5.4.3 Frequency Dependence

Acoustic $p-$modes are generated by near-surface convection. These turbulent motions generate waves at a large range of frequencies. Although higher frequencies are expected to heat more efficiently, there is less power in these waves due to velocity power spectrum following a power law. In order to test the impact of driver frequency on the heating of chromospheric plasma we run simulations at $\nu = 100, 50, 25$ and 12.5 mHz (periods of $10, 20, 40,$ and 80 s). Frequencies higher than 100 mHz have not been tested, as they are not sufficiently resolved by the 5 km grid. In order for the 12.5 mHz simulation to remain stable for 350 s, the simulation amplitude is reduced to 250 $\mathrm{m\,s^{-1}}$. This amplitude was shown to be high enough to produce significant damping of the Poynting flux in the simulation with a 25 mHz driver in Subsection 5.4.2.

In these simulations we average the Poynting flux over the period from 250 to 330 seconds, to capture one entire period of the 12.5 mHz wave. A spatial averaging radius of 250 km is used. Figure 5.11 shows the Poynting flux with height for each of the four frequencies. In Figure 5.12 we show the Poynting flux absorption $1 - F_z^{AW}/F_z^{W}$.

The dependence of the Poynting flux absorption on frequency shows a maximum absorption at 25 mHz of $1 - F_z^{AW}/F_z^{W} = 0.86$. The lower frequency 12.5 mHz driver begins to absorb Poynting flux at a lower height than at 25 mHz. The reduction in Poynting flux at the top of the box is not as high as 25 mHz, although it still reaches a significant $1 - F_z^{AW}/F_z^{W} = 0.65$. Surprisingly, absorption in the higher frequencies is also lower, reaching $1 - F_z^{AW}/F_z^{W} = 0.52$ at 50 mHz and $1 - F_z^{AW}/F_z^{W} = 0.31$ at 100 mHz.

In order to understand the reduced heating at higher frequencies, we study the relationship between ambipolar heating term and the fast and Alfvénic magnetic field perturbations. Histograms of δB_{fast} and δB_{Alf} versus $\eta_A J_\perp^2/\rho$ are plotted in Figure 5.13. These magnetic field components are calculated through projection in the direction given by Equations 5.55-5.57. For a driver amplitude $A = 250$ $\mathrm{m\,s^{-1}}$ a normalised histogram is made for each of the four frequencies at two simulation snapshots. The left two columns show a snapshot after 150 s and the right two columns show 300 s.

After 150 s of simulation time the first shock waves are starting to reach the upper

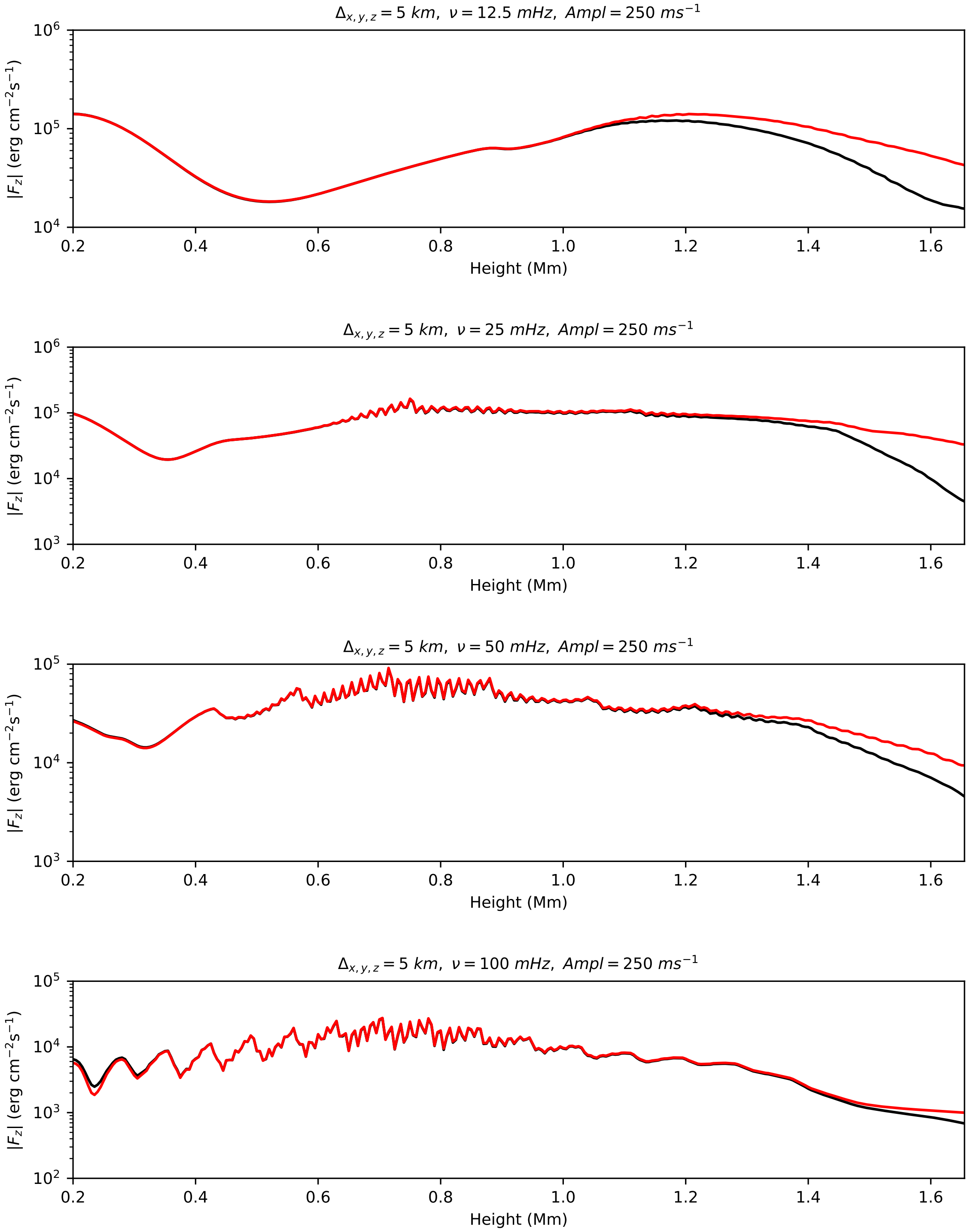

Fig. 5.11: Dependence of vertical Poynting Flux on with height for simulations with an acoustic driver of frequency 12.5 mHz, 25 mHz, 50 mHz and 100 mHz (from top to bottom), with F^{W} the red line, and F^{AW} the black line.

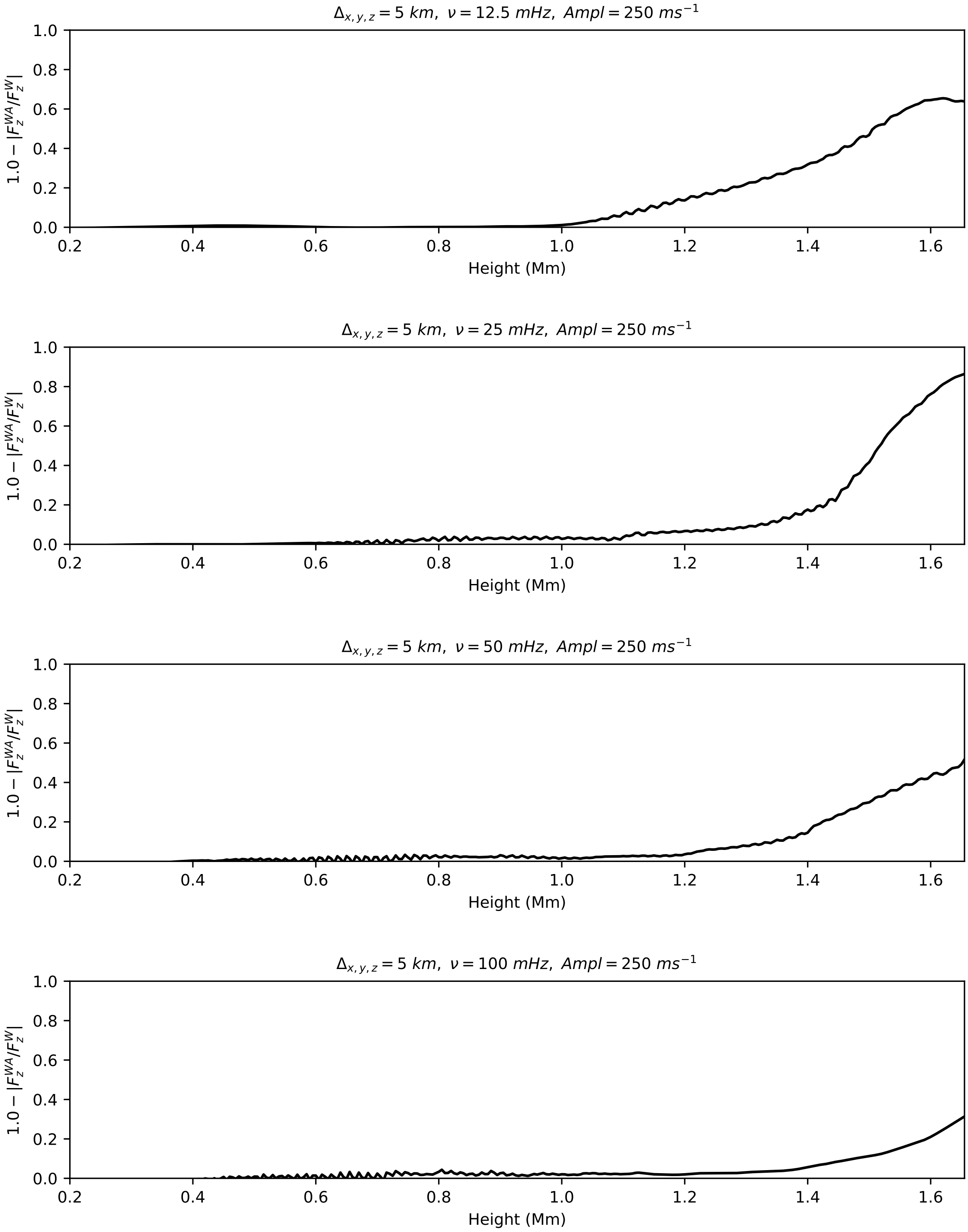

Fig. 5.12: Dependence of Poynting Flux absorption $1 - F_z^{AW}/F_z^{W}$ for the simulations of varying driver frequency 12.5 mHz, 25 mHz, 50 mHz and 100 mHz (from top to bottom).

chromosphere, as seen in Figure 5.4. In these snapshots there is a definite relationship between the frequency and the ambipolar heating term. As the frequency increases, from the top row to bottom row, the magnitude of the heating term is also seen to increase for both the fast and Alfvénic components.

After 300 s a number of wave fronts have passed through and deformed the upper layers of the flux tube. At lower frequencies there is a significant increase in the ambipolar heating term with δB_{alf}. The dependence on frequency also changes. The 12.5 mHz simulation showing the highest heating coefficient, which decreases for the 25 mHz and 50 mHz simulations. For the 100 mHz simulation there is only a small change in the histogram between the two snapshots, a slight reduction seen in the ambipolar heating term.

The reduction of Poynting flux and ambipolar heating with frequency, seen in Figures 5.11, 5.12 & 5.13, is unexpected. In order to understand the cause of this decrease we plot the wave components after 250 s in Figure 5.14. The top row shows v_{alf}, and the bottom rows v_{fast} for the (left to right column) 100, 50, and 25 mHz drivers. A substantial part of the energy in the high frequency drivers is seen to be deflected directly up along the outer field lines of the flux tube. This causes the high frequency drivers to have low amplitudes in the centre of the tube, with significantly reduced shocking and only a small deformation of the plasma-$\beta = 1$ contour.

In order to investigate whether we can absorb a higher fraction of the Poynting flux with the high frequency drivers we re-run the 50 mHz and 100 mHz simulations at a driver amplitude of 500 $\mathrm{m\,s^{-1}}$, and the 100 mHz simulation at 1000 $\mathrm{m\,s^{-1}}$. The resulting Poynting flux absorption coefficients $1 - F^{AW}/F^{W}$ are plotted in Figure 5.15. At high driver amplitudes a substantial Poynting flux absorption coefficient can be reached, $1 - F^{AW}/F^{W} = 0.6$ at 500 $\mathrm{m\,s^{-1}}$ for the $\nu = 50$ mHz driver, and $1 - F^{AW}/F^{W} = 0.52$ at 1000 $\mathrm{m\,s^{-1}}$ for the $\nu = 100$ mHz driver.

5.5 Discussion and Conclusions

In this work we have simulated the heating of chromospheric plasma by wave propagation and dissipation in and around a magnetic field concentration, designed to mimic quiet Sun intergranular magnetic flux concentration seen. Ion-neutral interactions have been taken into account using a quasi-single fluid MHD method to include Ohmic dissipation and ambipolar diffusion. To summarise, we found:

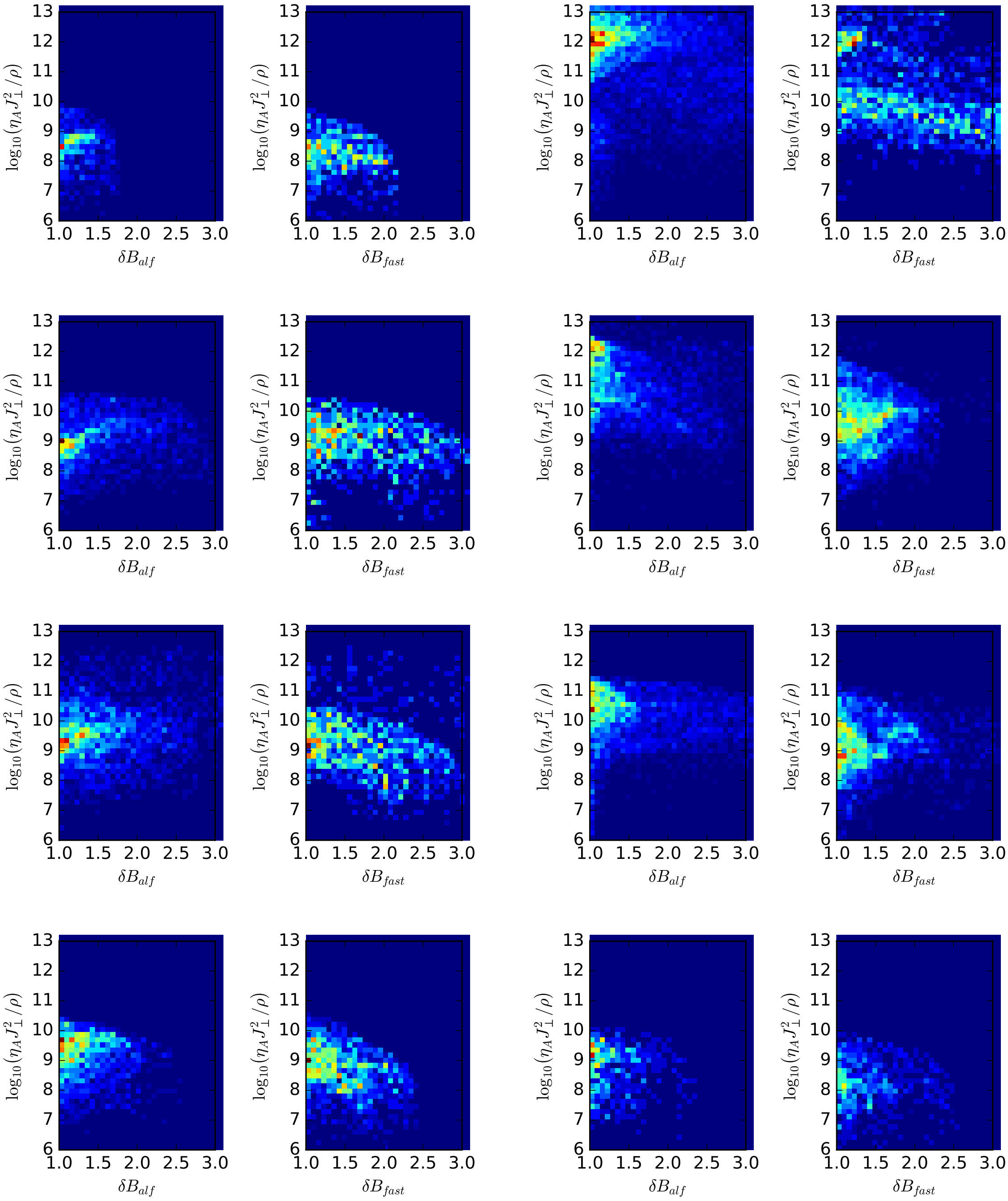

Fig. 5.13: Normalised histograms of the fast and Alfvén components of magnetic field perturbation versus the ambipolar heating term. The left two columns show the results for a simulation snapshot after 150 s and the right two after 300 s. From top to bottom, the panels show driving with a 12.5 mHz, 25 mHz, 50 mHz, and 100 mHz driver. The magnetic field components δB_{fast} and δB_{Alf} are calculated through projection of the magnetic field perturbations using Equations 5.55-5.57 over the region of the flux tube with $\beta < 1$.

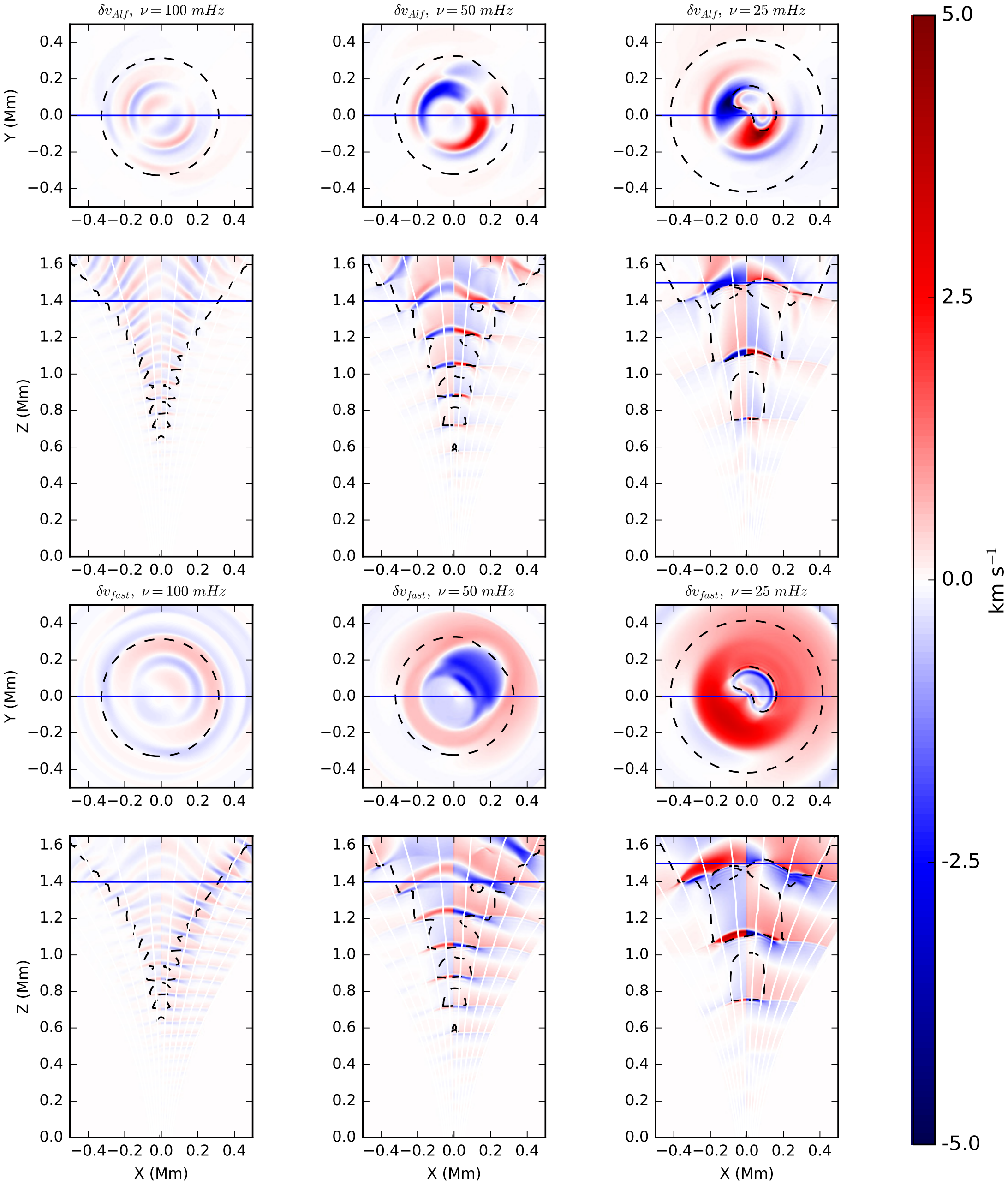

Fig. 5.14: Snapshots of the waves excited in the magnetic flux tube by acoustic drivers of frequency (left to right panels) 25, 50, and 100 mHz placed at the photosphere. The top panel is the Alfvén component, and the bottom panel the fast component, The snapshots are taken after 250 seconds of simulation time.

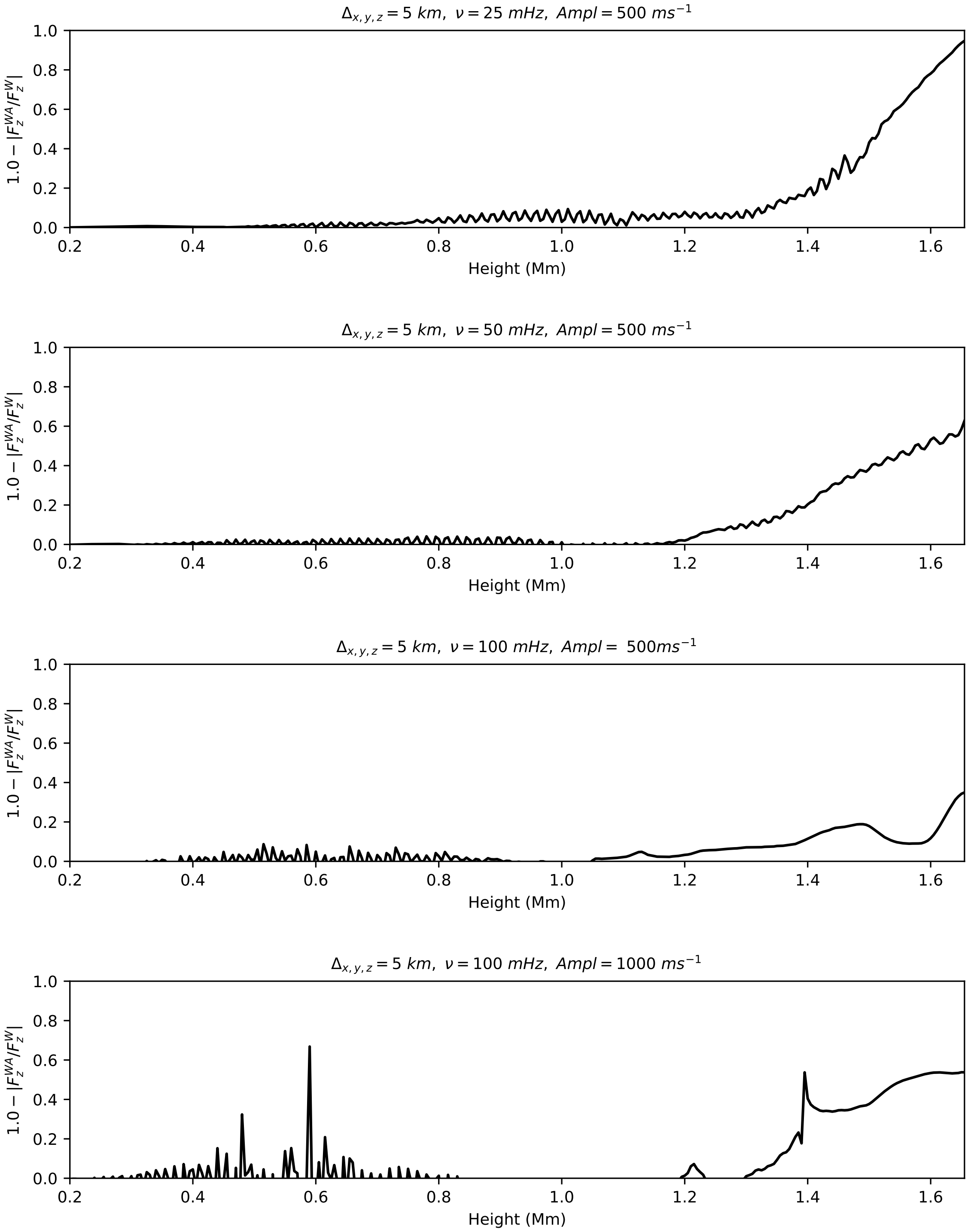

Fig. 5.15: Poynting flux absorption $1 - F^{AW}/F^{W}$ for the simulations of varying driver frequency, from top to bottom: 25 mHz, 50 mHz, and 100 mHz with a driver amplitude of 500 $\mathrm{m\,s^{-1}}$, and bottom 100 mHz with a higher driver amplitude of 1000 $\mathrm{m\,s^{-1}}$.

1. A pulse driver is used to generate 25 mHz frequency fast waves in the solar photosphere. These waves cross the $c_s/v_A = 1$ level of the magnetic flux concentration and undergo mode conversion to slow and Alfvén waves. Large Alfvénic perturbations are seen inside the low plasma-β regions of the magnetic flux concentration.

2. Waves are effectively damped by ion-neutral interactions. For the $\nu = 25$ mHz driver, at an amplitude of 500 m s^{-1}, a reduction in Poynting flux of up to 96% is seen by the top of the simulation domain.

3. Increase in resolution has a negligible effect for the simulation with a wave source of $\nu = 25$ mHz period.

4. The heating appears to be driven by non-linear effects. As the driver amplitude is lowered to 250 m s^{-1} and 50 m s^{-1} the height at which Poynting flux absorption occurs is seen to decrease. The fraction of the Poynting flux difference in the ambipolar simulations decreases to 20% at the top of the simulation domain. For the 5 m s^{-1} driver no noticeable Poynting flux absorption is seen.

5. Early in the simulation, as waves travel through the flux tube the Alfvén and fast wave components give an increase in the ambipolar heating coefficient with frequency. Later in the simulation, when a number of wavefronts have passed through the model, very high ambipolar heating coefficients are seen for lower frequencies, but not for higher frequencies.

6. The Poynting flux absorption term $(1-F^{AW}/F^{W})$ is highest at 25 mHz for driver amplitudes of $A = 250$ m s^{-1}, and 500 m s^{-1}. At $A = 250$ m s^{-1} the absorption is 86% at 25 mHz, decreasing to 52% for the 12.5 mHz driver. The Poynting flux absorption coefficient is also reduced at higher frequencies, reaching only 52% at 50 mHz and 31% at 100 mHz.

7. In higher frequency simulations a significant portion of the wave energy is deflected along the outer field lines of the flux tube model. This leads to lower velocity perturbations in the flux tube centre.

8. The Poynting flux absorption increases for the higher frequency simulations when higher driver amplitudes are used. For the 100 mHz driver the Poynting flux reduction was for a driver amplitude of 500 m s^{-1}, and for a driver amplitude of 1000 m s^{-1}.

Future work will involve increasing the simulations to higher frequencies. In order to accurately model higher frequencies a higher resolution will be required. Simulations at 2.5 km are currently computationally infeasible, however work is currently underway to introduce super-time-stepping and adaptive mesh refinement into the MANCHA code. These improvements will allow for simulation at significantly higher resolutions than those used in this chapter. In addition, this higher resolution will allow verification that Poynting flux absorption at higher frequencies is accurately resolved.

Further effort is being undertaken to investigate the impact of radiative cooling on the wave heating process. In the realistic solar chromosphere, heating processes are balanced by the radiative cooling of the plasma. The effects of the cooling on the power deposition must be taken into account to find out if the wave heating is sufficient to create a chromospheric thermal structure similar to the observed one. A selection of the previously run simulations will be repeated at high resolution with a grey approximation radiative cooling model enabled.

It could be possible to more efficiently generate Alfvén waves in the flux tube. Further work will test a driving function that can generate torsional Alfvénic oscillations through twisting of the magnetic flux tube footpoint. As suggested by the photospheric magneto-convection simulations, these motions are ubiquitous in the solar photosphere and carry the major part of mechanical energy. However, the low ionization fraction around the temperature minimum could greatly reduce the ability of Alfvén waves to carry a large energy flux from the photosphere. The Alfvén waves generated through the conversion of fast waves, as presented in this chapter, occur higher in the chromosphere and will be largely unaffected.

Chapter 6

Summary and perspective

In this thesis we investigated the behaviour of magnetohydrodynamic waves in solar magnetic field concentrations. We used MHD modelling and spectral line synthesis to generate observables of wave simulations. Study of the propagation of these waves, and their observable signatures is applied to two main research topics, i) helioseismic simulations of wave propagation in sunspots, ii) simulations of Alfvén wave heating of the chromosphere.

6.1 Helioseismic simulations of wave propagation in sunspots

Over Chapters 1-4 the machinery required to perform linear simulations of magnetohydrodynamic waves in a sunspot model and generate synthetic observables of these simulations were described. A summary of the main results and conclusions, as well as future research directions are presented below.

In Chapter 1 we introduced the linear SPARC MHD code. Improvements to the parallelisation and boundary conditions were described. The introduction of three-dimensional domain decomposition, in combination with a new finite difference scheme, and the HDF5 file format allows for a significant increase in computational speed. In addition, the cPML boundary conditions previously applied only to the vertical boundaries were extended to the horizontal boundaries to allow for better absorption of waves. Over the course of its development this upgraded code was, and continues to be, applied to a number of helioseismic modelling applications in addition to those presented in this thesis. These include; investigation of acoustic halos (See AppendicesA-B), development of new methods of time-distance helioseismology (Duvall et al. 2017, in prep), simulations of the seismic signatures of sunquakes (Donea et al. 2017, in prep), and the study of wave propagation in a twisted sunspot model (Pennicott et al. 2017, in prep).

Spectropolarimetry of wave simulations in the solar photosphere requires a background model that is both convectively stable and gives accurate radiation signatures. Quiet-sun models typically used for computational helioseismology often include an unrealistic photosphere and chromosphere, unsuitable for radiative modelling. Convectively stabilised semi-empirical quiet-sun models have previously been created using the method of Parchevsky & Kosovichev (2007). Currently available models were found to have a poor match to the solar limb-darkening curve, accurate limb-darkening is necessary for centre-to-limb observations. In Chapter 2 we apply the method of Parchevsky & Kosovichev (2007) in a way that will generate a convectively stable solar model and provide a good match to the original semi-empirical model over photospheric spectral line formation regions.

Additionally, in Chapter 2 we have investigated the cause of anomalous gaps found in helioseismic MHD simulations. Using a boundary value solver and SPARC MHD simulations we discovered that the cause of the gaps was driving at nodes in the solar $p-$mode eigenfunction. We identified two solutions; placing sources at a low depth with a large extent in z, or distributing sources in z. To better simulate the solar $p-$mode spectrum we developed a pseudo-random forcing function distributed over x, y, and z. Two possible extensions of this work were identified. Firstly, adjusting the random variables used in the distributed sources model to better fit the solar acoustic power spectrum.

Secondly, investigation of wave driving underneath and around sunspot models. As sunspots will inhibit convection they will affect the turbulent motions that generate the acoustic power spectrum. We can investigate the excitation of waves under a sunspot by changing the way in which driving occurs in a strong magnetic field and comparing the power spectrum to those of observed sunspots. In addition, this could be combined with a modified version of the sunspot presented in Chapter 4. The depth of the sunspot model could be varied and the surface wave signatures studied, similarly to Felipe & Khomenko (2017). Investigation of these waves could be used to answer the question of whether sunspots are deep (monolithic) or shallow (spaghetti) in nature.

An explanation of spectral line synthesis, used to produce the synthetic observables required, was given in Chapter 3. In Chapter 4 we described a modification of the sunspot model of Khomenko & Collados (2008). This new model is developed similarly in the quiet-sun model of Chapter 2, and incorporates a stabilised umbral model created using the same process. This sunspot model provides a more accurate line formation region, allowing spectral synthesis to be performed. We then analysed response functions in our model to understand synthesised centre-to-limb observations of the Fe I 6173 Å magnetically sensitive absorption line. Finally, we investigated wave propagation through the model using a three-dimensional magnetohydrodynamic simulation.

A time-series of synthetic observables were calculated using the simulation data, including; continuum intensities and Doppler velocities, and spectral line bisector measurements for multi-height observations. Maps of the acoustic power in the sunspot were generated to better understand the absorption line response to oscillations in the sunspot model and the effects of non-locality of radiative transport on helioseismic measurements. The major results of this chapter can be summarised as:

1. The sunspot absorbs or scatters the incoming acoustic wave energy in all but the 6 and 7 mHz frequency bands. Slight power enhancements are seen around the sunspot, with signatures of both far and near side acoustic halos observed.

2. A high-frequency anomalous power signature was seen in the centre of the sunspot. The umbral "belly button" – is observed at high (60°) inclinations. The geometry of the sunspots field lines suggests the power excess is driven by slow magneto-acoustic waves. It is seen when the horizontal velocity component dominates the *los* Doppler velocity measurement. Using spectral line bisectors to investigate the vertical extend of the power increase shows that it is present in the line core, but not the line wings. It is a highly localised phenomenon, demonstrating the importance of the non-locality of radiative transport on helioseismic measurements.

The umbral power increase is not seen in all sunspot observations. There are many differences in both sunspot properties and the radiative effects of HMI measurements that could explain this. These include changes in the Wilson depression, the wide range of the velocity response function in a magnetic structure (Figure 4.3), the low resolution and high-noise of the off disk centre measurements required, or issues with using discrete filters on highly split profiles. Future work using this sunspot model will involve the calculation of SDO-like observables exactly mimicking those of the HMI instrument and AIA 1600 and 1700 Å channels. Additionally, non-linear simulations can be performed to allow comparison to chromospheric spectral lines, such as used in the HELLRIDE instrument (Staiger, 2012).

Over the course of this thesis the models and code developed in Chapters 1-4 were used in three other publications that are not presented as part of this thesis. These papers can be seen in Appendices A - C. In all three, my contribution was in the development of a suitable sunspot model, assistance performing magnetohydodynamic simulations of wave propagation within this model, and the use of a radiative transfer code to calculate slices at a constant optical depth. Additionally, in the case of Appendix (B) synthetic continuum intensities were calculated to mimic the AIA 1600 and 1700 Å channels.

6.2 Simulations of Alfvén wave heating of the chromosphere

Photospheric vortex motions are observed in magnetoconvection simulations. They have been shown to be Alfvénic in nature and carry a Poynting flux sufficient to heat the solar atmosphere. However, there is no current mechanism to dissipate this energy flux.

In Chapter 3 we performed centre-to-limb observations to investigate the observational manifestation of these vortex motions. As they will be torsional motions, and therefore a horizontal velocity perturbation, a large inclination will be required to observe these motions. A range of centre-to-limb observables is generated for the Fe I 6302.5 Å spectral line, as used by the SOT on board Hinode. The main results of this chapter are:

1. Observation at high resolution and large viewing cosine $\mu > 0.5$ is required to see these torsional motions. They appear in intergranular solar magnetic field structures as alternating bands of red and blue shifted velocities.

2. Modern telescopes are unable to resolve these small-scale structures, however next generation observations with DKIST or EST will have a high enough resolution (25 km at disk centre).

We then investigate the potential of ion-neutral interactions to dissipate these Alfvénic motions, thereby heating the chromosphere. A non-linear, non-ideal simulation of wave propagation is performed in a model of an intergranular magnetic flux concentration. A quasi-single fluid MHD method is used, including Ohmic dissipation and ambipolar diffusion. To summarise the main results:

1. A 25 mHz fast wave driver is able to efficiently convert to Alfvén wave within the low plasma-β regions of the magnetic flux tube model.

2. The waves are effectively damped by ion-neutral interactions. For the $\nu = 25$ mHz driver, at an amplitude of 500 $\mathrm{m\,s^{-1}}$, a reduction in Poynting flux of up to 96% is seen by the top of the simulation domain.

3. The heating appears to be driven by non-linear effects. As the driver amplitude is lowered the minimum height at which Poynting flux absorption is seen to occur decreases. This height corresponds to the point shocks begin to form, large values of the ambipolar heating coefficient are seen in these shock fronts. For the 5 $\mathrm{m\,s^{-1}}$ driver no noticeable Poynting flux absorption is seen.

4. Early in the simulation, as waves travel through the flux tube, the Alfvén and fast wave components give an increase in the ambipolar heating coefficient with frequency. Later in the simulation, when a number of wavefronts have passed through the model, very high ambipolar heating coefficients are seen in the lower frequency simulations.

5. In higher frequency simulations a significant portion of the wave energy is deflected along the outer field lines of the flux tube model. This leads to lower velocity perturbations in the flux tube centre. The lower frequency simulations ($\nu = 12.5$ and 25 mHz) excite large amplitude velocity perturbations, these are efficiently dissipated, reducing the upwards Poynting flux in the flux tube centre. Even at higher frequencies ($\nu = 100$ mHz) and a driver amplitude of 250 $\mathrm{m\,s^{-1}}$ the Poynting flux dissipation is still greater than 30%, this increases to 35% for a driver amplitude of 500 $\mathrm{m\,s^{-1}}$, and 55% a driver amplitude of 1000 $\mathrm{m\,s^{-1}}$.

The dissipation of waves through ion-neutral interactions shows potential for heating the solar chromosphere through dissipation of Alfvén waves. The ability to efficiently dissipate lower frequency waves, even at relatively low amplitudes is promising to provide sufficient energy to the chromosphere. In order to properly quantify this heating it will be necessary to perform three additional sets of simulations. Firstly, simulation at a higher resolution will help determine if ambipolar diffusion is adequately resolved. Secondly, the inclusion of radiative transport will be required to model the full chromospheric energy balance. Finally, a study of different drivers is necessary to see if it is possible to excite and dissipate Alfvén waves more efficiently. One option is a torsional footpoint driver mimicking the convective buffeting of the flux tube. A second will be simulation with an acoustic driver with a solar frequency spectrum, rather than a monocromatic frequency spectrum as was used in Chapter 5.

Appendix A

MHD wave refraction and the acoustic halo effect around solar active regions: a 3D study

By C. Rijs, H. Moradi, D. Przybylski, and P.S. Cally.

Published 2015, ApJ, 801, 27R

Monash University

Declaration for Thesis Appendix A

Declaration by candidate

In the case of Appendix A, the nature and extent of my contribution to the work was the following:

Nature of contribution	Extent of contribution (%)
Assistance in code and model development.	10

The following co-authors contributed to the work. If co-authors are students at Monash University, the extent of their contribution in percentage terms must be stated:

Name	Nature of contribution	Extent of contribution (%) for student co-authors only
Carlos Rijs	Key ideas, development of code, modelling, production of all results, writing of paper	70
Paul Cally	Supervision and guidance	
Hamed Moradi	Co-supervision and guidance	

The undersigned hereby certify that the above declaration correctly reflects the nature and extent of the candidate's and co-authors' contributions to this work*.

Candidate's Signature	[redacted]	**Date** 17/2/17
Main Supervisor's Signature	[redacted]	**Date** 17/2/17

*Note: Where the responsible author is not the candidate's main supervisor, the main supervisor should consult with the responsible author to agree on the respective contributions of the authors.

Draft version January 7, 2015
Preprint typeset using LaTeX style emulateapj v. 5/2/11

MHD WAVE REFRACTION AND THE ACOUSTIC HALO EFFECT AROUND SOLAR ACTIVE REGIONS - A 3D STUDY

Carlos Rijs, Hamed Moradi, Damien Przybylski, and Paul S Cally
Monash Centre for Astrophysics and School of Mathematical Sciences,
Monash University, Clayton, Victoria 3168, Australia
Draft version January 7, 2015

ABSTRACT

An enhancement in high-frequency acoustic power is commonly observed in the solar photosphere and chromosphere surrounding magnetic active regions. We perform 3D linear forward wave modelling with a simple wavelet pulse acoustic source to ascertain whether the formation of the acoustic halo is caused by MHD mode conversion through regions of moderate and inclined magnetic fields. This conversion type is most efficient when high frequency waves from below intersect magnetic field lines at a large angle. We find a strong relationship between halo formation and the equipartition surface at which the Alfvén speed a matches the sound speed c, lending support to the theory that photospheric and chromospheric halo enhancement is due to the creation and subsequent reflection of magnetically dominated fast waves from essentially acoustic waves as they cross $a = c$. In simulations where we have capped a such that waves are not permitted to refract after reaching the $a = c$ height, halos are non-existent, which suggests that the power enhancement is wholly dependent on returning fast waves. We also reproduce some of the observed halo properties, such as a dual 6 and 8 mHz enhancement structure and a spatial spreading of the halo with height.

Subject headings: magnetohydrodynamics (MHD) – Sun: helioseismology – Sun: magnetic fields – Sun: oscillations – waves

1. INTRODUCTION

At present the local behaviour of wave modes in and around solar regions of significant magnetic field strength is not fully understood (see Gizon et al. 2010 and Moradi et al. 2010 for recent reviews). Strong field regions alter the characteristics of otherwise simple acoustic waves, resulting in vastly different behaviour for waves on either side of the fast/slow magneto-acoustic branch. The process of mode conversion has a significant effect on these incoming waves. As initially suggested by Spruit & Bogdan (1992), conversion from fast waves to downward travelling, field aligned slow waves has been shown to be the likely responsible mechanism (Cally & Bogdan 1997; Cally et al. 2003) for the well observed umbral p-mode absorption and associated phase shifts (Braun et al. 1987).

The physical mechanism behind the power enhancement observed around sunspots and active regions at frequencies above the local acoustic cutoff (the so called acoustic halo) is still unknown.

First observation of the halo began several years after the discovery of the aforementioned p-mode absorption. Braun et al. (1987), assessing the viability of acoustic power maps as a diagnostic tool for local helioseismology, noticed not only the well observed reduction of power at around 3 mHz, but also a high frequency enhancement at around 6 mHz extending many arcseconds radially. The discovery was soon verified by Brown et al. (1992) and by Toner & Labonte (1993). With the increasing observational accuracy made available with the *Solar and Heliospheric Observatory* (SOHO), it became clear that an enhancement was present only in the power of velocity amplitudes and not in measurements of the continuum intensity (Hindman & Brown 1998; Jain & Haber 2002).

More recently, Schunker et al. (2011) showed that halo power excess is prominent for moderate strength (150 G $< |\mathbf{B}| <$ 800G) and near horizontal field, and that, importantly, the peak halo frequency ν increases in proportion to the field strength.

Rajaguru et al. (2013), using the *Helioseismic and Magnetic Imager* (HMI) and *Atmospheric Imaging Assembly* (AIA) instruments onboard the *Solar Dynamics Observatory* (SDO), have calculated doppler velocities and intensities corresponding to observables at heights of between 0-430 km above the photosphere (where the continuum optial depth is unity). The most important findings can be summarised as follows:

1. The standard $5.5 - 7$ mHz doppler velocity halo observed by all above references is clearly visible and is strongest in near-horizontal field regions, decreasing in amplitude as the field becomes more vertically aligned. As the field strength increases, the halo peaks at a greater frequency (ν). (Schunker et al. 2011).

carlos.rijs@monash.edu

2. The presence of the halo is extremely dependent on height. At the base of the photosphere ($z = 0$) for weak field regions, there is a uniform wave power above the acoustic cutoff, which is to be expected. However, at heights of around 140 km (corresponding to HMI observations of the Fe 6173.34 Å line) the situation is markedly different, and the enhancement (with respect to quiet Sun values) comes into effect.

3. The enhancement is also visible in the chromosphere in intensities. A Fourier analysis of the AIA intensity data for the 1600 Å and 1700 Å wavelength channels (corresponding approximately to average heights of 430 and 360 km respectively) shows high frequency enhancements, which spread with height (Rajaguru et al. 2013). Once again, no enhancement is present in the continuum intensity power (taken from a height of around $z = 0$ km)

4. There is a secondary halo which exists in the 7.5-9.5 mHz range which is only manifested amongst stronger horizontal fields ($|\mathbf{B}| > 300G$). Such conditions likely correspond to a canopy field surrounding a strong sunspot, and this higher frequency halo is shown in power maps to be highly localized spatially. Radially outwards from this higher ν field is a region of significantly reduced power, which in turn is surrounded by a diffuse, weak halo region, extending radially many Mm into relatively quiet regions (Rajaguru et al. 2013).

There have been several recent theories attempting to explain the acoustic halo. Early theories suggested that the halos correspond to areas of increased acoustic emission (Brown et al. 1992). However enhancements are generally not observed in continuum intensity (Rajaguru et al. 2013), which casts doubt on this hypothesis.
Jacoutot et al. (2008) has performed radiative MHD simulations with an emphasis on the effect of the magnetic field on the frequencies of excitation originating from the solar convection zone. They found that the field shrinks the granulation scale size and shifts the local oscillation frequency upwards to higher values, consistent with halos.
Kuridze et al. (2008) shows analytically that it is possible for waves of azimuthal wave number $m > 1$ to become trapped under small canopy field regions, while Hanasoge (2009) suggests that the local oscillation is shifted preferentially from high to low mode mass (Bogdan et al. 1996) due to the flux tube acting as a wave scatterer, and that essentially mode energy is being reorganised more significantly for high frequency waves because of their greater propensity for scattering.
Additionally the overlying magnetic canopy itself has been shown to be linked with photospheric power enhancement by Muglach et al. (2005), and in particular the mode conversion process that is governed by the ratio of the Alfvén speed (a) and the sound speed (c).
We intend to follow up on the initial simulations and theory of Khomenko & Collados (2009), who have suggested that fast/slow mode conversion and transmission may be the dominant mechanism behind halo formation.
Khomenko & Collados (2009) have performed 2D wave propagation simulations through a magneto-hydrostatic sunspot atmosphere with a wavelet source and observed a power enhancement of around 40-60% in acoustic power with respect to the quiet sun. The enhancement also correlates well with the $a = c$ equipartition region for the photosphere (where they have defined the photosphere as the height at which the optical depth scale is unity).
The results suggest that the halos could occur simply as the addition of energy from high frequency non-trapped waves which have travelled above $a = c$ and undergone mode conversion. In this instance, when a and c coincide, the normally separate branches of magnetoacoustic waves (the fast and the slow wave) may interact. If the upcoming waves are of sufficiently high frequency to penetrate above the acoustic cut-off and travel into the $a > c$ atmosphere, the wave's energy will be partially re-assigned into the fast or slow mode depending on the relationship between the wavevector and the orientation of the magnetic field (See Cally 2006; Schunker & Cally 2006 for details or Cally 2007 for an easily accesible review). The slow waves are strongly field aligned at small β and may contribute to the diffuse, spatially extended halos observed by Rajaguru et al. (2013).
The fast waves however will refract due to the rapidly increasing profile of a, and eventually reflect where $\omega^2 = a^2 k_h^2$ (where ω is the angular freqnuecy and k_h is the horizontal component of the wavenumber), depositing energy into regions below. Low frequency power should therefore not be enhanced in any way, as these waves are unable to reach such heights, except in special wave-field configurations where the ramp effect may reduce the effective acoustic cutoff frequency (Cally 2006; Schunker & Cally 2006; Cally 2007).
The fast-acoustic-to-fast-magnetic conversion is favoured at a higher frequency and more importantly by a large attack angle between the incoming wave and the magnetic field lines, which potentially explains why halos are consistently observed at near horizontal fields (i.e. the line of sight component of velocity makes a large attack angle with a horizontal field). The mechanism also naturally explains the spreading of the halo that is observed with height (Braun et al. 1992; Brown et al. 1992), given that the $a = c$ height is located further outwards radially from sunspot center as a function of height.
Recently Kontogiannis et al. (2014) performed an interesting observational study by examining photospheric and chromospheric power enhancements as functions of mode conversion parameters, such as the attack angle. They

discovered chromospheric slow wave signatures corresponding to waves following the field lines upwards, as well as reflected fast wave signatures correlating with power enhancement regions for high frequency waves, lending further weight to the importance of mode conversion in this instance.

2. THE SIMULATION

We proceed by performing 3D simulations in the spirit of Khomenko & Collados (2009). The goal is to underake forward modeling of a simple wavepacket propagating through a sunspot-like magnetic field and atmosphere in full 3D and observe the structure of any resultant enhancements in time averaged acoustic power at high frequencies, both spatially and spectrally. In particular we wish to determine whether there is a correlation between the halo formation and the region most important to mode conversion - the $a = c$ equipartition height.

Halo formation is manifested on the Sun as an enhancement of time-averaged acoustic power (at frequencies above the acoustic cutoff) at near horizontal magnetic field inclinations with respect to the normal quiet-Sun values. We therefore perform quiet and magnetic simulations separately. After the simulations are complete, the time averaged power at each point of the magnetic simulation can be compared to the corresponding quiet point and regions of enhancement can be identified. In this paper, we shall focus on the power of the vertical component of the velocity perturbation (v_z), which corresponds observationally to the line-of-sight component of velocity when observing at disk centre.

For our quiet-Sun simulations we have used a convectively stabilised version of the Model S (Christensen-Dalsgaard et al. 1996) joined onto a VAL-C chromosphere (Vernazza et al. 1976) modified to minimize convective instabilities which do not lend themselves well to linear wave simulations (Parchevsky & Kosovichev 2007). For our magnetic wave propagation simulations, we use the magneto-hydrostatic (MHS) sunspot model of Khomenko & Collados (2008), who have joined the self-similar lower photospheric sunspot model of Schlüter & Temesváry (1958) and Low (1980), with the pressure distributed model of Pizzo (1986) to create a consistent magnetic atmosphere. The model has been further enhanced to provide a consistent MHS structure and a convectively stable stable pressure, density and temperature profile, accurate to empirical models of the solar photosphere (Przybylski. 2014 - in preparation).

We use the 3D wave propagation code SPARC (Hanasoge 2007; Hanasoge et al. 2007). The code solves the ideal linearised Eulerian MHD equations in cartesian coordinates for a given magnetic or quiet (non-magnetic) atmosphere. The code is ideally suited to the forward modelling of adiabatic wave propagation, with output consisting of the linear perturbations to the background states of the pressure (p), density (ρ), magnetic field ($\mathbf{B}$) and vector velocity ($\mathbf{v}$).

The computational box consists of square, horizontal dimensions $L_x = L_y = 200$ Mm, corresponding to 256 grid points and yielding a horizontal resolution of $dx = 0.78125$ Mm. We define a reference photosphere as the height at which $\log(\tau) = 0$ (where τ is the optical depth scale, as calculated from the known thermodynamic values at every point in the box), and the vertical dimension spans from 10 Mm below this surface to 1.85 Mm above it. The vertical axis is scaled in inverse proportion to the sound speed with 215 grid points, yielding grid spacing on the order of 20 km above the surface, to spacings of around 100 km at the bottom of the box.

In an attempt to keep the simulation as simple as possible and avoid any periodicity, we have implemented sponges along the sides of the box and perfectly matched layers (PML) along the top and bottom. The intention is to ensure that all outgoing waves are damped completely. The top PML takes effect over the top 15 grid points, resulting in a useable box top of 1.5 Mm

The most immediate problem when initiating forward modelling in a stratified magnetic atmosphere is the rapid increase with height of a (where $a = B/\sqrt{4\pi\rho(z)}$, with $B = |\mathbf{B}|$) caused by the swiftly decreasing profile of ρ. The CFL constraint on any explicit finite differences scheme requires that the maximum stable time step at any given point is inversely proportional to the local velocity scale there. In other words, if we extend the box too far into the atmosphere, the timestep required becomes impractically small. Methods of artificially capping a at some manageable value have been well described (Hanasoge et al. 2012; Rempel et al. 2009). We use the method of Rempel et al. (2009). When a begins to dominate over c, or in other words the plasma β becomes sufficiently small according to a chosen criteria, the limiter will take effect and prevent any further rise in a. It is important therefore to ensure that such a limiter takes effect well above the fast wave reflection heights for any high frequency waves of interest (see Moradi & Cally 2014 for a discussion on how Alfvén limiters may affect the helioseismology).

For our simulation we cap a at 80 km/s, yielding a fairly manageable simulation time step of 0.2 s for our sunspot, which has a peak surface field of 1.4 kG.

A contour plot giving an overview of the magnetic atmosphere that we have chosen to use is shown in Figure 1.

Note that the fast wave reflection height for a typical halo frequency wave is crucially between the $a = c$ layer and the $a = 80$ km/s contour, meaning that the primary body of fast waves which undergo mode conversion are free to reflect back downwards unhindered by our upper atmospheric meddling.

To begin, we set off a time dependent pulse (essentially adding a source term on the right hand side of the momentum

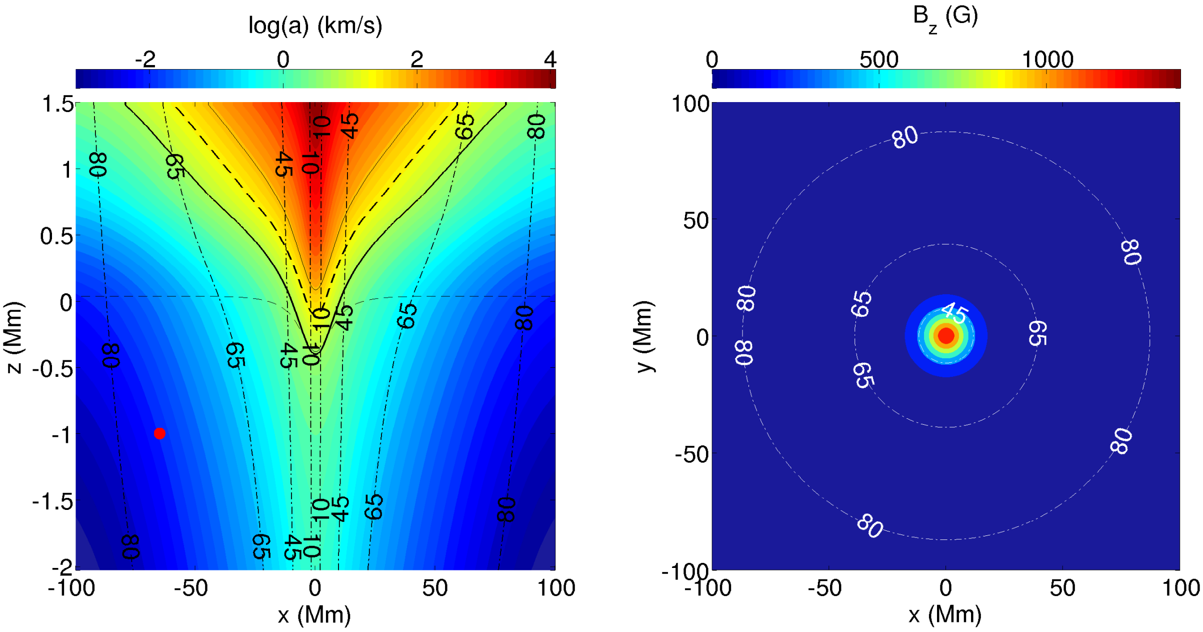

Figure 1. The left panel shows A 2D contour cut through the MHS sunspot atmosphere. Vertical dash-dotted curves are contours of field inclination (from the vertical). The thin black dashed curve corresponds to our reference photosphere, where $\log(\tau_{5000}) = 0$, with a Wilson depression of around 450 km. The thick solid curve is the $a = c$ equipartition height and the thin solid curve is the height at which $a = 80$ km/s. This is the height at which we have capped a. The thick dashed curve corresponds to the fast wave turning height for a 6.5 mHz magnetoacoustic wave with $k_h \approx 1.5$ Mm^{-1}. The background colour contour is $\log(a)$ in km/s. The dot corresponds to the location where the wave source was initiated. Note the highly stretched aspect ratio of the figure, with the abscissa spanning 200 Mm and the ordinate spanning only 3.5 Mm.
The right panel shows a contour plot of the vertical component of the magnetic field - B_z (in G) for the spot taken at the surface, along with various field inclination contours (dashed contours).

equation) similar to those used by Moradi & Cally (2014) and Shelyag et al. (2009), of the form

$$v_z = \sin\frac{2\pi t}{p}\exp(-\frac{(t-t_0)^2}{\sigma_t^2})\exp(-\frac{(\mathbf{x}-\mathbf{x_0})^2}{\sigma_{\mathbf{x}}{}^2}), \tag{1}$$

where v_z is the perturbation to the vertical component of the velocity, $p = 300s$, $t_0 = 300s$, $\sigma_t = 100s$ and $\mathbf{x} = (x, y, z)$. $\sigma_{\mathbf{x}}$ was chosen to give a pulse size of approximately 5 grid points in the x, y and z directions, with $\mathbf{x_0}$ =(-65, 0, -1) Mm. In other words the wave source is located 65 Mm from the sunspot umbra (which lies at (x,y)=(0,0)), in the y-plane cutting through the centre of the spot, and at a depth of 1 Mm below the surface (this position is shown by the red dot in Figure 1).
Such a pulse excites waves with a range of temporal frequencies around 3.3 mHz in somewhat of an approximation to the spectrum observed on the solar photosphere.
By utilising such a simple wave source, we may follow a wavepacket as it propagates from the quiet-Sun, through to the magnetically dominated regions of the the sunspot, and analyze any dynamical features (such as halos) as they appear.
Our primary goal was to analyse the power distribution on the near side of the sunspot (to the source). As such, the simulation was run for 2 solar hours, which is a sufficient time for the wavepacket to pass through the sunspot umbra. Figure 2 shows a summary of the simulation, including a power spectrum and time distance diagram for the 2 hour duration, as well as the frequency distribution of our source function and the associated frequency filters which were applied to the resultant power.

From panel a), it is clear that the sponges have been reasonably sucessful at damping the waves, however there is a small amount of reflection occuring off the left hand side sponges, resulting in some very small amplitude waves returning through the simulation domain. The fuzzy region observed at low wavenumber in b) results from wave interactions with the top and bottom box PML. d) gives an example of the filters we apply to the output to isolate specific frequency ranges.

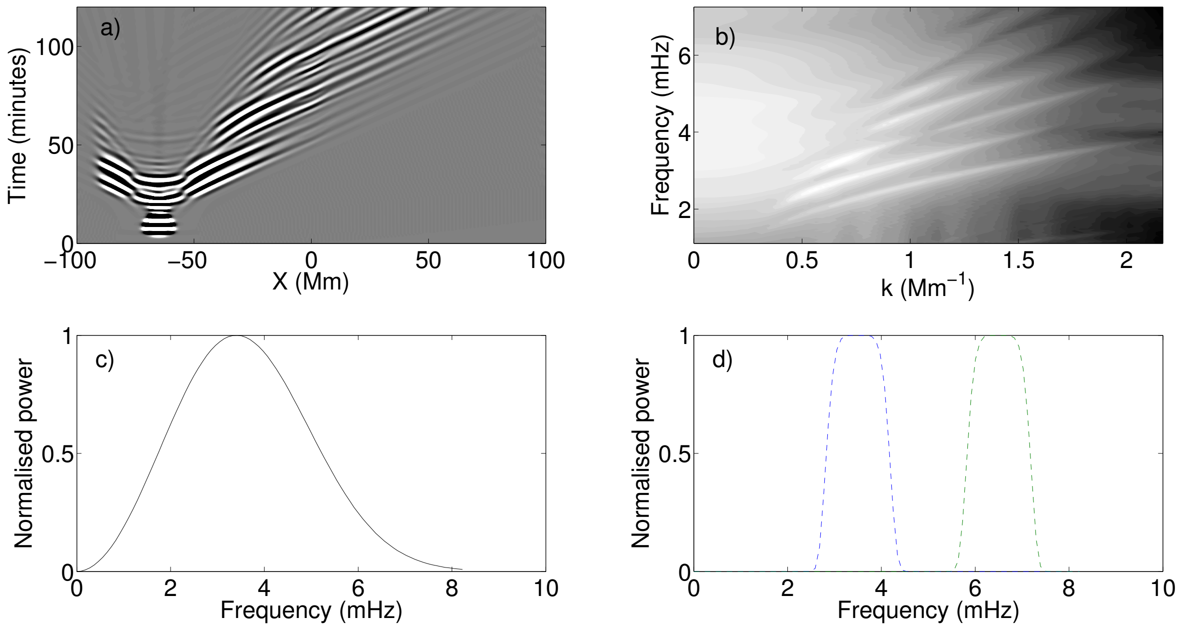

Figure 2. Panel a) shows the time-distance diagram of v_z, taken along the $\log(\tau_{5000}) = 0$ contour corresponding to the surface, through the centre of the sunspot. b) shows the full 2-hour azimuthally averaged surface power spectrum of the simulation. c): The frequency distribution of the wave source, centred at 3.3 mHz. d): The filtering functions used to isolate power at 3.5 and 6.5 mHz.

3. RESULTS

The main quantity which we shall use throughout the paper to denote a halo enhancement is $P = (P_{mag} - P_{quiet})/P_{quiet}$. P_{mag} is the 2-hour averaged Fourier power of v_z calculated at each point in the sunspot simulation at various heights. P_{quiet} is the analogue to P_{mag} for a completely separate quiet sun simulation. P is therefore the fractional enhancement in power for the sunspot simulation (with respect to the power from the quiet sun simulation) at any grid point. This power can then of course be filtered to isolate particular frequency ranges of interest (denoted as P_ν), prior to averaging over the remaining frequency domain.

We firstly identify that halos do indeed occur in our simulation. Figure 3 shows cuts through spot centre at 4 different heights, with P_ν plotted as a function of radial distance from the centre of the sunspot. We also show power maps for $P_{6.5}$ over the full $x-y$ plane in Figure 4 for the same choice of heights.

The top left panels correspond to the optical height unity, as shown in Figure 1, whereas the others are at constant geometrical heights, as labelled.

We have chosen to filter the power around both 3.5 and 6.5 mHz, using the filters shown in Figure 2 d). These frequencies are indicative of low frequency trapped waves (which generally cannot penetrate above the acoustic cut-off height to contribute to halos) and high frequency waves (which will undergo mode conversion and contribute to an enhancement) respectively. We of course expect to see the well observed p-mode absorption for the low frequency 3.5 mHz waves, which are suppressed in power when propagating through regions of high magnetic field strength. This can clearly be seen in Figure 3; $P_{3.5}$ shows a deficit with increasing proximity to the sunspot and no power enhancement whatsoever.

In contrast, there is a strong 6.5 mHz power enhancement visible at all heights. To be clear, a value of $P = 100\%$ indicates a doubling of quiet sun power; enhancements of $100-300\%$ are clearly seen, which is significantly larger than the observed halo values (Hindman & Brown 1998; Jain & Haber 2002; Schunker & Braun 2011; Rajaguru et al. 2013) of between 40-60% and indeed the values achieved in 2D simulations (Khomenko & Collados 2009; Zharkov et al. 2009). In our 3D simulations, where we have employed a simple gaussian wave source however, the magnitude is less of a concern than the qualitative behaviour of the enhancement.

We are primarily interested in whether mode conversion and the refraction of high frequency waves is the source of the halo enhancement. It is therefore necessary to ascertain whether the enhancements we see are true halos or simply an aberration caused by the magnetically modified atmosphere. In order to determine this we have run another simulation which we shall term the thermal case. The thermal simulation is performed with our 1.4 kG sunspot atmosphere as normal, however the background field itself is removed everywhere when the simulation begins. In this instance the

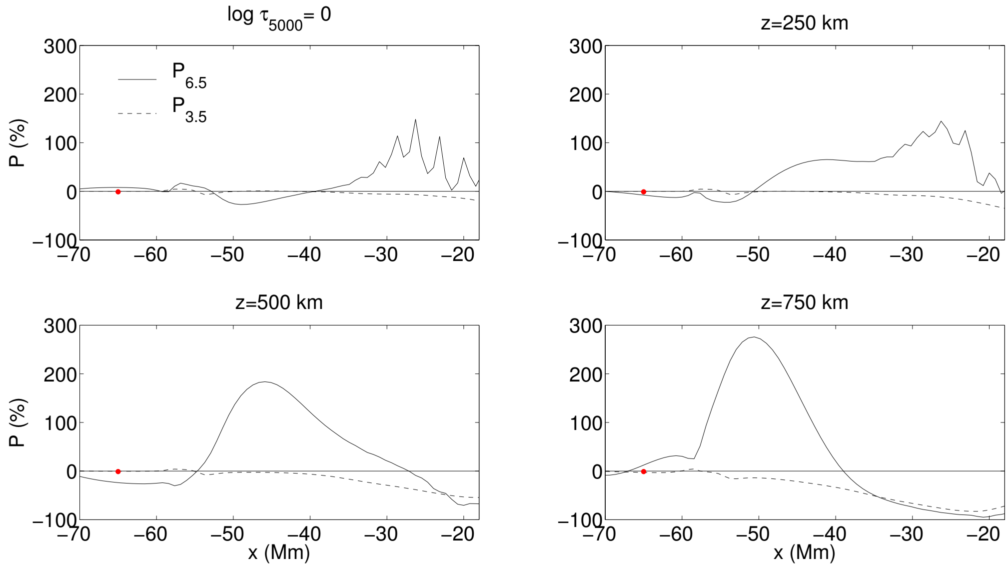

Figure 3. P_ν at the surface, and at constant geometrical heights of z = 250, 500 and 750 km, extending from around 20 to 70 Mm from the centre of the sunspot umbra. The solid line is the 6.5 mHz enhancement and the dashed line is the 3.5 mHz enhancement. The horizontal solid line indicates $P = 0\%$, which is a quiet sun value. Anything above this line we consider to be an enhancement. The source radial position of -65 Mm is shown by the red dot (although it is of course located 1 Mm below $z = 0$).

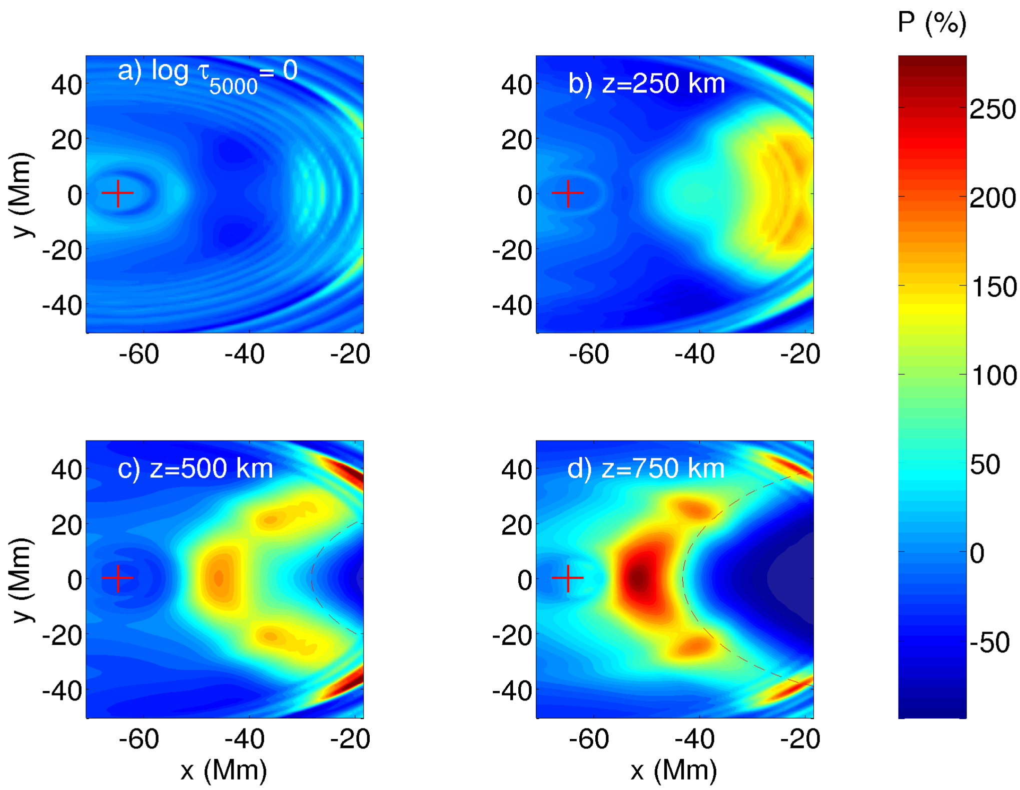

Figure 4. Power maps of $P_{6.5}$ at the same four heights for the x-y plane, restricted to the near side of the sunspot. The dashed curve visible at z = 500 km and 750 km is the $a = c$ contour for that particular height. The source radial position of -65 Mm is shown by the cross

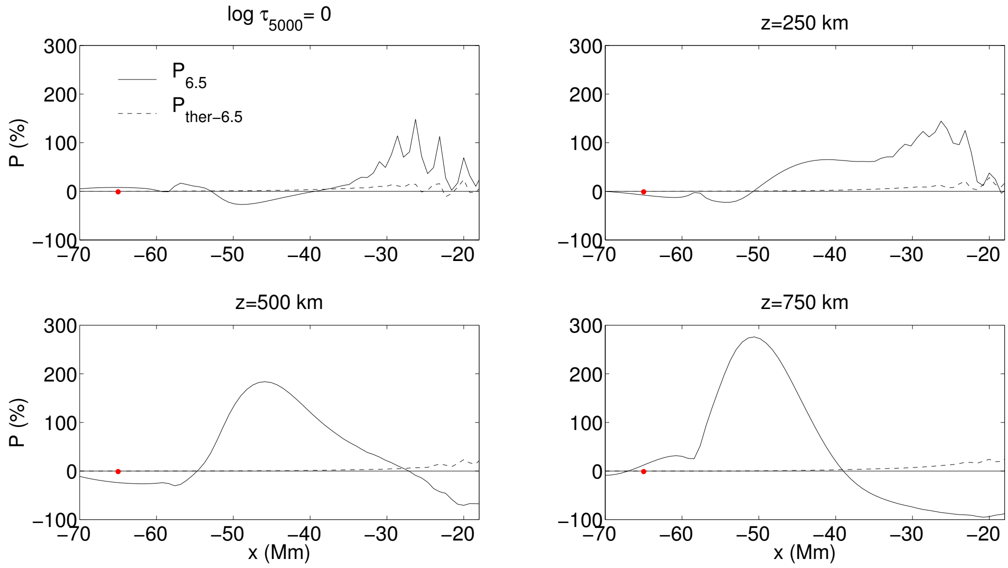

Figure 5. Similarly to Figure 3, we take cuts at 4 heights, including the surface. The solid curve is $P_{6.5}$, just as in Figure 3. The dashed curve is P_{ther} at 6.5 mHz.

atmosphere is not really in magneto-hydrostatic equilibrium, however it tells us if the enhancement is caused by wave-field interactions (as it should be if mode conversion is the cause); If the field is the cause of the halo we expect to see no enhancement in the thermal case.

Figure 5 shows the comparison between $P_{6.5}$ and $P_{\mathrm{ther}-6.5}$, where where P_{ther} is the analogue to P, denoting the time averaged power enhancement at every spatial point for the thermal case.

Clearly the thermal simulation yields no meaningful power enhancement, and so we conclude that the interaction between field and wave is key to the enhancement seen in this simulation.

To expand upon these simple findings we next show $P_{3.5}$, $P_{6.5}$ and $P_{\mathrm{ther}-6.5}$ as functions of x and z in Figure 6. Figure 6 is simply the 2D version of Figures 3 and 5, displayed for heights from $z = 0$ to $z = 1$ Mm above the surface, once again on the near side of the sunspot.

One can see from panel a) that the behaviour of P is quite complex. Significantly, the halo is correlated with the $a = c$ layer, manifesting below it and spreading radially outwards with height, agreeing with observations (Rajaguru et al. 2013; Schunker et al. 2011) and the prediction of Khomenko & Collados (2009). There are two lobes of larger power separated by a region of weaker - but still significant - enhancement. There is of course no halo in either the 3.5 mHz or the thermal cases.

We next test the validity of our original assertion that the acoustic halo is generated by downwards turning fast waves. If this is the case, then if fast waves are prevented from returning from above the $a = c$ layer, the halo should disappear. We proceeded by performing 3 additional simulations to the ones already discussed. These simulations are identical to our primary 2-hour simulation (from which we have calculated P) in every way except that we enforce successively lower Alfvén speed limits of 50, 20 and 7 km/s on the atmosphere in the manner described in section 2. A maximum Alfvén speed of 7 km/s is just above the value at which $a = c$; therefore upcoming fast acoustic waves which undergo mode conversion to fast magentic waves are never able to achieve the condition for refraction, that $a = \omega/k_h$ (as a is constant above this height), and so cannot return downwards and contribue to a halo.

Results of these simulations, showing the 6.5 mHz power enhancement, $P_{6.5}$, presented in the same manner as Figure 6 are displayed in Figure 7 below.

Panel d) clearly shows the complete reliance of the halo on the effects of the overlying magnetically dominated $a > c$ atmosphere. To be clear, the atmospheres used for the 4 simulations are all identical below the $a = c$ layer. For d) the atmosphere is modified above this point such that waves cannot reflect and refract. The lack of any enhancement indicates that the halo is manifested purely as a result of waves which have refracted and reflected downwards through this overlying $a > c$ atmosphere.

Further evidence for the mode conversion hypothesis is presented in Figure 8, which shows $P_{6.5}$ for the standard $B = 1.4$ kG case (top panel) and for a simulation where everything was kept identical except the peak field strength of the sunspot was doubled to around 2.8 kG (bottom panel).

In the case with the stronger 2.8 kG field, the halo is more spatially localised and the magnitude has increased by around 25%. The greater field strength has focused the fast waves into a more confined region due to the lower fast

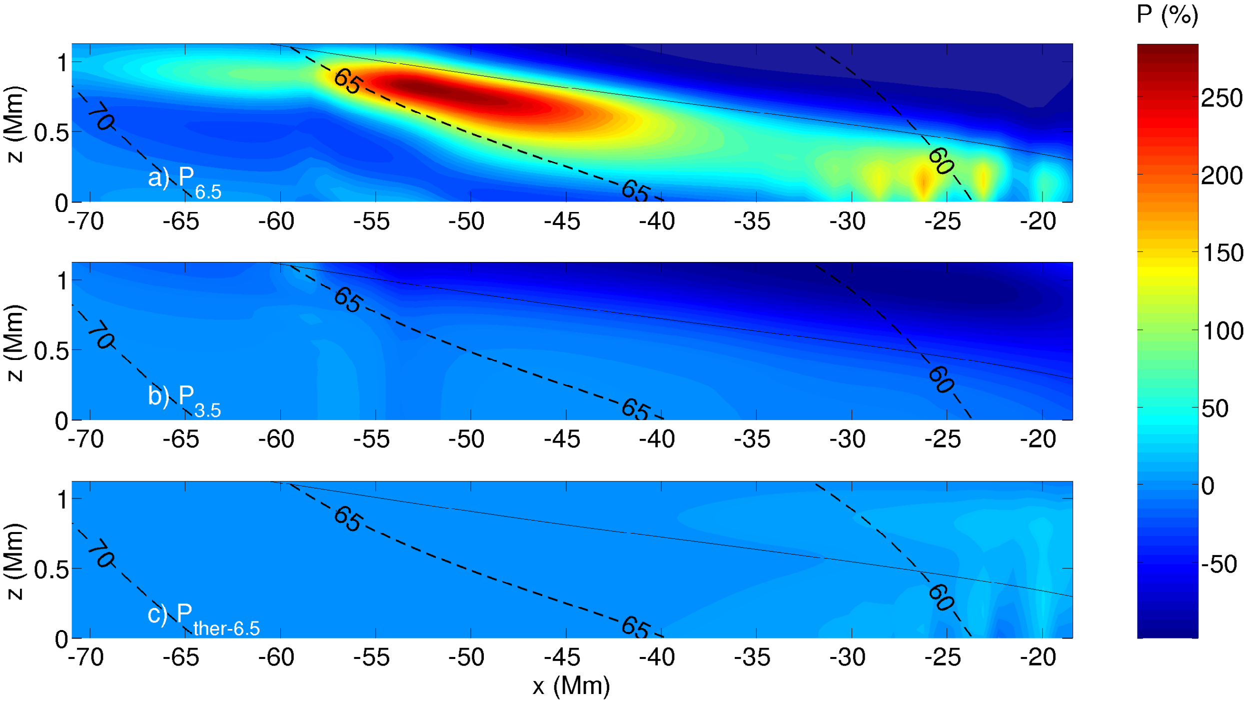

Figure 6. P and its relationship with the $a = c$ height. This is the vertical plane taken along the line $y = 0$ in figure 4. Panels a) and b) are $P_{6.5}$ and $P_{3.5}$. Panel c) shows the enhancement for the thermal case, $P_{\mathrm{ther}-6.5}$. The black solid curve is the $a = c$ height and the thick dashed labelled curves are contours corresponding to magnetic field inclinations of 70, 65 and 60 degrees (from left to right) with respect to the vertical.

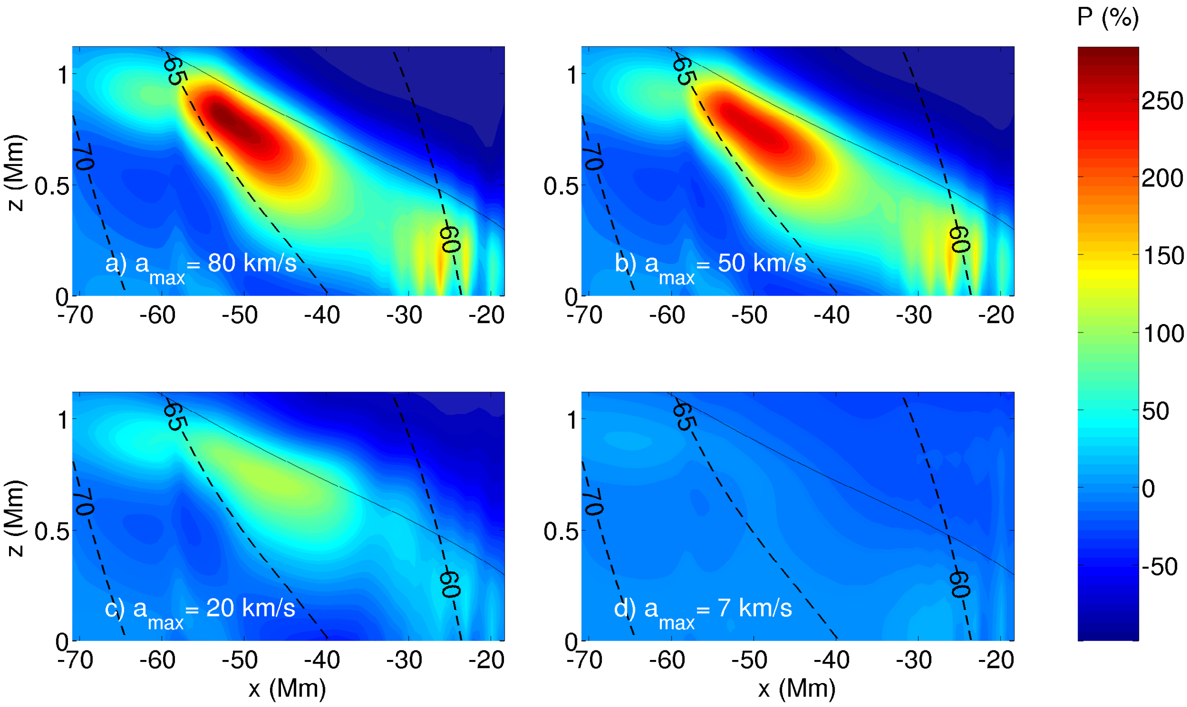

Figure 7. $P_{6.5}$ for the simulations with the background a limited at a) 80, b) 50, c) 20 and d) 7 km/s.

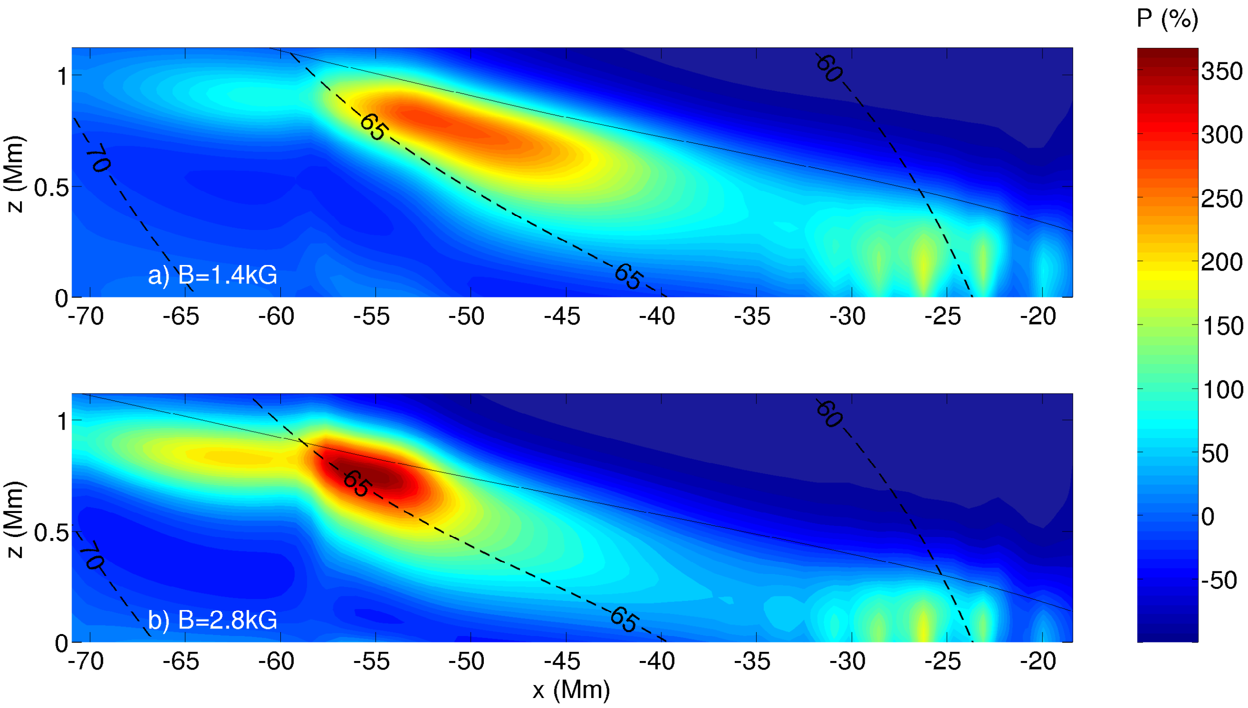

Figure 8. $P_{6.5}$ for the simulations with peak surface fields of a) 1.4 kG and b) 2.8 kG. The background a is limited at 80 km/s in both cases.

wave reflection height. The halo itself has also dropped in height, corresponding to the lower $a = c$ layer present in the stronger sunspot atmosphere.

Observations of acoustic halo power also exhibit quite a clear spectral behaviour. The power appears to peak at higher frequency for greater heights of z between 140 and 400 km and exhibits a dual lobe structure with peaks at around 6 and 8 mHz (Rajaguru et al. 2013). Shown in Figure 9 is the unfiltered acoustic power P as a function of height (above $z = 0$ km) and frequency.

The observed dual-lobe structure is evident in Figure 9, peaking at 6.3 and 7.6 mHz for heights between 0 to 800 km above the photosphere. The second enhancement lobe at 7.6 mHz is more compact than the lower frequency lobe, only appearing at heights greater than 300 km. The fact that such a simple wave pulse simulation reproduces many of both the spatial and spectral properties of acoustic halos observed in the actual solar photosphere and chromosphere is certainly encouraging.

4. DISCUSSION AND CONCLUSIONS

The results of our simple MHS sunspot wave propagation simulations show a marked power enhancement (by a factor between 1.5 and 4) with respect to quiet Sun values in the time averaged vertical component of velocity, v_z. The enhancement is present for relatively horizontal field (inclined 60 - 65 degrees from the vertical) which corresponds to weak field strengths of between 20-200 G. Spectrally, the enhancement exhibits twin peaks at approximately 6.3 mHz and 7.6 mHz, with the 7.6 mHz frequency peak manifesting slightly higher in the atmosphere than the lower frequency peak.

These characteristics (apart from the magnitude of the enhancement itself) match those determined observationally when acoustic power maps of halo regions have been analysed (Schunker et al. 2011; Rajaguru et al. 2013), indicating that we can, with reasonable certainty, refer to the enhancement as an acoustic halo. It is interesting that these features are brought out in such simple simulations with a wave source which differs so significantly from the bath of stochastically excited acoustic modes present in the real solar photosphere.

This fact suggests that the halo is a dynamic phenomenon brought about by the interaction of waves with the magnetic atmosphere, rather than any modification of the local acoustic oscillation frequency through granulation scale size shrinking (Jacoutot et al. 2008) or scattering effects (Hanasoge 2009).

The hypothesis with which we set out to investigate is that the acoustic halo is formed as extra energy is deposited into

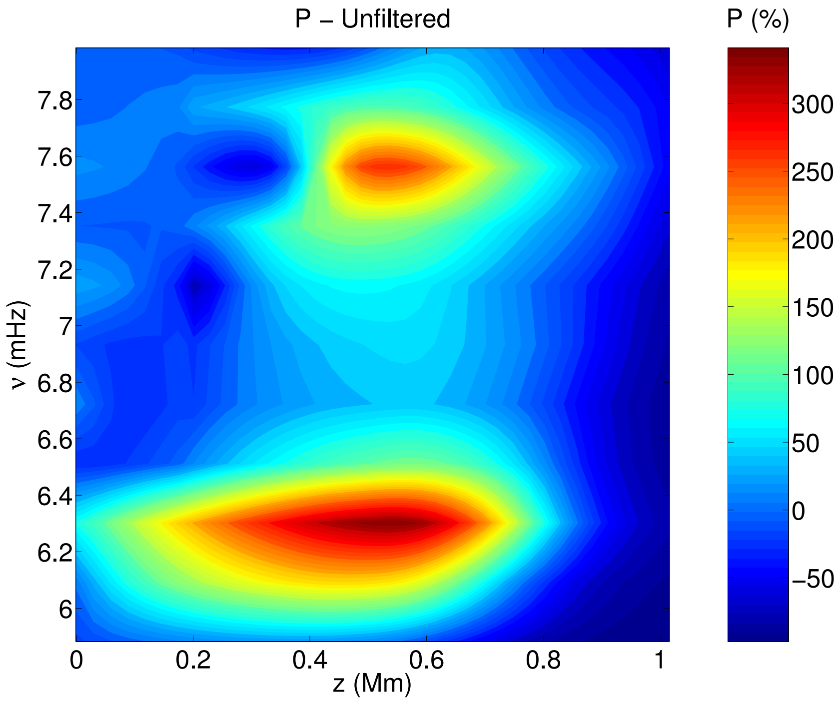

Figure 9. Unfiltered acoustic power P as a function of height, averaged over the points from $x = -60$ Mm to $x = -20$ Mm in Figure 7.

observable regions (in the photosphere and chromosphere) by downwards travelling fast waves which have refracted and reflected at the fast wave turning height. The idea was suggested and explored initially by Khomenko & Collados (2009).

In the quiet Sun, an upwards travelling high frequency (non trapped) acoustic wave will continue to propagate upwards and out of the local area, taking its energy with it. However if there is a magnetic field present in the gravitationally stratified atmoshpere, wave energy will branch into the fast magnetic and the slow acoustic modes at around the $a = c$ equipartition region. The slow acoustic waves in this case are the modes which take energy away along the field lines. The fast magnetic waves will continue to travel upwards while refracting until the condition for reflection, that $\omega/k_h = a$ is met. It is these waves that would then be responsible for the excess energy. The fact that the power enhancement so closely correlates wih the $a = c$ layer (figures 6 - 8) supports this hypothesis.

Furthermore, the halo magnitude scales with the value at which we cap the Alfvén speed, meaning that as we allow progressively more waves to return from the $a > c$ atmosphere, the halo becomes more apparent; When we do not permit upcoming waves to return downwards from above the $a = c$ layer, the halo disappears completely. This is the strongest piece of evidence in favour of the mode conversion mechanism.

The halo structure itself shows no evidence of any small-scale variations in magnitude, like the groupings of enhanced emission evident in egression power maps of active regions known as Glories (Braun & Lindsey 1999; Donea et al. 2000). This is most likely due to the simplicity of the monolithic field structure and wave source which we have utilised. It is likely that the small bead-like glories require less idealised magnetic configurations with more fine structure than we have used here.

We have not undertaken any analysis of intensity halos in this study, owing to the simple nature of the wave pulse which we have used. The calculation of intensities requires a strong and continuous wave source, and so we intend to follow up this work by performing simulations with a more realistic stochastic and spatially homogeneous wave bath. In this manner we hope to produce the well observed intensity halo and also determine to what extent the velocity halo properties uncovered here are reproduced and/or extended.

REFERENCES

Bogdan, T. J., Hindman, B. W., Cally, P. S., & Charbonneau, P. 1996, ApJ, 465, 406, 406
Braun, D. C., Duvall, Jr., T. L., & Labonte, B. J. 1987, apjl, 319, L27, L27
Braun, D. C., & Lindsey, C. 1999, ApJ, 513, L79, L79
Braun, D. C., Lindsey, C., Fan, Y., & Jefferies, S. M. 1992, apj, 392, 739, 739
Brown, T. M., Bogdan, T. J., Lites, B. W., & Thomas, J. H. 1992, apjl, 394, L65, L65

Cally, P. S. 2006, Royal Society of London Philosophical Transactions Series A, 364, 333, 333
—. 2007, Astronomische Nachrichten, 328, 286, 286
Cally, P. S., & Bogdan, T. J. 1997, apjl, 486, L67, L67
Cally, P. S., Crouch, A. D., & Braun, D. C. 2003, mnras, 346, 381, 381
Christensen-Dalsgaard, J., Dappen, W., Ajukov, S. V., et al. 1996, Science, 272, 1286, 1286
Donea, A.-C., Lindsey, C., & Braun, D. C. 2000, Sol. Phys., 192, 321, 321
Gizon, L., Birch, A. C., & Spruit, H. C. 2010, ARA&A, 48, 289, 289
Hanasoge, S., Birch, A., Gizon, L., & Tromp, J. 2012, Physical Review Letters, 109, 101101, 101101
Hanasoge, S. M. 2007, PhD thesis,
—. 2009, A&A, 503, 595, 595
Hanasoge, S. M., Duvall, Jr., T. L., & Couvidat, S. 2007, ApJ, 664, 1234, 1234
Hindman, B. W., & Brown, T. M. 1998, apj, 504, 1029, 1029
Jacoutot, L., Kosovichev, A. G., Wray, A., & Mansour, N. N. 2008, ApJ, 684, L51, L51
Jain, R., & Haber, D. 2002, aap, 387, 1092, 1092
Khomenko, E., & Collados, M. 2008, apj, 689, 1379, 1379
—. 2009, aap, 506, L5, L5
Kontogiannis, I., Tsiropoula, G., & Tziotziou, K. 2014, A&A, 567, A62, A62
Kuridze, D., Zaqarashvili, T. V., Shergelashvili, B. M., & Poedts, S. 2008, Annales Geophysicae, 26, 2983, 2983
Low, B. C. 1980, solphys, 67, 57, 57
Moradi, H., & Cally, P. S. 2014, ApJ, 782, L26, L26
Moradi, H., Baldner, C., Birch, A. C., et al. 2010, Sol. Phys., 267, 1, 1
Muglach, K., Hofmann, A., & Staude, J. 2005, A&A, 437, 1055, 1055
Parchevsky, K. V., & Kosovichev, A. G. 2007, ApJ, 666, 547, 547
Pizzo, V. J. 1986, apj, 302, 785, 785
Rajaguru, S. P., Couvidat, S., Sun, X., Hayashi, K., & Schunker, H. 2013, solphys, 287, 107, 107
Rempel, M., Schüssler, M., & Knölker, M. 2009, ApJ, 691, 640, 640
Schlüter, A., & Temesváry, S. 1958, in IAU Symposium, Vol. 6, Electromagnetic Phenomena in Cosmical Physics, ed. B. Lehnert, 263
Schunker, H., & Braun, D. C. 2011, solphys, 268, 349, 349
Schunker, H., & Cally, P. S. 2006, MNRAS, 372, 551, 551
Schunker, H., Cameron, R. H., Gizon, L., & Moradi, H. 2011, Sol. Phys., 271, 1, 1
Shelyag, S., Zharkov, S., Fedun, V., Erdélyi, R., & Thompson, M. J. 2009, A&A, 501, 735, 735
Spruit, H. C., & Bogdan, T. J. 1992, apjl, 391, L109, L109
Toner, C. G., & Labonte, B. J. 1993, apj, 415, 847, 847
Vernazza, J. E., Avrett, E. H., & Loeser, R. 1976, ApJS, 30, 1, 1
Zharkov, S., Shelyag, S., Fedun, V., Erdélyi, R., & Thompson, M. J. 2009, ArXiv e-prints, arXiv:0909.5332

Appendix B

3D simulations of realistic power halos in magnetohydrostatic sunspot atmospheres: Linking theory and observation

By C. Rijs, S.P. Rajaguru, D. Przybylski, H. Moradi, P.S. Cally, and S. Shelyag.

Published 2016, ApJ, 817, 45R

Monash University

Declaration for Thesis Appendix B

Declaration by candidate

In the case of Appendix B, the nature and extent of my contribution to the work was the following:

Nature of contribution	Extent of contribution (%)
Assistance in code and model development.	5

The following co-authors contributed to the work. If co-authors are students at Monash University, the extent of their contribution in percentage terms must be stated:

Name	Nature of contribution	Extent of contribution (%) for student co-authors only
Carlos Rijs	Key ideas, development of code, modelling, production of all results, writing of paper	70
Paul Cally	Supervision and guidance	
Hamed Moradi	Co-supervision and guidance	
Paul Rajaguru	Observational collaborations	
Hamed Moradi	Assistance in development of models	

The undersigned hereby certify that the above declaration correctly reflects the nature and extent of the candidate's and co-authors' contributions to this work*.

Candidate's Signature	[redacted]	Date 17/2/17
Main Supervisor's Signature	[redacted]	Date 17/2/17

*Note: Where the responsible author is not the candidate's main supervisor, the main supervisor should consult with the responsible author to agree on the respective contributions of the authors.

DRAFT VERSION DECEMBER 7, 2015
Preprint typeset using LATEX style emulateapj v. 5/2/11

3D SIMULATIONS OF REALISTIC POWER HALOS IN MAGNETO-HYDROSTATIC SUNSPOT ATMOSPHERES: LINKING THEORY AND OBSERVATION

CARLOS RIJS[1,2], S.P. RAJAGURU[3], DAMIEN PRZYBYLSKI[1,2], HAMED MORADI[1,2,4], PAUL S. CALLY[1,2], SERGIY SHELYAG[1,2]

(Dated: December 7, 2015)
Draft version December 7, 2015

ABSTRACT

The well-observed acoustic halo is an enhancement in time-averaged Doppler velocity and intensity power with respect to quiet-sun values which is prominent for weak and highly inclined field around the penumbra of sunspots and active regions. We perform 3D linear wave modelling with realistic distributed acoustic sources in a MHS sunspot atmosphere and compare the resultant simulation enhancements with multi-height SDO observations of the phenomenon. We find that simulated halos are in good qualitative agreement with observations. We also provide further proof that the underlying process responsible for the halo is the refraction and return of fast magnetic waves which have undergone mode conversion at the critical $a = c$ atmospheric layer. In addition, we also find strong evidence that fast-Alfvén mode conversion plays a significant role in the structure of the halo, taking energy away from photospheric and chromospheric heights in the form of field-aligned Alfvén waves. This conversion process may explain the observed "dual-ring" halo structure at higher (> 8 mHz) frequencies.

Subject headings: sun: magnetic fields – sun: oscillations – sun: photosphere – sun: chromosphere – sunspots

1. INTRODUCTION

A complete picture of the interaction between wave motions and magnetic field in the solar photosphere and chromosphere is not yet available to solar phycisists.
Significant uncertainties still exist in the computation of helioseismological inversions in active regions for instance, especially given that the atmosphere above photospheric levels undoubtedly plays a role in muddying the seismic observables at the surface (Cally & Moradi 2013).
The theory of mode conversion provides a framework as to how active regions act as a gateway between the subsurface and the overlying atmosphere and modify the properties of otherwise normal acoustic p - modes.
The first and most important property of active regions to be explained in a mode conversion context was the well known absorption of p - modes (Braun et al. 1987). Upon initial suggestion by Spruit & Bogdan (1992), it was eventually determined that both conversion to the field-aligned slow mode (which travels downwards into the interior) and to the upwards travelling acoustic mode (for non-trapped waves) were the responsible mechanisms (Cally & Bogdan 1997; Cally et al. 2003).
The acoustic halo was first noted in Dopplergrams alongside the aforementioned p - mode absorption as a peculiar enhancement in 6 mHz power (with respect to average quiet sun values) which extended several Mm radially outwards from the umbra (Braun et al. 1992; Brown et al. 1992; Toner & Labonte 1993).
Later, in studies utilising the *Michelson Doppler Imager* (MDI) (Scherrer et al. 1995) onboard the *Solar and Heliospheric Observatory* (SOHO), it was noted that the enhancement was not present in measurements of the continuum intensity (Hindman & Brown 1998; Jain & Haber 2002).
This suggests that either there is a process at work affecting observed power somewhere in the height range between the intensity continuum height and the Doppler velocity observation height, or that the mechanism causing the enhancement is not a process that is detectable in measurements of intensities.
It turns out that the former case is much more likely, as intensity halos taken from spectral lines at greater heights have since been observed and studied in detail (Moretti et al. 2007; Rajaguru et al. 2013).
Also using MDI, Schunker & Braun (2011) examined 7 days of observations of the active region AR 9787 and showed that halos are manifested for relatively horizontally aligned, weak-to-moderate magnetic fields (150 G $< |\mathbf{B}| <$ 350G). This study also noted the interesting property that the power spectrum ridges of the enhancement region were shifted towards a larger wavenumber (k) for a given frequency (ν) (compared to the ridges from an area of the quiet sun) and that this effect is more pronounced for larger k, which sugggests that shallower waves are being more strongly affected in the enhancement region.
The most comprehensive observational halo study to date, by Rajaguru et al. (2013) utilised the *Helioseismic and Magnetic Imager* (HMI) and *Atmospheric Imaging Assembly* (AIA) instruments onboard the *Solar Dynamics Observatory*.
The authors conducted a multi height analysis of several active regions, measuring the time-averaged power from intensities and velocities corresponding to 6 different heights. From the intensity continuum at $z = 0$ (the base of the photosphere, where the optical depth is unity) to Doppler velocities of the Fe I 6173.34 Å line at around $z = 140$ km to intensities measured from the AIA 1600 Å and 1700 Å chromospheric spectral lines, halo properties were compared and analysed in detail. The findings can be summarised as follows:

1. The halo is present for non-trapped frequencies, be-

carlos.rijs@monash.edu
[1] School of Mathematics, Monash University, Clayton, Victoria 3800, Australia
[2] Monash Centre for Astrophysics (MoCA), Monash University, Clayton, Victoria 3800, Australia
[3] Indian Institute of Astrophysics, Koramangala II Block, Bangalore 560034, India
[4] Trinity College, The University of Melbourne, Royal Parade, Parkville, Victoria 3052, Australia

ginning at 5.5 - 6 mHz (as observed by all references above) and is present up to at least 9-10 mHz. The 6 mHz halo is the strongest in measurements of the Fe I 6173.34 Å Doppler velocity at $z = 140$ km.

2. The halo magnitude is a clear function of height. There is no enhancement in the time-averaged intensity continuum ($z = 0$) power or in the derived line-wing Doppler velocity ($z = 20$ km). For weak-field regions at these heights, there is also a uniform wave power above the acoustic cutoff, which is to be expected. However, at $z = 140$ km (the aforementioned HMI Doppler velocity line) the situation is markedly different, and the halo comes into effect.

3. The halo is clearly present in observations of the chromosphere, as measured by AIA. The time-averaged power of the 1600 Å and 1700 Å wavelength channels (corresponding approximately to $z = 430$ and 360 km respectively) shows a halo in the 7-10 mHz range, that spreads radially with height, agreeing with the suggestions of Finsterle et al. (2004).

4. The spatial extent and structure of the halo changes above about 8 mHz. This higher frequency halo is seen in power maps to be thinner and more confined spatially than the more diffuse structure seen at 6 mHz. Radially outwards from this higher ν field is a region of slightly reduced power, which in turn is surrounded by a diffuse, weak halo region, extending radially many Mm into quiet regions (Rajaguru et al. 2013).

In this study we are interested in providing a consistent theoretical explanation for the acoustic halo. There are of course a variety of existing theories as to the mechanism behind the phenomenon.
By conducting radiative simulations for instance, Jacoutot et al. (2008) determined that strong magnetic fields can alter the scale size of granulation cells, which in turn can modify the local excitation frequency of resultant photospheric waves. They found that the stronger field also increases the amplitude of non-trapped waves at frequencies consistent with halos.
Kuridze et al. (2008) show semi-analytically that waves with $m > 1$ (where m is the azimuthal wave number) can become trapped under field free canopy regions, resulting in an enhancement of higher frequency wave power.
Hanasoge (2009) suggests that the halo is a consequence of the equilibrium state of the solar surface, and that the local oscillation can be shifted to a lower mode mass (Bogdan et al. 1996) due to scattering from the magnetic flux tube.
We will discuss why these theories do not appear viable in light of our simulation results in the discussion at the end of this paper.

1.1. *Mode conversion*

In Rijs et al. (2015), we performed 3D simulations to determine whether there was promise in the suggestion of Khomenko & Collados (2009) that it is in fact the *overlying* atmosphere that is directly responsible for the halo. Specifically that the addition of energy from high frequency non-trapped waves which have travelled above the Alfvén-acoustic equipartition ($a = c$) layer and undergone mode conversion and refraction are responsible. In this case, the process of mode conversion describes the intrinsic physics.
At greater depths below the solar photosphere, the plasma β (where $\beta = P_g/P_m$, with P_g and P_m being the gas and magnetic pressures respectively) increases. Several Mm below the surface the plasma is dominated by hydrodynamic physics and waves are governed by the standard gas sound speed (c).
Conversely (assuming one is in the proximity of an active region of some sort), well above the surface the gas density (ρ) drops, the β becomes small and waves are governed more strongly by the Alfvén speed (a), where $a \propto |\mathbf{B}|/\sqrt{\rho}$, and $|\mathbf{B}|$ is the local magnetic field strength.
There is therefore a layer of the atmosphere (roughly where $\beta = 1$) where a and c equate - the so called $a = c$ layer. At this height, the phase speeds of the magnetoacoustic fast and slow waves are equal, allowing the two modes to interact. Energy can be channeled from the fast to the slow branch or vice versa.
The fast wave is largely acoustic in nature when $a < c$ and magnetic when $a > c$, and it is this fast magnetoacoustic wave that will refract and then reflect at the fast wave turning height (where $\omega^2 = a^2 k_h^2$, with $\omega = 2\pi\nu$ and k_h being the horizontal component of the wavenumber, k), returning downwards from above the $a = c$ layer.
Energy is preferentially converted from the fast-acoustic mode to the fast-magnetic mode if there is a large attack angle between the wavevector of the incident wave and the orientation of the magnetic field. If the attack angle is small then energy will be primarily channeled into the field aligned slow mode. This perhaps explains why halos are observed amongst horizontal field; The line of sight component of the Doppler velocity is largely vertical (when observing at disk center) and provides a large attack angle with the horizontal field.
The theory can also explain the spreading of the halo that is observed with height (Rajaguru et al. 2013), given that the $a = c$ layer is located at greater radial distances from the umbra as a function of height.
Waves with frequencies below the acoustic cut-off are generally unable to reach the $a = c$ height, as they have reflected inwards, which is presumably why halos are only observed at non-trapped frequencies. The fast magneto-acoustic wave provides the excess energy in observable regions, which would otherwise not be present in the quiet sun (see Cally 2006; Schunker & Cally 2006 for further details on mode conversion or Cally 2007 for a succinct review of the theory).
Khomenko & Collados (2009) have performed simulations with both monochromatic and gaussian wave sources in a magneto-hydrostatic (MHS) sunspot atmosphere and show a clear correlation between the power halo and a suspicious increase in RMS velocities for non-trapped waves resulting from the interference pattern generated by downwards travelling fast waves.
In Rijs et al. (2015) we extended this work in 3D. By performing forward modelling simulations with a spatially localised gaussian (in space, time and frequency) wave pulse, the halo structure resulting from the vertical component of velocity (v_z) was analysed as a function of radius, height and frequency. A clear correlation between the position of the $a = c$ layer and the halo was shown and the dependancy of the halo on the overlying atmosphere was exhibited.
In this work we perform simulations in similar MHS sunspot atmospheres to those of Rijs et al. (2015). However we now

use a realistic distributed wave source, modelled as a slab of point sources at some depth below the photosphere. The sources are tuned to mimic the observed photospheric power spectrum, peaking at the 5 minute oscillation period ($\nu = 3.3$ mHz) and exhibiting solar-like amplitudes. In this way we are able to compare the halos present in our simulations with observations in a more rigorous manner.
For the observational comparisons we use a subset of the data corresponding to a single active region from Rajaguru et al. (2013) which provides a multi-height velocity and intensity halo data set with which to compare our simulations.

2. THE SIMULATION

In this section we present an overview of our simulations, including the details of the sunspot atmosphere used, a summary of the distributed wave source and details regarding the calculation of synthetic instensities, phase shifts and velocities.

2.1. *The MHS atmosphere*

A detailed description of the sunspot model we are using can be found in Przybylski et al. (2015), where the model of Khomenko & Collados (2008) is optimised in order to increase spectropolarimetric accuracy and produce more realistic line formation regions.
In short, the MHS configuration combines the self-similar sub-photospheric model of Low (1980) with the potential configuration of Pizzo (1986). Convective stability is enforced by the method of Parchevsky & Kosovichev (2007).
The model makes use of the Model S for the distribution of quiet subphotospheric thermodynamic variables (Christensen-Dalsgaard et al. 1996) and the Avrett umbra for the non-quiet variables (Avrett 1981). The VALIIIC chromosphere (Vernazza et al. 1981) is smoothly joined onto these distributions to complete the full model, yielding a sunspot-like magnetic field configuration embedded into the atmosphere.
The sunspots we use in this instance are similar to those used in Rijs et al. (2015) and Moradi et al. (2015), except for some parameters, such as the peak field strength, the inclination at the surface, and the simulation box size, which have been modified.
The sunspot model not only provides the freedom to choose the peak field strength at the surface of the photosphere but also the depth of the Wilson depression (the height at which the atmosphere becomes optically thin is depressed in high field regions such as the umbra). As such we make use of two model atmospheres in this study, one with a peak surface field strength of $|\mathbf{B}| = 1.4$ kG and another with $|\mathbf{B}| = 2.7$ kG. The atmospheres have Wilson depression depths of 250 and 400 km respectively, which are reasonably realistic values.
The surface of the atmosphere is defined as the photospheric height at which $\log(\tau) = 0$ (where τ is the optical depth scale, as calculated from the known thermodynamic values at every point in the box) and follows the Wilson depression. The surface corresponds to the height of formation of the 5000 Å intensity continuum ($z = 0$) in this atmosphere.

2.2. *Forward modelling*

As in our previous work, we use the SPARC code for forward modelling (Hanasoge 2007; Hanasoge et al. 2007). The code has been used several times for wave-sunspot interaction studies (Moradi & Cally 2013, 2014; Moradi et al. 2015).
The code solves the ideal linearised MHD equations in cartesian geometry.
As input, we define a background atmosphere and instigate wave propagation for the desired simulation length. The background atmosphere can be any magnetic plasma such as the sunspot atmospheres mentioned above or any quiet-sun atmosphere, provided it is convectively stable.
The output is the perturbations to the background states of the pressure (p), ρ, magnetic field ($\mathbf{B} = [B_x, B_y, B_z]$) and velocity ($\mathbf{v} = [v_x, v_y, v_z]$).
The computational domain in both cases is square in the horizontal with 256 points in each of the x and y directions (where $L_x = L_y = 200$ Mm) yielding a horizontal spatial resolution of $\delta x = 0.78125$ Mm. There are 220 grid points in the vertical direction, with spacings scaled by the local background sound speed. This results in vertical grid spacings of around 20 km near the surface and 100 km at depths of several Mm. The box extends from a depth of 10 Mm below the surface to 2.5 Mm above it in this manner.
Side boundary conditions in our simulations are periodic, and there are both damping sponges and perfectly matched layers (PML) in effect along the top and bottom boundaries of the box. The top 20 and the bottom 8 grid points are taken up by these sponges and the PML, resulting in a maximum useable box height of 2 Mm (above the surface).
In order to overcome the numerical challenges of explicit forward modelling in an atmosphere where the governing wave speed scale (the Alfvén speed, a) increases rapidly above the surface, we use the Alfvén speed limiter described by Rempel et al. (2009), which was also used in Rijs et al. (2015). This allows us to sidestep the requirement of using a prohibitively small simulation time step, imposed by the Courant-Friedrichs-Lewy (CFL) condition. Work has been done to ascertain whether the use of an Alfvén speed limiter has a detrimental effect on helioseismic travel times (Moradi & Cally 2014), with the conclusion being that one must be certain that the artificial capping is occuring well above heights where any relevant physics is occuring (such as the fast wave reflection height or the $a = c$ layer).
We have set our limiter at a value of $a_{lim} = 90$ km/s, yielding a simulation time step of around 0.2 seconds.
Figure 1 shows a cut through the centre of our 2.7 kG sunspot atmosphere (along the plane at $y = 0$). Overlaid are the $a = c$ and $a = 90$ km/s contours, as well as the photospheric surface, with a Wilson depression of around 400 km.
The vertical inclination contours show the rather rapid drop-off in field inclination, with the field reaching 30 degrees from the horizontal some 20 Mm from the umbra (at the surface).
To reiterate, the mode conversion effects occur around the $a = c$ layer, and so it is important that fast waves are given space to refract back downwards as they naturally would before the limiter at $a = 90$ km/s takes effect. We have taken care to ensure that this is the case and that the modification of the atmosphere will not affect these returning fast waves. In this regard, simulations have been run with Alfvén limiter values up to 200 km/s, with no change to the halo properties observed.

Regarding our wave source function, we are attempting to model the uncorrelated stochastic wave field seen on the solar photosphere. This wave field is, in reality, generated by subsurface convective cells. We choose a depth of 150 km below the surface and initiate a source function, S, in the manner of

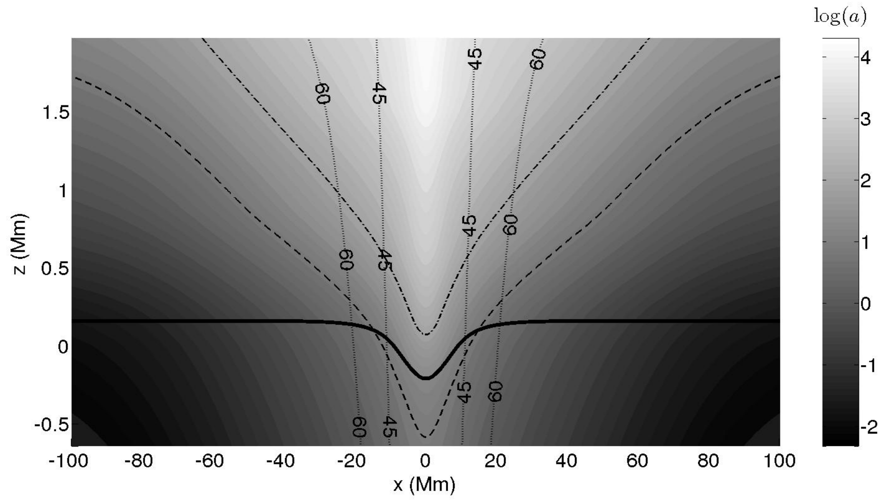

Figure 1. A cut through the sunspot center. Field inclination contours are shown for typical umbral/penumbral and penumbral/quiet sun values of 45 and 60 degrees from the vertical respectively. The surface or photosphere layer, where $\log(\tau) = 0$, is shown by the solid black curve. The dashed curve is the $a = c$ equipartition layer for this atmosphere and the dash-dotted curve is the $a = 90$ km/s layer, where the Alfvén limiter is in effect. The background contour is $\log(a)$ in km/s as it would appear without any Alfvén limiter in application. In our simulations a is constant above the $a = 90$ km/s curve. Note that the aspect ratio of the figure is highly stretched, with the horizontal dimension spanning 200 Mm and the vertical spanning only around 2 Mm.

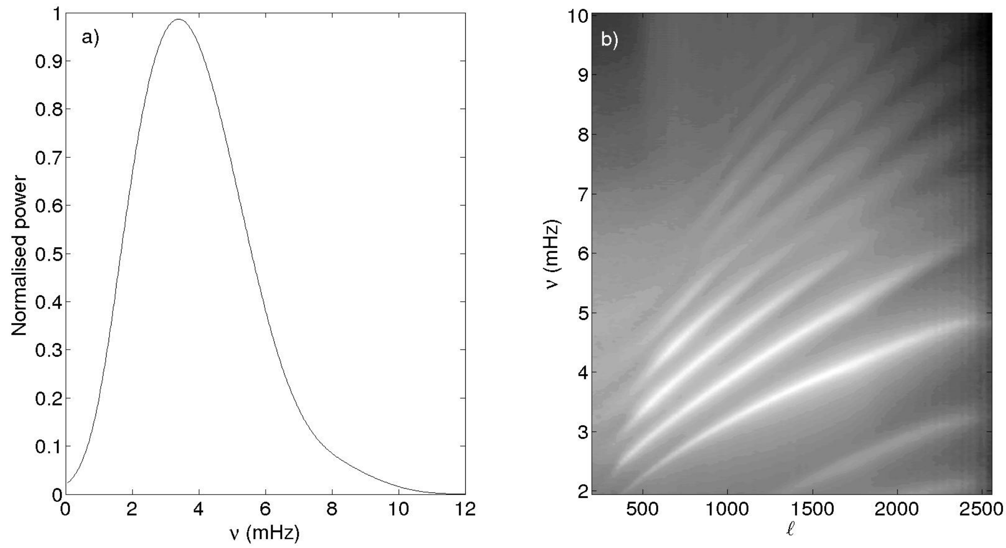

Figure 2. Panel a): The power spectrum of the wave source function used, tuned to provide a solar-like peak. b:) Arbitrarily normalised power ridges in ℓ-ν space for 6 hours of simulation time, calculated at the surface ($z = 0$) from v_z.

Hanasoge et al. (2007), i.e.

$$S(x,y,z,t) = \hat{S}(x,y,t)f(z) \tag{1}$$

where the horizontal function $\hat{S}(x,y,t)$ is a plane of spatial delta functions which are excited at a cadence of 30 seconds, and the function $f(z)$ is a gaussian function in depth with FWHM of approximately 100 km centered at 150 km below the surface.
The source power spectrum has been tuned such that it more-or-less fits the spectrum of power observed on the surface of the quiet sun. Panel a) of Figure 2 displays this spectrum, with a peak in power at around 3.3 mHz, and non zero power present until above 10 mHz. Panel b) shows the power ridges in ℓ-ν space calculated from 6 hours of v_z output at the surface.
In taking into account the fact that strong umbral fields inhibit subsurface convection and wave propagation, we do not excite waves in the umbra of the sunspot itself, smoothly suppressing the source amplitude as the magnetic field strength increases.
Wave propagation is initiated and run for 6 hours of solar time in total using both the 1.4 kG and 2.7 kG sunspot atmospheres (as separate simulations).
We analyse the power manifested in synthetic intensities corresponding to the 5000 Å continuum intensity, the AIA 1700 Å and 1600 Å intensity bands as well as both the vertical and horizontal components of the velocity perturbation (v_z and v_h respectively), which correspond observationally to the line-of-sight components of velocity when observing at disk centre (v_z) and at the limb (v_h).
In reality, the HMI Doppler camera (Scherrer et al. 2012) measures velocities from the Fe I 6173.34 Å line, which has its peak of formation at a height of around 140 km (Fleck et al. 2011; Rajaguru et al. 2013), while the AIA (Lemen et al. 2012) 1700 Å and 1600 Å wavelength intensity channels are formed at approximate heights of 360 km and 430 km respectively (Fossum & Carlsson 2005; Rajaguru et al. 2013).
Thus, in comparing the structure of power enhancements present in our simulations with the observed power behaviour from Rajaguru et al. (2013) we extract simulation velocity signals from a height of $z = 140$ km. We then calculate the synthetic intensities corresponding to the two above AIA channels as well as the 5000 Å continuum intensity for our 6 hour wave propagation simulations. The approximate 1600 Å and 1700 Å intensities are calculated by interpolating the ATLAS9 continuum and line opacity tables (Kurucz 1993) using the plasma parameters from the simulation and integrating them together with the corresponding LTE source function along the lines-of-sight for each column in the sunspot models. The routine used for the intensity calculation is similar to that of Jess et al. (2012). The filter bandwidths are set to 10 Å for both simulated AIA channels. No line-of-sight velocity or magnetic field information is used in this radiation intensity calculation.

3. COMPARISONS WITH OBSERVATIONS - VERTICAL VELOCITIES AND INTENSITIES

This section details the comparisons between the power structures present in our 6 hour simulations and those observed in the active region NOAA 11092.
As shown in observations, the acoustic halo is a phenomenon especially sensitive to $|\mathbf{B}|$ and to the local field inclination. We firstly demonstrate here some of the similarities and differences in these properties exhibited by the artificial sunspots and the real active region.
Figure 3 compares the topology of $|\mathbf{B}|$ and the unsigned field inclination from the vertical (γ) at the surface our 2.7 kG sunspot atmosphere and NOAA 11092.

For the observations of NOAA 11092, $|\mathbf{B}|$ is calculated from the disambiguated vector maps with components B_x, B_y and B_z, where $|\mathbf{B}| = \sqrt{B_x^2 + B_y^2 + B_z^2}$. γ in degrees is then simply defined as $\gamma = 90 - (180/\pi)|\arctan(B_z/B_h)|$ where $B_h = \sqrt{B_x^2 + B_y^2}$.
As can be seen in the figure, the field strength of NOAA 11092 drops off in a similar manner to the artificial sunspot, however the small scale features present in the real active region introduce many variations in both the field and its inclination which are not modelled in our simulations. The behaviour of γ around NOAA 11092 with radius for example is not the smooth monotonically increasing function yielded by the 2.7 kG sunspot model. We can therefore expect some differences between observed and simulated halo structure will result.
Firstly, we compare the acoustic power for v_z - from both the weak (1.4 kG) and strong (2.7 kG) sunspot atmospheres - with the 14 hour time averaged Doppler velocity power from NOAA 11092.
Power maps are shown in Figure 4 for a range of frequencies of interest. The power at every point has been divided by the average power of a quiet corner of the simulation domain, in order to represent an enhancement over quiet values. In both simulations, the enhancement comes into effect at around 5 mHz, when waves are in the non-trapped regime, just as in the observations.
The differences between the two sunspot simulations (rows 1 and 2) are immediately evident, with the 2.7 kG sunspot exhibiting a larger umbra. A consequence of having a stronger magnetic field strength is also that the $a = c$ height will be lower in the atmosphere, resulting in a spreading of this contour for a particular observation height. It is clear that the halo appears correlated with the $a = c$ contour in both cases.
An intriguing feature of the simulated halos is the clear dual-ring structure present for higher frequencies. The inner ring appears to conform qualitatively well at a glance with the observational halo. However the rings appear to be interrupted by a region of mild power deficit (with respect to the quiet sun).
Although not immediately visible in the power maps in the bottom row of Figure 4, observed halos do exhibit a similar structural change when observed at increasingly high frequencies. This feature can clearly be seen in power maps of observed Doppler velocity in Rajaguru et al. (2013) and Hanson et al. (2015) at 8 and 9 mHz respectively.
In section 5 of this paper we discuss how fast-Alfvén conversion likely leads to this dual-ring structure.
Comparing power maps in this way is of only so much use. To more rigorously compare the structure of observed and simulated power halos we plot unfiltered power enhancements as functions of $|\mathbf{B}|$ and ν (i.e. no frequency filter is applied during the fourier transform.) In this way we may fully examine the spectral structure of the halo (Figure 5).
Also present in Figure 5 is the power calculated from the AIA 1700 Å and AIA 1600 Å intensity bands, which we have synthetically calculated in our simulations in order to compare to observations.

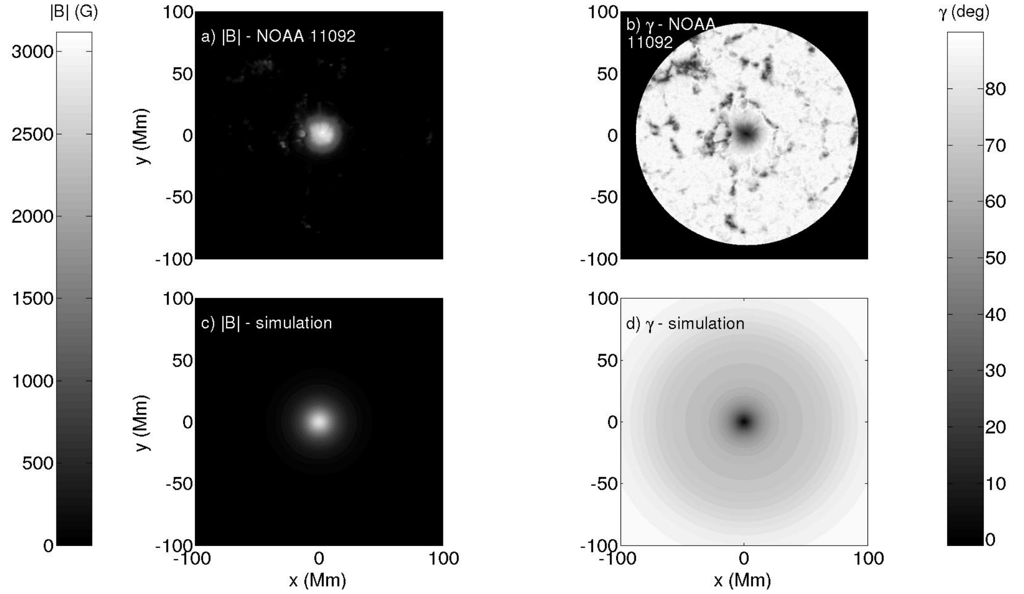

Figure 3. Panels a) and b) show $|\mathbf{B}|$ and the unsigned field inclination from vertical (γ) respectively for NOAA 11092. Panels c) and d) are the counterpart plots for the 2.7 kG simulated sunspot atmosphere.

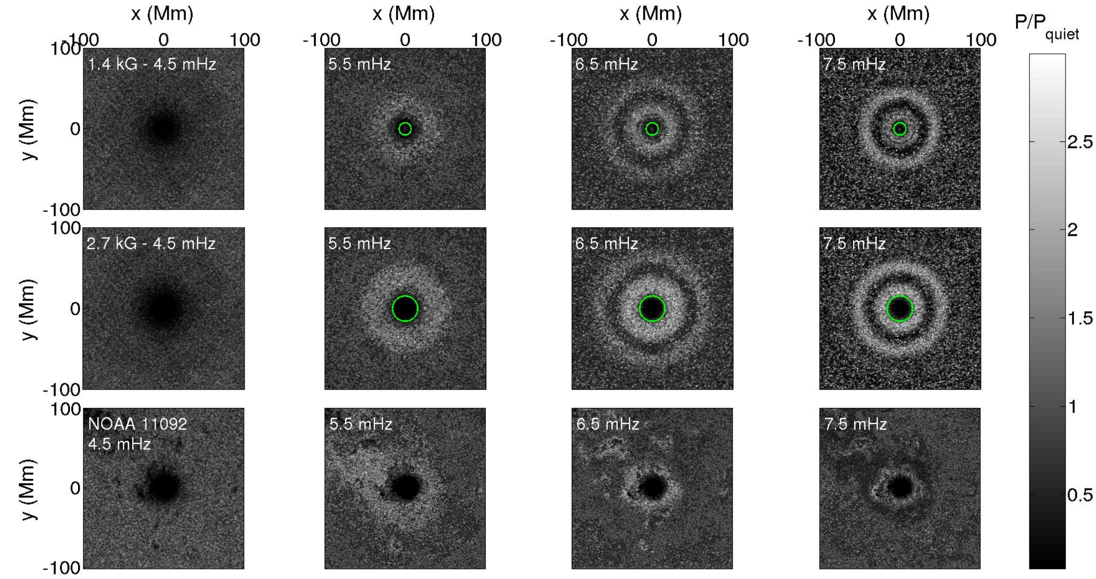

Figure 4. Top row - 6 hr time-averaged v_z power maps at the height of formation of the Fe 6173.34 Å line (z = 140 km) for 4 illustrative frequency ranges for the weak sunspot case (1.4 kG). Middle row - The same power maps for the stronger field case (2.7 kG). Bottom row - 14 hr time averaged observational Doppler velocity power maps of the active region NOAA 11092 for the same frequency ranges. The green contour in rows 1 and 2 is the $a = c$ contour at z = 140 km.

The left hand panels show the NOAA11092 power structure for the Doppler velocity and intensities, whereas the right hand panels correspond to simulation output for the 2.7 kG sunspot atmosphere. To be clear, panel b) of Figure 5 corresponds directly to the power maps in the middle row of Figure 4, it is simply unfiltered in frequency space and so is inclusive of the entire spectral structure. The power at every point has been binned according to the local value of $|\mathbf{B}|$ and then averaged so as to reveal not only the spectral structure of the halo but also how it behaves with respect to field strength.

The first thing to notice in Figure 5 is that the simulated v_z power structure (panel b) matches up reasonably well with the observed Doppler power (panel a). The halo has formed over relatively weak field (50 G < $|\mathbf{B}|$ < 700 G) as expected. In the simulation, $|\mathbf{B}|$ decreases (and γ increases) smoothly and uniformly as one moves away from the umbra. As such this field strength range corresponds to nearly horizontal inclinations of 55°< γ < 75°.
This seems to also agree with all other observational reports of enhancements which place the halo amongst moderate to

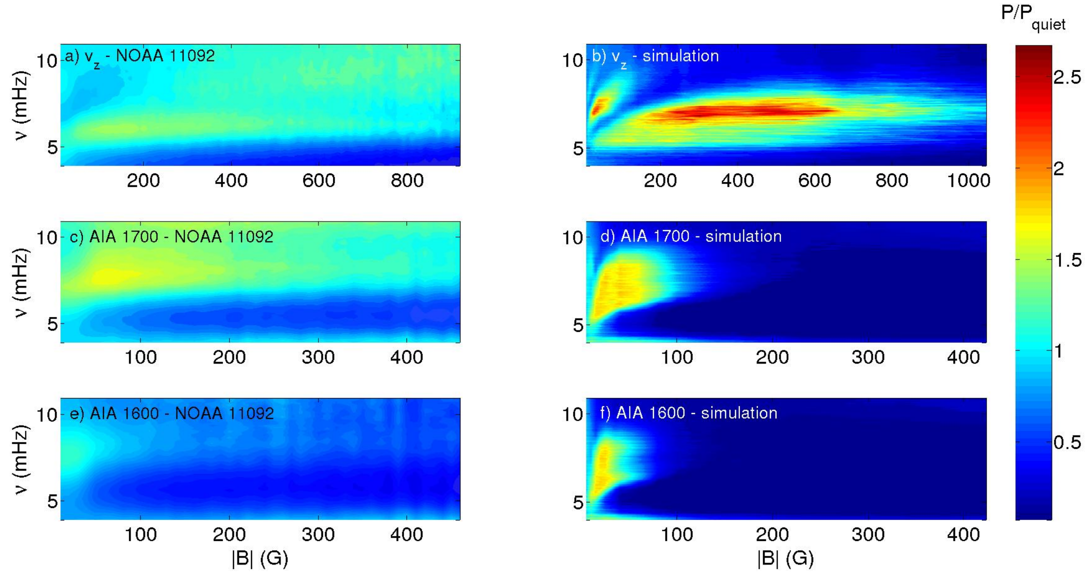

Figure 5. Panel a): Unfiltered Doppler velocity power as a function of $|B|$ and ν. b): 2.7 kG simulation unfiltered v_z power. c) & d): observed and 2.7 kG synthetic unfiltered AIA 1700 power respectively. e) & f): observed and 2.7 kG synthetic unfiltered AIA 1600 power respectively.

weak and horizontally inclined field (Jain & Haber 2002; Schunker & Braun 2011; Rajaguru et al. 2013).

The dual-ring structure can clearly be seen at higher frequencies in panel b), manifesting as the second lobe of enhancement for very weak field. Wedged between the two rings (at around $(|\mathbf{B}|, \nu) = (100, 6)$ is the clear region of power reduction.

Looking at greater heights in the form of the AIA 1700 Å and 1600 Å intensities (corresponding to heights of 360 km and 430 km above the base of the photosphere respectively) we also see a general agreement in $\nu, |\mathbf{B}|$ space. The spreading of the magnetic canopy at these heights has resulted in the intensity halos forming at much weaker field locations both in the observations and the simulations.

The magnitudes of the enhancements in the simulations are consistently larger than the observed values, as evident from this figure. This is a feature that was also noted in Rijs et al. (2015) and can most likely be attributed to the fact that our sunspot is symmetric and its magnetic field inclination is a steep, monotonically decreasing function of radial distance. The MHS structure is such that horizontal field is enforced at the side boundaries of the simulation domain and so there is a large expanse of nearly horizontal field. As explained previously, the fast-slow mode conversion mechanism for the generation of the halo relies on a large attack angle between wavevector and field and so, in analysing v_z power enhancements, it is reasonable to expect that this horizontal field will be very conducive to the conversion of energy into magnetic fast waves and hence, a prominent halo.

Power derived from the 5000 Å intensity continuum (at $z = 0$) was also calculated synthetically to compare with the observational intensity continuum power. It is well known that halos do not appear in measurements of intensity continuum power and we also found this to be the case, with no enhancement present.

Another intersting result, shown in Figure 6, is the comparison between observed and simulated phase shifts. A net upward or downward propagation of waves in an atmosphere can be diagnosed by calculating the temporal cross-spectrum of any wave quantity sampled at two different heights.

For example, for velocities $v(z_1, t)$ and $v(z_2, t)$ sampled at two different heights z_1 and z_2, the phase shift corresponding to a height evolution of the wave is given by the argument or phase of the complex cross-spectrum,

$$\phi_{1,2}(\nu) = \arg[\mathbf{V}(z_1, \nu)\mathbf{V}^*(z_2, \nu)], \tag{2}$$

where $\mathbf{V}$ is the Fourier transform of v. In the above convention, a positive phase-shift would mean that the wave is propagating from height z_1 to z_2, while the opposite holds for a negative phase-shift.

The phase shift contour maps of Figure 6 describe the phase shifts of waves at the AIA 1700 Å and 1600 Å intensity formation ($z = 360$ km and 430 km respectively) with respect to those at the height of formation of the intensity continuum.

The simulation yields a clean band of positive phase shifts at halo frequencies with respect to those at the surface at weak field regions. The same basic pattern is seen in the observations, however there is some extended phase shift structure at higher field strengths in the AIA 1700 Å power (panel a) which is not replicated in the simulation.

The simulation phase shifts are also of a greater magnitude than observations - particularly in the case of the AIA 1600 intensities.

These variations in features are not too surprising. Considering Figure 3 we see that NOAA 11092 exhibits a much more rapid horizontality of field away from the umbra than seen in the MHS model. We show in section 5 how these bands of positive phase shifts at given observation heights may be intrinsically related to the process of fast-Alfvén mode conversion. The physics of fast-Alfvén mode conversion are strongly tied to the local magnetic field inclination. Therefore the reason that NOAA 11092 exhibits such an extended phase shift structure into higher field regions (and our MHS sunspot does not) may be in part due to the more horizontal field at those radii for the active region.

4. THE THEORETICAL UNDERPINNINGS OF HALOS

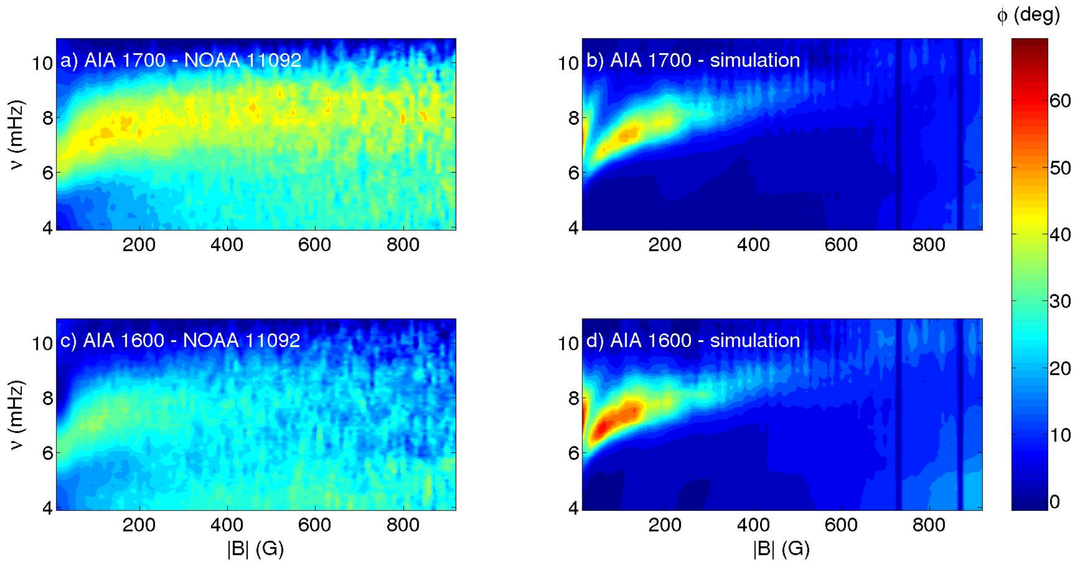

Figure 6. Phase shifts at the heights of formation of the AIA 1700 Å and 1600 Å lines of all waves with respect to those at the surface. Panels a) and c) correspond to observations and b) and d) to the 2.7 kG simulation.

In order to prove that the halo is produced by the return of reflected fast waves, we examine several intriguing features present in our simulations. Firstly, in a similar manner to Rijs et al. (2015) we perform several identical simulations to the 2.7 kG case examined above, except with incrementally smaller Alfvén limiter values.

After undergoing mode conversion at around the $a = c$ height, fast magnetic waves will begin to refract and then ultimately reflect at the point in the atmosphere where the horizontal phase speed equals the Alfvén speed (i.e. where $\omega/k_h = a$).

By reducing the height of the artificial 'cap' on the atmosphere we are allowing less and less room for fast waves to refract and deposit extra energy onto observable heights. Waves that impinge on the altered region of constant a will simply travel upwards and out of the top of the local area. As the original simulation had a value of $a_{lim} = 90$ km/s, we run simulations with $a_{lim} = 40$, 20 and 12 km/s and analyse the power in a similar manner to Figure 5, i.e. as a function of $|\mathbf{B}|$ and ν. The comparison is shown in Figure 7.

Panel d) corresponds to the case where the limiter is only barely above the $a = c$ height, enabling the mode conversion to take effect but yielding virtually no room for fast waves to return. Moreover in the intermediate cases of panels b) and c), the magnitude is reduced as the more vertically oriented waves are escaping to the top of the box, yielding contributions from only the more horizontally inclined waves.

Clearly the halo is entirely dependent on the overlying atmosphere and by restricting the refraction and return of the fast waves the enhancement is entirely absent.

The second theoretical check we perform is to compare the structure of the halo resulting from both the horizontal and vertical components of the velocity. A reasonable attack angle between the horizontal component of the wavevector, k_h and $\mathbf{B}$ is still entirely likely in our simulations, as the field is never entirely horizontal. Also, as noted by Khomenko & Collados (2009) we can expect that it would at least be of a similar strength to the v_z halo, as waves are largely horizontal at around the refraction height.

Figure 8 shows the comparison. A clear feature is that the v_h enhancement occurs at preferentially higher field strength than the v_z enhancement. This feature also makes sense as the field inclination is more vertical at these radii, providing a larger attack angle.

It would be extremely useful if there were any center-to-limb observational studies of halo features, so that we could compare the horizontal Doppler component with our v_h. Zharkov et al. (2009) have performed an analysis of the umbral "belly button" as a function of observation angle, but as of yet, no such studies focusing on halo properties have been conducted.

Finally, and perhaps most importantly, we explain the "dual-ring" power enhancement structure seen in the power maps earlier and in observations.

In Figure 9 we compare v_z power (once again at the standard observational height of 140 km) for both the 1.4 kG and the 2.7 kG simulations with the phase shifts at the same height. The phase shifts in this case are those calculated at $z = 140$ km height, with respect to waves at $z = 0$, so we are only looking at the phase shifts that the waves experience over a height change of 140 km in the simulation.

The black curves have been added simply by eye to aid in the comparisons here. In both simulations there is a similar phase shift pattern to that observed in both the simulated and observed intensities at greater heights, however the magnitude is less here as the waves have travelled a shorter vertical distance.

The key fact to note is that the strong branch of positive phase shifts corresponds precisely to the region between the dual rings of power enhancement. This enhancement gap in $|\mathbf{B}|$, ν space is the dark 'moat' seen between the two halo rings at various frequencies in the simulation power maps of Figure 4. The halo itself shows no real phase shift which most likely indicates a mixture of upwards and downwards travelling waves. This is to be expected at high, non-trapped frequencies as waves rise upwards towards the $a = c$ layer and are refracted back downwards. The halo structure itself does not appear to change too significantly with respect to the peak magnetic

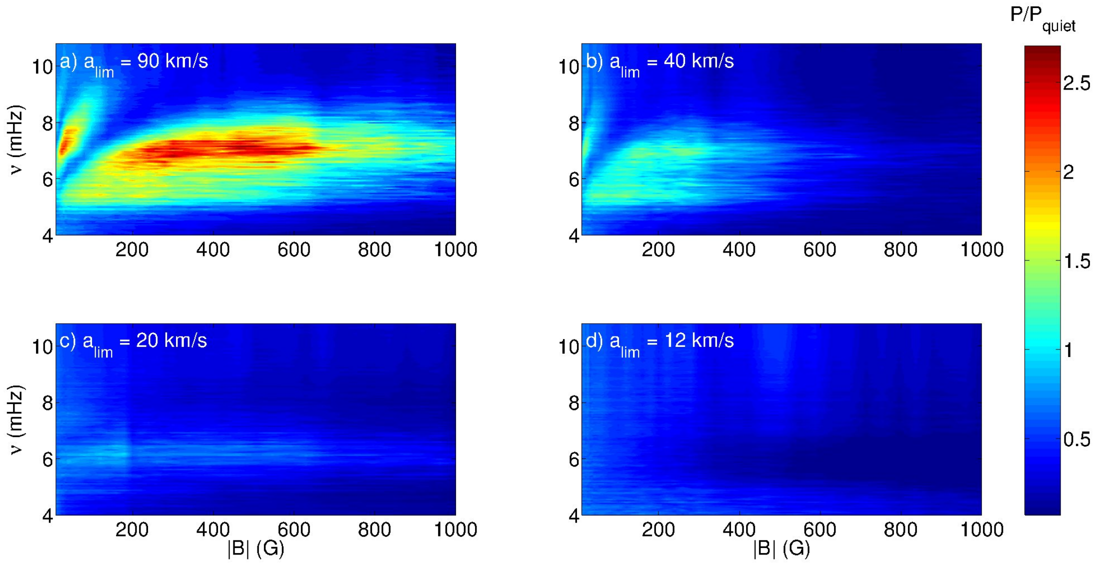

Figure 7. Panel a): Unfiltered v_z power halos in the case a_{lim} = 90 km/s. b), c) and d) show the same quantity from simulations with progressively lower values of a_{lim}.

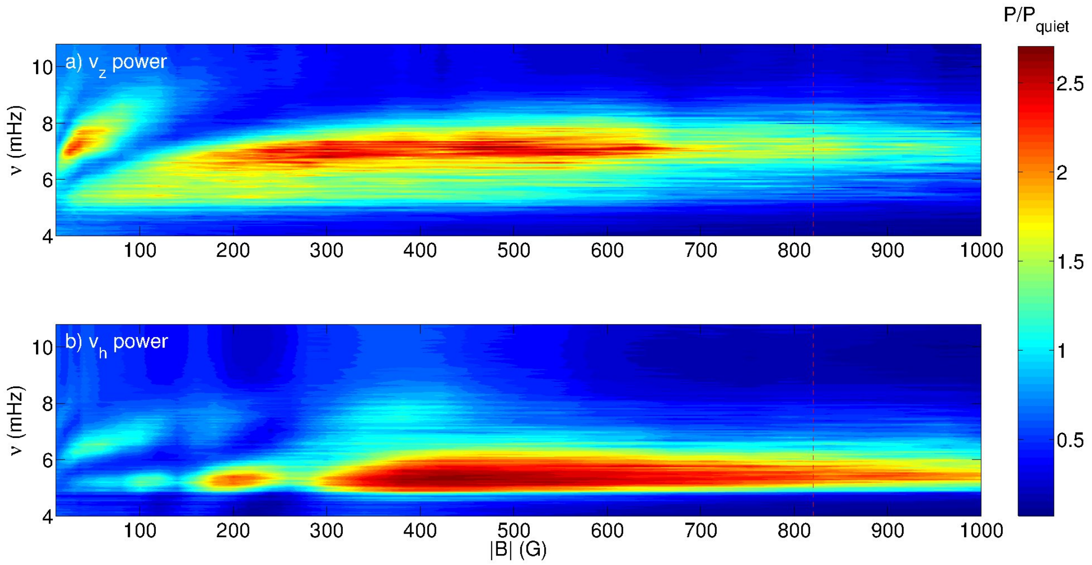

Figure 8. Panel a) is the standard binned v_z power for the 2.7 kG atmosphere. Panel b) is the binned power corresponding to the horizontal component of velocity, v_h. The dashed vertical line is the position of the $a = c$ for the observational height of z = 140 km.

field strength of the model, apart from the noted correlation with the $a = c$ layer. We certainly do not see any noticeable change in the peak halo frequency, as Khomenko & Collados (2009) suggested may be the case. This is most likely due to the fact that, although the peak field strengths of the two models are considerably different in the umbra (1.4 kG and 2.7 kG), at the halo radius (some 20 Mm out) the difference in the field strength will not be so significant.

The pertinent question is: why are there only upwards travelling waves in the moat in between the concentric halos?

5. FAST WAVE DAMPING AND ALFVÉN WAVES

The answer would appear to lie in the process of fast-Alfvén mode conversion, the basics of which are described in Cally (2011) and Cally & Hansen (2011).

Fast-Alfvén mode conversion has been well studied in both sunspot-like (Moradi & Cally 2014; Moradi et al. 2015) and simple magnetic field geometries: Pascoe et al. (2011, 2012) have studied the damping of transverse kink waves in terms of the associated Alfvén resonance and Cally & Goossens (2008) and later Khomenko & Cally (2011) have conducted parameter studies with monchromatic wave sources and simple inclined field magnetic structures. The finding of the latter two works was that fast wave energy is converted to the field-aligned Alfvén wave at favoured field inclinations (θ) and wavevector-to-field angles (ϕ). The process is also strongly dependent on both ν and k_h.

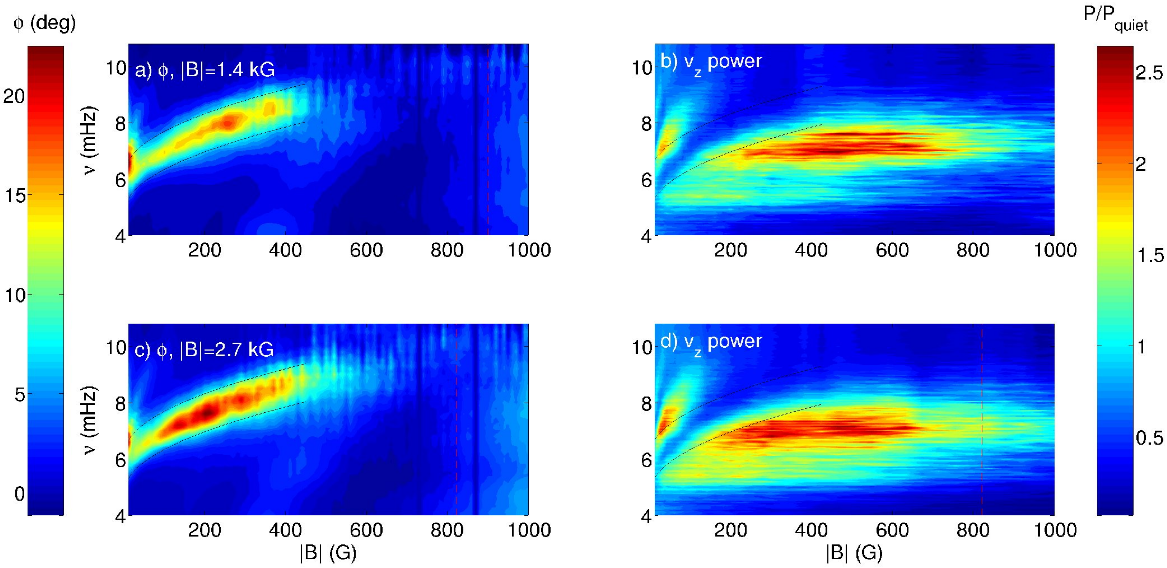

Figure 9. The top row corresponds to the weak field simulation, with peak field strength 1.4 kG, and the bottom row is from the strong field case (2.7 kG peak). On the left are phase shifts calculated at $z = 140$ km in height. On the right are the standard binned and unfiltered v_z power distributions. The black curves are drawn by eye to denote where the phase shifts would be in the power plots. Once again, the dashed vertical line is the position of the $a = c$ for the observational height.

In the case of our distributed source simulations, waves exhibit a distribution of wavenumbers and frequencies in a similar manner to the quiet sun and so the picture is somewhat muddied in comparison to such simulations. We can expect however that fast-Alfvén conversion will in some way act on fast waves as they reach the Alfvén resonance near their upper turning point (on the order of a few hundred kilometres above the $a = c$, depending on k_h).

As the halo appears to be generated by downwards turning fast waves, we would anticipate that some of this returning energy may be lost to the field aligned Alfvén wave, which will follow the local field lines until reaching the top (or the side) of the simulation domain.

In Figure 4 we noted the strong concentric halos and the gap of power enhancement in between them. Figure 9 shows this more comprehensively and associates this dark ring with a strong positive phase shift.

We suggest that the reason that the halo is not one continuous region is that for specific field inclinations, fast mode energy is lost to the Alfvén wave.

Figure 10 suggests this to be the case. Each panel of the figure corresponds to a specific frequency filtering. The top halves of the panels are the same as the panels in the middle row of Figure 4, i.e. filtered power maps corresponding to the stronger field 2.7 kG simulation at the Doppler velocity observational height of 140 km.

The bottom halves of the panels show the magnetic energy associated with the Alfvén wave in the form of the Poynting vector, **S**, where

$$\mathbf{S} = \frac{1}{\mu_0}(-\mathbf{v} \times \mathbf{B}) \times \mathbf{b}, \tag{3}$$

where **v** and **b** indicate the perturbations to the velocity and the background field respectively. The bottom panels show the vertical component of the vector, S_z, corresponding to the upcoming Alfvén flux, and are calculated at the very top of the simulation domain, at a height $z = 2$ Mm, just before the PML comes into effect at the top of the box. In each case the velocity has been pre-filtered around the associated frequency range prior to the calculation of S_z to match the power maps.

It is worth remembering that we have applied a cap to a above $a = 90$ km/s in the atmosphere and so any upwards travelling Alfvén waves will encounter our modified atmosphere and travel at a constant speed to the top of the box, instead of being subject to a rapidly increasing Alfvén speed.

The correlation between the Alfvén flux and the position of the dark ring is immediately noticeable, especially in the 5.5 and 6.5 mHz cases. Note that upwards travelling Alfvén waves will follow the field and that there is some field spreading with height in this MHS atmosphere which is why S_z is diffuse and does not align precisely with the dark ring at observation heights.

It seems clear that this Alfvén wave energy is responsible for the strong band of positive phase shifts (and thus upwards travelling waves) in the dark moat. There is no wave energy left to return downwards at these radii and field inclinations. Furthermore this supports the fast-wave halo mechanism rather strongly as the two processes are critically interlinked.

6. DISCUSSION AND CONCLUSION

Linear forward modelling in realistic MHS sunspot atmospheres has yielded acoustic halos that match up quite well with observations, both spatially and spectrally. Apart from the magnitudes of the enhancements themselves, most observed features seem to be reproduced in our simulations, not just when comparing Doppler and vertical velocities, but also intensity halos at multiple heights in the chromosphere. As in the observations we see no power enhancement in calculations of the time-averaged intensity continuum power.

We have also presented convincing evidence that the mechanism responsible for halo formation is the refraction and return of magneto-acoustic fast waves at non-trapped frequencies. The halo appears very sensitive to the position of the $a = c$ layer in the atmosphere, which is the critical loca-

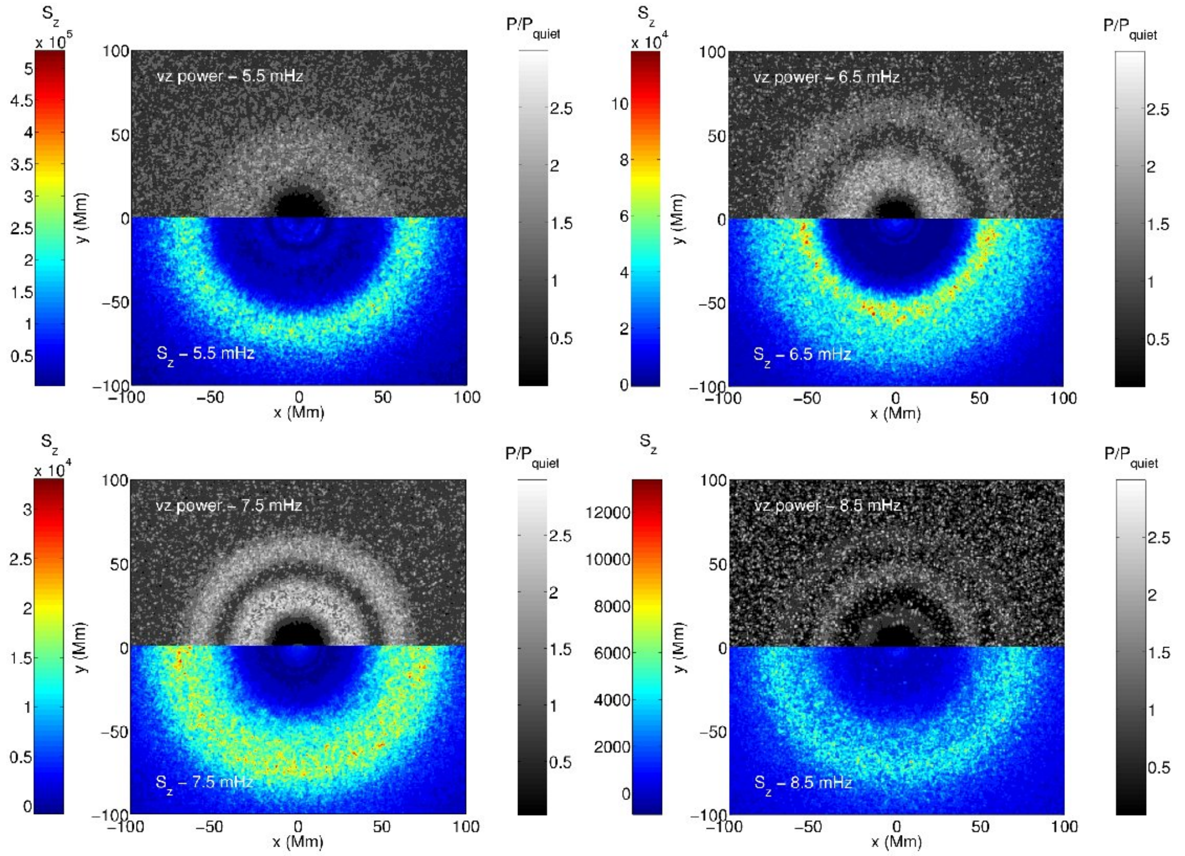

Figure 10. Power map - Poynting vector composites. Top halves are xy power maps at $z = 140$ km, filtered around the respective frequencies. Bottom halves are S_z in units of ergs/$m^2 s$, calculated at $z = 2$ Mm. Note that the Poynting vector scaling is not consistent from plot to plot, as there is significalty less energy arriving at the top of the box for each subsequently higher non-trapped frequency range.

tion for fast-wave mode conversion. With our realistic distributed wave source, we see a strong relationship between the strength of the halo and the extent to which fast waves are allowed to return downwards. This suggests that the halo is completely governed by the overlying $a > c$ atmosphere and the extra energy injected to observable heights by these returning fast waves.

The theory also predicts that an enhancement should be present in the power of v_h, as this component will also interact with the field, and that this enhancement should be concentrated toward more vertical field (as the horizontal component makes a larger attack angle with vertical field); this was shown to be the case as well. Unfortunately center-to-limb observational studies of the halo do not yet exist and so we cannot compare this horizontal velocity halo to the real thing.

Our simulations are performed in a MHS atmosphere, solving the linear MHD equations and using a wave excitation mechanism that approximates the wave bath of the solar photosphere. The fact that we see halos in such simulations (which are of course, entirely non-radiative and do not in any way include convective effects) suggests that the halo is not created by any convective cell-magnetic field interaction as suggested by Jacoutot et al. (2008).

Similarly, the idea of Kuridze et al. (2008) that $m > 1$ waves may become trapped in magnetic canopy structures cannot occur in our simulations as the field configuration is horizontally enforced at the boundaries and there is therefore no downwards oriented canopy.

The scattering mechanism of Hanasoge (2009) also cannot explain why the magnitude of the halo is determined entirely by the structure of the overlying atmosphere, as we have seen here.

As noted previously (and as can be seen in Figure 5 in particular), the primary difference between our simulated halos and those actually observed in the photosphere and chromosphere is the magnitude of the enhancement itself. Observed Doppler velocity halos have magnitudes up to 60% (over the quiet sun average at the same height). Our simulated v_z halos are greater than this by a factor of 2 or even 3, depending on frequency.

There are several possible explanations for this discrepancy. As we have postulated, the halo enhancement most likely occurs as a result of fast waves interacting with the sunspot magnetic field at large attack angles. This yields a large conversion fraction to the fast magnetic wave which refracts and deposits additional energy in the photopshere and chromosphere. The penumbral field structure of active regions differs significantly from the simple MHS model used here however. Our atmosphere does not explicitly include an umbra or penumbra, but rather consists of a smoothly decreasing field strength and vertical inclination component, yielding significant regions of smooth, nearly-horizontal field. Non-trapped waves which reach the $a = c$ equipartition layer will have a large vertical component and so we would expect these waves to interact strongly with primarily horizontal field. In nature, penumbrae contain fine structure, with bright and dark filaments giving rise to the now well-observed combed magnetic field configuration (Scharmer et al. 2002; Bellot Rubio et al. 2004). At the outer penumbral boundary, studies have shown up to a 60° difference in field inclination between dark (largely horizontal) and light (largely vertical) filaments (Weiss et al. 2004; Thomas et al. 2006). Energy corresponding to waves interacting with nearly vertical field at these radii would therefore be lost, transmitting primarily to the slow magneto-acoustic mode. This would have an overall effect of weakening the halo, and as these features are not represented in our model, they may be a contributing factor for our high halo magnitudes.

Another factor to consider is the non-ideal nature of the photosphere, which contains a large neutral component (Krasnoselskikh et al. 2010; Khomenko & Collados 2012). In our ideal MHD assumption we assume full ionization, and thus neglect any dissipative effects brought about by ion-neutral collisions. It is conceivable that these partial ionization dissipative effects (as well as any other dissipation brought about by small scale magnetic structure) in the real photosphere and chromosphere may reduce the observed velocity and intensity halos.

With regards to intensity halos, Figure 5 shows a good agreement between the magnitudes of the observed and simulated AIA 1700 Å halo. However the observed AIA 1600 Å halo is very weak, in contrast to the simulation. This may be due to the larger height range over which observational intensities are calculated. In particular, the height over which the AIA 1600 Å intensity band is determined observationally is some 185 km (centered at 430 km in height) (Fossum & Carlsson 2005), which may have the effect of smoothing out the 1600 Å intensity power, given that the corresponding synthetic intensities encompass a much narrower height range.

In our final discovery of note we have shown that not just fast-slow mode conversion but also fast-Alfvén conversion plays a considerable role in the formation of the halo. This conversion of the fast wave at preferential field inclinations takes energy away along the field lines in the form of the transverse Alfvén wave, resulting in the dual-ring halo structure seen at high frequency. In our simulations this is visible at 6.5 mHz and above - the halo is essentially being broken up into two concentric rings by this Alfvénic energy loss. Observationally this may help to explain the underlying process responsible for the 8-9 mHz dual-ring power halo structure (Hanson et al. 2015; Rajaguru et al. 2013), with its spatially localized zone of enhancement, dark moat and diffuse enhancement region structure.

The above work would not have been possible without the generous computing time provided by the center for Astrophysics and Supercomputing at Swinburne University of Technology (Australia), the Multi-modal Australian ScienceS Imaging and Visualisation Environment (MASSIVE; www.massive.org.au) and the NCI National Facility systems at the Australian National University.

REFERENCES

Avrett, E. H. 1981, in The Physics of Sunspots, ed. L. E. Cram & J. H. Thomas, 235–255
Bellot Rubio, L. R., Balthasar, H., & Collados, M. 2004, A&A, 427, 319
Bogdan, T. J., Hindman, B. W., Cally, P. S., & Charbonneau, P. 1996, ApJ, 465, 406
Braun, D. C., Duvall, Jr., T. L., & Labonte, B. J. 1987, ApJL, 319, L27
Braun, D. C., Lindsey, C., Fan, Y., & Jefferies, S. M. 1992, ApJ, 392, 739
Brown, T. M., Bogdan, T. J., Lites, B. W., & Thomas, J. H. 1992, ApJL, 394, L65
Cally, P. S. 2006, Royal Society of London Philosophical Transactions Series A, 364, 333
—. 2007, Astronomische Nachrichten, 328, 286
Cally, P. S. 2011, in Astronomical Society of India Conference Series, Vol. 2, Astronomical Society of India Conference Series, 221–227
Cally, P. S., & Bogdan, T. J. 1997, ApJL, 486, L67
Cally, P. S., Crouch, A. D., & Braun, D. C. 2003, MNRAS, 346, 381
Cally, P. S., & Goossens, M. 2008, SoPh, 251, 251
Cally, P. S., & Hansen, S. C. 2011, ApJ, 738, 119
Cally, P. S., & Moradi, H. 2013, MNRAS, 435, 2589
Christensen-Dalsgaard, J., et al. 1996, Science, 272, 1286
Finsterle, W., Jefferies, S. M., Cacciani, A., Rapex, P., & McIntosh, S. W. 2004, ApJL, 613, L185
Fleck, B., Couvidat, S., & Straus, T. 2011, SoPh, 271, 27
Fossum, A., & Carlsson, M. 2005, ApJ, 625, 556
Hanasoge, S. M. 2007, PhD thesis, Stanford University
—. 2009, A&A, 503, 595
Hanasoge, S. M., Duvall, Jr., T. L., & Couvidat, S. 2007, ApJ, 664, 1234
Hanson, C. S., Donea, A. C., & Leka, K. D. 2015, SoPh
Hindman, B. W., & Brown, T. M. 1998, ApJ, 504, 1029
Jacoutot, L., Kosovichev, A. G., Wray, A., & Mansour, N. N. 2008, ApJL, 684, L51
Jain, R., & Haber, D. 2002, A&A, 387, 1092
Jess, D. B., Shelyag, S., Mathioudakis, M., Keys, P. H., Christian, D. J., & Keenan, F. P. 2012, ApJ, 746, 183
Khomenko, E., & Cally, P. S. 2011, Journal of Physics Conference Series, 271, 012042
Khomenko, E., & Collados, M. 2008, ApJ, 689, 1379
—. 2009, A&A, 506, L5
—. 2012, ApJ, 747, 87
Krasnoselskikh, V., Vekstein, G., Hudson, H. S., Bale, S. D., & Abbett, W. P. 2010, ApJ, 724, 1542
Kuridze, D., Zaqarashvili, T. V., Shergelashvili, B. M., & Poedts, S. 2008, Annales Geophysicae, 26, 2983
Kurucz, R. 1993, ATLAS9 Stellar Atmosphere Programs and 2 km/s grid. Kurucz CD-ROM No. 13. Cambridge, Mass.: Smithsonian Astrophysical Observatory, 1993., 13
Lemen, J. R., et al. 2012, SoPh, 275, 17
Low, B. C. 1980, SoPh, 67, 57
Moradi, H., & Cally, P. S. 2013, Journal of Physics Conference Series, 440, 012047
—. 2014, ApJL, 782, L26
Moradi, H., Cally, P. S., Przybylski, D., & Shelyag, S. 2015, MNRAS, 449, 3074
Moretti, P. F., Jefferies, S. M., Armstrong, J. D., & McIntosh, S. W. 2007, A&A, 471, 961
Parchevsky, K. V., & Kosovichev, A. G. 2007, ApJ, 666, 547
Pascoe, D. J., Hood, A. W., de Moortel, I., & Wright, A. N. 2012, A&A, 539, A37
Pascoe, D. J., Wright, A. N., & De Moortel, I. 2011, ApJ, 731, 73
Pizzo, V. J. 1986, ApJ, 302, 785
Przybylski, D., Shelyag, S., & Cally, P. S. 2015, ApJ, 807, 20
Rajaguru, S. P., Couvidat, S., Sun, X., Hayashi, K., & Schunker, H. 2013, SoPh, 287, 107
Rempel, M., Schüssler, M., & Knölker, M. 2009, ApJ, 691, 640
Rijs, C., Moradi, H., Przybylski, D., & Cally, P. S. 2015, ApJ, 801, 27
Scharmer, G. B., Gudiksen, B. V., Kiselman, D., Löfdahl, M. G., & Rouppe van der Voort, L. H. M. 2002, Nat, 420, 151
Scherrer, P. H., et al. 1995, SoPh, 162, 129
—. 2012, SoPh, 275, 207
Schunker, H., & Braun, D. C. 2011, SoPh, 268, 349
Schunker, H., & Cally, P. S. 2006, MNRAS, 372, 551
Spruit, H. C., & Bogdan, T. J. 1992, ApJL, 391, L109
Thomas, J. H., Weiss, N. O., Tobias, S. M., & Brummell, N. H. 2006, A&A, 452, 1089
Toner, C. G., & Labonte, B. J. 1993, ApJ, 415, 847
Vernazza, J. E., Avrett, E. H., & Loeser, R. 1981, ApJS, 45, 635
Weiss, N. O., Thomas, J. H., Brummell, N. H., & Tobias, S. M. 2004, ApJ, 600, 1073
Zharkov, S., Shelyag, S., Fedun, V., Erdélyi, R., & Thompson, M. J. 2009, ArXiv e-prints

Appendix C

Directional time-distance probing of model sunspot atmospheres

By H. Moradi, P.S. Cally, D. Przybylski, and S. Shelyag.

Published 2015, MNRAS, 449,3,3074

Monash University

Declaration for Thesis Appendix C

Declaration by candidate

In the case of Appendix C, the nature and extent of my contribution to the work was the following:

Nature of contribution	**Extent of contribution (%)**
Assistance in code and model development.	5

The following co-authors contributed to the work. If co-authors are students at Monash University, the extent of their contribution in percentage terms must be stated:

Name	**Nature of contribution**	**Extent of contribution (%) for student co-authors only**
Hamed Moradi	Key ideas, development of code, modelling, production of all results, writing of paper.	
Paul Cally	Assistance in modelling.	
Sergiy Shelyag	Assistance in code and model development.	

The undersigned hereby certify that the above declaration correctly reflects the nature and extent of the candidate's and co-authors' contributions to this work*.

Candidate's Signature	D Przybylski	**Date**	
Main Supervisor's Signature	P. Cally	**Date** 17/2/17	

*Note: Where the responsible author is not the candidate's main supervisor, the main supervisor should consult with the responsible author to agree on the respective contributions of the authors.

Mon. Not. R. Astron. Soc. **000**, 000–000 (0000) Printed 17 March 2015 (MN LaTeX style file v2.2)

Directional Time-Distance Probing of Model Sunspot Atmospheres

H. Moradi, ⋆ P. S. Cally, D. Przybylski and S. Shelyag
Monash Centre for Astrophysics and School of Mathematical Sciences, Monash University, Victoria, Australia 3800

17 March 2015

ABSTRACT

A crucial feature not widely accounted for in local helioseismology is that surface magnetic regions actually open a window from the interior into the solar atmosphere, and that the seismic waves leak through this window, reflect high in the atmosphere, and then re-enter the interior to rejoin the seismic wave field normally confined there. In a series of recent numerical studies using translation invariant atmospheres, we utilised a "directional time-distance helioseismology" measurement scheme to study the implications of the returning fast and Alfvén waves higher up in the solar atmosphere on the seismology at the photosphere (Cally & Moradi 2013; Moradi & Cally 2014). In this study, we extend our directional time-distance analysis to more realistic sunspot-like atmospheres to better understand the direct effects of the magnetic field on helioseismic travel-time measurements in sunspots. In line with our previous findings, we uncover a distinct frequency-dependant directional behaviour in the travel-time measurements, consistent with the signatures of MHD mode conversion. We found this to be the case regardless of the sunspot field strength or depth of its Wilson depression. We also isolated and analysed the direct contribution from purely thermal perturbations to the measured travel times, finding that waves propagating in the umbra are much more sensitive to the underlying thermal effects of the sunspot.

Key words: Sun: helioseismology – Sun: oscillations – Sun: surface magnetism

1 INTRODUCTION

Sunspots and active regions (magnetic flux concentrations tens of thousands of kilometres across containing sunspots) are the most visible manifestation of solar magnetic activity on the solar surface. A detailed understanding of sunspots and magnetically active regions is therefore essential in order to establish accurate physical relationships between internal solar properties and magnetic activity in the photosphere.

Using observations of surface oscillations, helioseismology provides the most effective way to observationally probe structure inside the Sun. The combination of high spatial resolution, continuous observing, and simultaneous vector magnetograms provided by the Helioseismic and Magnetic Imager (HMI) instrument on board the Solar Dynamics Observatory (SDO) delivers unprecedented probing of magnetic active regions and sunspots.

However, important developments in the techniques of local helioseismology (i.e., both theoretical and observational) are required to realize the full potential that these observations offer. As highlighted by a number of detailed comparative studies and reviews on the matter (e.g., Gizon et al. 2009; Moradi et al. 2010; Moradi 2012), major challenges exist in the development of new helioseismic procedures that are robust in the presence of magnetism and capable of probing both subsurface magnetic structures and associated flows.

Over the years various local helioseismic techniques have substantially contributed to our understanding of the solar interior (see Gizon, Birch & Spruit 2010, for a comprehensive review). The most widely used measurement method in local helioseismology is time-distance helioseismology (Duvall et al. 1993). By correlating observations of Doppler velocity at different times and positions on the solar surface, a causative link is inferred and a travel time between pairs of points putatively determined. Comparing these travel times with those calculated for the quiet-Sun, one infers the presence of wave-speed anomalies beneath the surface that may be due to such features as magnetic fields, temperature variations or plasma flows.

With the noise level being substantially larger for group-time measurements (Kosovichev, Duvall & Scherrer 2000), time-distance travel times are typically derived from phase travel-times. While this is adequate for the quiet Sun, in-

⋆ E-mail: hamed.moradi@monash.edu

terpretation becomes more complicated when considering active regions, where phase shifts can naturally arise from changes in wave propagation speed (e.g., due to subsurface flows and sound speed perturbations induced by the presence of the magnetic field), but they can also result from other sources as well. For example, mode damping (Woodard 1997), acoustic source suppression (Gizon & Birch 2002), and the Wilson depression (Brüggen & Spruit 2000; Lindsey & Braun 2000) have all been identified as possible sources of phase shifts in active regions.

Another important source of phase shifts is via MHD mode conversion in the atmosphere. Mode conversion takes place in regions where the sound (c_s) and Alfvén speed (c_a) are comparable. It is expected to be significant for sunspot seismology because in the umbrae of sunspots, the layer where $c_a = c_s$ lies is just a few hundred kilometres below the formation height of the Fe I spectral line of the Helioseismic and Magnetic Imager (HMI) instrument on board the Solar Dynamics Observatory (SDO) .

"Fast- to-slow" mode conversion has been explored as a primary cause of acoustic wave (p-mode) absorption in sunspots for decades (Spruit & Bogdan 1992; Cally, Bogdan & Zweibel 1994; Cally 1995; Crouch & Cally 2003; Shelyag et al. 2009). In this scenario, the $p-$modes emerging in sunspots below the $c_a = c_s$ level are effectively (acoustic) fast waves. On passing through the $c_a = c_s$ layer the p-modes are partially transmitted into the solar atmosphere as (primarily acoustic) slow waves, most efficiently at small "attack angle" (the angle between the wavevector and the magnetic field). The transmitted sound waves propagate longitudinally along field lines at frequencies above the field-adjusted acoustic cutoff frequency and are reflected otherwise (Bel & Leroy 1977). If the attack angle is not small however, significant amounts of energy will be converted to (magnetic) fast waves (Schunker & Cally 2006). These fast waves are then reflected off the Alfvén wave speed gradient, at the height where their horizontal phase speed ($v_{ph} = \omega/k_h$; where ω is the angular frequency and k_h the horizontal wavenumber) is approximately equal to c_a, back down to the surface (having assumed $c_a \gg c_s$ at this level).

More recently it has been realised that fast waves created in this way are further subject to partial conversion to Alfvén waves higher in the atmosphere. Depending on the local relative inclinations and orientations of the background magnetic field and the wavevector, the fast wave may undergo partial mode conversion to either an upward or downward propagating Alfvén wave around the reflection height, where they are near-resonant (Cally & Goossens 2008; Cally & Hansen 2011; Khomenko & Cally 2011, 2012; Felipe 2012). After they reflect off the Alfvén wave speed gradient, the fast waves may re-enter the solar interior wave field. This could be problematic for helioseismology, since any phase changes produced by the "fast-to-Alfvén" mode conversion process would seriously compromise any inferences derived from helioseismic inversions of phase travel times (e.g., Duvall et al. 1996; Kosovichev, Duvall & Scherrer 2000; Couvidat et al. 2005), which would normally, but inaccurately, interpret such phase changes as "travel-time shifts" due to subsurface inhomogeneities alone.

In a series of recent numerical studies (Cally & Moradi 2013; Moradi & Cally 2013, 2014), we quantified the implications of the returning fast and Alfvén waves for the seismology of the photosphere by comparing Alfvénic losses higher up in the solar atmosphere with helioseismic travel-time shifts at the surface. Using 3-D numerical simulations of helioseismic wave propagation in simple translationally invariant atmospheres, we applied a "directional time-distance helioseismology" approach sensitive to magnetic field orientation, finding substantial wave "travel time" discrepancies of several tens of seconds (depending on field strength, frequency, and wavenumber) related to phase changes resulting from mode conversion, and not "actual" travel time changes. These results, which were also verified using the Boundary Value Problem (BVP) method of Cally & Goossens (2008) and Cally (2009), indicated that processes occurring higher up in the atmosphere are strongly influencing the core data products of helioseismology.

In these studies only translation invariant setups were used, which are most useful to study the effect in fundamental terms, but are not typically found on the Sun. Our best chance at constraining the interior structure of sunspots comes with constructing accurate forward models. Hence, in order to be able to make meaningful estimates of the direct role played by MHD mode conversion and wave reflection in helioseismic measurements, we extend our study to more realistic sunspot model atmospheres spanning the subphotosphere ($z = -10$ Mm, with $z = 0$ being the photosphere) to the chromosphere ($z = 1.9$ Mm) and study the sensitivity of directional helioseismology measurements to changes in the photospheric and subsurface structure of sunspot models. For practical computational reasons, we were unable to model the seismic effects of the Transition Region, though Hansen & Cally (2014) find it too has significant signatures.

2 THE BACKGROUND MODEL

The background models we employ consist of a number of azimuthally symmetric magneto-hydrostatic (MHS) sunspot atmospheres adopted from Khomenko & Collados (2008). To summarise, these models consist of a concatenation of a self-similar model in the deep photospheric layers, calculated following the method of Low (1980), with a potential solution above some arbitrary height using the method of Pizzo (1986). The thermodynamic variables for the sunspot axis are taken from the semi-empirical Avrett (1981) umbral-core model, while the "quiet-Sun" atmosphere variables are taken from Model S (Christensen-Dalsgaard et al. 1996) in the deep sub-photospheric layers, smoothly joined to the VAL-C (Vernazza, Avrett & Loeser 1981) model in the photospheric and chromospheric layers, and stabilised using the method outlined by Parchevsky & Kosovichev (2007).

The sunspot models possess a high degree of flexibility for conducting a detailed directional helioseismology study, with a number of variable parameters such as field strength on the axis, field inclination at the photosphere, and spot radius. Another important variable parameter in the models, is the Wilson depression – the height difference between the umbra and photosphere. This can be easily changed in the model by choosing the desired location of the constant optical depth $\log \tau_{5000} = 0$ (the formation height of the 5000 Å continuum radiation) of the semi-empirical umbral model. Studies have shown that the Wilson depression may be a signifiant source of travel time reductions in sunspots (Braun

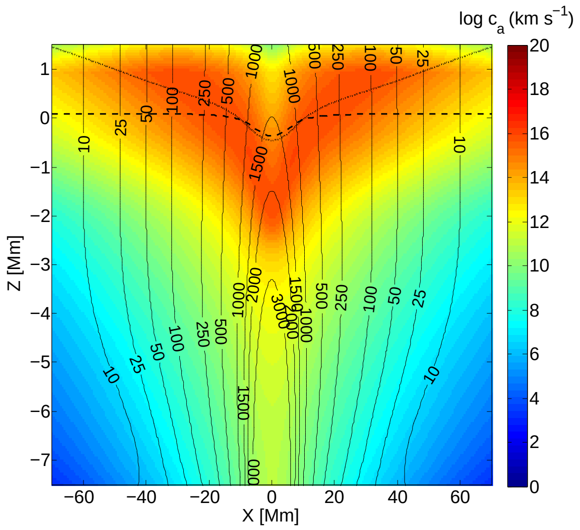

Figure 1. An example of the MHS sunspot atmosphere used in the forward modelling. A cut through $y = 0$ for a 1.5 kG sunspot with a Wilson depression of 400 km is shown here. The background colour-scale corresponds to $\log c_a$ (km s^{-1}). The contour lines represents the field strength (in G). The dotted line indicates the location of the plasma $\beta \approx 1$ layer, while the dashed line represents the reference observation height corresponding to $\log \tau_{5000} = -1.6$.

& Lindsey 2000; Lindsey, Cally & Rempel 2010), so it is important to observe what effects it may have on directional travel-time measurements.

We conduct a number of experiments with the sunspot models. In the first set of experiments, we study the sensitivity of directional travel times to sunspot field strength and inclination using two sunspots models with differing peak photospheric field strengths (1.5 and 2.5 kG) but with all other parameters fixed (i.e., spot size, field inclination at the photosphere and Wilson depression, which is fixed at 400 km). In the second set of experiments, we investigate the sensitivity of the directional travel times to the depth of the Wilson depression. Estimates from observations put the depth of Wilson depression in the range of $300 - 1500$ km (Bray & Loughhead 1964; Martínez Pillet & Vazquez 1993; Mathew et al. 2004; Watson et al. 2009). For our study we employ three identical sunspot models with a relatively moderate surface field strength (1.5 kG) with varying Wilson depressions depths of 300, 400 and 500 km respectively. In our final set of experiments, we ascertain the contribution of the underlying thermal perturbations to the travel-time shifts in contrast to the direct magnetic effects in a sunspot with surface field strength of 1.5 kG and a Wilson depression of 400 km. As shown in Moradi & Cally (2008) and Moradi, Hanasoge & Cally (2009) this can easily be achieved in linear numerical simulations by suppressing the direct magnetic effect on the waves. The combined outcomes from these experiments provide us with valuable diagnostics of both the thermal and magnetic structures of sunspots.

As all sunspot models encompass a Wilson depression, the simulated data are analysed at a constant optical depth $\log \tau_{5000} = -1.6$, which roughly represents the layer where the contribution function for FeI 6173 Å photospheric spectral line has its maximum (Khomenko et al. 2009). The optical depths are calculated using the routine described in Jess et al. (2012) by integrating the continuum and line opacities along the lines-of-sight for each column in the sunspot models. The ATLAS9 package (Kurucz 1993) opacities are used in the computation. We also have the ability to choose the line-of-sight viewing angle (from the vertical), but for simplicity we calculate and compare directional travel times using the photospheric velocity at disk centre. Some properties of these sunspot model atmospheres are shown in Figure 1.

3 THE FORWARD MODEL

As in our previous studies, we numerically solve the linearised equations of ideal MHD using the Seismic Propagation through Active Regions and Convection (SPARC) code (Hanasoge 2007) which has been successfully utilised in the past to study wave propagation through model sunspots (Moradi, Hanasoge & Cally 2009). The dimensions of the 3-D computational box employed for the numerical simulations are 140 Mm in the horizontal (x, y) directions and 11.9 Mm in the vertical (z) direction. The bottom boundary of the domain is located at 10 Mm below the photospheric level $z = 0$. The horizontal grid spacing consists of 256 equidistant points in x and y, with a resulting resolution of $\Delta x = \Delta y \approx 0.55$ km/pixel, while the vertical grid spacing Δz is nonuniform, ranging from tens of kilometres near and above the surface to just over one hundred kilometres near the bottom of the computational domain. The top ~ 500 and bottom ~ 800 km of the box are occupied by the vertical absorbing (PML) boundary layers, while absorbing sponges line the sides of the box.

The axis of the sunspot is placed at the centre of the computational domain. For each sunspot case studied, we conduct ten unique simulations using a Gaussian perturbation source positioned along the left hand side of the sunspot along $y = 0$, starting from the axis ($x = 0$, $y = 0$) and then at nine other locations along the negative x axis, as depicted in Figure 2. As the sunspot model is axisymmetric, this allows us to study each corresponding θ associated with the source location separately.

The acoustic source employed for our calculations is similar to that employed by Shelyag et al. (2009) and Moradi & Cally (2014), where a source term of the form:

$$v_z = \sin \frac{2\pi t}{t_1} \exp\left(-\frac{(r - r_0)^2}{\sigma_r^2}\right) \exp\left(-\frac{(t - t_0)^2}{\sigma_t^2}\right), \quad (1)$$

is added to the right hand side of the vertical momentum equation. In the equation above v_z is the perturbation to the vertical component of the velocity, $t_0 = 300$s, $t_1 = 300$s, $\sigma_t = 100$s, $\sigma_r = 4\Delta x$, and $r_0(x, y)$ is the source position. The source, which is always initiated below the surface at $z = -0.65$ Mm, generates a broad spectrum of acoustic waves in the 3.33 mHz range, mimicking wave excitation in the Sun. For each magnetic case we conduct a separate quiet-Sun run to act as the reference (unperturbed) model.

The relatively large field strengths associated with the sunspot models being considered, coupled with the exponential drop in density with height in the atmosphere, naturally results in a substantial c_a above the surface. For explicit numerical solvers, such as SPARC, this results in severe CFL ($\Delta t \approx \Delta z/c_a$) constraints, significantly compounding the computational expense of conducting a detailed parametric study. To alleviate the problem, we employ a Lorentz Force "limiter" to limit/cap the Alfvén wave speed at a particular value above the surface. This approach is commonly adopted by explicit numerical solvers in computational MHD studies of sunspot structure (Rempel, Schüssler & Knölker 2009; Cameron et al. 2011; Braun et al. 2012), allowing one to increase the simulation Δt to any desired or practical value.

However in Moradi & Cally (2014), we studied the physical implications of imposing an artificial limit on c_a and found that it can severely impact the fast-wave reflection height ($c_a \approx \omega/k_h$) in the sunspot atmosphere, which can be problematic for fast-to-Alfvén mode conversion and any subsequent helioseismic analyses. In fact, we found that unless the c_a cap is placed well above the horizontal phase speed associated with the wave travel distance being studied (thus ensuring minimal damage to the fast-wave reflection height), helioseismic travel time measurements could be severely affected. On the back of these findings, we decided to employ a limiter with a c_a cap at 80 km s^{-1}, but restrict our helioseismic analyses to waves with horizontal phase speeds well below this (see Table 1), so as to ensure our travel time measurements would not be compromised.

4 DIRECTIONAL TIME-DISTANCE HELIOSEISMOLOGY

With single source wave excitation, time-distance diagrams can easily be constructed by plotting the resulting velocity signal as functions of time for all horizontal locations. Moreover, each source location along the negative x-axis corresponds to a specific field inclination θ (from the vertical). As seen in Figure 2, with the source locations we have chosen we can sample θ in the range $0^\circ - 70^\circ$. By selecting a receiver location at a horizontal distance (Δ) away from the source location around the xy-plane, we isolate the magnetic field orientation with respect to the vertical plane of wave propagation, which we refer to as the "azimuthal" field angle (ϕ, where $0 \leqslant \phi \leqslant 180^\circ$, from the right- to the left-hand side of the sunspot) which we sample in 10° bins.

Prior to calculating the travel times, we first filter the data cubes in two frequency ranges: 3 and 5 mHz by employing a Gaussian frequency filter with a dispersion of 0.5 mHz. We also apply an f-mode filter to remove the contribution from surface gravity waves. We then measure the phase travel time perturbations $\delta\tau$ (i.e., the differences in the phase travel times between the magnetic and nonmagnetic simulations) using Gabor wavelet fits (Kosovichev & Duvall 1997) to the time-distance diagram at various Δ away from the source, for each source (θ) receiver (ϕ) pair of points. A rectangular window of width 14 minutes centred on the first-bounce ridge selects the fitting interval in time lag. The fits are done by minimising the misfit between the Gabor wavelet and the wave form. An initial guess of the Gabor wavelet parameter values is obtained by fitting the reference (quiet-Sun) wave form first. We use MATLAB's multidimensional unconstrained nonlinear minimisation routine *fminsearch* for the fitting, which employs the Nelder-Mead simplex algorithm (Lagarias, et al. 1998). This is a direct search method that does not use numerical or analytic gradients. We measured $\delta\tau$ for three typical skip distances Δ (Couvidat et al. 2005). The horizontal phase speeds associated with these distances are presented in Table 1.

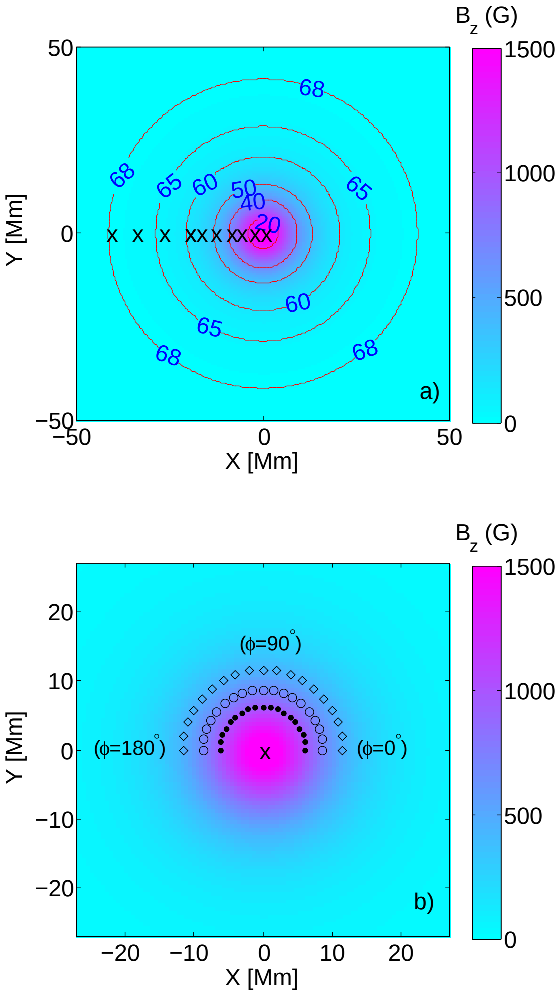

Figure 2. The one-way travel time measurement geometry. In both panels, the background represents the vertical component of magnetic field strength at the observation height $\log\tau_{5000} = -1.6$. In panel a) the contours are indicative of the magnetic field inclination from the vertical (θ in degrees) at the same height in the atmosphere, while the crosses represent the locations of the individual acoustic sources utilised in the forward modelling calculations. Panel b) shows an example of the receiver locations (which span from $0 \leqslant \phi \leqslant 180^\circ$, from the right- to the left-hand side of the sunspot, spaced $\phi = 10^\circ$ apart) for a source initiated at $\theta = 0^\circ$, denoted by the cross on the axis ($x = 0$, $y = 0$). The dots indicate the receiver locations at $\Delta = 6.2$ Mm, the circles $\Delta = 8.7$ Mm, and the diamonds represent $\Delta = 11.6$ Mm.

Table 1. Wave travel distances analysed and their associated horizontal phase speeds in the quiet Sun model.

Δ (Mm)	v_{ph} (km s^{-1})
6.2	12.6
8.7	14.1
11.6	16.4

5 RESULTS & ANALYSIS

5.1 Sensitivity of Directional Travel Times to Frequency, Field Strength and Inclination

The contour plots in Figures 3 and 4 depict the time-distance phase travel-time perturbations (with respect to the quiet solar model) as functions of wave source position/field inclination from vertical θ and receiver location/azimuthal direction ϕ, derived from sunspot models with surface field strengths of 1.5 and 2.5 kG respectively. The results shown are for the two frequency bands analysed, 3 (left column) and 5 (right column) mHz, and for waves which travel a horizontal distance of $\Delta = 6.2$ (panels a-b), 8.7 (panels c-d) and 11.6 Mm (panels e-f) from the source.

Pleasingly, the features we observe in Figures 3 – 4 are very much in accord with the directional travel times derived from previous studies using simple translationally invariant background atmospheres (Cally & Moradi 2013; Moradi & Cally 2014). Specifically, they show a clear manifestation of the acoustic cutoff at $\theta = 30^\circ - 40^\circ$ for 5 mHz and $\theta = 50^\circ - 60^\circ$ at 3 mHz. For θ below the acoustic cutoff, small positive $\delta\tau$ values of a few seconds are apparent. For larger θ (i.e, sufficient for the ramp effect to take hold $\omega > \omega_c \cos\theta$), the atmosphere is open to wave penetration and mode conversion. This results in significant negative $\delta\tau$ for these θ, particularly at small $\sin\phi$ (around 0° and 180°), which is due to the fast magnetically-dominated waves undergoing significant phase enhancement on returning to the surface after passing upward through the $c_a = c_s$ layer, reflecting near $\omega/k_h = c_a$, and finally re-entering the interior via $c_a = c_s$ again. However, away from $\phi = 0$ (and 180°), the fast waves lose energy as they are partially converted to the Alfvén wave, which results in a phase retardation that partially cancels the underlying negative travel time perturbation at small $\sin\phi$. In line with previous studies, the energy loss is at its maximum around $\phi = 80^\circ - 100^\circ$, orientations typically associated with peak fast-to-Alfvén conversion (Khomenko & Cally 2011, 2012; Cally & Moradi 2013).

However unlike our previous studies where the atmosphere and magnetic field were horizontally invariant, the presence of the sunspot, coupled with the distribution of the individual wave sources (on the left-hand side of the sunspot), results in a distinct asymmetry in $\delta\tau$ about ϕ. This is essentially due to one end of the wave path being in a stronger region of perturbation (i.e., inside the sunspot), and the other end being near or inside the "quiet Sun" region, which will naturally result in a directional bias in $\delta\tau$, with larger (negative) $\delta\tau$ expected for $\phi < 50^\circ$ (i.e., waves travelling primarily to the right/inside the "umbra" of our sunspot model). This effect is exacerbated as the wave travel distance is increased, as is evident in Figures 3 – 4 e) and f), for $\Delta = 11.6$ Mm.

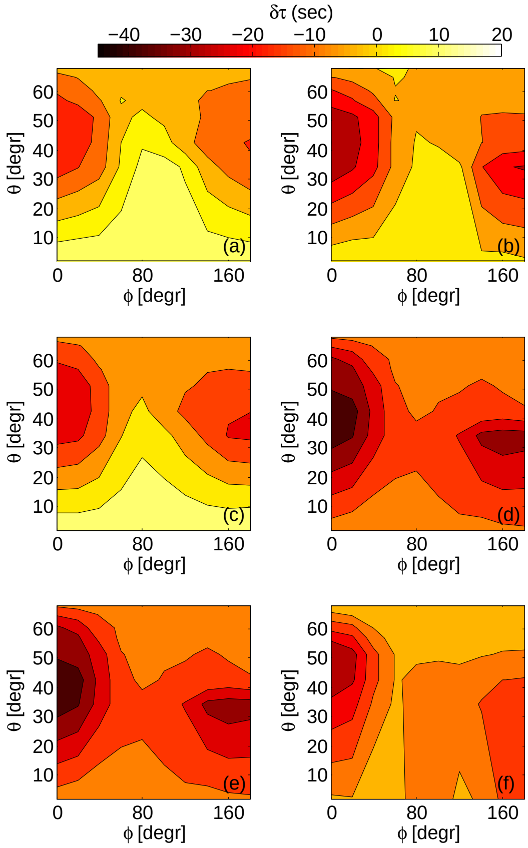

Figure 3. One-way phase travel-time perturbations ($\delta\tau$) derived from the 1.5 kG sunspot model calculations as a function of field inclination (θ) from the vertical, and azimuthal angle (ϕ) for wave travel distances of $\Delta = 6.2$ (a-b), 8.7 (c-d) and 11.6 (e-f) Mm. Left column represents 3 mHz and right column 5 mHz.

As expected, the magnitude of the $\delta\tau$ perturbations is also strongly dependant on frequency and magnetic field strength. Larger negative and smaller positive $\delta\tau$ are observed for all sunspot models and Δ as the frequency is increased from 3 to 5 mHz. This frequency dependance of helioseismic travel times has been well documented in the past (Braun & Lindsey 2000; Chou 2000; Braun & Birch 2006; Couvidat & Rajaguru 2007; Moradi, Hanasoge & Cally 2009). Increasing the field strength of the sunspot naturally shifts the location of the $c_a = c_s$ layer deeper below the surface, but the only direct effect on the directional $\delta\tau$ we observe at the photosphere is an increase in their magnitude at both 3 and 5 mHz for all Δ.

5.2 The Effect of the Wilson Depression

Figure 5 shows the directional $\delta\tau$ derived for $\Delta = 6.2$ Mm for three 1.5 kG sunspot models with varying Wilson depression depths (300, 400 and 500 km), calculated at 3 and 5 mHz. While the general behaviour of $\delta\tau$ across θ and ϕ for all three models is consistent with those derived in section 5.1,

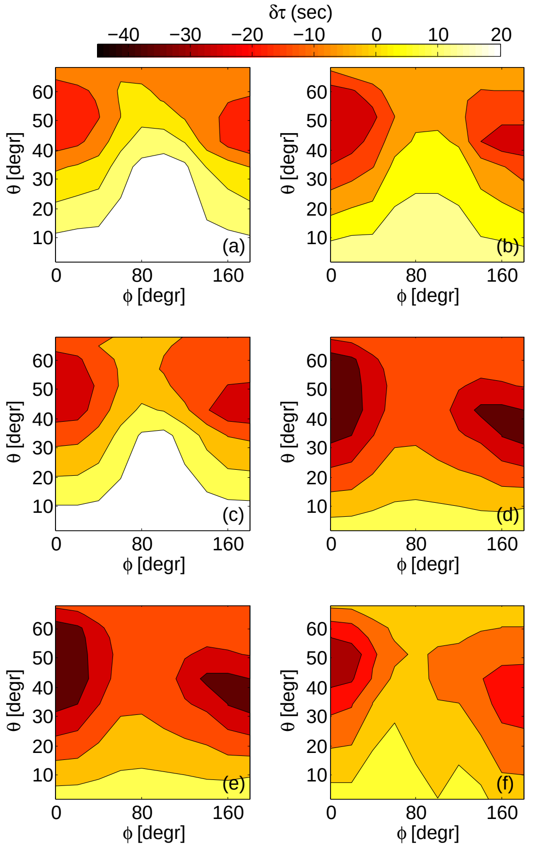

Figure 4. Same as Figure 3 but for the 2.5 kG sunspot model.

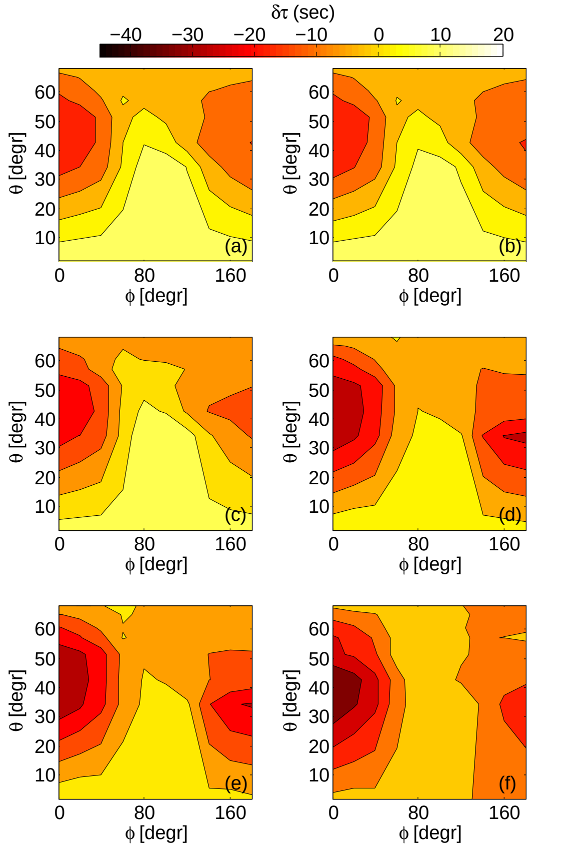

Figure 5. One-way phase travel time perturbations $\delta\tau$ as a function of field inclination from the vertical θ azimuthal angle ϕ for $\Delta = 6.2$ Mm, derived from three 1.5 kG sunspot models with Wilson depression of 300 (a-b), 400 (c-d) and 500 (e-f) km. Left column represents 3 mHz and right column 5 mHz.

it is also apparent that modifying the depth of the Wilson depression can have a direct and measurable impact on the directional travel times.

This is not entirely unexpected of course, as the Wilson depression is a physical displacement in the photosphere which will naturally give rise to a change in the path length of the waves. Modifying the depth of the Wilson depression also implies a change in the near surface density and temperature stratification of the sunspot, which in turn will also modify the actual wave speed (both c_s and c_a), the result of which should manifest itself in the travel time calculations.

These effects are evident in Figure 6, which shows a cut at $\theta \approx 32^\circ$ through Figure 5. Here we can clearly observe faster travel times associated with waves travelling towards the sunspot axis as the Wilson depression is shifted deeper below the surface. While the $\delta\tau$ differences between 300 and 400 km are very subtle (under ~ 1 second), more significant differences in $\delta\tau$ are observed with the Wilson depression at 500 km. At $\phi = 0$ we see a ~ 3 second difference to the $300 - 400$ km cases, and at 5 mHz it's ~ 7 seconds. Waves travelling away from spot centre (large ϕ) do not appear to be affected by the change in Wilson depression depth. We observed a similar behaviour for $\Delta = 8.7$ and 11.7 Mm (but have not shown them here for the sake of brevity).

These results are generally consistent with the recent findings of Schunker et al. (2013), who studied the sensitivity of helioseismic travel times to the depth of the Wilson depression using numerical forward modelling of plane wave packets through non-MHS sunspot model atmospheres. They found that a ~ 50 km change in the Wilson depression can be detected above the observational noise level.

5.3 The Effect of Thermal Perturbations

One of the advantages of forward modelling of waves in a model sunspot atmosphere is that it provides us with the opportunity to isolate the individual effects of the magnetic field and thermal perturbations on travel-time measurements (Moradi & Cally 2008; Moradi, Hanasoge & Cally 2009). In order to isolate the thermal contributions to the measured directional $\delta\tau$, we repeat our single source calculations, this time using a "thermal" sunspot model, where only the thermal perturbations corresponding to the 1.5 kG sunspot model with a Wilson depression of 400 km are

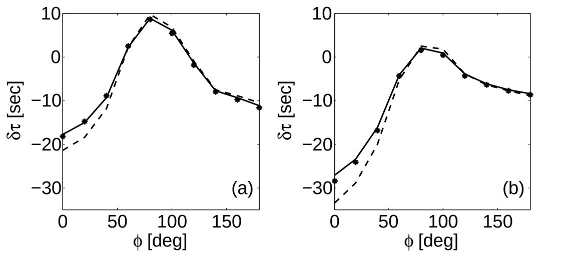

Figure 6. One-way phase travel time perturbations $\delta\tau$ for waves initiated at $\theta \approx 32^\circ$ as a function of azimuthal angle for $\Delta = 6.2$ Mm, derived from three 1.5 kG sunspot models with varying Wilson depression depths. The solid lines are the results from 300 km model, the dotted lines represents the 400 km model, and the dashed lines represent the 500 km model. Panel a) represents 3 mHz travel times and panel b) 5 mHz travel times.

present, but with the direct magnetic effects on the waves suppressed. The directional travel times are then measured in an identical manner as before, with the results shown in Figure 7. These travel times can be directly compared with those derived from the 1.5 kG magnetic sunspot in Figure 3, which we do so in Figure 8, where we show some line plots with the thermal and magnetic travel times plotted on the same scale for a selection of θ.

It is important to note that the resulting "thermal travel-time perturbations" produced from these calculations result from a combination of thermal perturbations and geometrical effects due to the presence of a Wilson depression. When considering purely thermal effects on their own, i.e, a cooler plasma with a reduced sound speed and no Wilson depression, one would expect to see positive travel-time shifts with respect to the quiet Sun, as waves travel slower in the cooler medium. On the other hand, the presence of a Wilson depression can change the wave-path length, depending on the wave propagation direction (towards or way from the umbra for example) and frequency.

In Figure 7 − 8 it is clearly evident that the geometrical effects introduced by the Wilson depression are indeed significant for waves travelling towards the "umbra" ($\phi < 50^\circ$), with the reduction in path length seemingly overriding the effects of the cooler plasma, resulting in similar (negative) travel-time shifts to those produced by the magnetic sunspot model. The combination of longer path length and cooler plasma results in positive $\delta\tau$ for waves travelling away from the spot centre, where in the magnetic sunspot model we observed negative $\delta\tau$. A closer look at comparison plots in Figure 8 also reveals that the travel time increase due to fast-to-Alfvén conversion, typically seen around $\phi \approx 80^\circ - 100^\circ$, is absent in the thermal travel times. This indicates that the phase shifts produced by fast-to-Alfvén mode conversion are indeed distinguishable from thermal/geometrical effects and have a distinct and significant effect on helioseismic travel time measurements in sunspots.

The measured thermal $\delta\tau$ at 3 and 5 mHz appear to reach their peak at $\theta \approx 32^\circ$ in Figure 7. However, we must remember that θ in the thermal calculations is purely representative of the source position, not actual field inclination from vertical, as magnetic effects are suppressed for

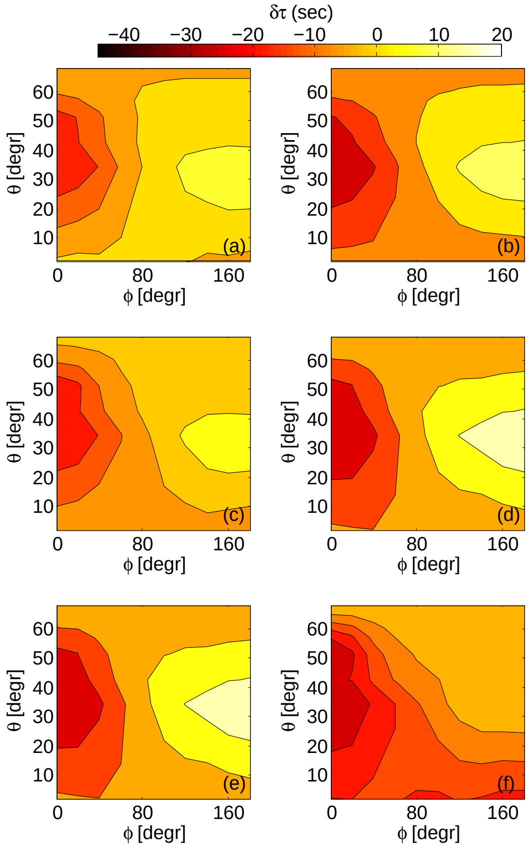

Figure 7. One-way phase travel time perturbations ($\delta\tau$) derived from a model where only the thermal perturbations corresponding to the 1.5 kG sunspot with a Wilson depression of 400 km are present. Panels (a-b) represent a wave travel distance of $\Delta = 6.2$ Mm, (c-d) represent $\Delta = 8.7$ Mm, and (e-f) represent $\Delta = 11.6$ Mm. Left column represents 3 mHz travel times and right column 5 mHz.

these calculations. Hence, this apparent dependance on θ is a purely geometrical effect and is distinctly different from the "ramp effect" and fast-to-slow mode conversion-induced phase shifts we can observe in the magnetic $\delta\tau$ at 3 and 5 mHz in Figure 3.

6 DISCUSSION AND CONCLUSIONS

As solar imaging hardware becomes increasingly sophisticated, the need for innovative diagnostic tools and precise modelling of wave propagation and transformation properties in strong magnetic field regions of sunspots is made ever more apparent. Building on previous numerical studies which employed simple plane-parallel atmospheres, we conducted a non-exhaustive parametric study of waves in model sunspot atmospheres in an attempt to further our understanding of the implications of MHD mode conversion on helioseismic measurements.

By using time-distance heliosiesmology and a travel-

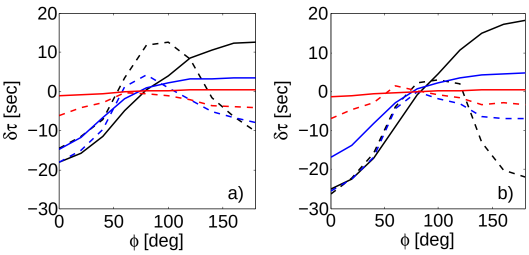

Figure 8. Line-plots of one-way phase travel time perturbations $\delta\tau$ along ϕ for waves initiated at $\theta \approx 34°$ (black), $\theta \approx 51°$ (blue) and $\theta \approx 65°$ (red) for $\Delta = 6.2$ Mm. The solid lines denote travel times derived from the 1.5 kG thermal sunspot model, while the dashed lines denote the magnetic sunspot model. Panel a) represents 3 mHz travel times and panel b) the 5 mHz travel times.

time measurement scheme sensitive to magnetic field orientation, we find that: i) The general behaviour of the travel-time shifts for the various sunspot models analysed is strikingly similar to that derived in Cally & Moradi (2013) and Moradi & Cally (2014), being strongly linked to mode conversion in the atmosphere; ii) the magnitude of the directional travel times is dependant on the sunspot field strength, wave frequency and travel distance; iii) the depth of the Wilson depression can produce a measurable change in travel times, with slightly faster travel times produced by waves travelling in the direction of the sunspot axis as the Wilson depression depth is increased from 300 to 500 km below the surface; and finally iv) wave path changes produced by the underlying thermal structure of the sunspot appear to be the most significant contributor to the travel-time shifts for waves travelling towards and inside the umbra. Away from the umbra however, it is the magnetic effects that dominate.

Overall, these results paint a fairly consistent picture: that the seismic waves' journey through the atmosphere can directly affect the wave travel times that are the basis of our inferences about the subsurface structure of sunspots, and in particular these effects are directional, depending on the orientation of the sunspot magnetic field. The close correspondence between these results and those derived previously using translationally invariant atmospheres, combined with the fact that directional filtering is directly extensible to real helioseismic data, argues strongly for the viability of directional time-distance probing of real solar magnetic regions. This will be the focus of future studies.

In conclusion, directional helioseismology significantly enhances our computational helioseismology toolkit, where recently a number of other important advances have been made in both forward (Schunker et al. 2013) and inverse (Hanasoge et al. 2012) modelling, ultimately leading to more precise helioseismic inferences of the subsurface structure and dynamics of sunspots.

This work was supported by an award under the Merit Allocation Scheme on the NCI National Facility at the ANU, as well as by the Multi-modal Australian ScienceS Imaging and Visualisation Environment (MASSIVE). A portion of the computations was also performed on the gSTAR national facility at Swinburne University of Technology. gSTAR is funded by Swinburne and the Australian Government's Education Investment Fund. Dr Shelyag is the recipient of an Australian Research Council's Future Fellowship (project number FT120100057).

REFERENCES

Avrett E. H., 1981, in The Physics of Sunspots, Cram L. E., Thomas J. H., eds., pp. 235–255
Bel N., Leroy B., 1977, A&A, 55, 239
Braun D. C., Birch A. C., 2006, ApJ, 647, L187
Braun D. C., Birch A. C., Rempel M., Duvall T. L., 2012, ApJ, 744, 77
Braun D. C., Lindsey C., 2000, Sol. Phys., 192, 307
Bray R. J., Loughhead R. E., 1964, Sunspots. The International Astrophysics Series, London: Chapman Hall, 1964
Brüggen M., Spruit H. C., 2000, Sol. Phys., 196, 29
Cally P. S., 1995, ApJ, 451, 372
Cally P. S., 2009, MNRAS, 395, 1309
Cally P. S., Bogdan T. J., Zweibel E. G., 1994, ApJ, 437, 505
Cally P. S., Goossens M., 2008, Sol. Phys., 251, 251
Cally P. S., Hansen S. C., 2011, ApJ, 738, 119
Cally P. S., Moradi H., 2013, MNRAS, 435, 2589
Cameron R. H., Gizon L., Schunker H., Pietarila A., 2011, Sol. Phys., 268, 293
Chou D.-Y., 2000, Sol. Phys., 192, 241
Christensen-Dalsgaard J. et al., 1996, Science, 272, 1286
Couvidat S., Gizon L., Birch A. C., Larsen R. M., Kosovichev A. G., 2005, ApJS, 158, 217
Couvidat S., Rajaguru S. P., 2007, ApJ, 661, 558
Crouch A. D., Cally P. S., 2003, Sol. Phys., 214, 201
Duvall T. L., Jefferies S. M., Harvey J. W., Pomerantz M. A., 1993, Nature, 362, 430
Duvall T. L. J., D'Silva S., Jefferies S. M., Harvey J. W., Schou J., 1996, Nature, 379, 235
Felipe T., 2012, ApJ, 758, 96
Gizon L., Birch A. C., 2002, ApJ, 571, 966
Gizon L., Birch A. C., Spruit H. C., 2010, ARA&A, 48, 289
Gizon L. et al., 2009, Space Sci. Rev., 144, 249
Hanasoge S., Birch A., Gizon L., Tromp J., 2012, Physical Review Letters, 109, 101101
Hanasoge S. M., 2007, PhD thesis, Stanford University
Hansen S. C., Cally P. S., 2014, Sol. Phys.
Jess D. B., Shelyag S., Mathioudakis M., Keys P. H., Christian D. J., Keenan F. P., 2012, ApJ, 746, 183
Khomenko E., Cally P. S., 2011, Journal of Physics Conference Series, 271, 012042
Khomenko E., Cally P. S., 2012, ApJ, 746, 68
Khomenko E., Collados M., 2008, ApJ, 689, 1379
Khomenko E., Kosovichev A., Collados M., Parchevsky K., Olshevsky V., 2009, ApJ, 694, 411
Kosovichev A. G., Duvall, Jr. T. L., 1997, in ASSL Vol. 225: SCORe'96 : Solar Convection and Oscillations and their Relationship, pp. 241–260
Kosovichev A. G., Duvall, Jr. T. L., Scherrer P. H., 2000, Sol. Phys., 192, 159

Kurucz R., 1993, ATLAS9 Stellar Atmosphere Programs and 2 km/s grid. Kurucz CD-ROM No. 13. Cambridge, Mass.: Smithsonian Astrophysical Observatory, 1993., 13
Lagarias, J. C., Reeds J. A., Wright M. H., E. W. P., 1998, SIAM Journal of Optimization, 9, 112
Lindsey C., Braun D. C., 2000, Sol. Phys., 192, 261
Lindsey C., Cally P. S., Rempel M., 2010, ApJ, 719, 1144
Low B. C., 1980, Sol. Phys., 67, 57
Martínez Pillet V., Vazquez M., 1993, A&A, 270, 494
Mathew S. K., Solanki S. K., Lagg A., Collados M., Borrero J. M., Berdyugina S., 2004, A&A, 422, 693
Moradi H., 2012, Astronomische Nachrichten, 333, 1003
Moradi H. et al., 2010, Sol. Phys., 267, 1
Moradi H., Cally P. S., 2008, Sol. Phys., 251, 309
Moradi H., Cally P. S., 2013, Journal of Physics Conference Series, 440, 012047
Moradi H., Cally P. S., 2014, ApJ, 782, L26
Moradi H., Hanasoge S. M., Cally P. S., 2009, ApJ, 690, L72
Parchevsky K. V., Kosovichev A. G., 2007, ApJ, 666, L53
Pizzo V. J., 1986, ApJ, 302, 785
Rempel M., Schüssler M., Knölker M., 2009, ApJ, 691, 640
Schunker H., Cally P. S., 2006, MNRAS, 372, 551
Schunker H., Gizon L., Cameron R. H., Birch A. C., 2013, A&A, 558, A130
Shelyag S., Zharkov S., Fedun V., Erdélyi R., Thompson M. J., 2009, A&A, 501, 735
Spruit H. C., Bogdan T. J., 1992, ApJ, 391, L109
Vernazza J. E., Avrett E. H., Loeser R., 1981, ApJS, 45, 635
Watson F., Fletcher L., Dalla S., Marshall S., 2009, Sol. Phys.
Woodard M. F., 1997, ApJ, 485, 890

Bibliography

Arber, T., Botha, G., & Brady, C. S. 2009, The Astrophysical Journal, 705, 1183 103

Arber, T., Brady, C. S., & Shelyag, S. 2016, The Astrophysical Journal, 817, 94 105

Arber, T., Haynes, M., & Leake, J. E. 2007, The Astrophysical Journal, 666, 541 103

Arregui, I. 2015, Phil. Trans. R. Soc. A, 373, 20140261 6

Avrett, E., Tian, H., Landi, E., Curdt, W., & Wülser, J.-P. 2015, The Astrophysical Journal, 811, 87 11, 40, 42

Avrett, E. H. 1981, in The Physics of Sunspots, 235–255 81

Avrett, E. H., & Loeser, R. 2008, The Astrophysical Journal Supplement Series, 175, 229 11, 40

Balraforth, N., & Gougb, D. 1988, SEISMOLOGY OF THE SUN & SUN-LIKE STARS, 47 21

Balthasar, H., Pillet, V. M., Schleicher, H., & Wöhl, H. 1998, Solar Physics, 182, 65 99

Barceló, S., Carbonell, M., & Ballester, J. 2011, Astronomy & Astrophysics, 525, A60 105

Barklem, P., Anstee, S., & O'Mara, B. 1998, Publications of the Astronomical Society of Australia, 15, 336 63

Bel, N., & Leroy, B. 1977, Astronomy and Astrophysics, 55, 239 5

Berenger, J.-P. 1994, Journal of computational physics, 114, 185 116

Berland, J., Bogey, C., & Bailly, C. 2006, Computers & Fluids, 35, 1459 27

Berland, J., Bogey, C., Marsden, O., & Bailly, C. 2007, Journal of Computational Physics, 224, 637 27

Bhattacharya, J., & Hanasoge, S. M. 2016, arXiv preprint arXiv:1605.09315 7

Birch, A., Braun, D., Hanasoge, S., & Cameron, R. 2009, Solar Physics, 254, 17 7

Birn, J., et al. 2001, Journal of Geophysical Research: Space Physics, 106, 3715 104

Bogdan, T., & Judge, P. 2006, Philosophical Transactions of the Royal Society of London A: Mathematical, Physical and Engineering Sciences, 364, 313 22

Bogey, C., & Bailly, C. 2004, Journal of Computational Physics, 194, 194 27

Bonet, J., Márquez, I., Almeida, J. S., Cabello, I., & Domingo, V. 2008, The Astrophysical Journal Letters, 687, L131 8

Braginskii, S. 1965, Reviews of plasma physics, 1, 205 108

Brandenburg, A., & Zweibel, E. G. 1994, The Astrophysical Journal, 427, L91 103

Cally, P. 2006, Philosophical Transactions of the Royal Society of London A: Mathematical, Physical and Engineering Sciences, 364, 333 3, 23, 42

—. 2007, Astronomische Nachrichten, 328, 286 3, 22, 23

Cally, P., Moradi, H., & Rajaguru, S. 2016, Low-Frequency Waves in Space Plasmas, 489 23

Cally, P. S., & Andries, J. 2016, in prep, Living Reviews in Solar Physics 17

Cally, P. S., & Goossens, M. 2008, Solar Physics, 251, 251 23

Cally, P. S., & Hansen, S. C. 2011, The Astrophysical Journal, 738, 119 5, 23

Cally, P. S., & Khomenko, E. 2015, The Astrophysical Journal, 814, 106 17, 104

Cally, P. S., & Moradi, H. 2013, Monthly Notices of the Royal Astronomical Society, stt1473 5, 22

Cameron, R., Gizon, L., & Daiffallah, K. 2007, Astronomische Nachrichten, 328, 313 7, 24

Cameron, R., Gizon, L., Schunker, H., & Pietarila, A. 2011, Solar Physics, 268, 293 11, 28, 79

Cargill, P., Warren, H., & Bradshaw, S. 2015, Phil. Trans. R. Soc. A, 373, 20140260 6

Caunt, S., & Korpi, M. 2001, Astronomy & Astrophysics, 369, 706 114

Christensen-Dalsgaard, J., Dappen, W., Ajukov, S., Anderson, E., et al. 1996, Science, 272, 1286 11, 40

Colonius, T. 2004, Annu. Rev. Fluid Mech., 36, 315 27, 32, 88

Courant, R., Friedrichs, K., & Lewy, H. 1928, Mathematische annalen, 100, 32 7

Couvidat, S. 2013, Solar Physics, 282, 15 8

Cowling, T. 1946, Monthly Notices of the Royal Astronomical Society, 106, 218 8

Cranmer, S., & Van Ballegooijen, A. 2005, The Astrophysical Journal Supplement Series, 156, 265 7

De Hoffmann, F., & Teller, E. 1950, Physical Review, 80, 692 110

De Pontieu, B., & Haerendel, G. 1998, Astronomy and Astrophysics, 338, 729 104

De Pontieu, B., Martens, P., & Hudson, H. 2001, The Astrophysical Journal, 558, 859 105

Deubner, F.-L., & Gough, D. 1984, Annual review of astronomy and astrophysics, 22, 593 21, 42

Díaz, A., Khomenko, E., & Collados, M. 2014, Astronomy & Astrophysics, 564, A97 103

Efremov, V., Parfinenko, L., Solov'ev, A., & Kirichek, E. 2014, Solar Physics, 289, 1983 9

Evans, J., & Michard, R. 1962, The Astrophysical Journal, 135, 812 1

Fedun, V., Shelyag, S., Verth, G., Mathioudakis, M., & Erdélyi, R. 2011, Annales Geophysicae-Atmospheres Hydrospheresand Space Sciences, 29, 1029 8, 111

Felipe, T. 2012, The Astrophysical Journal, 758, 96 24, 79

Felipe, T., Braun, D., Crouch, A., & Birch, A. 2016, The Astrophysical Journal, 829, 67 37

Felipe, T., Crouch, A., & Birch, A. 2014a, The Astrophysical Journal, 788, 136 8

Felipe, T., & Khomenko, E. 2017, arXiv preprint arXiv:1702.00997 141

Felipe, T., Khomenko, E., & Collados, M. 2010, The Astrophysical Journal, 719, 357 7, 24, 79, 112

—. 2011, The Astrophysical Journal, 735, 65 7

Felipe, T., Socas-Navarro, H., & Khomenko, E. 2014b, The Astrophysical Journal, 795, 9 79

Fleck, B., Couvidat, S., & Straus, T. 2011, Solar Physics, 271, 27 12, 100

Fontenla, J. 2005, Astronomy & Astrophysics, 442, 1099 103

Forteza, P., Oliver, R., Ballester, J., & Khodachenko, M. 2007, Astronomy & Astrophysics, 461, 731 104

Foukal, P., Bernasconi, P., Eaton, H., & Rust, D. 2004, The Astrophysical Journal Letters, 611, L57 83

Gedney, S. D., & Zhao, B. 2010, IEEE Transactions on Antennas and Propagation, 58, 838 33

Gent, F. A., Fedun, V., Mumford, S. J., & Erdélyi, R. 2013, Monthly Notices of the Royal Astronomical Society, 435, 689 111

Gizon, L., & Birch, A. C. 2005, Living Reviews in Solar Physics, 2, 1 3, 37

Gizon, L., et al. 2009, Space Science Reviews, 144, 249 79

Goedbloed, J. P., & Poedts, S. 2004, Principles of magnetohydrodynamics: with applications to laboratory and astrophysical plasmas (Cambridge university press) 15

Goldreich, P., & Keeley, D. 1977, The Astrophysical Journal, 212, 243 6

Goldreich, P., Murray, N., & Kumar, P. 1994, The Astrophysical Journal, 424, 466 37

Goodman, M., & Kazeminezhad, F. 2010, Memorie della Societa Astronomica Italiana, 81, 631 105

Goodman, M. L. 2005, The Astrophysical Journal, 632, 1168 105

—. 2011, The Astrophysical Journal, 735, 45 105

Gough, D. 2007, Astronomische Nachrichten, 328, 273 21

Grossmann-Doerth, U., Schüssler, M., Sigwarth, M., & Steiner, O. 2000, Astronomy and Astrophysics, 357, 351 69

Grossmann-Doerth, U., Schüssler, M., & Steiner, O. 1998, Astronomy and Astrophysics, 337, 928 6

Grotian, W. 1939, Naturwissenschaften, 27, 214 6

Gurman, J. B., & House, L. L. 1981, Solar Physics, 71, 5 9

Haerendel, G. 1992 105

Hagyard, M., West, E., & Cumings, N. 1977, Solar Physics, 53, 3 9

Hanasoge, S., Couvidat, S., Rajaguru, S., & Birch, A. 2008, Monthly Notices of the Royal Astronomical Society, 391, 1931 29, 41

Hanasoge, S., & Duvall, T. 2007, Astronomische Nachrichten, 328, 319 37

Hanasoge, S., Duvall Jr, T., & Couvidat, S. 2007, The Astrophysical Journal, 664, 1234 24

Hanasoge, S. M. 2008, The Astrophysical Journal, 680, 1457 7, 11, 94

—. 2011, Astrophysics Source Code Library, 1, 05006 7, 24, 88

Hanasoge, S. M., Birch, A., Gizon, L., & Tromp, J. 2011, The Astrophysical Journal, 738, 100 5

Hanasoge, S. M., Komatitsch, D., & Gizon, L. 2010, Astronomy & Astrophysics, 522, A87 26, 33, 47, 88

Hanasoge, S. M., & Tromp, J. 2014, The Astrophysical Journal, 784, 69 5

Hansen, S. C., & Cally, P. S. 2012, The Astrophysical Journal, 751, 31 24

Hart, A. 1954, Monthly Notices of the Royal Astronomical Society, 114, 17 6

Hill, F. 1988, The Astrophysical Journal, 333, 996 37

Hillier, A., Takasao, S., & Nakamura, N. 2016, Astronomy & Astrophysics, 591, A112 103

Irwin, A. W. 2012, Astrophysics Source Code Library, 1, 11002 65, 82

Ishikawa, R., Tsuneta, S., & Jurčák, J. 2010, The Astrophysical Journal, 713, 1310 5

Ishikawa, R., et al. 2008, Astronomy & Astrophysics, 481, L25 5

Jefferies, S. M., McIntosh, S. W., Armstrong, J. D., Bogdan, T. J., Cacciani, A., & Fleck, B. 2006, The Astrophysical Journal Letters, 648, L151 22

Jess, D. B., Mathioudakis, M., Erdélyi, R., Crockett, P. J., Keenan, F. P., & Christian, D. J. 2009, Science, 323, 1582 7

Judge, P. 2008, The Astrophysical Journal Letters, 683, L87 104

Jurčák, J., González, N. B., Schlichenmaier, R., & Rezaei, R. 2015, Astronomy & Astrophysics, 580, L1 9

Kato, Y., & Tsutomu, T. 1956 104

Kennel, C. F., Blandford, R. D., & Coppi, P. 1989, Journal of plasma physics, 42, 299 110

Khodachenko, M., Arber, T., Rucker, H. O., & Hanslmeier, A. 2004, Astronomy & Astrophysics, 422, 1073 104

Khomenko, E. 2015, in Highlights of Spanish Astrophysics VIII, Vol. 1, 677–688 17

Khomenko, E. 2016, Plasma Physics and Controlled Fusion, 59, 014038 103

Khomenko, E., & Cally, P. 2012, The Astrophysical Journal, 746, 68 7, 23, 25, 79, 100, 118

Khomenko, E., & Calvo Santamaria, I. 2013, in Journal of Physics: Conference Series, Vol. 440, IOP Publishing, 012048 6

Khomenko, E., & Collados, M. 2008, The Astrophysical Journal, 689, 1379 11, 41, 79, 80, 141

—. 2009, Astronomy & Astrophysics, 506, L5 7, 94

—. 2012, The Astrophysical Journal, 747, 87 104

Khomenko, E., Collados, M., Diaz, A., & Vitas, N. 2014, Physics of Plasmas (1994-present), 21, 092901 106

Khomenko, E., Collados, M., Solanki, S., Lagg, A., & Bueno, J. T. 2003, Astronomy & Astrophysics, 408, 1115 12

Khomenko, E., Shelyag, S., Solanki, S., & Vögler, A. 2005, Astronomy & Astrophysics, 442, 1059 12

Krasnoselskikh, V., Vekstein, G., Hudson, H., Bale, S., & Abbett, W. 2010, The Astrophysical Journal, 724, 1542 104, 105

Kulsrud, R. 2005, Plasma Physics for Astrophysics, Princeton series in astrophysics (Princeton University Press) 109

Kumar, N., & Roberts, B. 2003, Solar Physics, 214, 241 105

Kumar, P., & Basu, S. 2000, The Astrophysical Journal Letters, 545, L65 37

Kurucz, R. 1993, ATLAS9 Stellar Atmosphere Programs and 2 km/s grid. Kurucz CD-ROM No. 13. Cambridge, Mass.: Smithsonian Astrophysical Observatory, 1993., 13 62

Lamb, H. 1932, Hydrodynamics (Cambridge university press) 42

Leake, J. E., Arber, T., & Khodachenko, M. 2005, Astronomy & Astrophysics, 442, 1091 105

Leake, J. E., Lukin, V. S., Linton, M. G., & Meier, E. T. 2012, The Astrophysical Journal, 760, 109 103

Lehmann, A., & Wardle, M. 2016, Monthly Notices of the Royal Astronomical Society, 455, 2066 110

Leighton, R. B., Noyes, R. W., & Simon, G. W. 1962, The Astrophysical Journal, 135, 474 1

Low, B. 1975, The Astrophysical Journal, 197, 251 11, 81

—. 1980, Solar Physics, 67, 57 11, 80

Martínez Pillet, V. 1997, in 1st Advances in Solar Physics Euroconference. Advances in Physics of Sunspots, Vol. 118, 212 9

Martínez-Sykora, J., De Pontieu, B., & Hansteen, V. 2012, The Astrophysical Journal, 753, 161 104

McIntosh, S. W., & Jefferies, S. M. 2006, The Astrophysical Journal Letters, 647, L77 22

Mihalas, D., & Weibel-Mihalas, B. 1999, Foundations of Radiation Hydrodynamics, Dover Books on Physics (Dover) 116

Moradi, H., & Cally, P. 2013, in Fifty Years of Seismology of the Sun and Stars, Vol. 478, 263 3, 100

Moradi, H., Cally, P., Przybylski, D., & Shelyag, S. 2015, Monthly Notices of the Royal Astronomical Society, 449, 3074 5, 100

Moradi, H., & Cally, P. S. 2014, The Astrophysical Journal Letters, 782, L26 24, 28, 88

Moradi, H., Hanasoge, S., & Cally, P. 2008, The Astrophysical Journal Letters, 690, L72 11, 79

Moradi, H., et al. 2010, Solar Physics, 267, 1 9, 79

Müller, D., Marsden, R. G., Cyr, O. S., Gilbert, H. R., et al. 2013, Solar Physics, 285, 25 5

Murawski, K., Ballai, I., Srivastava, A., & Lee, D. 2013, Monthly Notices of the Royal Astronomical Society, 436, 1268 24

Murawski, K., Solov'ev, A., Musielak, Z., Srivastava, A., & Kraśkiewicz, J. 2015, Astronomy & Astrophysics, 577, A126 11

Murphy, N. A., & Lukin, V. S. 2015, The Astrophysical Journal, 805, 134 103

Nagashima, K., et al. 2014, Solar Physics, 289, 3457 12, 99, 100

Narain, U., & Ulmschneider, P. 1996, Space Science Reviews, 75, 453 6

Nordlund, Å., & Stein, R. 2001, The Astrophysical Journal, 546, 576 37

Osterbrock, D. E. 1961, The Astrophysical Journal, 134, 347 105

Pandey, B., & Wardle, M. 2008, Monthly Notices of the Royal Astronomical Society, 385, 2269 104

—. 2012, Monthly Notices of the Royal Astronomical Society, 426, 1436 103

Pandey, B. P., Vranjes, J., & Krishan, V. 2008, Monthly Notices of the Royal Astronomical Society, 386, 1635 105

Parchevsky, K., & Kosovichev, A. 2007, The Astrophysical Journal, 666, 547 27, 29, 37, 38, 39, 40, 92, 116, 141

Parchevsky, K. V., Zhao, J., & Kosovichev, A. G. 2008, The Astrophysical Journal, 678, 1498 37

Parker, E. 1975, Solar Physics, 40, 291 8

—. 1988, The Astrophysical Journal, 330, 474 6

Piddington, J. 1956, Monthly Notices of the Royal Astronomical Society, 116, 314 105

Pizzo, V. 1986, The Astrophysical Journal, 302, 785 11, 81

Priest, E. R. 2012, Solar magnetohydrodynamics, Vol. 21 (Springer Science & Business Media) 17

Przybylski, D., Shelyag, S., & Cally, P. 2015, The Astrophysical Journal, 807, 20 38

Rajaguru, S. 2011, Astronomical Society of India Conference Series, 2 79

Rajaguru, S., Couvidat, S., Sun, X., Hayashi, K., & Schunker, H. 2013, Solar Physics, 287, 107 5, 98

Rees, D., Durrant, C., & Murphy, G. 1989, The Astrophysical Journal, 339, 1093 57

Rempel, M., & Schlichenmaier, R. 2011, Living Reviews in Solar Physics, 8, 1 8

Rempel, M., Schüssler, M., & Knölker, M. 2009, The Astrophysical Journal, 691, 640 11, 28, 88

Rijs, C., Moradi, H., Przybylski, D., & Cally, P. S. 2015, The Astrophysical Journal, 801, 27 7, 38, 94

Rijs, C., Rajaguru, S., Przybylski, D., Moradi, H., Cally, P. S., & Shelyag, S. 2016, The Astrophysical Journal, 817, 45 7, 24, 37, 94

Rogers, B., Denton, R., Drake, J., & Shay, M. 2001, Physical review letters, 87, 195004 104

Santamaria, I. C., Khomenko, E., & Collados, M. 2015, Astronomy & Astrophysics, 577, A70 118

Scherrer, P. H., et al. 2012, Solar Physics, 275, 207 5, 100

Schlüter, A., & Temesváry, S. 1958, in Electromagnetic Phenomena in Cosmical Physics, Vol. 6, 263 11, 79, 81

Schmitz, F., & Fleck, B. 2003, Astronomy & Astrophysics, 399, 723 22

Schou, J., & Bogart, R. 1998, The Astrophysical Journal Letters, 504, L131 37

Schunker, H., & Cally, P. 2006, Monthly Notices of the Royal Astronomical Society, 372, 551 3

Schunker, H., Cameron, R., Gizon, L., & Moradi, H. 2011, Solar Physics, 271, 1 27, 29, 80

Schwabe, H. 1843, Astronomische Nachrichten, 20, 234 8

Schwarzschild, M. 1948, The Astrophysical Journal, 107, 1 37

Shay, M., Drake, J., Rogers, B., & Denton, R. 2001, Journal of Geophysical Research, 106, 3759 104

Shchukina, N. G., Trujillo Bueno, J., & Asplund, M. 2005, The Astrophysical journal, 618, 939 57

Shelyag, S., Cally, P., Reid, A., & Mathioudakis, M. 2013, The Astrophysical Journal Letters, 776, L4 103, 105

Shelyag, S., Erdélyi, R., & Thompson, M. 2006, The Astrophysical Journal, 651, 576 4

—. 2007, Astronomy & Astrophysics, 469, 1101 7, 62, 79, 83

Shelyag, S., Fedun, V., & Erdélyi, R. 2008, Astronomy & Astrophysics, 486, 655 7, 24

Shelyag, S., Mathioudakis, M., & Keenan, F. 2012, The Astrophysical Journal Letters, 753, L22 8, 65, 103, 105

Shelyag, S., Mathioudakis, M., Keenan, F., & Jess, D. 2010, Astronomy & Astrophysics, 515, A107 111

Shelyag, S., & Przybylski, D. 2014, Publications of the Astronomical Society of Japan, psu085 8, 12, 79, 105

Shelyag, S., Schüssler, M., Solanki, S., Berdyugina, S., & Vögler, A. 2004, Astronomy & Astrophysics, 427, 335 12

Shelyag, S., Zharkov, S., Fedun, V., Erdélyi, R., & Thompson, M. 2009, Astronomy & Astrophysics, 501, 735 11, 37, 47, 79, 89

Socas-Navarro, H., de la Cruz Rodriguez, J., Ramos, A. A., Bueno, J. T., & Cobo, B. R. 2015, Astronomy & Astrophysics, 577, A7 62, 65

Solanki, S., Walther, U., & Livingston, W. 1993, Astronomy and Astrophysics, 277, 639 11

Solanki, S. K. 1987, PhD thesis, Diss. Naturwiss. ETH Zürich, Nr. 8309, 0000. Ref.: Stenflo, JO; Korref.: Nussbaumer, H. 62, 83

Soler, R., Ballester, J., & Zaqarashvili, T. 2015, Astronomy & Astrophysics, 573, A79 105

Soler, R., Carbonell, M., Ballester, J., & Terradas, J. 2013, The Astrophysical Journal, 767, 171 105

Soler, R., Díaz, A., Ballester, J., & Goossens, M. 2012, The Astrophysical Journal, 749, 163 103

Soler, R., Goossens, M., Terradas, J., & Oliver, R. 2014, The Astrophysical Journal, 781, 111 105

Soler, R., Oliver, R., & Ballester, J. 2009, The Astrophysical Journal, 699, 1553 105

Spruit, H. 2013, arXiv preprint arXiv:1301.5572 20, 21

Staiger, J. 2012, in SPIE Astronomical Telescopes+ Instrumentation, International Society for Optics and Photonics, 844675–844675 5, 142

Stein, R., & Nordlund, Å. 1989, The Astrophysical Journal, 342, L95 37

—. 2001, The Astrophysical Journal, 546, 585 37

Stein, R. F., & Leibacher, J. 1974, Annual review of astronomy and astrophysics, 12, 407 1

Steiner, O., Rezaei, R., Schaffenberger, W., & Wedemeyer-Böhm, S. 2008, The Astrophysical Journal Letters, 680, L85 105

Stenflo, J. 1973, Solar Physics, 32, 41 6

—. 2013, The Astronomy and Astrophysics Review, 21, 1 56

Stokes, G. G. 1852, Philosophical Transactions of the Royal Society of London, 142, 463 56

Trujillo Bueno, I. 2003, Boletín informativo de la SEA, 6 55, 61

Tsap, Y. T., Stepanov, A. V., & Kopylova, Y. G. 2011, Solar Physics, 270, 205 7

Tsuneta, S., et al. 2008, Solar Physics, 249, 167 66

Ulrich, R. K. 1970, The Astrophysical Journal, 162, 993 2

Unno, W. 1956, Publications of the Astronomical Society of Japan, 8, 108 57

Unno, W., & Simoda, M. 1963, Publications of the Astronomical Society of Japan, 15, 78 83

Vernazza, J. E., Avrett, E. H., & Loeser, R. 1981, The Astrophysical Journal Supplement Series, 45, 635 11, 40, 111

Vichnevetsky, R., & Bowles, J. B. 1982, Fourier analysis of numerical approximations of hyperbolic equations, Vol. 5 (Siam) 27

Vögler, A., Shelyag, S., Schüssler, M., Cattaneo, F., Emonet, T., & Linde, T. 2005, Astronomy & Astrophysics, 429, 335 12, 27, 63, 65, 114, 116

Vranjes, J., Pandey, B., & Poedts, S. 2006, Planetary and Space Science, 54, 695 103

Vranjes, J., Poedts, S., Pandey, B., & De Pontieu, B. 2008, Astronomy & Astrophysics, 478, 553 7, 105

Waters, C., Lysak, R., & Sciffer, M. 2013, Earth, Planets and Space, 65, 385 104

Zaqarashvili, T., Khodachenko, M., & Rucker, H. 2011a, Astronomy & Astrophysics, 534, A93 7, 105

—. 2011b, Astronomy & Astrophysics, 529, A82 7, 105

Zaqarashvili, T., Khodachenko, M., & Soler, R. 2013, Astronomy & Astrophysics, 549, A113 7

Zharkov, S., Shelyag, S., Fedun, V., Erdélyi, R., & Thompson, M. 2013, Ann. Geophys, 31, 1357 79, 98, 99

Zweibel, E. G. 1989, The Astrophysical Journal, 340, 550 103